Mathematical Modelling of Pattern Formation in Yeast Biofilms

Alexander Tam

December 9, 2019

Thesis submitted for the degree of

Doctor of Philosophy

in

Applied Mathematics

at The University of Adelaide

Faculty of Engineering, Computer and Mathematical Sciences

School of Mathematical Sciences

THE UNIVERSITY *of* ADELAIDE

Contents

List of Figures

List of Tables

Abstract

We use mathematical modelling and experiments to investigate yeast biofilm growth and pattern formation. Biofilms are sticky communities of cells and fluid residing on surfaces. As yeast biofilms are a leading cause of hospital-acquired infections, researchers have developed methods of growing them on semi-solid agar. These biofilms initially form a thin circular shape, before transitioning to a non-uniform floral morphology. To quantify biofilm growth, we use a radial statistic the measure expansion speed, and an angular pair correlation function to quantify petal formation. These spatial statistics enable comparison between experiments and mathematical model predictions.

Our motivation is to improve understanding of the physical mechanisms governing biofilm formation. One hypothesised mechanism is nutrient-limited growth, in which movement and consumption of nutrients drives growth and generates patterns. Another hypothesis is that yeast biofilms expand by sliding motility, where cell proliferation and weak biofilm–substratum adhesion drive growth. Mathematical modelling enables us to investigate the contribution of each hypothesised mechanism to biofilm growth and pattern formation.

We use a reaction–diffusion system with non-linear, degenerate cell diffusion to model nutrient-limited biofilm growth. This model admits sharp-fronted travelling wave solutions that advance with constant speed, an assumption consistent with experimental data. To investigate whether the reaction–diffusion model can explain petal formation, we consider the linear stability of planar travelling wave solutions to transverse perturbations. There

is good agreement between the theory and experimental data, suggesting that nutrient-limited growth can explain floral pattern formation.

Next, we introduce biofilm mechanics by deriving a two-phase fluid model. We treat the biofilm as a mixture of cells and an extracellular matrix, and obtain governing equations from mass and momentum conservation. Since yeast biofilm height is small compared to their radius, we use the thin-film approximation in two scaling regimes to simplify the model. The extensional flow regime involves weak biofilm–substratum adhesion, and models expansion by sliding motility. In contrast, the lubrication regime involves strong biofilm–substratum adhesion, and large pressure and surface tension.

We compute axisymmetric numerical solutions to both thin-film models to investigate how mechanics affects biofilm growth. There is good agreement between the extensional flow model and experimental data, suggesting that sliding motility can explain expansion speed. Parameter sensitivity analyses show that increased nutrient supply and biomass production rates generate faster expansion. The effect of surface tension, which represents the strength of cell–cell adhesion, is the key difference between the two regimes. In the extensional flow model, surface tension inhibits ridge formation close to the leading edge, but does not affect expansion speed. In contrast, surface tension generates radial expansion in the lubrication regime.

Since the thin-film models enable us to predict biofilm height and nutrient uptake explicitly, they provide a more detailed description of biofilm growth than the reaction–diffusion model. However, their complexity makes it more difficult to use linear stability analysis to investigate two-dimensional patterns. This problem, and alternative expansion mechanisms such as osmotic swelling and agar deformation, provide avenues for future work.

Declaration

I certify that this work contains no material which has been accepted for the award of any other degree or diploma in my name, in any university or other tertiary institution and, to the best of my knowledge and belief, contains no material previously published or written by another person, except where due reference has been made in the text. In addition, I certify that no part of this work will, in the future, be used in a submission in my name, for any other degree or diploma in any university or other tertiary institution without the prior approval of the University of Adelaide and where applicable, any partner institution responsible for the joint-award of this degree.

I acknowledge that copyright of published works contained within this thesis resides with the copyright holder(s) of those works.

I also give permission for the digital version of my thesis to be made available on the web, via the University's digital research repository, the Library Search and also through web search engines, unless permission has been granted by the University to restrict access for a period of time.

I acknowledge the support I have received for my research through the provision of an Australian Government Research Training Program Scholarship.

Signed: ..... Date: .....

Acknowledgements

I am very grateful to the A. F. Pillow Trust for providing me with financial support throughout my PhD. The top-up scholarship is a generous gift to applied mathematics in Australia and New Zealand, and one that I was privileged to receive.

I would like to thank Brendan, Trent, and Tony, whose helpful comments on numerics influenced the work in my thesis. I am also grateful to the administrative staff, especially Maddy, Rachael, April, and Elaine, for arranging casual work and travel to several conferences. One of these conferences, my trip to ECMTB in Lisbon, was the highlight of my PhD experience.

It was a pleasure to work with Ee Lin, Jennie, Jo, and Vlad from the Department of Wine and Food Science. I am grateful for their kind and thoughtful responses to my many questions about yeast biology, and their experimental work was integral to my thesis.

I also give special thanks to Sarah, Jack, Thomas, and Hayden, whose friendship over the past few years I have valued so much. I also thank my family, Dianne, David, Emily, William, and San, for their constant support.

Finally, I have been very lucky to have had support and mentorship from three wonderful supervisors. I will always be grateful for the time and effort they have dedicated to my project. To Sanjeeva, thank you for agreeing to bring your enthusiasm and knowledge to my project. To Ed, thank you for teaching me so much, and your kindness and patience is an example for all to follow. To Ben, thank you for your belief in me over the years, which has had a profound impact on my life and career so far.

Chapter 1

Introduction

Pattern formation, the science of orderly visible structures that seemingly emerge spontaneously, is a discipline that has long fascinated applied mathematicians. This is especially so for the patterns generated by self-organisation of micro-organisms, which exhibit striking diversity (see Figure 1.1). An example of these colonies is the biofilm, in which cells collect on a surface and reside within an extracellular fluid matrix. Far from being a mere curiosity, biofilms are ubiquitous and have extensive effects on human life. Their ability to colonise medical devices makes them a leading cause of hospital-acquired infection, and their unique structure can make them impervious to antimicrobial agents. For these reasons, the mechanisms of biofilm formation have long fascinated researchers, and motivate the work in this thesis.

Biofilm formation is often investigated from a genetic perspective. However, although the mechanisms of pattern formation are often genetically-driven, the genes themselves cannot generate pattern and form. Understanding the physical mechanisms that drive pattern formation is required to obtain a detailed understanding of biofilm growth. Two prevailing mathematical theories of pattern formation guide our approach to modelling these mechanisms. The first is the chemical pre-patterning theory introduced by Turing [4]. His theory describes how reaction and diffusion of two chemical species can lead to the development of patterns such as stripes, spots, and spirals. These patterns

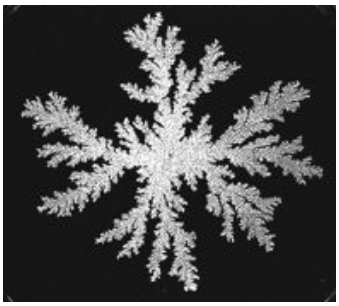

(a) Branched.

(b) Vortex.

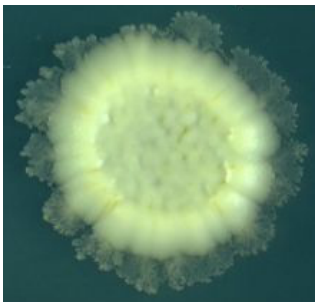

(c) Floral.

Figure 1.1: Examples of microbial colony patterns. (a) A colony of the bacterium *Bacillus subtilis*. Image from Fujikawa and Matsushita [1], reproduced in Tronnolone et al. [2] with permission from The Physical Society of Japan. (b) A colony of the bacterium *Paenibacillus vortex*. Image reproduced from Sirota-Madi et al. [3] under the Creative Commons Attribution 2.0 Generic (CC BY 2.0) License, https://creativecommons.org/licenses/by/2.0/. (c) A biofilm of the yeast *Saccharomyces cerevisiae*. Image: Zoltán Szenczi, Cambridge Systems Biology Centre and Department of Biochemistry, University of Cambridge.

can arise when uniform steady states of reaction–diffusion models are unstable. Turing's theory subsequently inspired significant use of reaction–diffusion models as prototype systems for understanding biological pattern formation [5] . More recently, Murray [6] popularised an alternative mechanochemical theory of pattern formation. This theory states that mechanical forces generated by interactions between cells and the environment can also give rise to pattern and form.

Biofilms in nature typically consist of multiple species of bacteria and yeast coexisting in a self-produced extracellular fluid matrix. In this thesis, we restrict our investigation to biofilm formation experiments of the budding yeast, *Saccharomyces cerevisiae*. These controlled experiments enable us to focus on the mechanisms of biofilm expansion, without the need to consider interactions between multiple species. Since *S. cerevisiae* is a common model organism in cell biology research, we expect that our results will apply to biofilms of any species. Therefore, our mathematical modelling is based on the current understanding of *S. cerevisiae*, and microbial biofilm formation in

general.

1.1 Yeast Biofilms

Yeasts are single-cell fungal organisms. As Figure 1.2 shows, each cell is typically ellipsoidal, with a length of approximately 4 µm along its major axis. There are approximately 1500 known yeast species [8], and they have

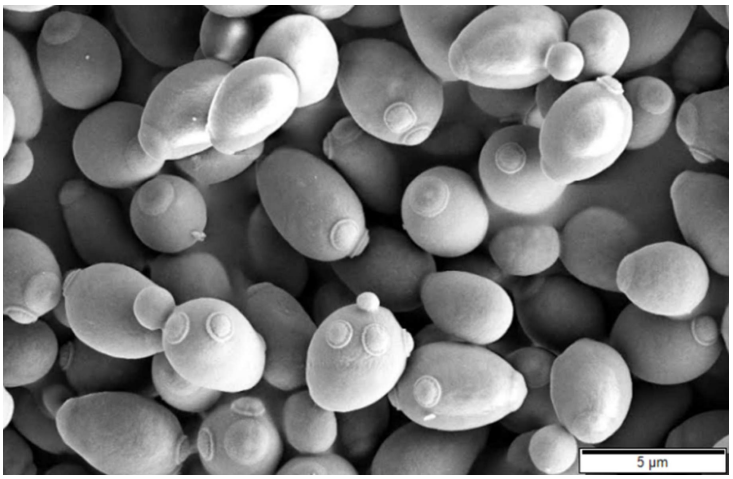

Figure 1.2: Cells of the budding yeast, *S. cerevisiae*. Image reproduced from Murtey and Ramasamy [7] under the Creative Commons Attribution–ShareAlike 3.0 Unported License (CC BY-SA 3.0), https://creativecommons.org/licenses/by-sa/3.0/.

wide-ranging effects on human life. For example, yeasts are used extensively in the production of food and drink such as bread and wine [9–13]. Another beneficial application is that genetically engineered yeasts are used in the sustainable production of chemicals and biofuels, which helps to reduce carbon emissions [14, 15].

In nature, yeast species often reside in complex, multi-cellular communities [10, 16–18]. A biofilm is a slimy community of bacteria or fungi existing on a surface. An estimated 80% of bacteria in nature exists in biofilm colonies [19]. For this reason, they have been described as the 'oldest, most successful and widespread form of life on Earth' [20], and have attracted significant research

attention. A distinguishing feature of biofilms is that the cells adhere to each other and reside within a self-produced extracellular matrix (ECM). This matrix consists of up to 97% water [21], with the remainder being extracellular polymeric substances (EPS). Although the composition and function of the ECM may vary, it provides biofilm colonies with several advantages over planktonic cells [20]. For example, the ECM has been observed to assist the transportation of nutrients and water [22, 23], and prevent penetration of harmful external substances [24].

Biofilms impact human life in many ways, and it would be advantageous to understand and potentially control their growth. In some contexts, biofilms can provide positive effects, for example in waste treatment [25] and microbial fuel cells [26]. However, they are also responsible for dental plaque, which can lead to tooth decay and gum disease [27]. Another important effect is that biofilms of pathogenic microbes often form on indwelling medical devices such as catheters, stents, and prostheses [19, 28, 29]. In particular, biofilms of the yeast *Candida albicans* are a leading cause of hospital-acquired infections [30], and are particularly threatening to immunocompromised people. These biofilms can be 30–2000 times more resistant to anti-fungal therapy than planktonic cells [19], and surgical intervention is often required to treat *C. albicans* infections effectively [30]. As well as being a health risk, this places a large financial burden on patients and health care providers [30]. If *C. albicans* biofilms persist, they can cause the serious progressive infection systemic candidiasis. This disease affects 1–2% of patients admitted to intensive care units, representing approximately 3–5 people per 100,000 of the general population at any time [31]. The overall mortality rate of systemic candidiasis is thought to be 10–20% [31], but 30–40% has also been quoted [32]. The most severe cases result in fulminant sepsis, which has a mortality rate exceeding 70% [31]. This provides a strong motivation to understand yeast biofilm growth.

The emergence of new pathogens compounds the clinical significance of yeast biofilms. For example, the emerging pathogen *Candida auris* has been

detected on five continents since being first observed in Japan in 2009 [33]. *C. auris* has attracted attention for its ability to resist common anti-fungal treatment, and reliable diagnostic tests are lacking [34]. Furthermore, *C. auris* is capable of biofilm formation [34], making it a threat to public health. Faced with the ever-changing range of clinically-relevant yeast species, it would be advantageous to elucidate common mechanisms that govern yeast biofilm formation and expansion. However, fungal biofilms are much less widely studied than bacterial biofilms [35].

In our work, we focus on the budding yeast *Saccharomyces cerevisiae*, which has emerged as a useful model organism in cell biology research [17]. In addition to being closely related to *Candida* yeast species [36], as a eukaryotic organism its basic cellular processes also have a lot in common with human cells [37], such as the presence of a distinct nucleus and compartmentalised sub-cellular organelles. Another advantage of *S. cerevisiae* in the scientific research context is that its genome has been sequenced [38], and a wide variety of genetic tools such as mutant libraries are available. It has therefore assumed an important role in the identification of new targets for anti-fungal therapy [17, 37], as well as understanding the division of cancer cells [35].

When studying yeast, it is common to grow colonies on agar plates in a laboratory. Depending on the conditions in which *S. cerevisiae* is grown, remarkably different patterns are possible. For example, when grown in low nitrogen environments, they form filamentous colonies characterised by a spatially non-uniform branched pattern (Figure 1.3a) [12]. In contrast, when grown on semi-solid agar, *S. cerevisiae* can form mat biofilms consisting of cells embedded in a self-produced ECM. An example of these is shown in Figure 1.3b. These biofilms are much larger than the filamentous colonies, and can grow to occupy an entire 90 mm Petri dish. Reynolds and Fink [17] were the first to perform mat formation experiments, and subsequently *S. cerevisiae* has been used a model for fungal biofilm formation.

In their experiments, Reynolds and Fink [17] inoculated yeast cells on a semi-solid agar substratum. Soon after inoculation, the yeast cells formed

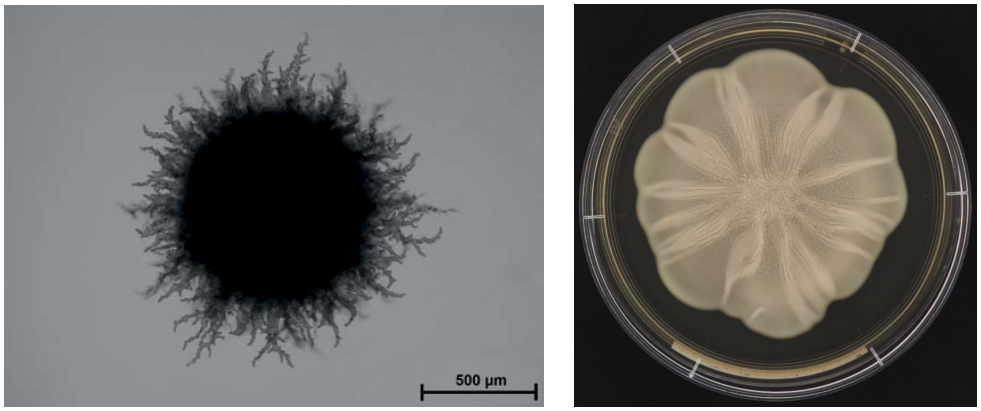

(a) (b)

Figure 1.3: Two examples of pattern formation in yeast colonies. (a) A filamentous yeast colony. Image reproduced from Binder et al. [11] under the Creative Commons Attribution 4.0 International License (CC BY 4.0), https://creativecommons.org/licenses/by/4.0/. (b) A yeast mat biofilm. Image: Ee Lin Tek, Department of Wine and Food Science, The University of Adelaide.

a thin round biofilm, referred to as a mat. This biofilm consists of yeast cells, which occupy approximately 90% of the colony, and a small quantity of extracellular matrix material. Initially, mats expand in a near uniform circular manner (Figure 1.4a). After three to five days, they then undergo a transition to a complex spatio-temporal pattern termed the floral morphology, which is characterised by the formation of petal-like structures along the biofilm edge (Figure 1.4b). As this pattern is observed in repeated experiments, one of our objectives is to understand its development.

According to current theory, biofilm development occurs in five stages [36, 39, 40], as illustrated in Figure 1.5. We summarise each of the five stages below.

1. Adsorption: also referred to as *initial attachment*, this stage involves the first physical contact between individual cells and the surface [18].

2. Adhesion: cells begin to produce extracellular material, enabling them to cluster and affix to the surface. This stage is also termed *irreversible*

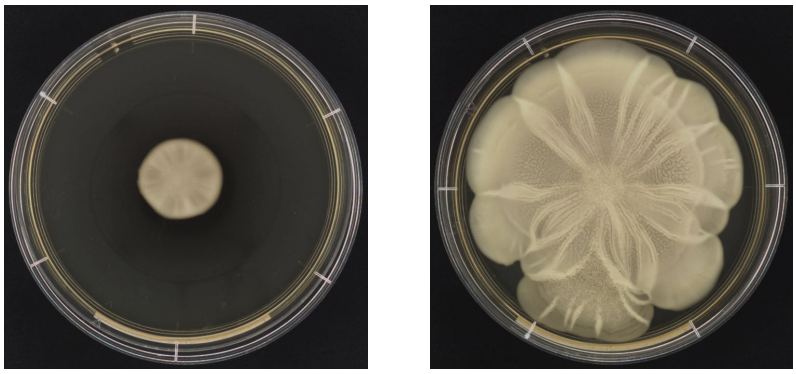

(a) 3 days after inoculation. (b) 10 days after inoculation.

Figure 1.4: Two images of a yeast biofilm, showing the transition from (a) circular growth to (b) the characteristic floral morphology. Images: Ee Lin Tek, Department of Wine and Food Science, The University of Adelaide.

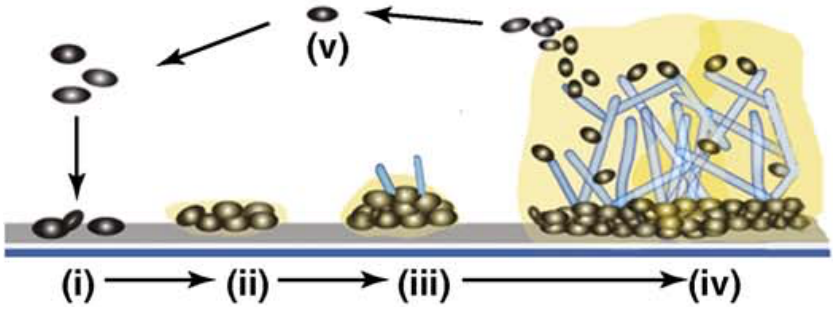

Figure 1.5: The five stages of biofilm development. (i): Adsorption. (ii): Adhesion. (iii): Early development. (iv): Maturation. (v): Dispersal. Image reprinted from Harding et al. [18] with permission from Elsevier.

attachment [39].

3. Early development: once the biofilm has adhered to the surface, cells begin to proliferate and increase production of EPS. The cells form larger aggregates known as microcolonies, which later combine to form the mature biofilm [40].

4. Maturation: in this stage, the biofilm attains its maximum size. As this occurs, the biofilm develops a complex structure, including the formation of water channels that aid nutrient transportation [18].

5. Dispersal: the mature biofilm releases single cells, which are then able to re-initiate the cycle [39].

We aim to model the transition from adhesion to maturity, where the biofilm expands and produces extracellular material. In this transition, nutrient availability and mechanical interactions between cells and their environment are both relevant to biofilm growth.

Interactions between yeast cells and a depleting nutrient supply is an important determinant of the colony pattern. Since yeast cells are non-motile, they cannot actively move in response to environmental cues such as nutrient gradients or the presence of a chemoattractant. Instead, yeast biofilms can only expand by cell proliferation, and this requires access to nutrients. Given sufficient nutrients, mother cells can reproduce asexually by dividing into two genetically identical daughter cells [41], and the colony invades new space to prevent overcrowding. This process continues until the biofilm occupies the entire Petri dish [17, 22, 24, 35, 42–44], at which point it can contain more than 1×10^{10} cells. If yeast cells become starved of nutrients, instead of immediately dying they can enter a stationary phase, and can begin to reproduce again if nutrient becomes available [45]. Due to this robustness, the majority of yeast cells in the biofilm remain living, as images from the end of an experiment in Figure 1.6 show. Since the overall proportion of dead cells is small, we do not expect large variations in living cell density throughout

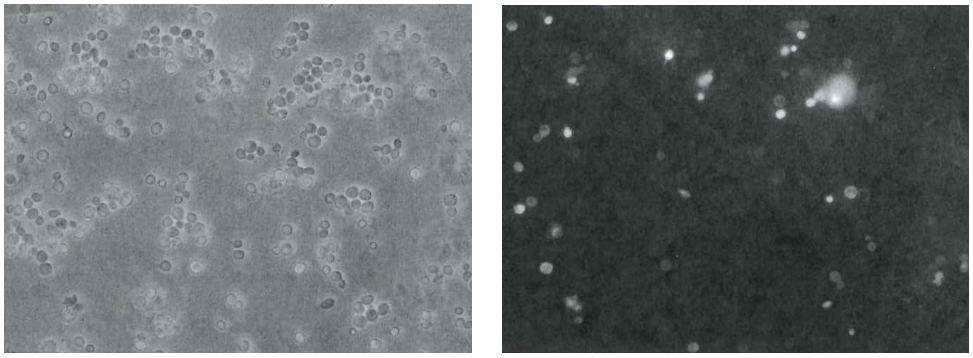

(a) Bright-field microscopy image of cells in a yeast biofilm.

(b) The same cells after application of the DiBAC4 vitality stain.

Figure 1.6: A cell viability assay, applied to cells obtained from a *S. cerevisiae* (1278b strain) biofilm eight days after inoculation. The membrane of dead cells is permeable, allowing dye to enter. This creates the fluorescence seen in Figure 1.6b. Images: Ee Lin Tek, Department of Wine and Food Science, The University of Adelaide.

the biofilm. Therefore, the distribution of nutrients is hypothesised to be a major influence on yeast biofilm pattern formation.

Mechanical interactions between cells and their environment are also thought to affect floral pattern formation. The extracellular matrix interacts closely with the cells, because both cells and extracellular material are produced by the catabolism of cellular synthesised glucose [46]. The combination of passive fluid and active biological matter gives biofilms distinctive mechanical properties. Although biofilms are viscoelastic in general, on time scales longer than the order of seconds they tend to behave as viscous fluids [20, 47, 48], with Reynolds numbers of $\mathrm{Re} < 1 \times 10^{-3}$ [49].

A notable finding of Reynolds and Fink [17] is that the glycoprotein Flo11p is required for mat formation. Similar glycopeptidolipids are known to increase the surface hydrophobicity of biofilms of the bacteria *Mycobacterium smegmatis*. As a result, adhesion between the biofilm and substratum is weak. Under these conditions, the prevailing hypothesis is that biofilms expand by sliding motility, a passive form of growth whereby the colony spreads as a unit, facilitated by the expansive forces of biomass production and reduced

friction between the cells and substrate [50]. Figure 1.7 provides a schematic of this mechanism.

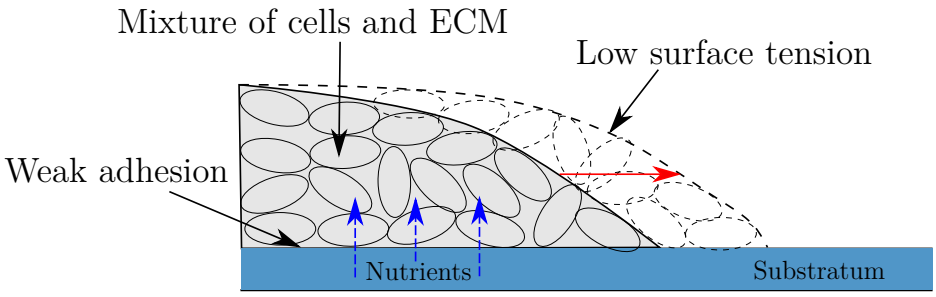

Figure 1.7: A schematic of biofilm expansion by sliding motility.

In other experiments, it is possible for cells to adhere strongly to the substratum. In these conditions, mats demonstrate wrinkling that is aligned with the floral pattern [35]. Furthermore, studies on bacterial biofilms have also revealed that osmotic swelling is another potential mechanism for biofilm expansion [51–53]. This requires production of EPS, which creates an osmotic pressure difference between the biofilm and environment. The biofilm then physically expands by taking up water from the agar [51]. The extent to which sliding motility and osmotic swelling contribute to expansion depends on the microbial species and environment [53]. In some bacteria, including *Bacillus subtilis*, osmotic swelling is the primary mechanism [51]. This is because the ECM fraction in bacterial biofilms is commonly 50–90% [54], and can be as high as 95–98% [21, 55]. The large proportion of extracellular material then drives the osmotic pressure gradient. In contrast, we observe that the ECM constitutes approximately 10% of *S. cerevisiae* mats by volume, and the effect of osmotic pressure gradients on yeast biofilm expansion is currently unclear. The complexity of these interacting mechanisms makes it difficult to derive a tractable mathematical model that includes all features simultaneously. Our objective is to develop simpler models for each of these mechanisms, to determine the extent to which each contributes to yeast biofilm pattern.

1.2 Mathematical Modelling of Biofilms

Owing to their ubiquity and importance to infections, biofilms have attracted significant attention in the applied mathematics community. A mathematical model for a biological process can be thought of as a 'logical machine' for deriving conclusions from a set of initial assumptions [56]. The challenges of modelling are therefore two-fold. First, the initial assumptions must adhere as closely as possible to the biological facts. Second, the model must be amenable to mathematical analysis that gives rise to biologically relevant conclusions. As discussed in §1.1, the mechanisms of yeast biofilm formation are complex, encompassing processes on the scale of individual cells to macroscopic environmental effects. It is inconceivable that we can construct a complete mathematical description of the relevant biological processes, such that the model remains mathematically tractable. However, we can use simpler models that retain a few key features, to investigate whether particular mechanisms can drive observed behaviour. Comparing the predictions of multiple models that capture different features can then help to provide a more complete understanding. This ability of mathematical models to decouple complex processes provides insight and predictive power that is not possible using experiments alone.

Mathematical models for biofilms fall into the two broad categories of discrete and continuous. Discrete models track the movement of individual cells in the colony [2, 57–60]. At this microscopic level, these models often incorporate stochastic laws describing events in the life cycle of individual cells, for example cell division and death. Since these processes depend on nutrient availability, discrete models often involve nutrient movement, either by considering individual nutrient particles [58], or treating the nutrient as a continuum [59] (the latter giving rise to hybrid models). In previous studies, discrete models have successfully replicated branched [61] and finger-like [57] morphologies in microbial colonies.

In contrast, continuum models adopt a macroscopic view, and assume

that substances of interest completely fill the space they occupy. The mathematical models then consider changes with space and time in the density of quantities such as cells, nutrients, and extracellular fluid. An advantage of continuum models is that they involve macroscopic parameters that are easier to estimate from experimental data. For micro-organisms, such models can be highly accurate, because colonies consist of millions of very small cells. Yeast mats can evolve to contain over 1×10^{10} cells, which is suitable for continuum modelling, and would make discrete models computationally expensive. Throughout this thesis, we will develop and analyse continuum models for pattern formation of yeast biofilms.

A common continuum modelling approach is to model cells and nutrients as a reaction–diffusion system [35, 44, 62–65]. The study of reaction–diffusion systems is a mature field, and well-established analytical techniques are available. These can help us to understand how spatio-temporal distributions of cells and nutrients can lead to pattern formation. A limitation of reaction–diffusion models is that they do not include the effect of colony mechanics, such as extracellular fluid flow [66]. This has motivated the development of continuum mechanical models, in which mechanical effects are combined with cell proliferation, and the movement and consumption of nutrients. In subsequent sections, we outline these two modelling approaches, and review how they have been applied to biofilm growth.

1.2.1 Reaction–Diffusion Models

Reaction–diffusion systems are mathematical models that describe the conservation of mass of one or more substances as they diffuse and interact. These models are highly versatile, and are widely applicable across chemistry [67–74], biology [5, 64, 75, 76], physics [77], and ecology [78]. In pattern formation, they have been commonly used as prototype models since Turing [4] developed his chemical pre-patterning theory.

We consider the application of a reaction–diffusion model to a yeast biofilm grown on an agar substratum. Our objective is to use a minimal model to de-

termine whether nutrient-limited growth alone can explain pattern formation. Many models have adopted a two-species reaction–diffusion model, where only cells and nutrient are present [35, 79, 80]. These predict the evolution of the numerical cell density, $n(\boldsymbol{x}, t)$, and the nutrient (glucose) concentration, $g(\boldsymbol{x}, t)$. Reaction–diffusion equations describing how the variables change with space and time are obtained from the principle of mass conservation. The general mass balance equation reads [6]

$$\frac{\partial \rho}{\partial t} + \nabla \cdot \boldsymbol{q} = J. \tag{1.1}$$

In (1.1), ρ represents the amount of a substance per unit volume. For yeast cells and nutrients, this could represent the numerical cell density and concentration respectively. The vector $\boldsymbol{q}$ is the flux, which describes the amount of the substance crossing a unit area per unit time. The source term J represents the net creation per unit volume of the substance per unit time.

Reaction–diffusion models neglect transport by bulk motion. As a result, the flux $\boldsymbol{q}$ consists of diffusion only. Diffusion is the process by which substances move from regions of high concentration to regions of low concentration. The rate at which this occurs is proportional to the local concentration gradient. In general, it can also depend on the cell density and nutrient concentration. We then obtain the general flux terms

$$\boldsymbol{q}_n = -\mathcal{D}_n(n, g)\nabla n, \tag{1.2a}$$

$$\boldsymbol{q}_g = -\mathcal{D}_g(n, g)\nabla g, \tag{1.2b}$$

where $\mathcal{D}_n$ and $\mathcal{D}_g$ are non-negative functions encoding the diffusivity of each species. Substituting the diffusive fluxes (1.2) into the mass balance equation (1.1) yields the general reaction–diffusion model,

$$\frac{\partial n}{\partial t} = \nabla \cdot [\mathcal{D}_n(n, g)\nabla n] + J_n(n, g), \tag{1.3a}$$

$$\frac{\partial g}{\partial t} = \nabla \cdot [\mathcal{D}_g(n, g)\nabla g] + J_g(n, g). \tag{1.3b}$$

The source terms J_n and J_g in (1.3) are the net creation of cells and nutrients respectively. In biofilm growth, these represent cell proliferation and the consumption of nutrients.

Many models for microbial colonies take the form (1.3). These are the simplest models that describe cell spread under nutrient-limited growth. Depending on the microbial species and environment, different forms of the diffusivities $\mathcal{D}_n$ and $\mathcal{D}_g$, and reaction terms J_n and J_g have been proposed. Gray and Kirwan [79] were the first to apply a reaction–diffusion model to yeast colony growth. They proposed reaction terms J_n and J_g that are proportional to the local cell density and nutrient concentration, a simple form used in many subsequent models [35, 62, 64, 80, 81]. In their paper, Gray and Kirwan [79] also incorporated a constant lag nutrient concentration g_1 such that $J_n = \chi n(g - g_1)$ and $J_g = -\sigma\chi n(g - g_1)$, but this can be subsequently scaled out [82]. Since nutrients disperse through the agar by standard Fickian diffusion, Gray and Kirwan [79] assumed that the diffusion coefficient $\mathcal{D}_g = D_g$ is constant. Finally, they appealed to the non-motile nature of yeast cells to assume that $\mathcal{D}_n = 0$. Their model was then

$$\frac{\partial n}{\partial t} = \chi n g, \tag{1.4a}$$

$$\frac{\partial g}{\partial t} = D_g \nabla^2 g - \sigma\chi n g, \tag{1.4b}$$

where the parameter χ is the cell proliferation rate, *i.e.* the rate of increase in colony area per unit of nutrient, and σ is the quantity of glucose consumed per new cell. A useful feature of this model is that travelling wave solutions exist for all D_g, and therefore it provides an explanation for constant speed colony expansion.

Edelstein-Keshet [82] proposed a modification to this model by assuming that yeast cells undergo random motion. Assuming the cell diffusivity $\mathcal{D}_n =$

D_n is also constant, they proposed

$$\frac{\partial n}{\partial t} = D_n \nabla^2 n + \chi n g, \tag{1.5a}$$

$$\frac{\partial g}{\partial t} = D_g \nabla^2 g - \sigma \chi n g, \tag{1.5b}$$

This form of linear cell diffusion model has been used extensively in models for bacterial and yeast colonies [63, 83–85], as well as applications such as autocatalytic chemical reactions [70, 86]. It has been the subject of much analysis, and Billingham and Needham [70] showed that it admits travelling wave solutions for all values of D_n and D_g. However, although (1.5) can explain constant speed expansion, the travelling wave solutions are linearly stable to all transverse perturbations [63]. Therefore, it cannot explain pattern formation in two-dimensions. This, in part, motivated the application of models with non-linear cell diffusion to microbial colonies, where $\mathcal{D}_n(n, g)$ is no longer constant.

Another motivation for non-linear diffusion models is that cells do not spread by standard Fickian diffusion. Many authors have proposed different forms of $\mathcal{D}_n(n, g)$, attempting to obtain a more accurate phenomenological description of cell spread. One possibility is to assume that the cell diffusivity $\mathcal{D}_n \propto ng$, which has been shown to produce branched patterns [62], and travelling wave solutions [81]. Another popular assumption is to propose that $\mathcal{D}_n \propto n^b$, for some $b > 0$ [35, 63, 64, 83, 87]. This gives rise to the system

$$\frac{\partial n}{\partial t} = D_n \nabla \cdot \left(n^b \nabla n \right) + \chi n g, \tag{1.6a}$$

$$\frac{\partial g}{\partial t} = D_g \nabla^2 g - \sigma \chi n g. \tag{1.6b}$$

Since the cell diffusivity is zero when cell density is zero, the diffusivity $\mathcal{D}_n \propto n^b$ in (1.6) is termed non-linear degenerate diffusion. Such forms of non-linear diffusion are relevant to modelling random motion of cells with aspect ratio not equal to unity [88]. An advantage of these models is that

they admit travelling wave solutions with compact support [64], unlike linear diffusion models. This feature makes them suitable for describing finite-sized colonies. Thus, non-linear diffusion models remain common in microbial modelling literature.

Some reaction–diffusion models for biofilm growth represented variations to the general coupled system (1.3). Many authors have introduced a third species by considering both living (or active) and dead (or inactive) cells [63, 83–85, 87], and modified the source term J_n to incorporate cell death. Some models have incorporated explicit mechanisms to ensure that the cell density does not exceed a carrying capacity. These approaches have included assuming that reactions occur according to Michaelis–Menten kinetics [62], and introducing a density-dependent diffusion coefficient that attains a singularity at the maximum cell density [65]. In addition, growth in some bacterial colonies depends on the concentration of a chemoattractant [89], which is captured by the well-known model of Keller and Segel [90]. In this thesis, we will not consider these variations in detail. As shown in §1.1, the rate of cell death in yeast biofilms is low, and yeasts tend to not undergo biased growth in response to chemical or nutrient gradients [2]. Instead of considering these complexities, our objective is to provide a detailed comparison with experimental data, to determine whether nutrient-limited growth is a possible mechanism for floral pattern formation.

Although reaction–diffusion models are common, less research exists providing detailed quantitative comparison with yeast biofilm formation experiments. Chen et al. [35] provided the first such comparison with *S. cerevisiae* mat formation experiments. They adopted a non-linear degenerate diffusion model of the form (1.6) with $b = 1$, and found good qualitative agreement in perimeter-to-area ratio between numerical solutions and experimental photographs. However, as this work did not involve estimating parameters from the experiments, it is not yet known whether the mathematical model will reproduce the experimental patterns on length and time scales relevant to the experiment. Addressing this question is crucial in determining whether

nutrient-limited growth is responsible for the floral pattern. Quantitative comparison requires appropriate spatial statistics to measure pattern formation in both experiments and model predictions. Although the perimeter-to-area ratio provides a coarse measurement of the biofilm shape, it does not describe the size and shape of petals in the floral morphology. Thus, there is still a need for a more detailed quantitative comparison between non-linear reaction–diffusion models and yeast biofilm growth experiments.

We aim to use a reaction–diffusion model to investigate whether nutrient-limited growth is the mechanism by which floral patterns form in *S. cerevisiae* mats. To limit the number of parameters that we need to estimate from experiments, we adopt a minimal modelling philosophy, and restrict ourselves to a coupled system of the form (1.3). These models admit travelling wave solutions, which we can exploit to help estimate parameters in the experiments. This enables us to build on the work of Chen et al. [35] to provide a detailed quantitative study into whether nutrient-limited growth can explain the floral morphology. Careful comparison requires quantitative methods to measure pattern formation in both experiments and model predictions. Implementation of suitable spatial statistical methods is therefore part of the modelling process, and we undertake this in Chapter 2.

1.2.2 Continuum Mechanical Models

Although commonly-used, reaction–diffusion models do not account for the mechanical behaviour of the cells, agar, or extracellular fluid. Continuum mechanical models address this weakness, and provide a more detailed description of biofilm growth than reaction–diffusion models. This is because they can incorporate features such as the mechanics of cells and the flow of extracellular fluid, in addition to nutrient movement and cell proliferation. We review previous mechanical models of biofilm growth to identify how these models can be adapted for *S. cerevisiae* biofilms.

The first attempts to systematically incorporate hydrodynamics into biofilm models involved biofilms growing on solid, non-reactive substrata,

immersed in a liquid culture medium from which they obtain nutrients. These models incorporated the hydrodynamics of bulk fluid in the medium. They then described vertical biofilm growth perpendicular to the substratum. For example, the influential model of Wanner and Gujer [91] considered a biofilm growing vertically into a bulk fluid, and accounts for interactions between multiple species, biomass detachment, and variations in nutrient concentration in the bulk fluid. Eberl, Parker, and van Loosdrecht [92] extended this approach by using the Stokes equations to model the flow of the bulk fluid explicitly. This enabled them to model spatially non-uniform biofilm profiles. However, as these models treated the biofilm as rigid, they did not incorporate the mechanics of cells and the extracellular matrix. For this reason, and because our yeast biofilms primarily spread in the radial direction, we do not consider these models of vertical growth in detail. We direct the reader to the review by Klapper and Dockery [93] for further information.

An alternative approach is to model the biofilm constituents themselves as fluids. This is relevant to *S. cerevisiae* mats, for which cell and ECM mechanics are hypothesised to affect growth. Parallels between collections of cells and viscous fluids have been prevalent since Steinberg [94] introduced the differential adhesion hypothesis (DAH). According to the DAH, cell populations behave like viscous liquids, where adhesive and cohesive interactions between cells is analogous to surface tension [95]. Some early attempts at incorporating fluid mechanics into models of microbial colony growth were based on parallels between diffusion-limited aggregation and flow in a Hele-Shaw cell [96–98]. Based on the similarity in patterns exhibited by both systems, these models hypothesised that the colony could be modelled as a viscous fluid. Since then, this hypothesis has been validated in experiments, showing that biofilms behave as viscous fluids on time scales longer than the order of seconds [99, 100]. However, models based on Hele-Shaw flow do not provide an explicit theory for modelling biofilm mechanics.

To address the deficiencies of Hele-Shaw models, some authors treated the biofilm as a single fluid, but included additional features such as reaction–

diffusion equations for nutrient transport. For example, Lega and Passot [101] coupled a reaction–diffusion system for bacteria and nutrients with hydrodynamic equations for the fluid in the biofilm. Nguyen et al. [102] considered the effect of cell–cell adhesion in a fluid model for a yeast colony. Giverso, Verani, and Ciarletta [103] showed that a model in which a spreading bacterial colony is treated as a viscous fluid satisfying Darcy's law can model the fingering pattern seen in experiments.

When modelling biofilms, it is necessary to consider interactions between cells, EPS, and external fluid. Multi-phase models provide a way to do this, and involve each constituent being modelled as a fluid with its own behaviour and properties. They have been used extensively in mathematical biology, for example the crawling of individual cells [104, 105], and the growth of tissues [106, 107] and tumours [108, 109]. We focus on multi-phase models as a promising approach for biofilms. A detailed framework for the construction of multi-phase models was provided by King and Oliver [110]. Under this framework, biofilms are typically modelled as multi-phase mixtures of cells, EPS, and external liquid [48, 55, 66, 111–115]. Applying conservation of mass and momentum for each fluid phase then enables the different mechanical behaviour of each fluid, and interactions between phases, to be taken into account. This is important, as the birth and death of cells results in material changing phase. This cannot be captured in single-fluid models.

Multi-phase models involve assuming that each region of space is occupied by some fraction of each species by volume. This is the no-voids assumptions, which is

$$\sum_{\alpha=1}^{N} \phi_\alpha = 1, \tag{1.7}$$

where $\phi_\alpha(\boldsymbol{x}, t)$ represents the volume fraction of phase α, and N is the number of phases in the mixture. Since it is not physically possible for multiple species to occupy the same space simultaneously, obtaining a macroscopic model first requires an averaging process, for example volume-averaging. Throughout this thesis, we implicitly assume appropriate averaging has occurred, and direct the reader to the paper by Drew [116] for further details. We obtain

equations governing the evolution of the volume fraction of each phase from the principle of mass conservation. Denoting the velocity of each phase by $\boldsymbol{u}_\alpha(\boldsymbol{x}, t)$, and assuming that each phase has constant density [110], the mass balance equations read

$$\rho_\alpha \left[\frac{\partial \phi_\alpha}{\partial t} + \nabla \cdot (\boldsymbol{u}_\alpha \phi_\alpha) \right] = J_\alpha, \tag{1.8}$$

where ρ_α is the density, and J_α is the net fluid production for each phase α. Conservation of momentum then provides equations for the fluid velocities. To each phase, we apply the Cauchy momentum equation [117],

$$\rho_\alpha \frac{\mathrm{D}}{\mathrm{D}t} (\phi_\alpha \boldsymbol{u}_\alpha) = \nabla \cdot (\phi_\alpha \boldsymbol{\sigma}_\alpha) + \boldsymbol{F}_\alpha, \tag{1.9}$$

where $\boldsymbol{\sigma}_\alpha$ is the stress tensor for phase α, and $\boldsymbol{F}_\alpha$ represents net body forces. In many biological processes, including biofilm growth, the fluid flow is slow, with Reynolds numbers on the order of $\mathrm{Re} \approx 0.001$ [49]. For these fluids, it is standard to neglect inertial terms in (1.9), so we obtain the momentum balance equations [110]

$$\nabla \cdot (\phi_\alpha \boldsymbol{\sigma}_\alpha) + \boldsymbol{F}_\alpha = \mathbf{o}. \tag{1.10}$$

Given appropriate constitutive laws for the source terms J_α, stress tensors $\boldsymbol{\sigma}_\alpha$, and body forces $\boldsymbol{F}_\alpha$, we can obtain a closed model for the volume fractions of each phase in the mixture.

Through the constitutive laws, the basic framework of multi-phase models can incorporate features of biofilm, tumour, and tissue growth. In these models, a common constitutive assumption is to consider the phases as Newtonian viscous fluids. The stress tensor is then given by

$$\sigma_{ij} = -\left(p + \frac{2\mu}{3} \frac{\partial u_k}{\partial x_k} \right) \delta_{ij} + 2\mu e_{ij}, \tag{1.11}$$

where p is the pressure, μ is the dynamic viscosity, δ_{ij} is the Kronecker delta,

and e_{ij} is the rate of strain tensor, given by

$$e_{ij} = \frac{1}{2}\left(\frac{\partial u_i}{\partial x_j} + \frac{\partial u_j}{\partial x_i}\right). \tag{1.12}$$

In general, biological models retain the divergence term in the stress tensor (1.11). In passive fluids these terms vanish due to incompressibility, but they can be non-zero in biological contexts due to local fluid production, for example by cell proliferation. The coefficient of $-2\mu/3$ for the divergence terms arises from Stokes' hypothesis [118–120].

In some biological models, the authors introduced a modification to the standard stress tensor for viscous fluids. This is because some biological materials, such as cells, can generate forces by responding actively to environmental cues [107, 109, 119, 121–123]. These forces generate an additional intraphase pressure, denoted Σ. The total pressure on each phase is then

$$p_\alpha = p + \Sigma_\alpha, \tag{1.13}$$

An example of these environmental cues is the concentration of a chemoattractant, which can prompt active movement by chemotaxis [123]. Another is cell–cell contact, whereby cells can experience additional stress when densely packed, which occurs in regions of high cell volume fraction [121]. The functions Σ_α can therefore depend, for example, on the chemoattractant concentration and cell volume fraction. Although bacteria growing on soft agar can undergo chemotaxis facilitated by flagella-mediated motility [124], we do not expect these additional pressure terms to play a major role in yeast biofilm formation. This is because yeast cells do not possess flagella, and thus cannot undertake this active motion. As yeast cells are non-motile, we focus on models using the standard Newtonian viscous constitutive relation (1.11).

In addition to mechanics, models for biofilm formation commonly include additional equations to describe nutrient transport [52, 111, 113, 114, 125–127], and the effect of quorum sensing molecules [112, 120, 128]. Recent work has also established the importance of osmotic swelling to bacteria biofilm

expansion [51, 53, 127]. In this mechanism, the production of EPS in the biofilm generates an osmotic imbalance between the biofilm and agar [51, 52]. The biofilm then restores equilibrium by drawing in water from the substratum. This results in physical swelling of the biofilm. In the multiphase fluid models, osmotic influx is represented by an additional source term for the extracellular fluid phase [51, 127]. For example, Srinivasan, Kaplan, and Mahadevan [127] assumed a mass balance for extracellular fluid of the form

$$\frac{\partial}{\partial t}\left(h\phi_2\right) + \frac{\partial}{\partial x}\left(Q_2(x)\right) = Q_0\phi_2\left(\phi_1^3 - \phi_0^3\right), \tag{1.14}$$

where h is the biofilm height, Q_2 represents the horizontal flux of passive fluid, ϕ_1 is the volume fraction of active material, ϕ_2 is the volume fraction of passive extracellular fluid, and Q_0 and ϕ_0 are constants. In addition to osmotic swelling, a series of papers by Trinschek, John, and Thiele [52] included the contribution of surface forces in a model for osmotic swelling-driven expansion of bacterial biofilms [52, 129, 130]. Their results suggested that wettability and the strength of surface tension govern colony morphology [130].

Experimental and modelling work by Seminara et al. [51] provided convincing evidence that osmotic swelling is a more important driver of expansion than sliding motility in *B. subtilis* biofilms. However, in these colonies the volume fraction of cells is estimated to be approximately 2–10%. In contrast, we estimate that 90% of *S. cerevisiae* mats are taken up by cells. Therefore, we expect that cell proliferation will play a larger role than osmotic swelling in driving *S. cerevisiae* mat expansion. This occurs in sliding motility, which was hypothesised by Reynolds and Fink [17] as the mechanism of expansion. In addition, as sliding motility involves weak cell adhesion, we expect that surface forces will also play a reduced role. In this context, the Newtonian viscous constitutive relation is suitable for modelling yeast biofilm expansion. We also assume that the incompressibility of the material is sufficient to facilitate expansion when cells proliferate, without invoking osmotic swelling.

Once the constitutive laws, initial conditions, and boundary conditions have been established, the resulting model is often complicated. A common

technique in applied mathematics is to simplify this model by considering distinguished limits as some parameter becomes large or small. To obtain accurate models, the choice of distinguished limit requires physical insight. A relevant example is that the radius of *S. cerevisiae* biofilms significantly exceeds their height. Biofilms are consequently well-suited to the thin-film approximation. These are a class of approximations applied when the physical domain is thin in one direction relative to another. The theory originated in the study of lubricated bearings in machinery [131], and is therefore also known as *lubrication theory*. Applying this theory involves introducing a slenderness parameter

$$\varepsilon = \frac{H}{L}, \tag{1.15}$$

where the domain has characteristic height H and characteristic length L, and where $0 < \varepsilon \ll 1$. Scaling the variables by their natural length scale introduces the small parameter ε into the model. Asymptotic analysis then provides a way to obtain simpler models, in which physical effects of similar importance are balanced, and less important features are neglected.

In many previous works that adopted the thin-film approximation in multi-phase models, the authors derived a fourth-order generalised lubrication equation for the biofilm height [51, 52, 120, 125–127, 129, 130]. For a Newtonian viscous fluid, in one spatial dimension this equation takes the form

$$\frac{\partial h}{\partial t} + \frac{\gamma^*}{3}\frac{\partial}{\partial x}\left(h^3\frac{\partial^3 h}{\partial x^3}\right) = J, \tag{1.16}$$

where γ^* is the dimensionless surface tension coefficient (or inverse capillary number), and J is a source term that accounts for biomass production. A common feature of these models is that the derivation of a generalised lubrication equation requires the assumption of strong adhesion between the biofilm and substratum. As a result, flow is driven by a large pressure that must be balanced with a comparatively large surface tension. Although these models have been commonly applied to bacterial colonies, *S. cerevisiae* mats are hypothesised to expand by sliding motility. This involves increased cell

surface hydrophobicity, and hence weak adhesion between the biofilm and agar. Modelling sliding motility therefore requires a different approach.

In addition to strong adhesion, Ward and King [120] also considered the possibility that the biofilm behaves as an extensional flow. As this requires assuming weak adhesion between the biofilm and substratum, it is particularly relevant to sliding motility. In their model, Ward and King [120] treated a bacterial biofilm as a multi-phase mixture of cells and water, and used the thin-film approximation to derive a model for the early-time spread of the colony. The key step was assuming no stress on the biofilm–substratum interface. This is as opposed to the no-slip condition, which is used to derive the generalised lubrication equation (1.16). Under the no-stress assumption, the leading-order fluid velocity is independent of vertical position z, and therefore the flow is termed *extensional*. In one dimension, the extensional model of Ward and King [120] consisted of two coupled partial differential equations,

$$\frac{\partial h}{\partial t} + u\frac{\partial h}{\partial x} = f(h), \tag{1.17a}$$

$$h\frac{\partial u}{\partial x} = f(h), \tag{1.17b}$$

where h is the biofilm height, u is the fluid velocity, and $f(h)$ is a function representing biomass production.

Although the model of Ward and King [120] is relevant to sliding motility, they considered a biofilm immersed in a nutrient-rich liquid culture medium. This is unlike *S. cerevisiae* mats, which receive nutrients from the agar substratum; their ability to spread therefore depends on the supply of a depleting nutrient, which is also relevant to biofilm growth in nature or in a human host [13]. Ward and King [120] also only considered early biofilm development, and thus neglected ECM production and spatio-temporal variations in the cell volume fraction. Both of these become important on the length and time scales of our experiments. Furthermore, multi-phase fluid models have also only previously been applied to bacterial biofilms, rather than the yeast biofilms considered here. Based on these considerations, we

aim to extend previous thin-film models to model *S. cerevisiae* mat formation experiments.

1.3 Thesis Objectives and Structure

Our literature review has illuminated the need for new models of yeast mat formation, and more detailed quantitative comparison between modelling and experiments. Our objective is to determine the extent to which nutrient-limited growth and sliding motility can explain yeast biofilm growth. We can measure this growth by quantifying the speed of biofilm expansion, and the transition from circular to floral morphology. We will then undertake mathematical modelling to investigate which mechanisms drive the observed behaviour. To achieve this objective, we define the following goals for this thesis:

1. Develop and apply spatial statistical methods to quantify the expansion speed of *S. cerevisiae* mat biofilms, and the transition from circular to floral morphology.

2. Use a reaction–diffusion system as a minimal model for biofilm expansion. Analyse the model and perform a quantitative comparison with experiments to investigate whether nutrient-limited growth can explain the floral morphology.

3. Develop a general multi-phase fluid model for *S. cerevisiae* mat formation. This model will incorporate the mechanics of the cells and extracellular fluid, and nutrient limitation. Use the thin-film approximation to derive two simplified models. First, consider biofilm growth by sliding motility, and then expansion driven by surface tension and strong biofilm–substratum adhesion.

4. Compare solutions to the thin-film extensional flow model with experiments, to determine the extent to which sliding motility can explain yeast biofilm expansion.

5. Use the thin-film model in the lubrication regime to investigate qualitative differences between sliding motility and expansion under strong biofilm–substratum adhesion and comparatively large surface tension and pressure.

A key part of this thesis is to compare our new mathematical models with experimental data for yeast biofilms. In Chapter 2, we develop the quantitative methods used to achieve this. We first describe the method used to grow yeast biofilms *in vitro*, and collect data in the form of a time series of images of biofilm growth. Converting these photographs to binary images then enables us to apply spatial statistics to quantify the growth. To quantify pattern formation, it is important to measure expansion speed and petal formation. The remainder of the chapter thus involves introducing the radial statistic used the measure biofilm size, and the angular pair-correlation statistic used to quantify the number of petals. To conclude the chapter, we apply these spatial statistics to the yeast biofilm photographs, yielding experimental data that is used throughout the thesis.

We focus on the second objective of our thesis in Chapter 3. Therein, we use a reaction–diffusion system with non-linear cell diffusion to investigate pattern formation due to nutrient-limited growth alone. Our analysis of the model begins by constructing travelling wave solutions. We first prove that travelling wave solutions exist in one-dimensional planar geometry, in the limit of zero cell diffusivity. Then, we apply geometric singular perturbation theory to investigate the structure of travelling wave solutions with small cell diffusivity. Experimental data for the expansion speed enables us to estimate the cell diffusion coefficient. We then investigate whether the model predicts two-dimensional pattern formation. Comparison of petal width predictions from a linear stability analysis and experimental data show that nutrient-limited growth is a possible mechanism for floral pattern formation. Numerical solutions confirm that this holds in a circular geometry.

The remainder of the thesis is devoted to the derivation and analysis of a multi-phase fluid model for biofilm growth. We derive the model in

Chapter 4, beginning with a description of mass and momentum conservation. We then apply the thin-film approximation, and derive distinct models for biofilm expansion in the extensional flow and lubrication regimes. The extensional flow model involves weak adhesion between the biofilm and substratum. This is suitable for modelling biofilm expansion by sliding motility. In contrast, we consider strong adhesion in the lubrication regime, where we assume that surface tension and pressure can be large. In both regimes, we identify appropriate distinguished limits to balance physical effects such as the transport, uptake, and consumption of nutrients, and cell proliferation.

We analyse the extensional flow model in Chapter 5, to investigate whether sliding motility can explain yeast biofilm expansion. We first consider the one-dimensional axisymmetric form of the model, which enables us to compare expansion speed with experiments. Fitting numerical solutions to experimental data, we obtain excellent agreement with $\mathcal{O}(1)$ parameters estimated from experiments. This establishes sliding motility as a possible explanation for the experimental expansion speed. We conclude the chapter by performing a local sensitivity analysis to investigate the effect of deviations from experimental parameters on biofilm size and shape.

We contrast the results for the extensional flow model by performing a similar analysis in the lubrication regime in Chapter 6. This investigates biofilm expansion when there is strong biofilm–substratum adhesion and comparatively large surface tension and pressure. Unlike the extensional flow regime, the fluid velocities and cell volume fraction depend on z, and therefore the axisymmetric model remains two-dimensional. We propose initial and boundary conditions, and regularise the model, which enables us to undertake numerical solution of the two-dimensional model. These solutions show that the cell volume fraction depends weakly on z. We exploit this by considering a simplification whereby the cell volume fraction is independent of z, which reduces the model to one dimension. We then investigate the effect of parameters on expansion speed and biofilm thickness. These results are

qualitatively similar to the extensional flow regime, with the key difference that the surface tension coefficient becomes a determinant of expansion speed.

Finally, in Chapter 7, we summarise and conclude the thesis. This combines insights from the reaction–diffusion and mechanical models to obtain a more complete description of biofilm growth. The minimal reaction–diffusion model is amenable to travelling wave and stability analysis, enabling us to predict the floral pattern. The mechanical model captures interactions between cells, extracellular fluid, and nutrients, providing a more detailed explanation of expansion speed than the reaction–diffusion model. Using the mechanical models to investigate floral pattern formation and alternative expansion mechanisms is the subject of future work.

This thesis contains material that has been published in peer-reviewed journals, and full citation of these works appears below.

1. **A. Tam**, J. E. F. Green, S. Balasuriya, E. L. Tek, J. M. Gardner, J. F. Sundstrom, V. Jiranek, B. J. Binder (2018), "Nutrient-limited growth with non-linear cell diffusion as a mechanism for floral pattern formation in yeast biofilms", *Journal of Theoretical Biology* 448, pp. 122–141, doi: 10.1016/j.jtbi.2018.04.004 [44].

2. H. Tronnolone, **A. Tam**, Z. Szenczi, J. E. F. Green, S. Balasuriya, E. L. Tek, J. M. Gardner, J. F. Sundstrom, V. Jiranek, S. G. Oliver, B. J. Binder (2018), "Diffusion-limited growth of microbial colonies", *Scientific Reports* 8, 5992, doi: 10.1038/s41598-018-23649-z [2].

3. **A. Tam**, J. E. F. Green, S. Balasuriya, E. L. Tek, J. M. Gardner, J. F. Sundstrom, V. Jiranek, B. J. Binder (2019), "A thin-film extensional flow model for biofilm expansion by sliding motility", *Proceedings of the Royal Society of London A* 475, 20190175, doi: 10.1098/rspa.2019.0175 [132].

Chapter 2

Quantifying Yeast Biofilm Growth

Our objective is to quantify the extent to which different mechanisms, such as nutrient-limited growth and sliding motility, contribute to yeast biofilm pattern formation. To test each of these hypotheses, we require experimental data with which to compare predictions from mathematical modelling. We describe how we obtain this data in this chapter. In §2.1, we provide details of the experimental method used to grow yeast biofilms in the laboratory. The raw data collected in these experiments consist of a time series of photographs as the biofilms develop. To quantify the growth, we first process the photographs by converting them to binary images that capture the area occupied by the biofilm. We then define and implement a series of spatial statistics, enabling us to quantify the speed of biofilm expansion, and the transition from circular to floral morphology. This process is described in §2.2. Finally, in §2.3 we obtain and present data from repeated mat formation experiments. This facilitates comparison with the mathematical modelling in subsequent chapters.

2.1 Mat Formation Experiments

In this work, we refer to repeated mat formation experiments performed by Ee Lin Tek at the Department of Wine and Food Science at the University of

Adelaide. The yeast biofilm growth experiments involved producing two mat assays of the *S. cerevisiae* wine yeast strain L2056, which yielded a total of thirteen mats. For each mat preparation, a 90 mm diameter Petri dish was filled with 25 g Yeast Peptone Dextrose (YPD), and solidified with low-density (0.3%) agar. This ensured a uniform initial concentration of nutrients in the dish. The YPD consisted of 95% double-distilled water, 2% Bacto peptone, 1% yeast extract, and 2% glucose, providing a complete medium for yeast growth. In each experiment, the centre of the dish was inoculated with a small droplet containing approximately 5000 yeast cells and fluid using a pipette. The fluid then rapidly absorbed into the medium, leaving behind a thin layer of cells on the surface. Following this, each plate was incubated at 25 °C, allowing the yeast to initiate biofilm formation.

The raw data collected from these experiments consisted of a series of images taken on the third, fifth, seventh, and tenth day of growth (approximately 68, 117, 164, and 237 hours after incubation respectively). These photographs were taken from directly above the centre of the dish using the ProtoCOL 3 (Synbiosis, Cambridge UK) system. They therefore enable us to track the two-dimensional evolution of the biofilm. The mat formation experiment was considered to have concluded after taking the fourth photograph. Immediately following this, the total number of cells was estimated by washing the mat from the medium, and counting the number of cells in a small sample of the washed material. Since the cell count destroyed the biofilm, we could only do this at the end of the experiment.

Like the experiments of Reynolds and Fink [17], each mat formed a similar, reproducible structure. To illustrate this, Figure 2.1 shows an example series of photographs, while the remainder are presented in Appendix A.1. Initially, the cells formed a thin round mat with approximately circular shape, as observed in Figure 2.1a. After growing in this manner for several days, the mat underwent a transition to a spatially non-uniform complex structure, characterised by the formation of petals. Development of this floral morphology, which became more noticeable over time, is shown in Figures 2.1b–

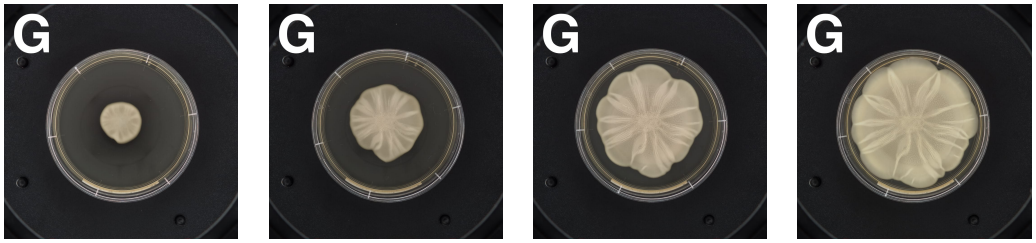

(a) 68 h (b) 117 h (c) 164 h (d) 237 h

Figure 2.1: A time series of images for a *S. cerevisiae* mat formation experiment [44]. Captions indicate time after incubation at which each photograph was taken.

2.1d. Since we observed the floral morphology in other experiments (see Appendix A.1), we expect it to originate from common mechanisms. To facilitate comparison between experiments and mathematical models for candidate mechanisms, we quantify the expansion speed and petal formation.

2.2 Image Processing and Spatial Statistics

Quantifying expansion speed and petal formation requires a method of tracking the area occupied by yeast cells over time. The first step in this process is to convert the experimental photographs to binary images. We then develop spatial statistics and apply them to this data. We use a radial metric to determine the biofilm radius at a given time, which enables us to quantify speed of expansion. For the transition to floral patterning, we compute an angular pair-correlation function, the power spectrum of which gives a count of the number of petals.

Converting a photograph to a binary image assigns the value zero or one to each pixel in the photograph, depending on whether the pixel is occupied by the biofilm. The pixels in each photograph define a two-dimensional square domain $\mathcal{D}$, consisting of an integer lattice with unit spacing. At each lattice

site $(x, y) \in \mathcal{D}$, we use the method of Binder et al. [11] and define the function

$$M(x,y) = \begin{cases} 0 & \text{if site } (x,y) \text{ is vacant,} \\ 1 & \text{if site } (x,y) \text{ is occupied.} \end{cases} \tag{2.1}$$

For each image, computing (2.1) involves applying a thresholding algorithm to determine whether a pixel is occupied. First, we apply the `imbinarize` MATLAB function to each photograph, which uses Otsu's method [133] to convert them to binary images. This identifies light coloured pixels, which include the mat and often the edge of the Petri dish. To isolate the mat, if necessary we manually edit the images to prevent the biofilm overlapping with the edge of the Petri dish. We then use the `regionprops` MATLAB function to isolate the mat and remove the dish from the image. The result is a binary image that describes the locations of yeast cells only.

The `regionprops` function also enables us to compute the centroid of the binary image, which we denote as $(\bar{x}, \bar{y})$. The centroid definition enables us to calculate several important quantities. First, it is convenient to write the lattice site locations (x, y) in terms of the position vectors

$$\boldsymbol{r}(x,y) = (x - \bar{x}, y - \bar{y}), \tag{2.2}$$

from which we can define the set of position vectors for occupied sites,

$$\mathcal{P} = \{\boldsymbol{r}(x,y) \mid M(x,y) = 1, (x,y) \in \mathcal{D}\}. \tag{2.3}$$

This allows us to define the inner and outer radii of the biofilm as

$$R_i = \min_{\boldsymbol{r} \notin \mathcal{P}} |\boldsymbol{r}|, \quad \text{and} \quad R_o = \max_{\boldsymbol{r} \in \mathcal{P}} |\boldsymbol{r}|. \tag{2.4}$$

The inner radius, R_i, is the minimum distance from the centroid at which we find an unoccupied pixel, whereas the outer radius R_o is the maximum distance from the centroid at which we find an occupied pixel. The annular region bounded by concentric circles with these radii is where we expect to

see the floral pattern. Finally, we define the mean field density

$$\varrho = \frac{N_s}{\pi R_o^2}, \tag{2.5}$$

where

$$N_s = |\mathcal{P}| = \sum_{x,y} M(x,y) \tag{2.6}$$

is the number of occupied pixels in the binary image. These quantities become important when implementing the spatial statistics to quantify pattern formation.

To illustrate the process of creating a binary image, we consider the photograph in Figure 2.1d as an example. The ProtoCOL 3 system used to

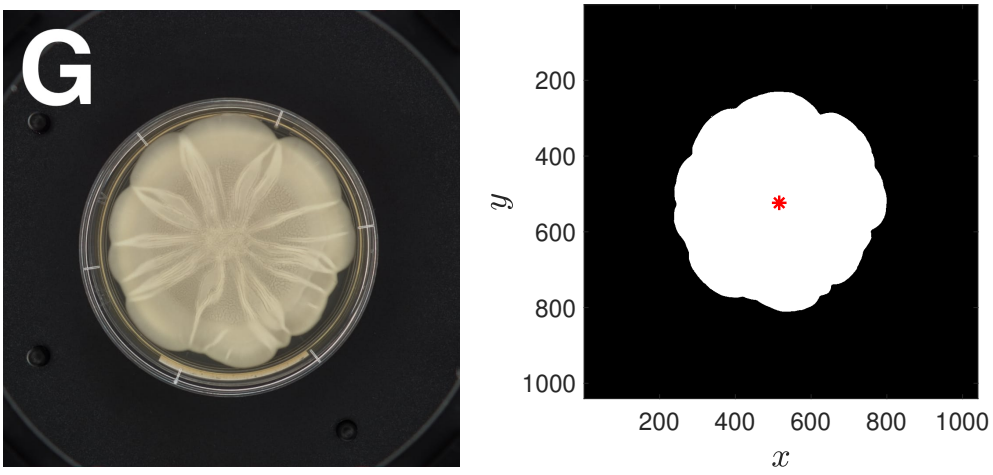

(a) An experimental mat photograph, taken 237 h after incubation.

(b) The corresponding binary image. The asterisk denotes the centroid $(\bar{x}, \bar{y})$.

Figure 2.2: An experimental photograph and corresponding binary image.

take the photographs consists of a 1.4 megapixel camera, yielding a photograph with 1040×1040 pixel resolution (Figure 2.2a). After manually distinguishing the mat boundary from the Petri dish and applying Otsu's method, the resulting binary image is shown in Figure 2.2b. This image consists of $N_s = 242033$ occupied lattice sites, shown in white in Figure 2.2b. Using `regionprops`, we also find that the mat centroid is located at $(\bar{x}, \bar{y}) =$

$(515.77, 523.44)$, as indicated by the asterisk in Figure 2.2b. As the camera position in the ProtoCOL 3 system is fixed, we use the fact that the inner diameter of the Petri dish is 83 mm to find that the width of one pixel represents approximately 0.14 mm. Having generated this binary image, the next step is to implement the spatial statistics.

2.2.1 Radial Statistic

For each binary image, we use the radial statistic of Binder et al. [11] to quantify the biofilm size. The radial statistic is a scaled count of the number of occupied sites at a given radial distance from the centroid. To construct it, we partition $[0, R_o]$ into L equispaced intervals. We then classify the position vectors of occupied sites according to their magnitude, by defining the subsets

$$\mathcal{S}_r(i) = \{\boldsymbol{r} \mid \Delta_r(i-1) \leq |\boldsymbol{r}| < \Delta_r i, \boldsymbol{r} \in \mathcal{P}\}, \tag{2.7}$$

for $\Delta_r = R_o/L$, and $i = 1, \ldots, L$. The subsets (2.7) are defined such that $\mathcal{S}_r(i) \subset \mathcal{P}$ for each $i = 1, \ldots, L$, and $\mathcal{S}_r(1) \cup \cdots \cup \mathcal{S}_r(L) = \mathcal{P}$. The number of elements $|\mathcal{S}_r(i)|$ in each subset gives a count of the number of occupied sites in the annular region where $\Delta_r(i-1) \leq |\boldsymbol{r}| < \Delta_r i$. To obtain the radial statistic, we normalise these counts with respect to the expected number of occupied sites if the annular domain was populated uniformly at random. This reference value is the product of the annulus area $\pi\Delta_r^2(2i-1)$, and the mean field density ϱ. The radial statistic is then

$$F_r(i) = \frac{|\mathcal{S}_r(i)|}{\pi\varrho\Delta_r^2(2i-1)}. \tag{2.8}$$

As an example computation of the radial statistic (2.8), we consider the processed image in Figure 2.2. For this image, $R_i = 254.97$ and $R_o = 292.48$, from which can compute $\varrho = 0.901$. We then compute the radial statistic (2.8), using $\Delta_r = 1$ and $L = 293$. This gives the result shown in Figure 2.3. We observe that for $r < R_i$, where all sites in the binary image are occupied,

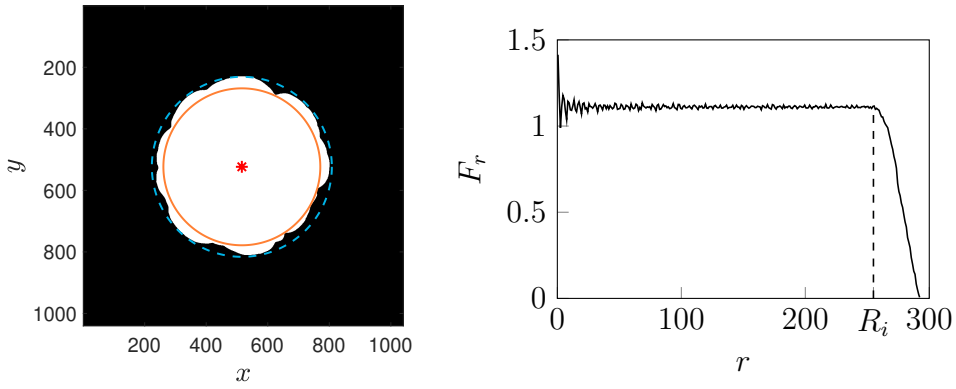

(a) The binary image. (b) The radial statistic.

Figure 2.3: A plot of the binary image and radial statistic (2.8) for the yeast biofilm in Figure 2.2. The inner radius $R_i = 252.97$, and outer radius $R_o = 292.48$ are indicated by the solid and dashed lines respectively in the binary image.

the radial statistic oscillates about the value $F_r = 1/\varrho$. Larger oscillations appear close to $r = 0$, as the corresponding annuli occupy smaller areas, and are therefore more prone to errors caused by assigning square pixels to annular domains. However, these errors are unimportant, because we are most interested in the leading edge, which indicates biofilm size. The annulus $R_i < r < R_o$ corresponds to the transition from the inner region where all sites are occupied, to the region outside the biofilm where no cells are present. Accordingly, Figure 2.3b shows that the radial statistic decreases from approximately $F_r(R_i) = 1/\varrho$, to $F_r(R_o) = 0$. For all $r > R_o$, the radial statistic takes the value $F_r = 0$, as this region contains no occupied pixels.

We would like to use information provided by the radial statistic to measure the speed of biofilm expansion. For each image, it is advantageous to define the median radius,

$$R_m = \min_{r\in[R_i,R_o]} \left\{ r \;\middle|\; F_r(r) \leq \frac{1}{2\varrho} \right\}. \tag{2.9}$$

This is illustrated in Figure 2.4b. As the median radius corresponds to the minimum radius at which less than or equal to half of the pixels are occupied,

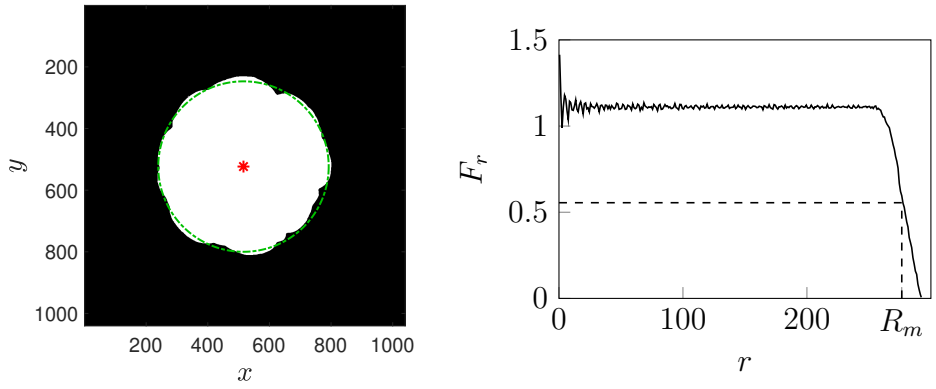

(a) The binary image. (b) The radial statistic.

Figure 2.4: A plot of the binary image and radial statistic (2.8) for the yeast biofilm in Figure 2.2. The median radius $R_i = 276.50$, is indicated by the dashed lines.

it provides a useful single measure of the biofilm size. We use this median radius when providing experimental results in §2.3, and subsequently in Chapters 3 and 5 when comparing mathematical models with experiments.

2.2.2 Angular Pair-Correlation Function

Quantifying the transition to floral morphology requires understanding the angular position of an occupied sites relative to others. The angular pair-correlation function (APCF) introduced by Binder et al. [11] provides a way to do this. To isolate the floral pattern, we consider the annular region $R_i \leq |\boldsymbol{r}| \leq R_o$, which contains both occupied and unoccupied sites. Computing the APCF requires considering all possible pairs of pixels in this region, and is therefore computationally expensive. We therefore restrict attention to a random subset of these sites, and define

$$\mathcal{P}_\theta = \{\boldsymbol{r}_j \mid R_i \leq |\boldsymbol{r}_j| \leq R_o, \boldsymbol{r}_j \in \mathcal{P}, j = 1, \ldots, M\}, \tag{2.10}$$

where M is the number of sampled points. The APCF is then a scaled count of the acute angles between all possible pairs of position vectors $(\boldsymbol{r}_i, \boldsymbol{r}_j)$,

where $\boldsymbol{r}_i, \boldsymbol{r}_j \in \mathcal{P}_\theta$. To construct it, we modify the approach of Binder et al. [11], and instead partition the interval $[0, \pi]$ into $N-1$ interior bins of width $\Delta_\theta = \pi/N$, and two bins of width $\Delta_\theta/2$ at either end. The mid points of each bin then represent $N+1$ equispaced data points at $\theta_j = j\Delta_\theta$, for $j = 0, \ldots, N$. If we let the partition midpoints be $\theta_j^m = (\theta_{j+1} + \theta_j)/2$, for $j = 0, \ldots, N-1$, We can define the subsets for the angles between pairs of position vectors,

$$\mathcal{S}_\theta(\theta_0) = \left\{ (\boldsymbol{r}_1, \boldsymbol{r}_2) \;\middle|\; 0 \leq \arccos\left(\frac{\boldsymbol{r}_1 \cdot \boldsymbol{r}_2}{|\boldsymbol{r}_1||\boldsymbol{r}_2|} \right) < \theta_0^m, \boldsymbol{r}_1, \boldsymbol{r}_2 \in \mathcal{P}_\theta \right\}, \tag{2.11a}$$

$$\mathcal{S}_\theta(\theta_k) = \left\{ (\boldsymbol{r}_1, \boldsymbol{r}_2) \;\middle|\; \theta_{k-1}^m \leq \arccos\left(\frac{\boldsymbol{r}_1 \cdot \boldsymbol{r}_2}{|\boldsymbol{r}_1||\boldsymbol{r}_2|} \right) < \theta_k^m, \boldsymbol{r}_1, \boldsymbol{r}_2 \in \mathcal{P}_\theta \right\}, \tag{2.11b}$$

$$\mathcal{S}_\theta(\theta_N) = \left\{ (\boldsymbol{r}_1, \boldsymbol{r}_2) \;\middle|\; \theta_{N-1}^m \leq \arccos\left(\frac{\boldsymbol{r}_1 \cdot \boldsymbol{r}_2}{|\boldsymbol{r}_1||\boldsymbol{r}_2|} \right) < \pi, \boldsymbol{r}_1, \boldsymbol{r}_2 \in \mathcal{P}_\theta \right\}, \tag{2.11c}$$

for $k = 1, \ldots, N-1$, and we compute angles using the `pdist` function in MATLAB. In a similar way to the radial statistic, when constructing the APCF we normalise the number of elements $|\mathcal{S}_\theta(\theta_j)|$ in each subset by the number of elements expected if the domain was populated uniformly at random. As there are $M(M-1)/2$ possible pair combinations, the APCF is given by

$$F_\theta(\theta_j) = \frac{2Nc_j\,|\mathcal{S}_\theta(\theta_j)|}{M(M-1)}, \tag{2.12}$$

where $c_j = 2$ for $j = 0, N$, and $c_j = 1$ otherwise.

Values of $F_\theta(\theta_j)$ greater than unity indicate that the likelihood of finding two pixels separated by an angle θ in the range $\theta_{j-1} \leq \theta \leq \theta_j$ exceeds what would be expected if the domain was populated uniformly at random. Local maxima of the function $F_\theta(\theta_j)$ therefore indicate regions of cell aggregation, whilst local minima indicate regions of cell segregation. We illustrate this using the yeast biofilm in Figure 2.2. The APCF in Figure 2.5b shows that at the biofilm edge, there are alternating regions of cell aggregation and segregation. Localised regions of cell aggregation surrounded by adjacent regions of segregation correspond to the petals of the floral morphology. To quantify the number of petals, we follow Binder and Simpson [134] and

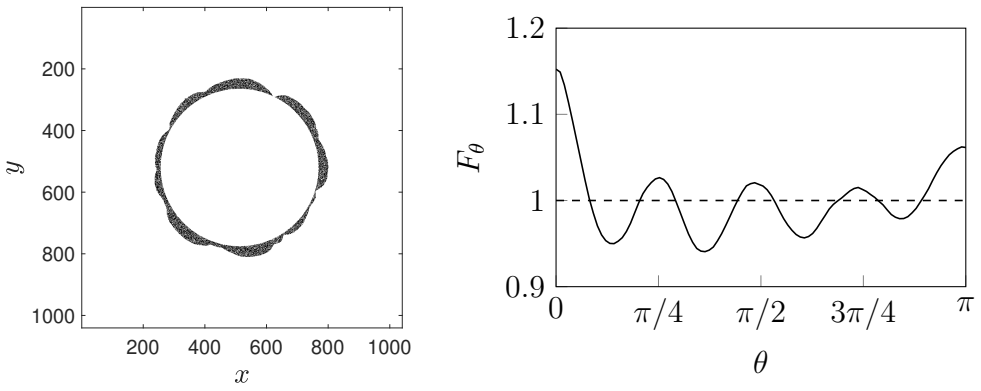

(a) The sampled binary image. (b) The angular pair-correlation function.

Figure 2.5: The sampled binary image and computed angular pair-correlation function for the yeast biofilm in Figure 2.2. We use $M = 25000$ samples, and sampled pixels are indicated in black.

compute the spectrum of F_θ. As we are only interested in the even periodic extension of F_θ, this involves taking the discrete cosine transform,

$$\hat{f}_k = \frac{2}{N c_k} \sum_{j=0}^{N} \frac{F_\theta(\theta_j)}{c_j} \cos(k\theta_j), \quad k = 0, \ldots, N. \tag{2.13}$$

The power spectrum $\hat{f}_k^2$ indicates the relative contribution of a floral pattern with k petals to the overall pattern. Therefore, the value of $\hat{f}_k^2$ indicates whether it is reasonable to conclude that the mat contains k petals. To illustrate this, we consider the mat in Figure 2.5, and plot the power spectrum in Figure 2.6. The power spectrum has the dominant mode of $k = 8$, suggesting that it is reasonable to conclude that this biofilm contains eight petals. As the power spectrum also contains peaks for other modes, some qualitative judgement is required when considering the total number of petals. However, the method provides quantitative justification that the floral morphology develops before the end of the experiment.

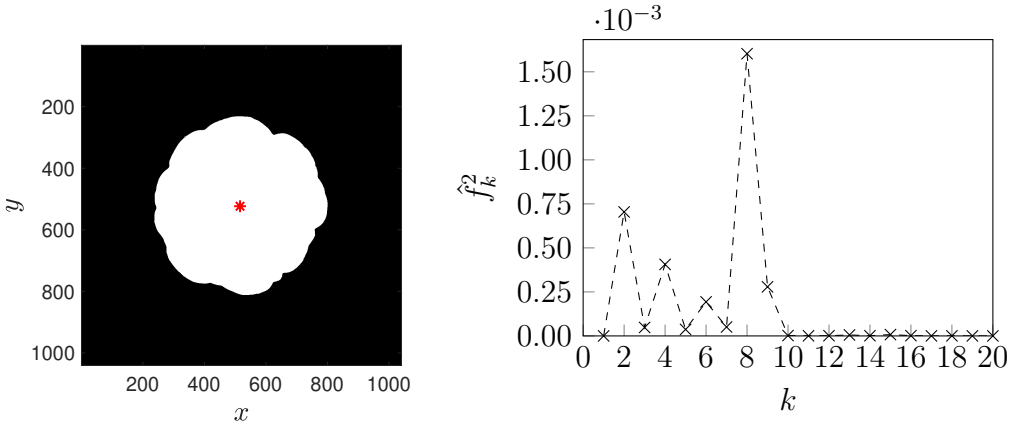

(a) The binary image.

(b) The power spectrum with $N = 100$.

Figure 2.6: The binary image and angular pair-correlation function power spectrum for the mat in Figure 2.2a.

2.3 Experimental Results

We use the spatial statistics defined in §2.2 to obtain experimental results that we can compare with mathematical models. Our first objective is to measure the experimental speed of expansion. This involves using the radial statistic to compute the median radius R_m in each photograph. We first apply the scale factor $1\,\text{pixel} = 0.14\,\text{mm}$ to convert the median radius to a physical distance. Then, we estimate the expansion speed using the mean biofilm size at the four times for which we have photographs. These results are presented in Figure 2.7. Therein, the dots represent mean data from the thirteen experiments, and the error bars indicate the maximum and minimum sizes observed across the experiments. Raw data used to obtain this plot are presented in Table A.1 in Appendix A.2.

We compute a linear least-squares fit to interpret the experimental data. Since the line of best fit (the dashed curve in Figure 2.7) passes within the experimental range at each data point, we initially adopt the assumption that the biofilm expands radially at a constant speed. This is the simplest assumption that is consistent with our collected data. The slope of the graph, $2.55 \times 10^{-3}\,\text{mm} \cdot \text{min}^{-1}$, then provides a single estimate of biofilm expansion

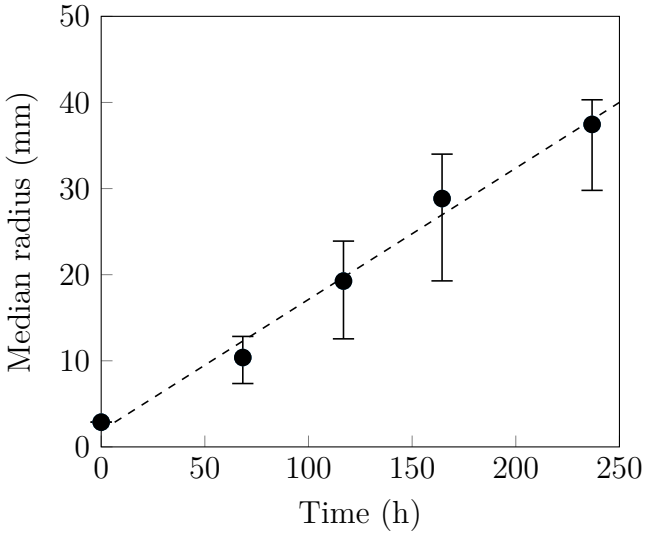

Figure 2.7: The median radius, R_m, scaled to mm, for all experimental photographs. The dots represent the mean size at a particular time, and error bars indicate the range observed over the thirteen experiments. The dashed line is a linear best-fit to the data, and has the slope $2.55 \times 10^{-3}\,\mathrm{mm} \cdot \mathrm{min}^{-1}$.

speed. Mathematically, the assumption of a single, constant expansion speed is advantageous for the travelling wave analysis presented in §3.2. Under this assumption, to account for biological variation, we use the raw data in Table A.1 to compute the mean expansion speed between all pairs of consecutive images across all experiments. This analysis gives expansion speeds that lie between $1.09 \times 10^{-3}\,\mathrm{mm} \cdot \mathrm{min}^{-1}$ and $4.67 \times 10^{-3}\,\mathrm{mm} \cdot \mathrm{min}^{-1}$. We will use this range when comparing the reaction–diffusion model with experimental data in Chapter 3, and will revisit the assumption of constant expansion speed when analysing the extensional flow model in Chapter 5.

We can also use the APCF to quantify the transition from circular to floral morphology observed in experiments. This involves computing the power spectrum for each experimental image, and these results are provided in full in Appendix A.3. Although the dominant modes are typically $k \in \{2, 3, 4\}$, as each mat grows differently, we see a wider range of modes represented across all experiments. When constructing mathematical models, we seek to explain the overall behaviour seen across all experiments. Therefore, we

introduce the function

$$\hat{F_k}^2 = \max_j \left(\frac{\hat{f}_k^2}{\sum_k \hat{f}_k^2} \right)_j , \tag{2.14}$$

for $j = 1, \ldots, 13$. This is the maximum value of each power spectrum coefficient $\hat{f}_k^2$, normalised with respect to the other coefficients from the same experiment. For each biofilm, we consider the power spectrum of images at the end of the experiment, which provides the longest possible time for the floral pattern to develop. A plot of $\hat{F_k}^2$ is given in Figure 2.8.

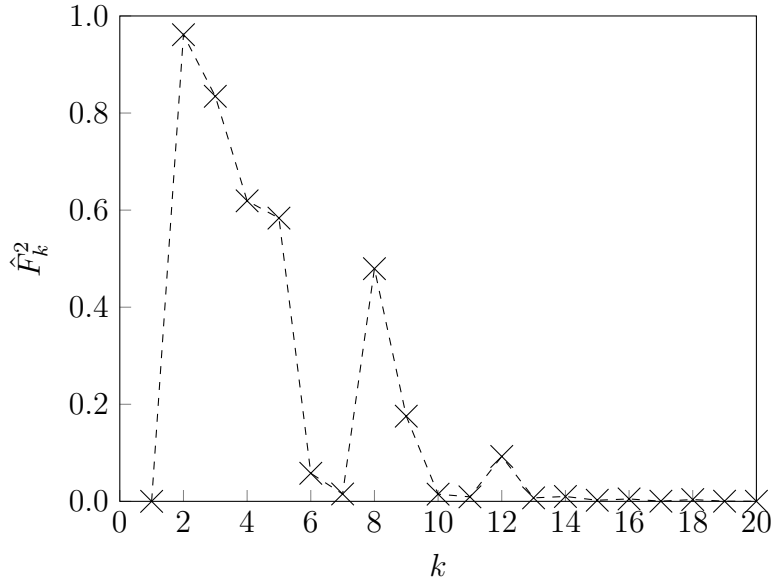

Figure 2.8: Normalised power spectrum: maximum value across thirteen mat formation experiments.

When quantifying the number of petals in a mat, the power spectrum results retain scope for qualitative interpretation. Across the experiments, we find that there is at least one case where each of the modes $k \in \{2, 3, 4, 5, 8\}$ is the dominant mode in the power spectrum (see Appendix A.3). Accordingly, these modes are strongly represented in in Figure 2.8. However, although not a dominant mode, there is also a noticeable peak for $k = 12$. We conclude that it is reasonable to expect a mat to have between $k = 2$ and $k = 12$

petals at the end of the experiment, with $k \in \{2, 3, 4, 5\}$ the most expected result. This result will be used when comparing the reaction–diffusion model of Chapter 3 with experiments.

In conjunction with the median radius data, these petal counts enable us to estimate the characteristic petal width in experiments. When the photographs were taken at the end of the experiments, the median radius across all biofilms was in the range $R_m \in [29.8, 40.3]$ mm, with a mean of $R_m = 37.45\,\text{mm}$. If we assume that petals develop from a circular biofilm, the experimental petal width is

$$w_p = \frac{2\pi R_m}{k}. \tag{2.15}$$

If we allow $k \in [2, 12]$, the range of possible petal widths is $w_p \in [15.6, 126.6]$ mm. We compare this result with a linear stability analysis of the reaction–diffusion model performed in §3.3.1.

2.4 Summary

We have used spatial statistical methods to quantify yeast biofilm growth. In an experimental mat formation assay of *S. cerevisiae*, yeast biofilms repeatedly adopted a floral morphology. This involved a transition from initially circular growth, to a spatially non-uniform pattern characterised by petal-like structures at the edge of the biofilm. As the floral morphology occurred in repeated experiments, we expect it to originate from common mechanisms. Our objective is to construct mathematical models for candidate mechanisms for biofilm growth. Spatial statistics enable us to compare mathematical model results with experiments in a quantitative way.

A suitable mathematical model needs to capture the speed of biofilm expansion and petal formation observed in experiments. Our experimental data consisted of a time series of photographs of biofilm growth, taken from directly above the colony. We converted these to binary images in MATLAB,

which enabled us to develop spatial statistics to quantify expansion speed and petal formation. To measure expansion speed, we implemented a radial statistic, which is a scaled count of pixels occupied by the biofilm at a given distance from the centroid. We then computed the minimum distance from the centroid for which the proportion of pixels occupied does not exceed 50%, and used this as the measure of biofilm size. To quantify petal formation, we implemented the angular pair-correlation function (APCF). This is a scaled count of the acute angles between all possible pairs of occupied pixels. Peaks in the APCF correspond regions of cell aggregation in the biofilm. To obtain a count of these regions, and hence the number of petals in the biofilm, we computed the discrete cosine transform of the APCF. With the radial statistic, this provided a way to measure the characteristic petal width, which we can compare between experiments and predictions from a mathematical model.

Having introduced the spatial statistics, we then applied them to photographs from an assay of thirteen yeast mat biofilms. We assumed that biofilms expand radially at a constant speed, which was the simplest assumption consistent with results for the radial statistic. Using linear least-squares fitting, we obtained a mean expansion speed of $2.55 \times 10^{-3}\,\mathrm{mm} \cdot \mathrm{min}^{-1}$, which lay between the feasible expansion speed range of $1.09 \times 10^{-3}\,\mathrm{mm} \cdot \mathrm{min}^{-1}$ to $4.67 \times 10^{-3}\,\mathrm{mm} \cdot \mathrm{min}^{-1}$. As the biofilms expanded, we found that they eventually adopted the floral morphology in each experiment. Using the APCF, we found that mature biofilms typically contained two to five petals, and that it was possible to observe up to twelve petals.

Our experimental data enables us to compare the two key characteristics of floral morphology, biofilm size and petal formation, with predictions from mathematical models. However, the need for non-invasive data collection methods limits the extent to which quantitative comparison is possible. Obtaining potentially useful measurements, for example of the number of cells and nutrient concentration, would require the biofilm to be destroyed. In this context, our objective was to perform the first quantitative comparison between mathematical models and experiments, while acknowledging that

there remains scope to improvements our data collection methods. For example, using a larger number of photographs would provide greater certainty on whether the constant expansion speed assumption is valid. Other studies have also obtained three-dimensional measurements of biofilm shape [127], which is not possible from our experimental images. Having established that it is possible to obtain meaningful quantitative measurements of colony morphology, in the future we plan to collaborate with experimental colleagues to develop new techniques that will enable more extensive data collection.

Chapter 3

A Reaction–Diffusion Model for Nutrient-Limited Yeast Biofilm Growth

In this chapter, we neglect biofilm mechanics, and focus on the hypothesis that nutrient-limited growth is the mechanism by which biofilms expand and petals form. To investigate this, we adopt a minimal mathematical model for mat growth. Our model takes the form of a coupled system of reaction–diffusion equations, with a non-linear, degenerate diffusion term for the spread of cells. The simplicity of our model ensures that we are able to estimate the relevant parameters from yeast mat formation experiments. This enables us to isolate the extent to which nutrient-limited growth alone is a possible explanation for the floral morphology.

The chapter is structured as follows. In §3.1, we present our minimal reaction–diffusion model for nutrient-limited mat formation, and estimate all parameters except the diffusion ratio from experimental data. In §3.2, we exploit the assumption that mats expand at a constant radial speed by constructing one-dimensional travelling wave solutions to our model. We use a combination of geometric singular perturbation theory and numerics to show that such solutions exist, and estimate the diffusion ratio using the speed of mat expansion. In §3.3, we apply the linear stability analysis of Müller and van Saarloos [64], which shows that two-dimensional planar travelling

waves are linearly unstable for the experimental range of parameters. We use this to predict the characteristic petal width, and compute two-dimensional numerical solutions to verify the analysis. We summarise the results in §3.4.

3.1 Mathematical Model

We use a reaction–diffusion model to investigate the effect of nutrient-limited growth in a yeast biofilm. Our objective is to analyse a minimal model, in which mechanical features and complex cellular behaviour are neglected. As outlined in §1.2.1, reaction–diffusion systems are prototype models that capture the essential features of nutrient-limited growth. They describe the spread of cells and nutrient, and consumption of nutrient by the cells, without requiring complicated descriptions of how these occur. In our context, their simplicity will enable detailed analysis, and comparison with experimental data.

Beginning with the general reaction–diffusion system (1.3), we need to determine appropriate forms of the diffusion and reaction terms. Since yeast cells are non-motile, they do not undergo standard Fickian diffusion. To account for this, we adopt the non-linear degenerate diffusion model (1.6) as a phenomenological description of cell spread. Throughout this work, we analyse the simplest form of this model, featuring $b = 1$. The reaction–diffusion model under consideration is then

$$\frac{\partial n}{\partial t} = D_n \nabla \cdot (n \nabla n) + \chi n g, \tag{3.1a}$$

$$\frac{\partial g}{\partial t} = D_g \nabla^2 g - \sigma \chi n g, \tag{3.1b}$$

where D_n and D_g are constants. An advantage of the system (3.1) is that it admits compactly supported solutions whereby cell density is only non-zero in a finite envelope [64]. It is therefore more suitable for modelling finite-sized experimental biofilms than linear diffusion models.

3.1.1 Scaling and Non-Dimensionalisation

We begin the analysis by writing the reaction–diffusion system (3.1) in dimensionless form. To achieve this, we introduce the dimensionless variables denoted by hats,

$$\hat{t} = G\chi t, \quad \hat{x_i} = \sqrt{\frac{G\chi}{D_g}} x_i, \quad \hat{n}(\hat{\boldsymbol{x}}, \hat{t}) = \frac{n(\boldsymbol{x}, t)}{N}, \quad \hat{g}(\hat{\boldsymbol{x}}, \hat{t}) = \frac{g(\boldsymbol{x}, t)}{G}, \tag{3.2}$$

where N is the measured mean final cell density, and G is the initial glucose concentration. In terms of these new dimensionless variables (3.2), the model (3.1) becomes (dropping hats)

$$\frac{\partial n}{\partial t} = D\nabla \cdot (n\nabla n) + ng, \tag{3.3a}$$

$$\frac{\partial g}{\partial t} = \nabla^2 g - \sigma^* ng. \tag{3.3b}$$

In writing (3.3), we have introduced the dimensionless parameters

$$D = \frac{ND_n}{D_g}, \quad \text{and} \quad \sigma^* = \frac{\sigma N}{G}, \tag{3.4}$$

where D is the ratio of cell to nutrient diffusivities, and σ^* is the dimensionless nutrient consumption rate.

3.1.2 Parameters

Estimating the dimensional parameters in (3.2) enables us to quantify the length and time scales. We use the empirical relationship of Slade, Cremers, and Thomas [135],

$$\frac{D_g}{D_0} = 1 - 0.023 w_a, \tag{3.5}$$

to estimate the diffusivity of glucose in agar, D_g. In (3.5), the reference value $D_0 = 4.04 \times 10^{-2}\,\mathrm{mm}^2 \cdot \mathrm{min}^{-1}$ is the diffusivity of glucose in water [136], and w_a is the weight percentage of the agar. We used 0.3% agar in each

experiment, which gives the estimate

$$D_g = 4.01 \times 10^{-2}\,\mathrm{mm}^2 \cdot \mathrm{min}^{-1}. \tag{3.6}$$

In our scaling, we use the initial concentration as the reference glucose concentration, G. The initial mass of glucose added to each plate was 0.5 g, and the agar medium occupied a circular area with diameter of approximately 83 mm. From this, we determine that the initial concentration of glucose in each experiment was

$$G = 9.24 \times 10^{-5}\,\mathrm{g} \cdot \mathrm{mm}^{-2}. \tag{3.7}$$

Since we could only measure the cell density at the end of the experiment, we use this single measurement as the reference cell density, N. Using the method described in §2.1, we obtained a mean of 1.46×10^{10} cells per mat. By analysing processed images in MATLAB, we found the mean mat area to be $4.46 \times 10^3\,\mathrm{mm}^2$ at the conclusion of the experiment. The mean reference cell density from the experiments was therefore

$$N = 3.34 \times 10^6\,\mathrm{cells} \cdot \mathrm{mm}^{-2}. \tag{3.8}$$

Table A.2 in Appendix A.2 contains the raw data used to derive this result.

To estimate σ, we assume that all of the consumed glucose is used for the creation of new cells, giving the dimensionless parameter $\sigma^* = 1$. We also assume that all of the glucose is consumed by the end of the experiment, which gives the estimate

$$\sigma = \frac{G}{N} = 2.77 \times 10^{-11}\,\mathrm{g} \cdot \mathrm{cell}^{-1}, \tag{3.9}$$

for the quantity of glucose consumed per new cell.

The cell proliferation rate, χ, cannot be measured directly, and is the most difficult parameter to estimate. To obtain an order of magnitude estimate, we

isolate χ by considering the dimensional model in the absence of diffusion,

$$\frac{\partial n}{\partial t} = \chi n g, \tag{3.10a}$$

$$\frac{\partial g}{\partial t} = -\sigma \chi n g. \tag{3.10b}$$

Multiplying equation (3.10a) by the constant σ, adding the result to (3.10b), and integrating once with respect to t, yields $\sigma n + g = \sigma N_0 + G$, where $N_0 = n(0)$ is the initial cell density. Hence, we can rewrite (3.10a) as

$$\frac{\partial n}{\partial t} = \chi n(\sigma N_0 + G - \sigma n). \tag{3.11}$$

Equation (3.11) is a first-order, non-linear, Bernoulli ordinary differential equation, which has the solution

$$n(t) = \frac{N_0(\sigma N_0 + G)\mathrm{e}^{\chi t(\sigma N_0 + G)}}{\sigma N_0 \mathrm{e}^{\chi t(\sigma N_0 + G)} + G}. \tag{3.12}$$

In each experiment, we placed 5000 cells on the Petri dish, concentrated in circular regions with a mean diameter of 5.75 mm. We therefore estimate the initial cell density to be $N_0 = 144.5\,\text{cells} \cdot \text{mm}^{-2}$. The final cell density, $n(t)$, is the mean cell density at the end of the experiment, N. We can then estimate the cell proliferation rate by rearranging (3.12) to give

$$\chi = \frac{N}{14208G(N_0 + N)} \log\left(\frac{N^2}{N_0^2}\right). \tag{3.13}$$

Using the experimental parameters already determined, we obtain

$$\chi = 15.28\,\text{mm}^2 \cdot \text{g}^{-1} \cdot \text{min}^{-1}. \tag{3.14}$$

Parameter estimation for the reaction–diffusion model is now complete, and we present a summary of these parameters in Table 3.1.

According to (3.2), knowledge of D_g, G, and χ enables us to compute the dimensionless length and time scales for the experiments. The time scale is

Table 3.1: Experimental estimates for the dimensional parameters used in the reaction–diffusion model.

Parameter	Value	Units	Source
D_g	4.01×10^{-2}	$\text{mm}^2 \cdot \text{min}^{-1}$	[135], [136]
G	9.24×10^{-5}	$\text{g} \cdot \text{mm}^{-2}$	Experimental design
N	3.34×10^{6}	$\text{cells} \cdot \text{mm}^{-2}$	Mat images
χ	15.28	$\text{mm}^2 \cdot \text{g}^{-1} \cdot \text{min}^{-1}$	Experimental data
σ	2.77×10^{-11}	$\text{g} \cdot \text{cell}^{-1}$	Assumption

$\hat{t} = (1.412 \times 10^{-3})t$, for t in minutes. As we grew the biofilms for 14 208 min, the end of the experiment corresponds to a dimensionless time of $\hat{t} = 20.1$. We can then calculate the expansion speed using the dimensionless length scale, which is $\hat{x} = 0.1933x$, for x given in millimetres. In §2.3, we found a mean expansion speed of $2.55 \times 10^{-3}\,\text{mm} \cdot \text{min}^{-1}$, which corresponds to a dimensionless speed of $c = 0.348$. Across all experiments, we observed speeds between $1.09 \times 10^{-3}\,\text{mm} \cdot \text{min}^{-1}$ and $4.67 \times 10^{-3}\,\text{mm} \cdot \text{min}^{-1}$, which gives a feasible range of dimensionless speeds of $c \in [0.150, 0.639]$. The length scale also enables us to find the dimensionless petal width. Using data in §2.3, the median radius across all biofilms lies in the range $\hat{x} \in [5.71, 7.54]$, with a mean of $\hat{x} = 7.02$. The dimensionless range of petal widths is then $\hat{w}_p \in [2.99, 23.68]$.

So far, we have not yet estimated the diffusivity ratio, D. This parameter is also difficult to estimate, because it cannot be measured in experiments. However, previous reaction–diffusion models have found a one-to-one relationship between the speed of travelling wave solutions and D [70]. If such a relationship exists for the model (3.3), we can use experimental measurements of expansion speed to infer D. We undertake a travelling wave analysis to investigate this possibility.

3.2 Travelling Wave Analysis

Many living things, from micro-organisms to complex multi-cellular organisms, have the ability to grow in size while maintaining their shape [82]. Travelling waves are solutions that advance at a constant speed while retaining their shape, and therefore provide a possible explanation for this phenomenon. Constructing travelling wave solutions is a common technique in the analysis of reaction–diffusion models. We seek a travelling wave solution to (3.3), which we can then relate to the expansion speed of yeast biofilms.

In the non-dimensionalisation (3.2), our choice of length scale implicitly assumes Cartesian geometry. When constructing the travelling wave solution, we consider the one-dimensional planar form of (3.3), which gives

$$\frac{\partial n}{\partial t} = D\frac{\partial}{\partial x}\left(n\frac{\partial n}{\partial x}\right) + ng, \tag{3.15a}$$

$$\frac{\partial g}{\partial t} = \frac{\partial^2 g}{\partial x^2} - ng. \tag{3.15b}$$

However, yeast biofilm growth is initially circular, for which the equivalent one-dimensional formulation is

$$\frac{\partial n}{\partial t} = D\left[\frac{\partial}{\partial r}\left(n\frac{\partial n}{\partial r}\right) + \frac{n}{r}\frac{\partial n}{\partial r}\right] + ng, \tag{3.16a}$$

$$\frac{\partial g}{\partial t} = \frac{\partial^2 g}{\partial r^2} + \frac{1}{r}\frac{\partial g}{\partial r} - ng. \tag{3.16b}$$

Due to the terms involving $1/r$, it is not possible to construct travelling wave solutions to (3.16). However, for large r the contribution of these terms is negligible compared to the higher derivative terms, and in the limit as $r \to \infty$, (3.16) approaches (3.15). Therefore, the solution to (3.16) will tend asymptotically to the travelling wave solution to (3.15) as $r \to \infty$ [6]. Our analysis therefore focuses on travelling wave solutions to (3.15), which we subsequently apply to our yeast biofilm experiments. A similar planar assumption was performed by Gallegos, Mazzag, and Mogilner [80] in

a model for swarming myxobacteria. As it is possible to fit a straight line to experimental data for biofilm size (see Figure 2.7), we expect the planar approximation to be valid on the length scale of our experiments.

Constructing a travelling wave solution involves introducing a variable that moves with the wave front. Without loss of generality, we can assume that the travelling waves advance rightward, and make the ansatz

$$z = x - ct, \tag{3.17}$$

where $c \in \mathbb{R}^+$ is the constant wave speed. Introducing the travelling wave co-ordinate (3.17) enables us to reduce (3.15) to the ordinary differential equations

$$D\frac{\mathrm{d}}{\mathrm{d}z}\left(n\frac{\mathrm{d}n}{\mathrm{d}z}\right) + c\frac{\mathrm{d}n}{\mathrm{d}z} + ng = 0, \tag{3.18a}$$

$$\frac{\mathrm{d}^2 g}{\mathrm{d}z^2} + c\frac{\mathrm{d}g}{\mathrm{d}z} - ng = 0. \tag{3.18b}$$

We now seek to solve (3.18) on the entire real line $z \in (-\infty, \infty)$, subject to four boundary conditions that depend on limiting behaviour in both space and time.

We obtain two boundary conditions by considering $z \to -\infty$, which corresponds to behaviour far behind the travelling wave, or long-time behaviour as $t \to \infty$. There, we expect to see a colony consisting entirely of cells, with all nutrients having been consumed. In contrast, the boundary $z \to \infty$ corresponds to the behaviour far ahead of the travelling wave. There, we expect to see no cells, and the nutrient concentration at its maximum level. If the cell density far behind the travelling wave is the mean final cell density, N, we obtain the boundary conditions

$$\begin{aligned} \lim_{z\to\infty} n(z) &= 0, \quad & \lim_{z\to-\infty} n(z) &= 1, \\ \lim_{z\to\infty} g(z) &= 1, \quad & \lim_{z\to-\infty} g(z) &= 0, \end{aligned} \tag{3.19}$$

with all derivatives of n and g with respect to z vanishing as $z \to \pm\infty$.

So far, we have introduced the ansatz (3.17) with no guarantee that travelling wave solutions exist. Establishing the existence of travelling wave solutions is important, as this indicates whether a yeast colony is able to expand at a constant speed while maintaining its shape. A travelling wave solution to (3.15) only exists if it is possible to solve the ordinary differential equations (3.18) such that the boundary conditions (3.19) are satisfied.

We can make analytical progress by rewriting (3.18) as a system of first-order ordinary differential equations. If we multiply (3.18a) by σ, and add to (3.18b), integrate once with respect to z, and apply the boundary conditions (3.19), we obtain

$$H_c := Dn\frac{\mathrm{d}n}{\mathrm{d}z} + \frac{\mathrm{d}g}{\mathrm{d}z} + c(n+g-1) = 0 \tag{3.20}$$

This holds for all $z \in (-\infty, \infty)$, so we refer to H_c as a conserved quantity. To construct the travelling wave solution, it is convenient to introduce the new variables

$$u(z) = n\frac{\mathrm{d}n}{\mathrm{d}z}, \quad \text{and} \quad w(z) = \frac{\mathrm{d}g}{\mathrm{d}z}, \tag{3.21}$$

whereby

$$\lim_{z\to-\infty} u(z) = \lim_{z\to\infty} u(z) = 0, \quad \text{and} \quad \lim_{z\to-\infty} w(z) = \lim_{z\to\infty} w(z) = 0. \tag{3.22}$$

Using these variables, we write (3.18) as the four-dimensional dynamical system

$$n\frac{\mathrm{d}n}{\mathrm{d}z} = u, \tag{3.23a}$$

$$\frac{\mathrm{d}g}{\mathrm{d}z} = w, \tag{3.23b}$$

$$D\frac{\mathrm{d}u}{\mathrm{d}z} = -\frac{cu}{n} - ng, \tag{3.23c}$$

$$\frac{\mathrm{d}w}{\mathrm{d}z} = ng - cw. \tag{3.23d}$$

Owing to the conserved quantity (3.20), there is a three-dimensional invariant

surface on which the dynamics of (3.23) occur. Replacing the variable u, by rearranging (3.20) and exploiting (3.21), allows us to reduce (3.23) to the three-dimensional system,

$$n\frac{\mathrm{d}n}{\mathrm{d}z} = \frac{1}{D}\left(c - cn - w - cg\right), \tag{3.24a}$$

$$\frac{\mathrm{d}g}{\mathrm{d}z} = w, \tag{3.24b}$$

$$\frac{\mathrm{d}w}{\mathrm{d}z} = ng - cw. \tag{3.24c}$$

We now use the technique first proposed by Aronson [137] to remove the singularity as $n \to 0$ in (3.24a). This involves introducing a new independent variable, ζ, defined by

$$\frac{\mathrm{d}\zeta}{\mathrm{d}z} = n^{-1} \implies \zeta = \int_0^z n^{-1}\,\mathrm{d}s. \tag{3.25}$$

The three-dimensional system (3.24) then becomes

$$\frac{\mathrm{d}n}{\mathrm{d}\zeta} = \frac{1}{D}\left(c - cn - w - cg\right), \tag{3.26a}$$

$$\frac{\mathrm{d}g}{\mathrm{d}\zeta} = wn, \tag{3.26b}$$

$$\frac{\mathrm{d}w}{\mathrm{d}\zeta} = n^2 g - cwn. \tag{3.26c}$$

Although (3.26) is topologically equivalent to (3.24), it has the advantage that the derivative in (3.26a) no longer vanishes as $n \to 0$.

We can use the three-dimensional dynamical system (3.26) to investigate the existence of travelling wave solutions to the model (3.15). By inspection, the fixed points of (3.26) are $(n, g, w) = (1, 0, 0)$ and $(0, 1, 0)$. These correspond to the asymptotic boundary conditions (3.19) as $z \to -\infty$ and $z \to \infty$ respectively. A travelling wave solution to the model (3.15) exists if there is a heteroclinic connection between these two equilibria. Identifying such connections is the key step in proving the existence of travelling waves.

3.2.1 Geometric Singular Perturbation Theory

So far, we have demonstrated that constructing travelling wave solutions to reaction–diffusion equations gives rise to a dynamical system. Geometric singular perturbation theory (GSPT) is a useful technique for analysing some dynamical systems that contain a small parameter. This is relevant to yeast growth, because we anticipate that glucose diffusion will occur much faster than the spread of yeast cells. As a result, we expect that $ND_n \ll D_g$, and therefore $0 < D = \varepsilon \ll 1$. Applying this to (3.26), we obtain

$$\varepsilon \frac{\mathrm{d}n}{\mathrm{d}\zeta} = c - cn - w - cg, \tag{3.27a}$$

$$\frac{\mathrm{d}g}{\mathrm{d}\zeta} = wn, \tag{3.27b}$$

$$\frac{\mathrm{d}w}{\mathrm{d}\zeta} = n^2 g - cwn, \tag{3.27c}$$

The system (3.27) is in the standard form for applying GSPT, and we refer to it as the *slow subsystem*.

If we attempt to study the leading-order behaviour of the perturbed system (3.27) by setting $\varepsilon = 0$, we obtain the regular problem

$$0 = c - cn - w - cg, \tag{3.28a}$$

$$\frac{\mathrm{d}g}{\mathrm{d}\zeta} = wn, \tag{3.28b}$$

$$\frac{\mathrm{d}w}{\mathrm{d}\zeta} = n^2 g - cwn, \tag{3.28c}$$

which we refer to as the *reduced problem*. However, as the slow subsystem (3.27) is singularly perturbed, the solution to (3.28) is not a valid approximation to the solution of the full system (3.27). To illustrate this singular nature, we observe that taking $\varepsilon = 0$ transforms the ordinary differential equation (3.27a) to the algebraic equation (3.28a). In doing so, we lose important information about how the fast variable n changes.

Despite this, further progress is possible by recognising that the small

parameter defines a clear separation of scales, whereby changes in g and w with respect to ζ occur much slower than changes in n. For this reason, we refer to g and w as the slow variables, and to n as a fast variable. This separation of scales is essential to the application of GSPT. If we introduce a new independent variable $\gamma = \zeta/\varepsilon$, we obtain

$$\frac{\mathrm{d}n}{\mathrm{d}\gamma} = c - cn - w - cg, \tag{3.29a}$$
$$\frac{\mathrm{d}g}{\mathrm{d}\gamma} = \varepsilon wn, \tag{3.29b}$$
$$\frac{\mathrm{d}w}{\mathrm{d}\gamma} = \varepsilon\left(n^2 g - cwn\right). \tag{3.29c}$$

which we refer to as the *fast subsystem*. This system is topologically equivalent to the slow system (3.27), but if we now examine the leading-order behaviour by taking $\varepsilon = 0$, we obtain

$$\frac{\mathrm{d}n}{\mathrm{d}\gamma} = c - cn - w - cg, \tag{3.30a}$$
$$\frac{\mathrm{d}g}{\mathrm{d}\gamma} = 0, \tag{3.30b}$$
$$\frac{\mathrm{d}w}{\mathrm{d}\gamma} = 0. \tag{3.30c}$$

This system is different from the reduced problem (3.28), which implies that it is not possible to approximate the leading-order behaviour of (3.27) and (3.29) by taking $\varepsilon = 0$. We refer to this second distinct regular problem (3.30) as the *layer problem*. When viewed with respect to the fast scale γ, the slow variables g and w do not change, and instead act as parameters in (3.30). The layer problem then describes how the fast variable n changes with respect to the independent variable. This information is missing from the reduced problem.

According to GSPT, the solutions to the reduced and layer problems together provide enough information to construct a valid approximation of the solution to the full perturbed system. The mathematical basis for this

result was proved by Fenichel [138], and hence GSPT is sometimes referred to as Fenichel theory. Applying the theory involves introducing the *critical manifold*, which is the set

$$\mathcal{S}_0 := \{(n, g, w) \mid c - cn - w - cg = 0\}. \tag{3.31}$$

The critical manifold (3.31) links the reduced and layer problems. In the layer problem (3.30), the plane $\mathcal{S}_0$ consists entirely of fixed points, and is the centre manifold of these equilibria. By (3.30), g and w are constant under the layer flow, so (3.30a) is a linear ODE in n with a negative coefficient. Solution trajectories of the layer problem (3.30) are therefore attracted exponentially quickly to $\mathcal{S}_0$, along rays of constant g and w. Viewed from the perspective of the reduced problem, this layer flow occurs instantaneously. This is because the critical manifold, $\mathcal{S}_0$, also represents the points at which the differential equations (3.28b) and (3.28c) of the reduced problem are defined. The reduced problem then describes how flow evolves on the critical manifold. This demonstrates how the two distinct problems exploit the separation of scales inherent in singularly perturbed problems.

Fenichel theory enables us to extend this analysis beyond the leading-order case, to consider $\varepsilon \neq 0$. The theory consists of three main theorems, and for precise statement and proof of these, we refer to Fenichel's original papers [138, 139], or other references on the subject [140, 141]. Here, we discuss their implications for constructing valid approximate solutions to singularly perturbed dynamical systems such as (3.27) and (3.29). The theorems state that if $\mathcal{S}_0$ is a normally hyperbolic invariant manifold, then for $\varepsilon > 0$ but sufficiently small, there exists an invariant smooth *slow manifold*, $\mathcal{S}_\varepsilon$, that lies $\mathcal{O}(\varepsilon)$ away from $\mathcal{S}_0$. Importantly, the fast flow to $\mathcal{S}_\varepsilon$ is a regular perturbation to the fast flow to $\mathcal{S}_0$. This means that concatenating solutions to the leading-order problems (3.28) and (3.30) provides a good approximation to the solutions of the full system (either (3.27) or (3.29)) for sufficiently small $\varepsilon > 0$. This is not possibly by simply setting $\varepsilon = 0$ in either the slow (3.27) or fast (3.29) subsystems. Thus, Fenichel theory provides a means to

construct travelling wave solutions to singularly perturbed systems [142].

Reduced Problem

When applying Fenichel theory to our model, we first consider the reduced problem. Owing to the algebraic constraint (3.28a), the reduced problem (3.28) simplifies to the two-dimensional system

$$\frac{\mathrm{d}g}{\mathrm{d}\zeta} = w\left(1 - \frac{w}{c} - g\right), \tag{3.32a}$$

$$\frac{\mathrm{d}w}{\mathrm{d}\zeta} = \left(1 - \frac{w}{c} - g\right)^2 g - cw\left(1 - \frac{w}{c} - g\right). \tag{3.32b}$$

This demonstrates another advantage of Fenichel theory, that the reduced and layer problems are both of lower dimension to the full system. We can simplify (3.32) further using the change of variables

$$\frac{\mathrm{d}\bar{\zeta}}{\mathrm{d}\zeta} = 1 - \frac{w}{c} - g \implies \bar{\zeta} = \int_0^\zeta \left(1 - \frac{w}{c} - g\right) \mathrm{d}s, \tag{3.33}$$

which yields

$$\frac{\mathrm{d}g}{\mathrm{d}\bar{\zeta}} = w, \tag{3.34a}$$

$$\frac{\mathrm{d}w}{\mathrm{d}\bar{\zeta}} = \left(1 - \frac{w}{c} - g\right) g - cw. \tag{3.34b}$$

A travelling wave solution to the full system (3.27) corresponds to a heteroclinic connection between $(1, 0, 0)$ and $(0, 1, 0)$. In the two-dimensional reduced system (3.34), this corresponds to a heteroclinic connection between $(g, w) = (0, 0)$ and $(1, 0)$, which are the fixed points of (3.34). Linearisation about these points shows that for any $c > 0$ the point $(0, 0)$ has a one-dimensional unstable manifold in the direction $(c/2 + \sqrt{c^2 + 4}/2, 1)$, and that $(1, 0)$ is a stable node. Furthermore, a trajectory leaving $(0, 0)$ along the

unstable direction is confined to the forward-invariant triangular region

$$\{(g, w) \mid 0 \leq g \leq 1, 0 \leq w \leq c(1-g)\}, \tag{3.35}$$

because flow on the boundaries of this region is never outwards. As $(0, 0)$ and $(1, 0)$ are the only two equilibria of (3.34), the Poincaré–Bendixson theorem then guarantees that the equilibrium $(1, 0)$ is the ω-limit set of a trajectory emanating from $(0, 0)$ [143]. This proves that a heteroclinic connection between $(0, 0)$ and $(1, 0)$ exists for the system (3.34). Thus, travelling wave solutions to the full system (3.26) exist for $D = 0$.

Although flow along the critical manifold always remains in the region $w \leq c(1-g)$, we cannot yet confirm the existence of travelling wave solutions for $\varepsilon \neq 0$. This is because when $\varepsilon \neq 0$ it may be possible for a trajectory of the full system (3.27) to intersect the (g, w) plane such that $w > c(1-g)$. If this occurs, then the change of variables (3.33) scales the independent variable negatively. Therefore, when $w > c(1-g)$, flow of the reduced problem (3.32) is in the opposite direction to (3.34). Without making the change of variables, in the reduced problem (3.32), a heteroclinic connection between $(0, 0)$ and $(1, 0)$ will not exist if the trajectory enters the region $w > c(1-g)$. The direction field plot in Figure 3.1 illustrates this. We investigate this further by studying the layer problem and fast subsystem.

Layer Problem

In the layer problem (3.30), the critical manifold $\mathcal{S}_0 : c - cn - w - cg = 0$ consists entirely of fixed points. By (3.30b) and (3.30c), the slow variables g and w are parameters of the layer problem. Layer flow is then given by the solution to the ordinary differential equation (3.30a). These solution trajectories are attracted exponentially quickly to the critical manifold along rays of constant g and w, as shown in Figure 3.2. We can then concatenate these solutions with those of the reduced problem (3.32) to construct travelling waves for $\varepsilon = 0$.

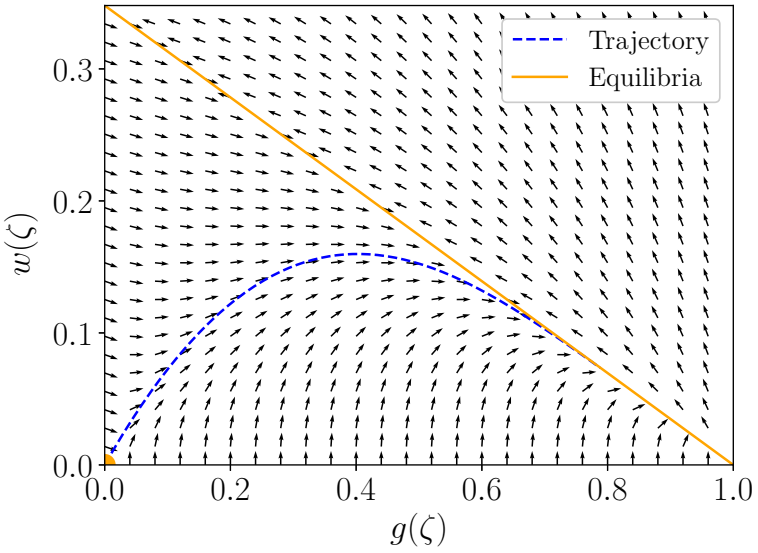

Figure 3.1: Direction field of the reduced problem (3.32) with the experimental wave speed $c = 0.348$ (black arrows). The equilibria, including the line $w = c(1 - g)$ and the point $(0, 0)$ are shown in orange, and the dashed blue line is a trajectory computed numerically using the fourth-order Runge–Kutta method.

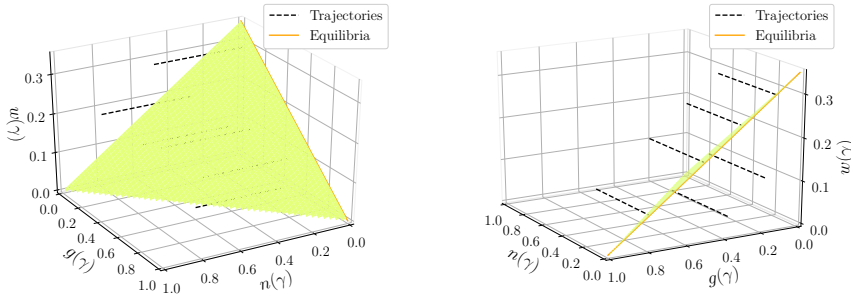

Figure 3.2: Two views of example solution trajectories of the layer problem (3.30). These trajectories are attracted exponentially quickly to the critical manifold along rays of constant g and w. The critical manifold is shown in yellow.

Fenichel theory guarantees that the slow manifold is a regular perturbation to the critical manifold. Therefore, we can write this surface as

$$\mathcal{S}_\varepsilon : n = 1 - g - \frac{w}{c} + \varepsilon f(g, w) + \mathcal{O}(\varepsilon^2), \tag{3.36}$$

for some function f. Dynamics of the fast subsystem (3.29) then enable us to approximate the shape of $\mathcal{S}_\varepsilon$ analytically. Differentiating (3.36) with respect to the fast variable γ, we obtain

$$\frac{\mathrm{d}n}{\mathrm{d}\gamma} = -\frac{\mathrm{d}g}{\mathrm{d}\gamma} - \frac{1}{c}\frac{\mathrm{d}w}{\mathrm{d}\gamma} + \varepsilon\left(\frac{\partial f}{\partial g}\frac{\mathrm{d}g}{\mathrm{d}\gamma} + \frac{\partial f}{\partial w}\frac{\mathrm{d}w}{\mathrm{d}\gamma}\right) + \mathcal{O}(\varepsilon^2). \tag{3.37}$$

Substituting relevant terms from the fast subsystem (3.29), we obtain

$$\mathcal{S}_\varepsilon : w_\varepsilon = c(1 - n - g) + \varepsilon\frac{n^2 g}{c} + \mathcal{O}(\varepsilon^2), \tag{3.38}$$

which is an asymptotic approximation to the shape of the slow manifold as $\varepsilon \to 0$. As expected, the leading-order approximation to $\mathcal{S}_\varepsilon$ is the critical manifold $\mathcal{S}_0$.

To test the accuracy of (3.38), we integrate the fast subsystem (3.29) numerically. We do this using a fourth-order Runge–Kutta scheme [144], with $N_\gamma = 25000$ points, and $\Delta\gamma = 1$. Since there is a one-dimensional unstable manifold associated with the equilibrium $(1, 0, 0)$, we take our initial condition to be a small distance from this point in the unstable direction. After obtaining the numerical solution, we compute

$$d_\varepsilon(w, w_\varepsilon) = \sqrt{\sum_{i=1}^{N_\gamma}(w - w_\varepsilon)_i^2}, \tag{3.39}$$

which is the L^2–norm of the vector of distances between points along the fast subsystem trajectory $(n, g, w)_i$, and the slow manifold $(n, g, w_\varepsilon)_i$, for $i = 1, \ldots, N_\gamma$. We compute this quantity for different values of ε with $c \in \{0.150, 0.348, 0.639\}$, and plot it in Figure 3.3. The presented results follow straight lines on the logarithmic scale. Therefore, $d_\varepsilon(w, w_\varepsilon) \sim \mathcal{O}(\varepsilon^m)$ as

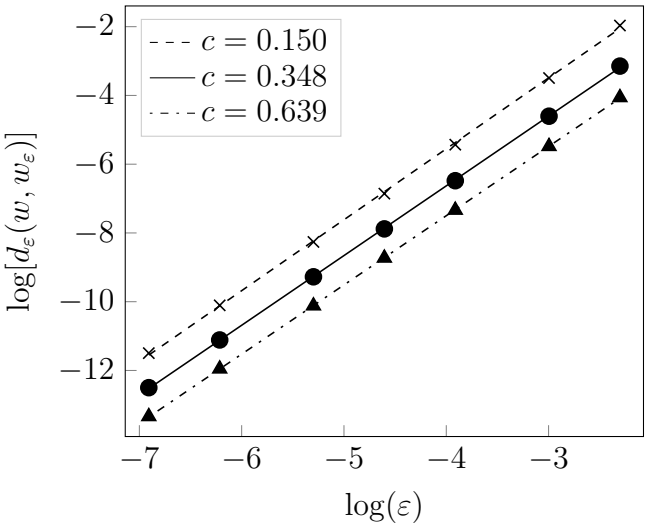

Figure 3.3: A log–log plot of $d_\varepsilon(w, w_\varepsilon)$ for $\varepsilon \in [0.001, 0.1]$, computed for the biologically relevant wave speeds $c \in \{0.150, 0.348, 0.639\}$.

$\varepsilon \to 0$, where m is the slope of the graph. We find that $m = 2.06$, $m = 2.03$, and $m = 2.01$ for $c = 0.150$, $c = 0.348$, and $c = 0.639$ respectively, which verifies the slow manifold approximation (3.38). To illustrate this further, we plot the solution trajectory for $c = 0.348$ and $\varepsilon = 0.1$ in Figure 3.4. As predicted, the trajectory closely follows the slow manifold.

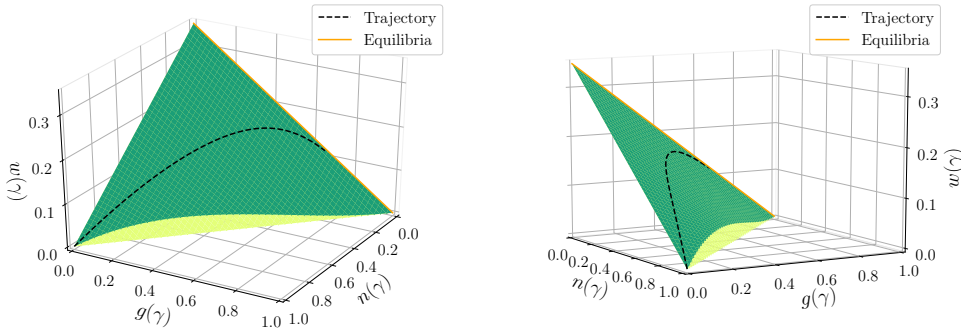

(a) (b)

Figure 3.4: Two views of the critical manifold $\mathcal{S}_0$ (yellow), and approximate slow manifold $\mathcal{S}_\varepsilon$ (green), for $c = 0.348$, and $\varepsilon = 0.1$. The dashed curve is a trajectory of the numerical solution to the fast subsystem (3.29), and the equilibria of (3.29) are shown in orange.

Although this analysis shows that the formula (3.38) is accurate, the slow manifold approximation breaks down close to $n = 0$. This is because $\mathcal{S}_0$ loses normal hyperbolicity there, and thus Fenichel theory only applies away from $n = 0$. Numerical integration of the full dynamical system (3.27) is required to determine whether solution trajectories intersect the (g, w) plane such that $w > c(1 - g)$. This is the final step in our travelling wave analysis, and allows us to investigate travelling waves beyond the small diffusion ratio regime.

3.2.2 Numerical Integration and Sharp-Fronted Travelling Waves

We explore the existence of biologically relevant travelling waves for $D > 0$ by integrating the slow subsystem (3.27) numerically. Fixing D, we observe three qualitative types of behaviour depending on c. For $D = 0.47$, these possibilities are illustrated in Figure 3.5, which correspond to the travelling wave profiles in Figure 3.6. If the wave speed is sufficiently small, for example $c = 0.25$ in Figure 3.5a, the trajectory intersects the (g, w) plane such that $w > c(1 - g)$. As the reduced problem direction field predicts, no biologically relevant travelling wave solution exists in this case. Figure 3.6a, in which we see negative cell density $n(\zeta)$ and nutrient concentration $g(\zeta)$, confirms this. In contrast, for $c = 0.5$ the trajectory eventually enters $(1, 0, 0)$, giving rise to the biologically valid travelling wave solution in Figure 3.6c. Between these two wave speeds, there is a minimum speed for which a biologically relevant travelling wave solution exists. For $D = 0.47$, this is $c = 0.348$, for which the trajectory of (3.27) reaches an equilibrium in the (g, w) plane along the line $w = c(1 - g)$. The travelling wave solution then has $n(\zeta) = 0$ and $g(\zeta) \neq 1$ in the far field as $\zeta \to \infty$, as Figure 3.6b confirms.

For all values of D, we observe the same three types of solution as Figures 3.5 and 3.6. This suggests that there is a critical minimum wave speed $c_{min}(D)$ associated with each D, such that a continuum of biologically relevant travelling waves exist for $c \geq c_{min}$. However, yeast biofilms have finite size, so

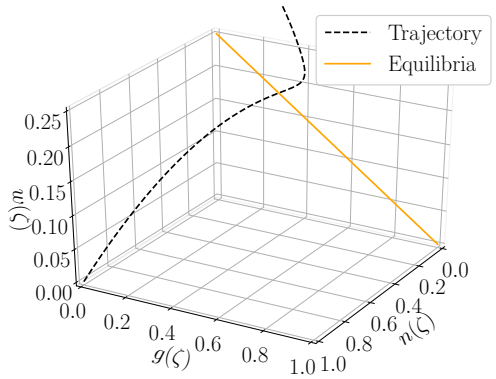

(a) $c = 0.25$.

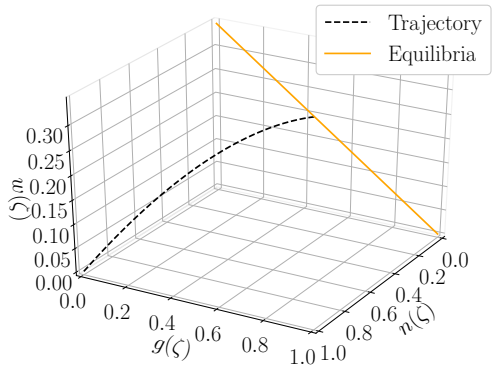

(b) $c = 0.348$.

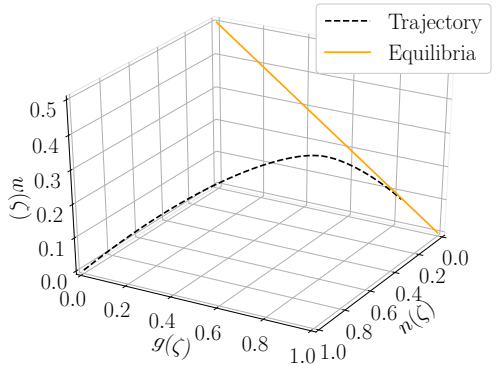

(c) $c = 0.5$.

Figure 3.5: Numerical solutions of the full dynamical system (3.26) for $D = 0.47$ and different c.

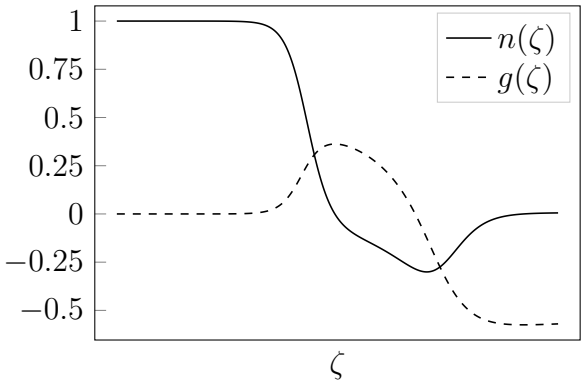

(a) $c = 0.25$.

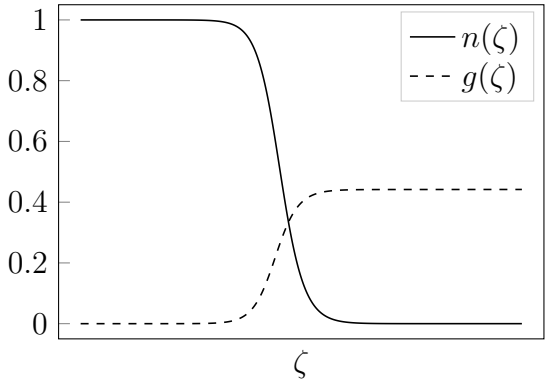

(b) $c = 0.348$.

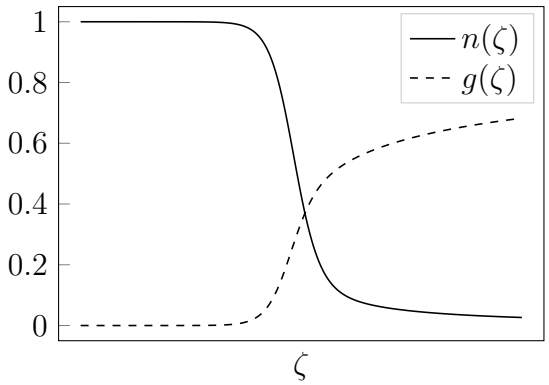

(c) $c = 0.5$.

Figure 3.6: Travelling wave solutions corresponding to Figure 3.5

a biologically relevant solution needs to have a sharp cell density front in the original travelling wave co-ordinate z. As Figure 3.6b shows, for $c = 0.348$, which is the minimum wave speed for $D = 0.47$, the solution attains $n = 0$ with $g < 1$. By the boundary conditions (3.19), this must occur for $z < \infty$. However, for $c > c_{min}$, the equilibrium corresponding to $\zeta \to \infty$ has $n = 0$ and $g = 1$, which occurs as $z \to \infty$. This suggests that a sharp-fronted profile only exists when $c = c_{min}$. Furthermore, the sharp-fronted profile emerges and propagates at c_{min} in numerical solutions to (3.15) with arbitrary initial conditions. Therefore, we adopt c_{min} as the experimental expansion speed.

3.3 Comparison with Experiments

We use the analysis of Müller and van Saarloos [64] to compare the reaction–diffusion model with experimental data. They used a numerical shooting method to compute sharp-fronted travelling waves that move at the minimum wave speed c_{min}. For each diffusion ratio D, they showed that $c_{min}(D)$ is unique, and only depends on D. Implementing their shooting method therefore enables us to determine the effect of the diffusion ratio on the speed of biofilm expansion. We illustrate this in Figure 3.7.

There is a monotonic relationship between the diffusion ratio and the minimum wave speed. Observing the expansion speed in an experiment therefore enables us to estimate the diffusion ratio. Across all of the experiments, we found expansion speeds in the range $c \in [0.150, 0.639]$. Using Figure 3.7, the corresponding range of possible diffusion ratios is $D \in [0.181, 1.02]$. The mean experimental expansion speed of $c = 0.348$ gives a diffusion ratio of $D = 0.47$. This is our estimate for D, and completes our set of experimental parameters.

By fitting a travelling wave solution to experimental data, we have shown that the reaction–diffusion model can explain a constant biofilm expansion speed, which was consistent with *S. cerevisiae* mat formation experiments. However, we have not yet accounted for changes in the biofilm shape as it grows. If our model can explain these, it would provide convincing evidence

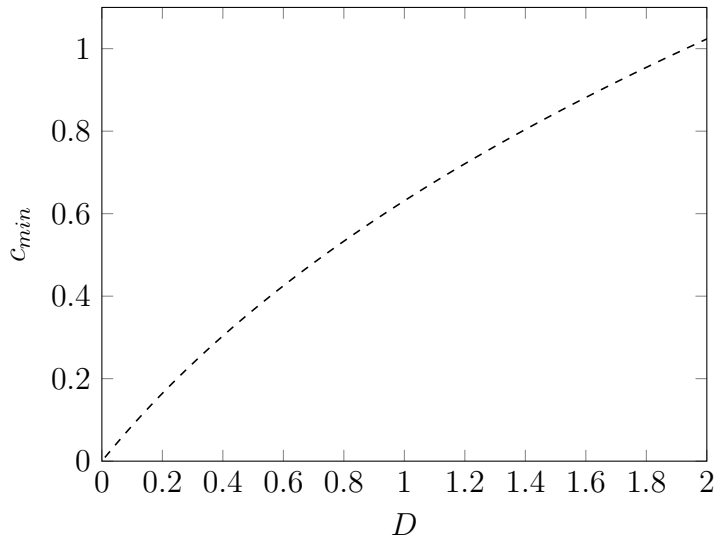

Figure 3.7: The relationship between the diffusion ratio, D, and the minimum travelling wave speed, c_{min}.

that non-linear, degenerate cell diffusion is a possible explanation for yeast biofilm growth. We investigate this by comparing the linear stability analysis of Müller and van Saarloos [64] with experimental data.

3.3.1 Linear Stability Analysis

In experiments, yeast biofilms undergo a transition from initially circular growth to the floral morphology, as we show in Figure 2.1. A possible explanation for this is that a biofilm experiences small deviations in its shape and cell distribution as new cells grow. Imperfections in the agar will also cause small non-uniformity in the concentration of nutrients. Non-linear cell diffusion is a plausible explanation for floral pattern formation if these small perturbations from uniformity can grow with time, which would enable the floral morphology to develop without active behaviour from the cells. Undertaking a linear stability analysis of two-dimensional planar travelling wave solutions to the model provides a theoretical way of investigating whether this can occur.

Linear stability analysis of the model equations (3.3) was performed by

Müller and van Saarloos [64]. As we seek to understand pattern formation in two-dimensions, we write (3.3) in two-dimensional Cartesian form,

$$\frac{\partial n}{\partial t} = D\frac{\partial}{\partial x}\left(n\frac{\partial n}{\partial x}\right) + D\frac{\partial}{\partial y}\left(n\frac{\partial n}{\partial y}\right) + ng, \tag{3.40a}$$

$$\frac{\partial g}{\partial t} = \frac{\partial^2 g}{\partial x^2} + \frac{\partial^2 g}{\partial y^2} - ng, \tag{3.40b}$$

where $n = n(x, y, t)$ and $g = g(x, y, t)$. This introduces the y co-ordinate normal to the direction of travelling wave propagation, which approximates a large circular biofilm. To account for small variations in biofilm shape, we make the change of variables

$$\xi = x - ct + \delta e^{iqy+\omega t}, \quad y^\dagger = y, \quad t^\dagger = t, \tag{3.41}$$

where $0 < \delta \ll 1$ is the small perturbation amplitude, $q > 0$ is the perturbation wave number, and ω is the growth rate [69, 72]. The new independent variable, ξ, follows the perturbed travelling wave front as it advances. We then investigate the effect of sinusoidal perturbations in the transverse direction on the cell density and nutrient concentration by expanding the variables as (dropping daggers on the new variables)

$$n(\xi, y, t) \sim n_0(\xi) + \delta n_1(\xi) e^{iqy+\omega t} + \mathcal{O}(\delta^2), \tag{3.42a}$$

$$g(\xi, y, t) \sim g_0(\xi) + \delta g_1(\xi) e^{iqy+\omega t} + \mathcal{O}(\delta^2), \tag{3.42b}$$

as $\delta \to 0$ [71, 73]. Upon applying (3.41) and (3.42) to the two-dimensional model (3.40), at leading-order we obtain the travelling wave equations (3.18) for $n_0(\xi)$ and $g_0(\xi)$. Linearising about these travelling wave solutions yields a spectral problem at $\mathcal{O}(\delta)$, consisting of the two second-order ordinary differential equations

$$D\frac{\partial^2}{\partial \xi^2}(n_0 n_1) + c\frac{\partial n_1}{\partial \xi} + g_0 n_1 + n_0 g_1 = \left(\omega + Dn_0 q^2\right)\left(n_1 + \frac{\partial n_0}{\partial \xi}\right), \tag{3.43a}$$

$$\frac{\partial^2 g_1}{\partial \xi^2} + c\frac{\partial g_1}{\partial \xi} - g_0 n_1 - n_0 g_1 = \left(\omega + q^2\right)\left(g_1 + \frac{\partial g_0}{\partial \xi}\right). \tag{3.43b}$$

Since the leading-order problem satisfies the boundary conditions (3.19), the higher-order corrections $n_1(\xi)$ and $g_1(\xi)$ and their derivatives must decay to zero as $\xi \to \pm\infty$. The boundary conditions associated with (3.43) are then

$$\begin{aligned} \lim_{\xi\to-\infty} n_1(\xi) = \lim_{\xi\to\infty} n_1(\xi) = 0, \quad \lim_{\xi\to-\infty} g_1(\xi) = \lim_{\xi\to\infty} g_1(\xi) = 0, \\ \lim_{\xi\to-\infty} \frac{\partial n_1}{\partial \xi} = \lim_{\xi\to\infty} \frac{\partial n_1}{\partial \xi} = 0, \quad \lim_{\xi\to-\infty} \frac{\partial g_1}{\partial \xi} = \lim_{\xi\to\infty} \frac{\partial g_1}{\partial \xi} = 0. \end{aligned} \tag{3.44}$$

Müller and van Saarloos [64] use a numerical shooting method to solve (3.43) and (3.44) for the first-order correction functions $n_1(\xi)$ and $g_1(\xi)$. In doing so, they prescribe D and q, and find that the growth rate $\omega(D, q)$ depends uniquely on these parameters. In (3.42), the sign of ω governs the long-time behaviour of the perturbations, and therefore the linear stability of the travelling wave solution (n_0, g_0). If $\Re\{\omega(q)\} > 0$, then the travelling wave solution is linearly unstable to a perturbation with wave number q. An initially small perturbation of wave number q will grow exponentially, and result in a visible pattern. Conversely, if $\Re\{\omega(q)\} < 0$, the perturbations will decay exponentially in time, and only the base solution will remain. This indicates that the travelling wave solution is linearly stable.

Applying the shooting method of Müller and van Saarloos [64] enables us to compute the dispersion relations $\omega(D, q)$ for the experimentally relevant diffusion ratios, $D = 0.181$, $D = 0.470$, and $D = 1.02$. These results are shown in Figure 3.8. For each experimentally feasible value of D, there is a range of wave numbers for which the travelling wave solution is linearly unstable. The wave number q contains spatial information about the perturbations that we expect to be unstable. As the perturbations (3.42) are sinusoidal, the wave number describes the characteristic perturbation width, which is given by $\hat{w} = 2\pi/q$. The perturbation widths of unstable modes then provides a prediction of the petal width in yeast biofilm experiments. For example, we observe instability for $q \in (0, 0.672)$ with $D = 0.47$. The theoretical

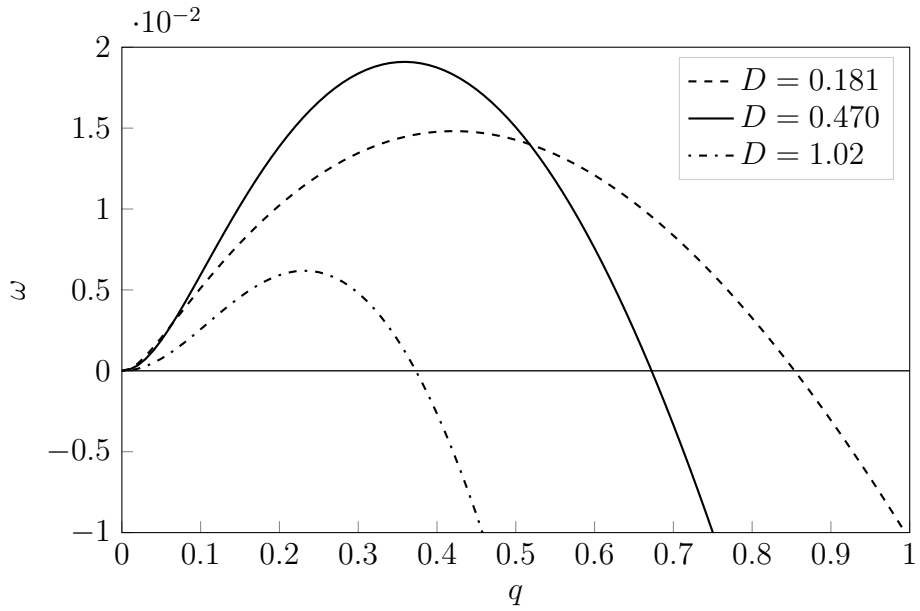

Figure 3.8: Dispersion curves showing the dependence of the growth rate ω on the wave number q and diffusion ratio D, for three experimentally feasible values of D.

prediction of petal width is therefore $\hat{w}_p > 9.35$. This overlaps the feasible experimental range $\hat{w} \in [2.99, 23.68]$, which suggests that the combination of nutrient-limited cell proliferation and non-linear diffusion is a potential mechanism for floral pattern formation.

Furthermore, we expect the wave number corresponding to the fastest growth rate ω to eventually dominate the experimental pattern. The dispersion curves of Figure 3.8 therefore allow us to predict the number of petals in an experimental mat. The most unstable wave numbers for $D = 0.181$, $D = 0.47$, and $D = 1.02$ are $q = 0.420$, $q = 0.358$, and $q = 0.232$ respectively. The predicted number of petals is then given by $k = q\hat{r}$, where $\hat{r} = 7.02$ is the mean final radius. For each experimentally feasible value of D, this gives $k = 1.63$, $k = 2.51$, and $k = 2.95$ respectively. Rounded to the nearest integer number of petals, the most unstable wave number range corresponds to $k \in \{2, 3\}$, which agrees well with the dominant modes of experimental images (see Figure A.5 in Appendix A.3). However, the linear stability analysis

presented here is only valid for large mats with negligible curvature, and for short times after the onset of instability. Previous studies have shown that curvature can have a significant effect on the wave speed [145, 146]. To investigate pattern evolution beyond the linear regime, and in finite-sized circular mats, we compute numerical solutions to the partial differential equations (3.40).

3.3.2 Two-Dimensional Numerical Solutions

We use a Crank–Nicolson scheme to compute numerical solutions to the two-dimensional reaction–diffusion model (3.40). At each time step, this gives rise to a large sparse linear system, which we solve iteratively using the generalised minimal residual (GMRES) method [147]. Based on a grid convergence study, we find that a grid spacing of $\Delta x = \Delta y = 0.1$, and time step size of $\Delta t = 0.001$ produces accurate solutions that are independent of both grid spacing and time step size. We employ these in all of our numerical solutions. For full details of the numerical scheme and convergence tests, see Appendix B.1.

We first use numerical solutions to validate the linear stability analysis of Müller and van Saarloos [64]. In these solutions, we omit $\mathcal{O}(\delta^2)$ terms from (3.42), prescribe a growth rate q, and use perturbations of the form

$$n(\xi, y, t) = n_0(\xi) + \delta n_1(\xi)\cos(qy)\mathrm{e}^{\omega t}, \tag{3.45a}$$

$$g(\xi, y, t) = g_0(\xi) + \delta g_1(\xi)\cos(qy)\mathrm{e}^{\omega t}. \tag{3.45b}$$

The functions $n_0(\xi)$ and $g_0(\xi)$ are the travelling wave solutions, and $n_1(\xi)$ and $g_1(\xi)$ are the first-order correction functions, both of which we compute using the numerical shooting method outlined by Müller and van Saarloos [64]. We then obtain a formula for the numerical growth rate ω by rearranging (3.45a), to give

$$\omega t = \log\left[1 + \frac{n(\xi, y, t) - n(\xi, y, 0)}{\delta n_1(\xi)\cos(qy)}\right]. \tag{3.46}$$

We obtain the initial condition $n(\xi, y, 0)$ from (3.45a) and the known solutions for $n_0(\xi)$ and $n_1(\xi)$, and use our iterative Crank–Nicolson scheme to compute the numerical solution $n(x, y, t)$. The formula (3.46) then enables us to compute the growth rate ω in numerical results.

We compute the dispersion relation numerically for the mean experimental value of $D = 0.470$. To do so, we solve (3.40) numerically, and compute the quantity (3.46) for $t \in [0, 100]$ in increments of ten. We then employ least squares linear fitting to obtain an estimate for the growth rate $\omega(D, q)$, and repeat this process for five theoretically unstable wave numbers. In each case, our numerical method reproduces the predicted instability, an example of which is shown in Figure 3.9. In addition, the growth rate predictions show good agreement with the theory, as illustrated in Figure 3.10. These results validate the linear stability analysis of Müller and van Saarloos [64].

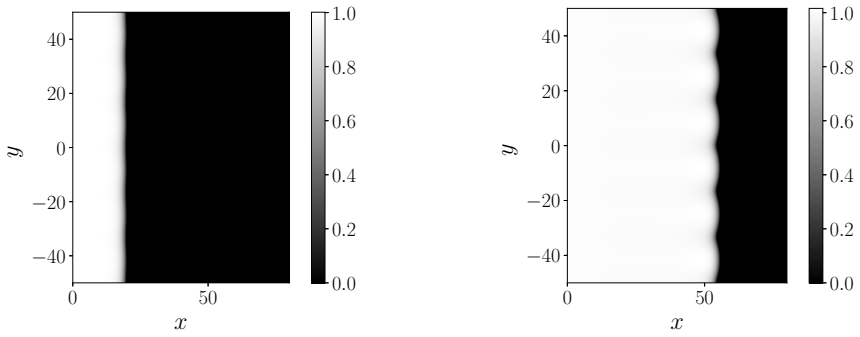

(a) $t = 0$. (b) $t = 100$.

Figure 3.9: Numerical cell density solutions $n(x, y, t)$ to the two-dimensional reaction–diffusion model (3.40), showing the predicted instability. Solutions computed using the ansatz (3.45) for the initial condition, and parameter values $D = 0.470$, $q = 0.3770$, and $\delta = 0.1$.

In addition to validating the linear stability analysis for planar fronts, we are also interested in whether our model captures petal formation in the circular geometry relevant to yeast colony growth. To investigate this, we compute solutions using a perturbed circular front as the initial condition.

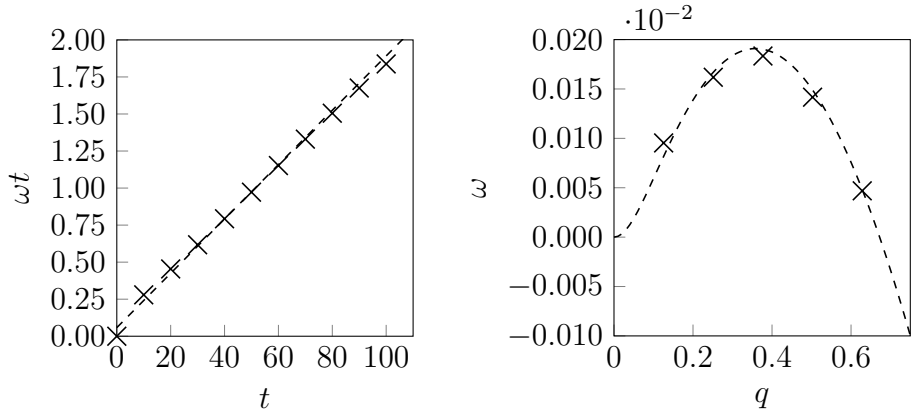

(a) Linear regression to calculate ω from (3.46), for $q = 0.3770$. The coefficient of determination is $r^2 = 0.9958$.

(b) The theoretical dispersion relation (dashed curve), and numerical computation (crosses) for $D = 0.470$.

Figure 3.10: Calculation of the growth rate and dispersion relation for $D = 0.470$, and $\delta = 0.1$.

We impose perturbations of the form

$$\xi_r = r - ct + \delta f_p(\theta), \tag{3.47a}$$

$$n(\xi_r, \theta, 0) = n_0(\xi_r - R_0) + \delta n_1(\xi_r - R_0) f_p(\theta), \tag{3.47b}$$

$$g(\xi_r, \theta, 0) = g_0(\xi_r - R_0) + \delta g_1(\xi_r - R_0) f_p(\theta), \tag{3.47c}$$

where $\theta \in [0, 2\pi]$, R_0 is the initial radius of the unperturbed colony, and correction functions n_1 and g_1 correspond to the theoretically most unstable wave number. The perturbation takes the form

$$f_p(\theta) = \sum_{k=2}^{12} \alpha_k \cos(k\theta), \tag{3.48}$$

which represents perturbations with k petals of amplitude α_k for $k = 2, \ldots, 12$. We draw each of the coefficients α_k randomly from the continuous uniform distribution $U(-1, 1)$, and then normalise them such that $\max_\theta |f_p(\theta)| = 1$. This ensures that δ represents the maximum perturbation amplitude. Based on the experimental length and time scales calculated in §3.1.1, the end of the

experiment corresponds to a dimensionless time of $\hat{t} = 20.1$, at which time the mean dimensionless mat radius is $\hat{r} = 7.02$. To ensure that the numerical solutions are on an appropriate scale, we initiate the perturbation at $R_0 = 5$ and compute solutions for $t \in [0, 10]$. We then compare these solutions with experimental results and linear stability analysis predictions.

To determine whether petal formation occurs in the solutions, we use (2.13) to compute the spectrum $\hat{f}_k$ of the angular pair-correlation function of images of the numerical solutions. For a given number of petals k, we conclude that the wave number corresponding to k petals is unstable if the amplitude of $\hat{f}_k^2$ increases over time. Alternatively, if the amplitude of $\hat{f}_k^2$ decreases, we conclude that the relevant mode is stable. To illustrate this process, we plot the binary images of a numerical solution with $D = 0.47$, and the corresponding power spectra for $t \in \{0, 5, 10\}$ in Figures 3.11 and 3.12.

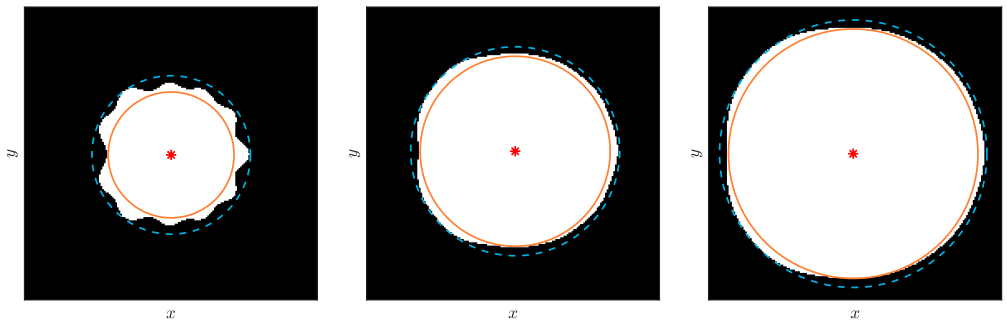

(a) $t = 0$. (b) $t = 5$. (c) $t = 10$.

Figure 3.11: Processed binary images of numerical solutions to (3.40) using the initial condition (3.47), for $D = 0.47$, $\delta = 0.5$, and $R_0 = 5$. The mat centroid is indicated with the red asterisk, and the inner and outer radii are shown in the solid orange and dashed blue lines respectively.

As Figure 3.12 shows, the magnitude of the power spectrum increases for the modes $k \in \{2, 3, 4\}$, and decreases for modes $k \geq 5$. Since we impose random perturbations, we repeat these computations three times for $D = 0.181$, $D = 0.47$, and $D = 1.02$ to ensure that all modes are adequately represented. The ensembles of random perturbations used are given in full in Appendix B.1.2. Analysing these repeated solutions, we find that modes

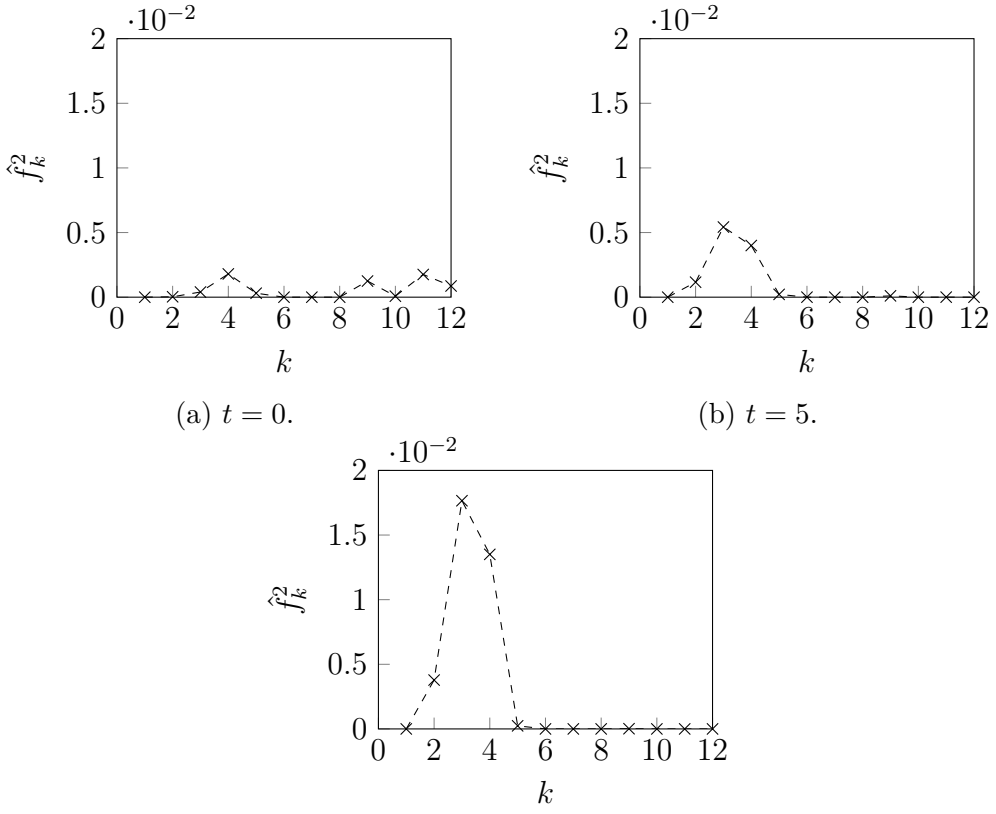

(a) $t = 0$.

(b) $t = 5$.

(c) $t = 10$.

Figure 3.12: Angular pair-correlation power spectra for the numerical solutions in Figure 3.11. The magnitude of $\hat{f}_k^2$ increases for $k \in \{2, 3, 4\}$, which suggests that these modes are unstable.

for $k \in \{2, 3, 4, 5, 6\}$ are unstable for $D = 0.181$, the modes $k \in \{2, 3, 4\}$ are unstable for $D = 0.47$, and the modes $k \in \{2, 3\}$ are unstable for $D = 1.02$ (see the power spectra in Figures B.2–B.4 in Appendix B.1.2). Qualitatively, this agrees well with the dispersion relations computed in Figure 3.8, where there is a range of unstable modes for all of $D = 0.181$, $D = 0.47$, and $D = 1.02$. Furthermore, the widest range of unstable modes occurs for $D = 0.181$, and the narrowest for $D = 1.02$, which also agrees with the theoretical results in Figure 3.8. The results for mean data with $D = 0.47$ also agree well with the experimental power spectra in Figure A.5, in which the modes $k \in \{2, 3, 4\}$, are predominantly represented. This confirms that nutrient-limited growth with non-linear degenerate cell diffusion is a plausible explanation for the experimentally observed floral pattern formation in circular geometry.

3.4 Summary

In this chapter, our objective was to determine the extent to which nutrient-limited growth alone could explain floral pattern formation. To achieve this, we used a reaction–diffusion system for the numerical cell density and nutrient concentration as a mathematical model for yeast biofilm growth. The key feature of the model was a non-linear, degenerate diffusion term for cell spread. This provided a phenomenological description of finite-sized yeast colonies, in which cell spread does not obey Fick's law of diffusion. The simplicity of the model enabled mathematical analysis of the biofilm expansion speed and petal formation.

We investigated travelling wave solutions to the model. These are suitable for biofilms that expand at a constant radial speed, an assumption consistent with experimental data for *S. cerevisiae*. Introducing the travelling wave co-ordinate, we reduced the reaction–diffusion model to a three-dimensional dynamical system. To construct travelling wave solutions, we first considered the limit where the cell diffusion was small compared to nutrient diffusion. This small parameter gave rise to a singularly perturbed, slow–fast dynamical

system, which we analysed using geometric singular perturbation theory. We used the reduced problem to show that travelling wave solutions exist for zero cell diffusion. Analysis of the layer problem then provided numerical evidence of a slow manifold on which the solutions for small, but non-zero cell diffusion exist. We completed the investigation by integrating the dynamical system numerically, which confirmed that there is a one-to-one relationship between the ratio of diffusion coefficients, D, and the travelling wave speed, c. We then used experimental data for the expansion speed to infer D, and obtain a complete set of estimated parameters.

Having estimated the parameters, we next investigated whether the model could predict floral pattern formation. Linear stability analysis by Müller and van Saarloos [64] showed that, provided D is not too large, planar travelling wave solutions are unstable to transverse perturbations with a range of wave numbers. We found that this instability occurred for all experimentally feasible values of D. The reaction–diffusion system therefore predicted that petals would form in an experiment. Furthermore, we found good agreement between the theoretical range of unstable wave numbers and experimental measurements of petal width. Based on this evidence, we concluded that nutrient-limited growth is a possible explanation for petal formation, and that non-linear, degenerate cell diffusion is appropriate for modelling cell spread.

When interpreting these results, it is important to consider some limitations of our study. Biological variation between experiments can make parameters difficult to determine accurately. We adopted several assumptions to obtain estimates. These included assuming that the cell density is constant at the end of the experiment, and calculating the cell proliferation rate in the absence of diffusion. Alternative methods, such as using numerical solutions to fit multiple parameters to experimental data, provide an avenue for future work.

In our two-dimensional numerical solutions, we initiated a perturbation at a single radius. In contrast, experimental mats are continually subjected to small-amplitude perturbations as they grow. Owing to this difficulty,

our numerical solutions only indicate which of the modes are unstable, and cannot recreate observed patterns with complete fidelity. Another limitation is that we performed travelling wave analysis in planar geometry, which is only valid asymptotically in the limit of large biofilm radius. Investigating the stability of solutions in radial geometry would provide additional evidence that nutrient-limited growth can drive petal formation, and is another subject for future work.

Finally, the minimal reaction–diffusion model does not capture all of the mechanisms thought to contribute to the floral morphology. Although we do not need to invoke alternative mechanisms to explain the floral pattern, the reaction–diffusion model provides a framework onto which we can add more features. For example, extracellular fluid flow may provide an alternative means of biofilm expansion as cells proliferate [101, 120]. Investigation of these mechanical features requires a more complicated modelling approach, which we undertake in subsequent chapters.

Chapter 4

Multi-Phase Fluid Modelling of Yeast Biofilm Growth: Derivation and Thin-Film Limits

In Chapter 3, we used a minimal model to show that nutrient-limited growth in the absence of mechanics is a possible explanation for the floral morphology observed in yeast biofilms. However, this model does not provide a complete description of biofilm formation, as it neglects the complex mechanical interactions between the cells, extracellular matrix, and environment. Experimental observations of Reynolds and Fink [17], who hypothesised that yeast biofilms expand by sliding motility, justify the need to include these features in the model. We now aim to extend our model for nutrient-limited growth to include macroscopic mechanical effects, including the flow of extracellular fluid.

In §4.1, we derive a general mechanical model for yeast biofilm expansion. Our model treats the biofilm as a two-phase mixture of living cells and extracellular fluid, both of which we assume to be viscous fluids. Since this model incorporates mechanics in addition to nutrient limitation, it is more complex than the reaction–diffusion system considered in Chapter 3. To obtain two simpler models, we apply the thin-film approximation in both the

extensional flow (§4.2) and lubrication (§4.3) scaling regimes. The extensional flow model enables us to test the hypothesis of Reynolds and Fink [17] that yeast biofilms expand by sliding motility, and the lubrication model describes growth when there is strong biofilm–substratum adhesion, and large pressure and surface tension. These simplified models are more amenable to mathematical analysis and numerical computation than the general model.

4.1 Formulation and Governing Equations

We consider three-dimensional growth of a yeast biofilm on a solid substratum, and adopt a cylindrical co-ordinate system (r, θ, z). Similar to Howell, Scheid, and Stone [148], we define the compactly-supported domain

$$\Omega\,(t) = \{(r, \theta) \mid 0 < r < S(\theta, t)\} \tag{4.1}$$

to be the projection of the area inhabited by the biofilm onto $z = 0$. We refer to $S(\theta, t)$, which is the boundary $\partial\Omega(t)$ of the domain $\Omega(t)$, as the *contact line*. The biofilm is bounded below by a rigid substratum of thickness H_s, and bounded above by a free surface $z = h(r, \theta, t)$. Biofilm growth occurs with characteristic height H_b, and a characteristic radius R_b. A sketch of the problem domain, which closely resembles that of Ward and King [120], is shown in Figure 4.1.

We adopt a macroscopic continuum modelling approach, and treat the biofilm as a mixture of two viscous fluid phases. These comprise a living cell phase denoted with the subscript n, and an extracellular matrix (ECM) phase denoted with the subscript m. This ECM incorporates the extracellular polymeric substances and all extracellular fluid. We define the volume fractions of living cells and ECM to be $\phi_n(r, \theta, z, t)$ and $\phi_m(r, \theta, z, t)$ respectively, and assume that the fluid mixture contains no voids, that is

$$\phi_n + \phi_m = 1. \tag{4.2}$$

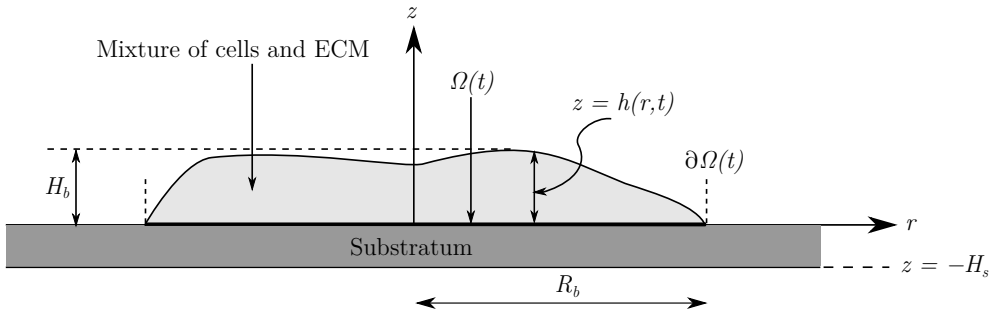

Figure 4.1: A simplified representation of a vertical slice through the centre of the biofilm and substratum. The biofilm exists in the region $0 < z < h(r, \theta, t)$, where $(r, \theta) \in \Omega(t)$.

As indicated in §1.2.2, when defining these volume fractions we implicitly assume that an appropriate averaging process has taken place, and do not discuss the details here.

Along with biofilm mechanics, we incorporate the uptake of nutrients from the substratum. To enable this, we introduce $g_s(r, \theta, z, t)$, the nutrient concentration in the substratum defined for $-H_s < z < 0$, and $g_b(r, \theta, z, t)$, the nutrient concentration in the biofilm, defined for $0 < z < h(r, \theta, t)$ and $(r, \theta) \in \Omega(t)$. We use two distinct nutrient concentrations because the nutrient concentration is initially discontinuous across the biofilm–substratum interface. As the experiment proceeds, nutrients can enter the biofilm across this interface, at which point they become available for consumption by the cells. We assume that nutrients disperse by diffusion in the substratum, and by both diffusion and advection with extracellular fluid inside the biofilm.

4.1.1 Mass and Momentum Balance

We derive the governing equations of our general model using the conservation of mass and momentum for each species. The general mass balance equation is

$$\frac{\partial \rho}{\partial t} + \nabla \cdot \boldsymbol{q} = J, \tag{4.3}$$

where ρ is the density, $\boldsymbol{q}$ represents the flux, and J is the net volumetric source term. In each fluid phase, we assume that the flux is entirely advective. That is, $\boldsymbol{q}_\alpha = \phi_\alpha \boldsymbol{u}_\alpha$, where $\alpha = n, m$ denotes a fluid phase, and $\boldsymbol{u}_\alpha = (u_r, u_\theta, u_z)_\alpha$ are the fluid velocity vectors. Assuming that both the cellular and ECM phases have constant density, the conservation of mass equation for each phase reads

$$\frac{\partial \phi_\alpha}{\partial t} + \nabla \cdot (\phi_\alpha \boldsymbol{u}_\alpha) = J_\alpha. \tag{4.4}$$

For the fluid production terms J_α, we adapt the bilinear forms used in Chapter 3 to incorporate cell death, which was neglected in our reaction–diffusion model. Assuming that dead cells immediately become part of the ECM, we write

$$J_n = \psi_n \phi_n g_b - \psi_d g_b, \quad J_m = \psi_m \phi_n g_b + \psi_d g_b, \tag{4.5}$$

where ψ_n, ψ_m, and ψ_d are constants. In (4.5), cell death is proportional to cell density only, while production of both living cells and ECM increases with local cell density and nutrient concentration. This is consistent with the experimental observation that cellular components and the ECM are both formed by catabolism of cellular synthesised glucose. Since (4.5) describes mass creation in the biofilm, the fluid velocities for each phase do not satisfy the usual incompressibility condition $\nabla \cdot \boldsymbol{u}_\alpha = 0$.

Regarding nutrients, we need to consider the nutrients in the substratum and nutrients in the biofilm separately. In the substratum, nutrient movement obeys Fick's law of diffusion, and therefore we obtain the standard diffusion equation

$$\frac{\partial g_s}{\partial t} = D_s \nabla^2 g_s, \tag{4.6}$$

where D_s is the coefficient of diffusion for glucose in agar. However, once nutrients enter the biofilm, they become available for consumption by the cells, and we assume that total flux is comprised of both diffusion and advection with the extracellular fluid. Similar to Chapter 3, we also assume that the rate of nutrient consumption is proportional to the local cell volume fraction

and nutrient concentration. The mass balance equation for glucose in the biofilm then reads

$$\frac{\partial g_b}{\partial t} + \nabla \cdot (\phi_m g_b \boldsymbol{u}_m) = D_b \nabla^2 g_b - \eta \phi_n g_b, \tag{4.7}$$

where D_b is the glucose diffusivity in the biofilm, and η is the maximum rate at which nutrient is consumed.

We obtain the remaining governing equations from the principle of momentum conservation. Since experiments show that inertial effects are negligible on the time and length scales of biofilm growth [99], the momentum balance equations for each of the two phases are

$$\nabla \cdot (\phi_\alpha \boldsymbol{\sigma}_\alpha) + \boldsymbol{F}_\alpha = \mathbf{o}, \tag{4.8}$$

where $\boldsymbol{\sigma}$ is the stress tensor, and $\boldsymbol{F}$ represents net sources of momentum. Equation (4.8), together with the mass balance equations (4.4), (4.6) and (4.7), provide the basis for our model.

To write our equations in terms of physical properties of the fluids, we require constitutive relations for the stress tensors $\boldsymbol{\sigma}_\alpha$ and momentum source terms $\boldsymbol{F}_\alpha$. These describe the mechanical behaviour of the cells and extracellular fluid. For the stress tensors, we assume that both phases are Newtonian viscous fluids. Owing to cell proliferation and local ECM production, the stress components include terms involving $\nabla \cdot \boldsymbol{u}_\alpha$, which would otherwise vanish due to incompressibility. In cylindrical co-ordinates, the stress tensor is [149]

$$\boldsymbol{\sigma}_\alpha = \begin{bmatrix} \sigma_{rr} & \sigma_{r\theta} & \sigma_{rz} \\ \sigma_{\theta r} & \sigma_{\theta\theta} & \sigma_{\theta z} \\ \sigma_{zr} & \sigma_{z\theta} & \sigma_{zz} \end{bmatrix}_\alpha, \tag{4.9}$$

with the components

$$\sigma_{rr\alpha} = -p_\alpha - \frac{2\mu_\alpha}{3} \nabla \cdot \boldsymbol{u}_\alpha + 2\mu_\alpha \frac{\partial u_{r\alpha}}{\partial r}, \tag{4.10a}$$

$$\sigma_{r\theta\alpha} = \sigma_{\theta r\alpha} = \mu_\alpha \left[r \frac{\partial}{\partial r} \left(\frac{u_{\theta\alpha}}{r} \right) + \frac{1}{r} \frac{\partial u_{r\alpha}}{\partial \theta} \right], \tag{4.10b}$$

$$\sigma_{rz\alpha} = \sigma_{zr\alpha} = \mu_\alpha \left(\frac{\partial u_{r\alpha}}{\partial z} + \frac{\partial u_{z\alpha}}{\partial r} \right), \tag{4.10c}$$

$$\sigma_{\theta\theta\alpha} = -p_\alpha - \frac{2\mu_\alpha}{3} \nabla \cdot \boldsymbol{u}_\alpha + \frac{2\mu_\alpha}{r} \left(\frac{\partial u_{\theta\alpha}}{\partial \theta} + u_{r\alpha} \right), \tag{4.10d}$$

$$\sigma_{\theta z\alpha} = \sigma_{z\theta\alpha} = \mu_\alpha \left(\frac{\partial u_{\theta\alpha}}{\partial z} + \frac{1}{r} \frac{\partial u_{z\alpha}}{\partial \theta} \right), \tag{4.10e}$$

$$\sigma_{zz\alpha} = -p_\alpha - \frac{2\mu_\alpha}{3} \nabla \cdot \boldsymbol{u}_\alpha + 2 \frac{\partial u_{z\alpha}}{\partial z}, \tag{4.10f}$$

where for each phase p_α is the pressure, and μ_α is the dynamic viscosity, and these viscosities for each phase are assumed constant. When writing the stress tensor components, we invoke Stokes' hypothesis, giving the coefficient $-2\mu_\alpha/3$ for the divergence terms [118–120] in (4.10). Here, we also neglect growth pressure due to cell–cell contact, which was previously considered in similar models [107, 121]. This is because yeast cells are non-motile, and we expect them to be unable to actively generate forces in response to environmental cues. By making this assumption, we suggest that the incompressibility of the material is sufficient to drive expansion when cells proliferate.

Regarding the sources of momentum, we follow Green et al. [123] by assuming that the ECM exerts a drag force on the cells. We therefore prescribe the momentum sources as

$$\boldsymbol{F}_n = -k \left(\boldsymbol{u}_n - \boldsymbol{u}_m \right) + p_n \nabla \phi_n, \quad \boldsymbol{F}_m = -k \left(\boldsymbol{u}_m - \boldsymbol{u}_n \right) + p_m \nabla \phi_m, \tag{4.11}$$

where $k(\phi_n, \phi_m) \geq 0$ is the inter-phase viscous drag coefficient. The second term on the right-hand side of each momentum source (4.11) represents interfacial forces between cells and the ECM.

Now, if we substitute the constitutive relations for the stress tensors (4.9) and momentum source terms (4.11) into the momentum balance equations

(4.8), we obtain

$$\begin{aligned} &-\frac{\partial}{\partial r}\left(\phi_\alpha p_\alpha\right)-\frac{2\mu_\alpha}{3}\frac{\partial}{\partial r}\left(\phi_\alpha \nabla\cdot\boldsymbol{u}_\alpha\right)+\mu_\alpha\nabla\cdot\left(\phi_\alpha\frac{\partial \boldsymbol{u}_\alpha}{\partial r}\right)\\ &\quad+\mu_\alpha\nabla\cdot\left(\phi_\alpha\nabla u_{r\alpha}\right)-\frac{2\mu_\alpha\phi_\alpha}{r^2}\left(\frac{\partial u_{\theta\alpha}}{\partial\theta}+u_{r\alpha}\right)\\ &\quad-\frac{\mu_\alpha}{r^2}\frac{\partial}{\partial\theta}\left(\phi_\alpha u_{\theta\alpha}\right)-k\left(u_{r\alpha}-u_{r\beta}\right)+p_\alpha\frac{\partial\phi_\alpha}{\partial r}=0, \end{aligned} \tag{4.12a}$$

$$\begin{aligned} &-\frac{1}{r}\frac{\partial}{\partial\theta}\left(\phi_\alpha p_\alpha\right)-\frac{2\mu_\alpha}{3r}\frac{\partial}{\partial\theta}\left(\phi_\alpha\nabla\cdot\boldsymbol{u}_\alpha\right)+\mu_\alpha\nabla\cdot\left(\frac{\phi_\alpha}{r}\frac{\partial\boldsymbol{u}_\alpha}{\partial\theta}\right)\\ &\quad+\mu_\alpha\nabla\cdot\left(\phi_\alpha\nabla u_{\theta\alpha}\right)+\frac{2\mu_\alpha}{r^2}\frac{\partial}{\partial\theta}\left(\phi_\alpha u_{r\alpha}\right)+\mu_\alpha\phi_\alpha\frac{\partial}{\partial r}\left(\frac{u_{\theta\alpha}}{r}\right)\\ &+\frac{\mu_\alpha\phi_\alpha}{r^2}\frac{\partial u_{r\alpha}}{\partial\theta}-\frac{\mu_\alpha}{r}\frac{\partial}{\partial r}\left(\phi_\alpha u_{\theta\alpha}\right)-k\left(u_{\theta\alpha}-u_{\theta\beta}\right)+\frac{p_\alpha}{r}\frac{\partial\phi_\alpha}{\partial\theta}=0, \end{aligned} \tag{4.12b}$$

$$\begin{aligned} &-\frac{\partial}{\partial z}\left(\phi_\alpha p_\alpha\right)-\frac{2\mu_\alpha}{3}\frac{\partial}{\partial z}\left(\phi_\alpha\nabla\cdot\boldsymbol{u}_\alpha\right)+\mu_\alpha\nabla\cdot\left(\phi_\alpha\frac{\partial\boldsymbol{u}_\alpha}{\partial z}\right)\\ &\quad+\mu_\alpha\nabla\cdot\left(\phi_\alpha\nabla u_{z\alpha}\right)-k\left(u_{z\alpha}-u_{z\beta}\right)+p_\alpha\frac{\partial\phi_\alpha}{\partial z}=0, \end{aligned} \tag{4.12c}$$

where β represents the opposite phase to α. Given appropriate initial and boundary conditions, these momentum balance equations (4.12), together with the mass balance equations (4.4), (4.6) and (4.7), define a system of governing equations for the fluid pressures, fluid velocities, and nutrient concentrations.

4.1.2 Initial and Boundary Conditions

To close the model, we require initial and boundary conditions for all of the physical variables. When constructing the general model, we will leave the initial conditions arbitrary. We write

$$h(r,\theta,0)=\mathcal{H}(r,\theta), \tag{4.13a}$$

$$\phi_\alpha(r,\theta,z,0)=\Phi_\alpha(r,\theta,z), \tag{4.13b}$$

and so on, where the initial conditions for g_s, and g_b take the same form as (4.13b).

We obtain the first boundary condition using the fact that nutrient cannot pass through the base of the substratum, which is assumed to be rigid. Hence, the no-flux condition on the substratum base is

$$(-D_s \nabla g_s) \cdot \hat{\boldsymbol{n}} = \frac{\partial g_s}{\partial z} = 0, \quad \text{on} \quad z = -H_s, \tag{4.14}$$

where throughout this section $\hat{\boldsymbol{n}}$ will denote the unit outward normal vector to the relevant surface. To enable cell proliferation and expansion, the biofilm takes up nutrients from the substratum. We assume that the flux of nutrients across the biofilm–substratum interface is proportional to the local concentration difference. As there is no nutrient in the biofilm when the cells are plated, this difference is initially non-zero, and we expect that advection and consumption of nutrients in the biofilm will sustain the difference. Assuming fluid cannot pass through the interface, we then have

$$(-D_s \nabla g_s) \cdot \hat{\boldsymbol{n}} = D_s \frac{\partial g_s}{\partial z} = -Q\,(g_s - g_b) \quad \text{on} \quad z = 0, \tag{4.15a}$$

$$(g_b \phi_m \boldsymbol{u}_m - D_b \nabla g_b) \cdot \hat{\boldsymbol{n}} = D_b \frac{\partial g_b}{\partial z} = -Q\,(g_s - g_b) \quad \text{on} \quad z = 0, \tag{4.15b}$$

$$\boldsymbol{u}_\alpha \cdot \hat{\boldsymbol{n}} = u_{z\alpha} = 0 \quad \text{on} \quad z = 0, \tag{4.15c}$$

for $(r, \theta) \in \Omega(t)$. In equations (4.15a) and (4.15b), the constant Q is the nutrient mass transfer coefficient, which indicates the permeability of the biofilm. We also impose a general tangential stress condition on the substratum–biofilm interface, similar to that of Green et al. [123]. This condition reads

$$\hat{\boldsymbol{t}} \cdot (\phi_\alpha \boldsymbol{\sigma}_\alpha \cdot \hat{\boldsymbol{n}}) = -\lambda_\alpha \left(\phi_\alpha \boldsymbol{u}_\alpha \cdot \hat{\boldsymbol{t}}\right) \quad \text{on} \quad z = 0, \tag{4.16}$$

where $\hat{\boldsymbol{t}}$ is any unit tangent vector, and λ_α are coefficients representing the strength of adhesion between the fluid and substratum for each phase. This

gives the two general slip conditions

$$\mu_\alpha \left(\frac{\partial u_{r\alpha}}{\partial z} + \frac{\partial u_{z\alpha}}{\partial r} \right) = -\lambda_\alpha u_{r\alpha}, \quad \text{on} \quad z = 0, \tag{4.17a}$$

$$\mu_\alpha \left(\frac{\partial u_{\theta\alpha}}{\partial z} + \frac{1}{r}\frac{\partial u_{z\alpha}}{\partial \theta} \right) = -\lambda_\alpha u_{\theta\alpha}, \quad \text{on} \quad z = 0, \tag{4.17b}$$

for $(r, \theta) \in \Omega(t)$.

On the free surface, we assume that nutrient cannot pass through the biofilm–air interface. This no-flux condition is

$$(g_b \phi_m \boldsymbol{u}_m - D_b \nabla g_b) \cdot \hat{\boldsymbol{n}} = 0 \quad \text{on} \quad z = h. \tag{4.18}$$

Given that the unit outward normal to the free surface is

$$\hat{\boldsymbol{n}} = \frac{\nabla (z-h)}{|\nabla (z-h)|} = \frac{1}{\sqrt{1 + \left(\frac{\partial h}{\partial r}\right)^2 + \left(\frac{1}{r}\frac{\partial h}{\partial \theta}\right)^2}} \left(-\frac{\partial h}{\partial r}, -\frac{1}{r}\frac{\partial h}{\partial \theta}, 1 \right), \tag{4.19}$$

this condition reads

$$\begin{aligned} g_b \phi_m \left(u_{rm}\frac{\partial h}{\partial r} + \frac{u_{\theta m}}{r}\frac{\partial h}{\partial \theta} - u_{zm} \right) \\ = D_b \left(\frac{\partial g_b}{\partial r}\frac{\partial h}{\partial r} + \frac{1}{r^2}\frac{\partial g_b}{\partial \theta}\frac{\partial h}{\partial \theta} - \frac{\partial g_b}{\partial z} \right) \quad \text{on} \quad z = h. \end{aligned} \tag{4.20}$$

We also impose the kinematic condition

$$\frac{\mathrm{D}}{\mathrm{D}t}(z-h) = \left(\frac{\partial}{\partial t} + \boldsymbol{u}_\alpha \cdot \nabla \right)(z-h) = 0, \tag{4.21}$$

on each phase, which states that fluid particles on the free surface must remain there. By expanding the material derivative and gradient operators, we can re-write this as

$$\frac{\partial h}{\partial t} + u_{r\alpha}\frac{\partial h}{\partial r} + \frac{u_{\theta\alpha}}{r}\frac{\partial h}{\partial \theta} = u_{z\alpha} \quad \text{on} \quad z = h. \tag{4.22}$$

We obtain stress boundary conditions by noting that a free surface is subject to zero tangential stress, and normal stress that is proportional to its local curvature. In general, these conditions read

$$\hat{\boldsymbol{t}} \cdot (\phi_\alpha \boldsymbol{\sigma}_\alpha \cdot \hat{\boldsymbol{n}}) = 0 \quad \text{on} \quad z = h, \tag{4.23a}$$

$$\hat{\boldsymbol{n}} \cdot (\phi_\alpha \boldsymbol{\sigma}_\alpha \cdot \hat{\boldsymbol{n}}) = -\gamma_\alpha \kappa \quad \text{on} \quad z = h, \tag{4.23b}$$

where γ_α is the surface tension coefficient of phase α, and $\kappa = \nabla \cdot \hat{\boldsymbol{n}}$ is the mean free surface curvature. Similar to other models in biology [95], this surface tension represents the strength of cell–cell adhesion at the biofilm–air interface. These forces are thought to be weak in sliding motility, but have greater relevance if there is strong adhesion to the substratum.

The stress tensors (4.9), and tangential and normal vectors enable us to expand the general free surface stress conditions (4.23), to obtain

$$\begin{aligned} &-2\frac{\partial h}{\partial r}\left(\frac{\partial u_{r\alpha}}{\partial r} - \frac{\partial u_{z\alpha}}{\partial z}\right) - \frac{\partial h}{\partial \theta}\left[\frac{1}{r^2}\frac{\partial u_{r\alpha}}{\partial \theta} + \frac{\partial}{\partial r}\left(\frac{u_{\theta\alpha}}{r}\right)\right] \\ &\quad + \frac{\partial u_{r\alpha}}{\partial z} + \frac{\partial u_{z\alpha}}{\partial r} - \left(\frac{\partial h}{\partial r}\right)^2\left(\frac{\partial u_{z\alpha}}{\partial r} + \frac{\partial u_{r\alpha}}{\partial z}\right) \\ &\quad - \frac{1}{r}\frac{\partial h}{\partial r}\frac{\partial h}{\partial \theta}\left(\frac{\partial u_{\theta\alpha}}{\partial z} + \frac{1}{r}\frac{\partial u_{z\alpha}}{\partial \theta}\right) = 0 \quad \text{on} \quad z = h, \end{aligned} \tag{4.24a}$$

$$\begin{aligned} &-\frac{2}{r}\frac{\partial h}{\partial \theta}\left(\frac{1}{r}\frac{\partial u_{\theta\alpha}}{\partial \theta} + \frac{u_{r\alpha}}{r} - \frac{\partial u_{z\alpha}}{\partial z}\right) - \frac{\partial h}{\partial r}\left[r\frac{\partial}{\partial r}\left(\frac{u_{\theta\alpha}}{r}\right) + \frac{1}{r}\frac{\partial u_{r\alpha}}{\partial \theta}\right] \\ &\quad + \frac{\partial u_{\theta\alpha}}{\partial z} + \frac{1}{r}\frac{\partial u_{z\alpha}}{\partial \theta} - \frac{1}{r}\frac{\partial h}{\partial r}\frac{\partial h}{\partial \theta}\left(\frac{\partial u_{z\alpha}}{\partial r} + \frac{\partial u_{r\alpha}}{\partial z}\right) \\ &\quad - \frac{1}{r^2}\left(\frac{\partial h}{\partial \theta}\right)^2\left(\frac{1}{r}\frac{\partial u_{z\alpha}}{\partial \theta} + \frac{\partial u_{\theta\alpha}}{\partial z}\right) = 0 \quad \text{on} \quad z = h, \end{aligned} \tag{4.24b}$$

$$
\begin{aligned}
-\frac{p_\alpha}{\mu_\alpha} - \frac{2}{3}\nabla\cdot\boldsymbol{u}_\alpha + 2\left[\left(\frac{\partial h}{\partial r}\right)^2 + \left(\frac{1}{r}\frac{\partial h}{\partial \theta}\right)^2 + 1\right]^{-1}\Bigg\{\left(\frac{\partial h}{\partial r}\right)^2 \frac{\partial u_{r\alpha}}{\partial r} \\
-\frac{\partial h}{\partial r}\left(\frac{\partial u_{r\alpha}}{\partial z} + \frac{\partial u_{z\alpha}}{\partial r}\right) + \frac{\partial h}{\partial r}\frac{\partial h}{\partial \theta}\left[\frac{1}{r^2}\frac{\partial u_{r\alpha}}{\partial \theta} + \frac{\partial}{\partial r}\left(\frac{u_{\theta\alpha}}{r}\right)\right] \\
+\frac{1}{r^3}\left(\frac{\partial h}{\partial \theta}\right)^2\left(\frac{\partial u_{\theta\alpha}}{\partial \theta} + u_{r\alpha}\right) - \frac{1}{r}\frac{\partial h}{\partial \theta}\left(\frac{\partial u_{\theta\alpha}}{\partial z} + \frac{1}{r}\frac{\partial u_{z\alpha}}{\partial \theta}\right) \\
+\frac{\partial u_{z\alpha}}{\partial z}\Bigg\} = -\frac{\gamma_\alpha \kappa}{\mu_\alpha} \quad \text{on} \quad z = h,
\end{aligned}
\tag{4.24c}
$$

where the mean curvature of the free surface is

$$
\begin{aligned}
\kappa = \left[\left(\frac{\partial h}{\partial r}\right)^2 + \left(\frac{1}{r}\frac{\partial h}{\partial \theta}\right)^2 + 1\right]^{-3/2}\Bigg\{-\frac{1}{r}\frac{\partial}{\partial r}\left(r\frac{\partial h}{\partial r}\right) - \frac{1}{r^2}\frac{\partial^2 h}{\partial \theta^2} \\
-\frac{1}{r}\frac{\partial h}{\partial r}\left[\left(\frac{\partial h}{\partial r}\right)^2 + 2\left(\frac{1}{r}\frac{\partial h}{\partial \theta}\right)^2\right] - \frac{1}{r^2}\left(\frac{\partial h}{\partial r}\right)^2\frac{\partial^2 h}{\partial \theta^2} \\
-\frac{1}{r^2}\left(\frac{\partial h}{\partial \theta}\right)^2\frac{\partial^2 h}{\partial r^2} + \frac{2}{r^2}\frac{\partial h}{\partial r}\frac{\partial h}{\partial \theta}\frac{\partial^2 h}{\partial r \partial \theta}\Bigg\}.
\end{aligned}
\tag{4.25}
$$

This completes the boundary conditions associated with the model.

4.1.3 Model Reduction

Before applying the thin-film approximation, we make further assumptions to simplify the general model derived in §4.1.1 and §4.1.2. First, following O'Dea, Waters, and Byrne [106], we assume that the inter-phase drag is large, and set $k \to \infty$. Under this assumption, we need to impose that both fluid phases move with a common velocity for the momentum source terms (4.11) to remain bounded. We define this velocity to be $\boldsymbol{u} = \boldsymbol{u}_n = \boldsymbol{u}_m$. This assumption matches the experimental hypothesis that yeast biofilms expand by sliding motility, in which cells and extracellular fluid spread as a unit [150]. Furthermore, since both the cells and ECM are primarily composed of water, it is reasonable to expect the physical properties of each phase to be similar.

We then define

$$\rho = \rho_n = \rho_m, \quad \mu = \mu_n = \mu_m, \quad \text{and} \quad \gamma = \gamma_n = \gamma_m, \tag{4.26}$$

all of which we assume constant, as well as $p = p_n = p_m$. These assumptions, combined with the no voids assumption (4.2), reduce the governing equations (4.4), (4.6), (4.7) and (4.12) to

$$\frac{1}{r}\frac{\partial}{\partial r}(ru_r) + \frac{1}{r}\frac{\partial u_\theta}{\partial \theta} + \frac{\partial u_z}{\partial z} = (\psi_n + \psi_m)\,\phi_n g_b, \tag{4.27a}$$

$$\frac{\partial \phi_n}{\partial t} + \frac{1}{r}\frac{\partial}{\partial r}(ru_r\phi_n) + \frac{1}{r}\frac{\partial}{\partial \theta}(u_\theta\phi_n) + \frac{\partial}{\partial z}(u_z\phi_n) = \psi_n\phi_n g_b - \psi_d g_b, \tag{4.27b}$$

$$\frac{\partial g_s}{\partial t} = D_s\left[\frac{1}{r}\frac{\partial}{\partial r}\left(r\frac{\partial g_s}{\partial r}\right) + \frac{1}{r^2}\frac{\partial^2 g_s}{\partial \theta^2} + \frac{\partial^2 g_s}{\partial z^2}\right], \tag{4.27c}$$

$$\begin{aligned}\frac{\partial g_b}{\partial t} + \frac{1}{r}\frac{\partial}{\partial r}\left[ru_r(1-\phi_n)g_b\right] + \frac{1}{r}\frac{\partial}{\partial \theta}\left[u_\theta(1-\phi_n)g_b\right] \\ + \frac{\partial}{\partial z}\left[u_z(1-\phi_n)g_b\right] = D_b\left[\frac{1}{r}\frac{\partial}{\partial r}\left(r\frac{\partial g_b}{\partial r}\right)\right. \\ \left. + \frac{1}{r^2}\frac{\partial^2 g_b}{\partial \theta^2} + \frac{\partial^2 g_b}{\partial z^2}\right] - \eta\phi_n g_b,\end{aligned} \tag{4.27d}$$

$$\begin{aligned}-\frac{\partial p}{\partial r} + \frac{2\mu}{r}\frac{\partial}{\partial r}\left(r\frac{\partial u_r}{\partial r}\right) - \frac{2\mu}{3}\frac{\partial}{\partial r}\left[\frac{1}{r}\frac{\partial}{\partial r}(ru_r) + \frac{1}{r}\frac{\partial u_\theta}{\partial \theta} + \frac{\partial u_z}{\partial z}\right] \\ + \frac{\mu}{r}\frac{\partial}{\partial \theta}\left(\frac{\partial u_\theta}{\partial r} + \frac{1}{r}\frac{\partial u_r}{\partial \theta}\right) + \mu\frac{\partial}{\partial z}\left(\frac{\partial u_z}{\partial r} + \frac{\partial u_r}{\partial z}\right) \\ - \frac{3\mu}{r^2}\frac{\partial u_\theta}{\partial \theta} - \frac{2\mu}{r^2}u_r = 0,\end{aligned} \tag{4.27e}$$

$$\begin{aligned}-\frac{1}{r}\frac{\partial p}{\partial \theta} + \frac{2\mu}{r^2}\frac{\partial^2 u_\theta}{\partial \theta^2} - \frac{2\mu}{3r}\frac{\partial}{\partial \theta}\left[\frac{1}{r}\frac{\partial}{\partial r}(ru_r) + \frac{1}{r}\frac{\partial u_\theta}{\partial \theta} + \frac{\partial u_z}{\partial z}\right] \\ + \frac{\mu}{r}\frac{\partial}{\partial r}\left(\frac{\partial u_r}{\partial \theta} + r\frac{\partial u_\theta}{\partial r}\right) + \mu\frac{\partial}{\partial z}\left(\frac{1}{r}\frac{\partial u_z}{\partial \theta} + \frac{\partial u_\theta}{\partial z}\right) \\ + \frac{3\mu}{r^2}\frac{\partial u_r}{\partial \theta} - \frac{\mu}{r^2}u_\theta = 0,\end{aligned} \tag{4.27f}$$

$$
\begin{aligned}
&-\frac{\partial p}{\partial z}+2\mu\frac{\partial^2 u_z}{\partial z^2}-\frac{2\mu}{3}\frac{\partial}{\partial z}\left[\frac{1}{r}\frac{\partial}{\partial r}\left(ru_r\right)+\frac{1}{r}\frac{\partial u_\theta}{\partial \theta}+\frac{\partial u_z}{\partial z}\right]\\
&+\frac{\mu}{r}\frac{\partial}{\partial r}\left[r\left(\frac{\partial u_r}{\partial z}+\frac{\partial u_z}{\partial r}\right)\right]+\frac{\mu}{r}\frac{\partial}{\partial \theta}\left(\frac{\partial u_\theta}{\partial z}+\frac{1}{r}\frac{\partial u_z}{\partial \theta}\right)=0,
\end{aligned}
\tag{4.27g}
$$

where (4.27a) is obtained by summing the mass balance equations (4.4) for ϕ_n and ϕ_m. Equations (4.27), with the initial and boundary conditions outlined in §4.1.2, completes the derivation of our general model for biofilm growth.

4.1.4 Thin-Film Approximation

The process of simplifying the model begins with the non-dimensionalisation. We seek to scale the model such that the relative magnitude of physical effects are appropriately taken into account. The problem geometry is a key consideration in thin-film approximations. Observing that the radius of a biofilm significantly exceeds both its height and the depth of the substratum, we assume that the aspect ratio

$$
\varepsilon=\frac{H_s}{R_b} \tag{4.28}
$$

is a small parameter such that $0<\varepsilon\ll 1$, and that we also have $H_b/R_b=\mathcal{O}(\varepsilon)$ as $\varepsilon\to 0$. We then non-dimensionalise the governing equations with this in mind. The choice of scaling regime depends on the relevant physics. First, we investigate whether sliding motility is a possible mechanism for yeast biofilm expansion. As biofilm–substratum adhesion is weak in sliding motility, it is appropriate to model the biofilm as an extensional flow. However, strong biofilm–substratum adhesion is also possible, and the lubrication regime is appropriate in this scenario. We consider the extensional flow regime in §4.2, and the lubrication regime in §4.3. In both regimes, we use asymptotic analysis to reduce the complexity of the models. We achieve this by ensuring that physical effects of similar importance are balanced, and neglecting those that are comparatively small.

4.2 Extensional Flow Regime

We first perform the thin-film reduction in the extensional flow regime. The result of this analysis is a simplified model which we will use to investigate the hypothesis that sliding governs yeast mat expansion. To obtain this model, we first non-dimensionalise based on the thin aspect ratio assumption, taking care that our scaling captures the reduced surface tension and pressure in the extensional flow regime. We then use asymptotic analysis to systematically reduce the model to a two-dimensional system, in which the z-dependence is eliminated.

4.2.1 Scaling and Non-Dimensionalisation

To non-dimensionalise the equations, we use the initial biofilm radius, R_b, as the length scale, and scale time by the cell production rate, ψ_n, and initial nutrient concentration, G. The scaled variables are (where hats denote dimensionless quantities)

$$\begin{aligned}(r,\theta,z) &= (R_b\hat{r},\hat{\theta},\varepsilon R_b\hat{z}),\\ (u_r,u_\theta,u_z) &= (\psi_n G R_b\hat{u_r},\psi_n G R_b\hat{u_\theta},\varepsilon\psi_n G R_b\hat{u_z}),\\ t = \frac{\hat{t}}{\psi_n G},\quad g_s = G\hat{g}_s,\quad g_b &= G\hat{g}_b,\quad p_\alpha = \psi_n G\mu_\alpha\hat{p}_\alpha.\end{aligned} \tag{4.29}$$

Under this scaling, the dimensionless form of the governing equations (4.27) becomes (dropping hats)

$$\frac{1}{r}\frac{\partial}{\partial r}(ru_r)+\frac{1}{r}\frac{\partial u_\theta}{\partial\theta}+\frac{\partial u_z}{\partial z}=(1+\Psi_m)\,\phi_n g_b, \tag{4.30a}$$

$$\frac{\partial\phi_n}{\partial t}+\frac{1}{r}\frac{\partial}{\partial r}(ru_r\phi_n)+\frac{1}{r}\frac{\partial}{\partial\theta}(u_\theta\phi_n)+\frac{\partial}{\partial z}(u_z\phi_n)=\phi_n g_b-\Psi_d\phi_n, \tag{4.30b}$$

$$\frac{\partial g_s}{\partial t}=D\left[\frac{1}{r}\frac{\partial}{\partial r}\left(r\frac{\partial g_s}{\partial r}\right)+\frac{1}{r^2}\frac{\partial^2 g_s}{\partial\theta^2}+\frac{1}{\varepsilon^2}\frac{\partial^2 g_s}{\partial z^2}\right], \tag{4.30c}$$

$$\begin{aligned}\mathrm{Pe}\left\{\frac{\partial g_b}{\partial t}+\frac{1}{r}\frac{\partial}{\partial r}\left[ru_r\left(1-\phi_n\right)g_b\right]+\frac{1}{r}\frac{\partial}{\partial\theta}\left[u_\theta\left(1-\phi_n\right)g_b\right]\right.\\ \left.+\frac{\partial}{\partial z}\left[u_z\left(1-\phi_n\right)g_b\right]\right\}=\frac{1}{r}\frac{\partial}{\partial r}\left(r\frac{\partial g_b}{\partial r}\right)+\frac{1}{r^2}\frac{\partial^2 g_b}{\partial\theta^2}\\ +\frac{1}{\varepsilon^2}\frac{\partial^2 g_b}{\partial z^2}-\Upsilon\phi_n g_b,\end{aligned} \tag{4.30d}$$

$$\begin{aligned}-\frac{\partial p}{\partial r}+\frac{2}{r}\frac{\partial}{\partial r}\left(r\frac{\partial u_r}{\partial r}\right)-\frac{2}{3}\frac{\partial}{\partial r}\left[\frac{1}{r}\frac{\partial}{\partial r}\left(ru_r\right)+\frac{1}{r}\frac{\partial u_\theta}{\partial\theta}+\frac{\partial u_z}{\partial z}\right]\\ +\frac{1}{r}\frac{\partial}{\partial\theta}\left(\frac{\partial u_\theta}{\partial r}+\frac{1}{r}\frac{\partial u_r}{\partial\theta}\right)+\frac{\partial}{\partial z}\left(\frac{\partial u_z}{\partial r}+\frac{1}{\varepsilon^2}\frac{\partial u_r}{\partial z}\right)\\ -\frac{3}{r^2}\frac{\partial u_\theta}{\partial\theta}-\frac{2u_r}{r^2}=0,\end{aligned} \tag{4.30e}$$

$$\begin{aligned}-\frac{1}{r}\frac{\partial p}{\partial\theta}+\frac{2}{r^2}\frac{\partial^2 u_\theta}{\partial\theta^2}-\frac{2}{3r}\frac{\partial}{\partial\theta}\left[\frac{1}{r}\frac{\partial}{\partial r}\left(ru_r\right)+\frac{1}{r}\frac{\partial u_\theta}{\partial\theta}+\frac{\partial u_z}{\partial z}\right]\\ +\frac{1}{r}\frac{\partial}{\partial r}\left(\frac{\partial u_r}{\partial\theta}+r\frac{\partial u_\theta}{\partial r}\right)+\frac{\partial}{\partial z}\left(\frac{1}{r}\frac{\partial u_z}{\partial\theta}+\frac{1}{\varepsilon^2}\frac{\partial u_\theta}{\partial z}\right)\\ +\frac{3}{r^2}\frac{\partial u_r}{\partial\theta}-\frac{u_\theta}{r^2}=0,\end{aligned} \tag{4.30f}$$

$$\begin{aligned}-\frac{\partial p}{\partial z}+2\frac{\partial^2 u_z}{\partial z^2}-\frac{2}{3}\frac{\partial}{\partial z}\left[\frac{1}{r}\frac{\partial}{\partial r}\left(ru_r\right)+\frac{1}{r}\frac{\partial u_\theta}{\partial\theta}+\frac{\partial u_z}{\partial z}\right]\\ +\frac{1}{r}\frac{\partial}{\partial r}\left[r\left(\frac{\partial u_r}{\partial z}+\varepsilon^2\frac{\partial u_z}{\partial r}\right)\right]+\frac{1}{r}\frac{\partial}{\partial\theta}\left(\frac{\partial u_\theta}{\partial z}+\frac{\varepsilon^2}{r}\frac{\partial u_z}{\partial\theta}\right)=0,\end{aligned} \tag{4.30g}$$

where we have introduced the dimensionless constants

$$\begin{gathered}\Psi_m=\frac{\psi_m}{\psi_n},\quad \Psi_d=\frac{\psi_d G}{\psi_n},\\ D=\frac{D_s}{\psi_n G R_b^2},\quad \mathrm{Pe}=\frac{\psi_n G R_b^2}{D_b},\quad \text{and}\quad \Upsilon=\frac{\eta R_b^2}{D_b},\end{gathered} \tag{4.31}$$

all of which we assume to be $\mathcal{O}(1)$ as $\varepsilon\to 0$. In (4.31), Ψ_m and Ψ_d are the dimensionless ECM production and cell death rates respectively, scaled by the cell production rate and initial nutrient concentration. The parameter D is the coefficient of diffusion for nutrients in the substratum, scaled by the cell production rate and biofilm radius. The Péclet number, Pe, is the ratio of the rates of advective transport to diffusive transport within the biofilm. The

parameter Υ is the dimensionless nutrient consumption rate. We also note that we scale Υ differently to the corresponding term in Ward and King [120]. In their model, the biofilm was immersed in a nutrient-rich liquid culture medium, and hence they balanced nutrient consumption with diffusion in the z-direction. In contrast, our biofilms grow on a nutrient-limited thin substratum, making it appropriate to balance nutrient consumption with the temporal derivative and in-plane advection and diffusion.

Sliding motility is thought to occur if adhesion between the biofilm and substratum is weak, and surface tension is not important [150]. To model this we assume that $\lambda_\alpha = 0$, and subsequently the general slip conditions (4.17) correspond to perfect slip conditions, which were considered by Ward and King [120]. The dimensionless boundary conditions are then

$$\frac{\partial g_s}{\partial z} = 0, \quad \text{on} \quad z = -1, \tag{4.32a}$$

$$\frac{\partial g_s}{\partial z} = -\varepsilon^2 Q_s \left(g_s - g_b\right) \quad \text{on} \quad z = 0, \tag{4.32b}$$

$$\frac{\partial g_b}{\partial z} = -\varepsilon^2 Q_b \left(g_s - g_b\right) \quad \text{on} \quad z = 0, \tag{4.32c}$$

$$u_z = 0 \quad \text{on} \quad z = 0, \tag{4.32d}$$

$$\frac{\partial u_r}{\partial z} + \varepsilon^2 \frac{\partial u_z}{\partial r} = 0, \quad \text{on} \quad z = 0, \tag{4.32e}$$

$$\frac{\partial u_\theta}{\partial z} + \frac{\varepsilon^2}{r} \frac{\partial u_z}{\partial \theta} = 0, \quad \text{on} \quad z = 0, \tag{4.32f}$$

$$\begin{aligned} \mathrm{Pe} g_b \left(1 - \phi_n\right) \left(u_r \frac{\partial h}{\partial r} + \frac{u_\theta}{r} \frac{\partial h}{\partial \theta} - u_z\right) = \frac{\partial g_b}{\partial r} \frac{\partial h}{\partial r} \\ + \frac{1}{r^2} \frac{\partial g_b}{\partial \theta} \frac{\partial h}{\partial \theta} - \frac{1}{\varepsilon^2} \frac{\partial g_b}{\partial z} \quad \text{on} \quad z = h, \end{aligned} \tag{4.32g}$$

$$\frac{\partial h}{\partial t} + u_r \frac{\partial h}{\partial r} + \frac{u_\theta}{r} \frac{\partial h}{\partial \theta} = u_z \quad \text{on} \quad z = h, \tag{4.32h}$$

$$
\begin{aligned}
&-2\frac{\partial h}{\partial r}\left(\frac{\partial u_r}{\partial r}-\frac{\partial u_z}{\partial z}\right)-\frac{\partial h}{\partial \theta}\left[\frac{1}{r^2}\frac{\partial u_r}{\partial \theta}+\frac{\partial}{\partial r}\left(\frac{u_\theta}{r}\right)\right]\\
&+\frac{1}{\varepsilon^2}\frac{\partial u_r}{\partial z}+\frac{\partial u_z}{\partial r}-\left(\frac{\partial h}{\partial r}\right)^2\left(\varepsilon^2\frac{\partial u_z}{\partial r}+\frac{\partial u_r}{\partial z}\right)\\
&-\frac{1}{r}\frac{\partial h}{\partial r}\frac{\partial h}{\partial \theta}\left(\frac{\partial u_\theta}{\partial z}+\frac{\varepsilon^2}{r}\frac{\partial u_z}{\partial \theta}\right)=0 \quad \text{on} \quad z=h,
\end{aligned}
\tag{4.32i}
$$

$$
\begin{aligned}
&-\frac{2}{r}\frac{\partial h}{\partial \theta}\left(\frac{1}{r}\frac{\partial u_\theta}{\partial \theta}+\frac{u_r}{r}-\frac{\partial u_z}{\partial z}\right)-\frac{\partial h}{\partial r}\left[r\frac{\partial}{\partial r}\left(\frac{u_\theta}{r}\right)+\frac{1}{r}\frac{\partial u_r}{\partial \theta}\right]\\
&+\frac{1}{\varepsilon^2}\frac{\partial u_\theta}{\partial z}+\frac{1}{r}\frac{\partial u_z}{\partial \theta}-\frac{1}{r}\frac{\partial h}{\partial r}\frac{\partial h}{\partial \theta}\left(\varepsilon^2\frac{\partial u_z}{\partial r}+\frac{\partial u_r}{\partial z}\right)\\
&-\frac{1}{r^2}\left(\frac{\partial h}{\partial \theta}\right)^2\left(\frac{\varepsilon^2}{r}\frac{\partial u_z}{\partial \theta}+\frac{\partial u_\theta}{\partial z}\right)=0 \quad \text{on} \quad z=h,
\end{aligned}
\tag{4.32j}
$$

$$
\begin{aligned}
&-p-\frac{2}{3}\left[\frac{1}{r}\frac{\partial}{\partial r}\left(ru_r\right)+\frac{1}{r}\frac{\partial u_\theta}{\partial \theta}+\frac{\partial u_z}{\partial z}\right]+2\left[\varepsilon^2\left(\frac{\partial h}{\partial r}\right)^2\right.\\
&\left.+\varepsilon^2\left(\frac{1}{r}\frac{\partial h}{\partial \theta}\right)^2+1\right]^{-1}\left\{\varepsilon^2\left(\frac{\partial h}{\partial r}\right)^2\frac{\partial u_r}{\partial r}\right.\\
&+\varepsilon^2\frac{\partial h}{\partial r}\frac{\partial h}{\partial \theta}\left[\frac{1}{r^2}\frac{\partial u_r}{\partial \theta}+\frac{\partial}{\partial r}\left(\frac{u_\theta}{r}\right)\right]-\frac{\partial h}{\partial r}\left(\frac{\partial u_r}{\partial z}+\varepsilon^2\frac{\partial u_z}{\partial r}\right)\\
&+\frac{\varepsilon^2}{r^3}\left(\frac{\partial h}{\partial \theta}\right)^2\left(\frac{\partial u_\theta}{\partial \theta}+u_r\right)-\frac{1}{r}\frac{\partial h}{\partial \theta}\left(\frac{\partial u_\theta}{\partial z}+\frac{\varepsilon^2}{r}\frac{\partial u_z}{\partial \theta}\right)\\
&\left.+\frac{\partial u_z}{\partial z}\right\}=-\gamma^*\kappa^* \quad \text{on} \quad z=h,
\end{aligned}
\tag{4.32k}
$$

where we have introduced the dimensionless parameters

$$
Q_s=\frac{QR_b}{\varepsilon D_s}, \quad Q_b=\frac{QR_b}{\varepsilon D_b}, \quad \text{and} \quad \gamma^*=\frac{1}{\mathrm{Ca}}. \tag{4.33}
$$

Like (4.31), we also assume these to be $\mathcal{O}(1)$ as $\varepsilon \to 0$, and will validate these assumptions with experimental estimates in §5.1.2. In (4.33), Q_s is a coefficient that describes the rate of nutrient depletion in the substratum, and Q_b describes the rate of nutrient uptake by the biofilm. We define the dimensionless surface tension coefficient, γ^*, as the reciprocal of the capillary

number,

$$\mathrm{Ca} = \frac{\psi_n G R_b \mu}{\varepsilon \gamma}, \tag{4.34}$$

which is the ratio of viscous forces to surface tension forces. The normal stress condition (4.32k) also depends on the dimensionless free surface curvature, κ^*, which is given by

$$\begin{aligned}\kappa^* = \left[\varepsilon^2\left(\frac{\partial h}{\partial r}\right)^2 + \varepsilon^2\left(\frac{1}{r}\frac{\partial h}{\partial \theta}\right)^2 + 1\right]^{-3/2} \left[-\frac{1}{r}\frac{\partial}{\partial r}\left(r\frac{\partial h}{\partial r}\right) - \frac{1}{r^2}\frac{\partial^2 h}{\partial \theta^2}\right. \\ -\frac{\varepsilon^2}{r}\left(\frac{\partial h}{\partial r}\right)^3 - \frac{2\varepsilon^2}{r^3}\frac{\partial h}{\partial r}\left(\frac{\partial h}{\partial \theta}\right)^2 - \frac{\varepsilon^2}{r^2}\left(\frac{\partial h}{\partial r}\right)^2\frac{\partial^2 h}{\partial \theta^2} \\ \left.-\frac{\varepsilon^2}{r^2}\left(\frac{\partial h}{\partial \theta}\right)^2\frac{\partial^2 h}{\partial r^2} + \frac{2\varepsilon^2}{r^2}\frac{\partial h}{\partial r}\frac{\partial h}{\partial \theta}\frac{\partial^2 h}{\partial r \partial \theta}\right].\end{aligned} \tag{4.35}$$

The governing equations (4.30) and boundary conditions (4.32) then complete the dimensionless form of our extensional flow model, on which we apply the thin-film reduction.

4.2.2 Thin-Film Equations

We now use the thin-film assumption introduced in §4.1.4 to systematically simplify the dimensionless extensional flow model derived in §4.2.1. This involves expanding the dependent variables as asymptotic series in powers of ε^2,

$$h(r,\theta,t) \sim h_0(r,\theta,t) + \varepsilon^2 h_1(r,\theta,t) + \mathcal{O}\left(\varepsilon^4\right), \tag{4.36a}$$

$$\phi_n(r,\theta,z,t) \sim \phi_{n0}(r,\theta,z,t) + \varepsilon^2 \phi_{n1}(r,\theta,z,t) + \mathcal{O}\left(\varepsilon^4\right), \tag{4.36b}$$

and so on, where series for p, u_r, u_θ, u_z, g_s, and g_b take the same form as (4.36b).

Substituting the expansions (4.36) into the governing equations (4.30) and boundary conditions (4.32) enables us to balance physical effects of similar magnitude. In practice, we simplify the model by considering the leading-

order behaviour only, which represents the strongest physical features, the remainder being $\mathcal{O}(\varepsilon^2)$ as $\varepsilon \to 0$, and hence much less significant. Applying this process to our fluid model, at leading order we obtain

$$\frac{1}{r}\frac{\partial}{\partial r}\left(ru_{r0}\right) + \frac{1}{r}\frac{\partial u_{\theta 0}}{\partial \theta} + \frac{\partial u_{z0}}{\partial z} = \left(1 + \Psi_m\right)\phi_{n0} g_{b0}, \tag{4.37a}$$

$$\begin{aligned} \frac{\partial \phi_{n0}}{\partial t} + \frac{1}{r}\frac{\partial}{\partial r}\left(r\phi_{n0}u_{r0}\right) + \frac{1}{r}\frac{\partial}{\partial \theta}\left(\phi_{n0}u_{\theta 0}\right) \\ + \frac{\partial}{\partial z}\left(\phi_{n0}u_{z0}\right) = \phi_{n0}g_{b0} - \Psi_d \phi_{n0}, \end{aligned} \tag{4.37b}$$

$$\frac{\partial^2 g_{s0}}{\partial z^2} = \frac{\partial^2 g_{b0}}{\partial z^2} = 0, \tag{4.37c}$$

$$\frac{\partial^2 u_{r0}}{\partial z^2} = \frac{\partial^2 u_{\theta 0}}{\partial z^2} = 0, \tag{4.37d}$$

$$-\frac{\partial p_0}{\partial z} + \frac{1}{3}\frac{\partial}{\partial z}\left[\frac{1}{r}\frac{\partial}{\partial r}\left(ru_{r0}\right) + \frac{1}{r}\frac{\partial u_{\theta 0}}{\partial \theta} + \frac{\partial u_{z0}}{\partial z}\right] + \frac{\partial^2 u_{z0}}{\partial z^2} = 0. \tag{4.37e}$$

These are subject to the leading-order boundary conditions

$$\frac{\partial g_{s0}}{\partial z} = 0 \quad \text{on} \quad z = -1, 0, \tag{4.38a}$$

$$\frac{\partial g_{b0}}{\partial z} = 0 \quad \text{on} \quad z = 0, h_0, \tag{4.38b}$$

$$\frac{\partial u_{r0}}{\partial z} = \frac{\partial u_{\theta 0}}{\partial z} = 0 \quad \text{on} \quad z = 0, \tag{4.38c}$$

$$\frac{\partial u_{r0}}{\partial z} = \frac{\partial u_{\theta 0}}{\partial z} = 0 \quad \text{on} \quad z = h_0, \tag{4.38d}$$

$$u_{z0} = 0 \quad \text{on} \quad z = 0, \tag{4.38e}$$

$$\frac{\partial h_0}{\partial t} + u_{r0}\frac{\partial h_0}{\partial r} + \frac{u_{\theta 0}}{r}\frac{\partial h_0}{\partial \theta} = u_{z0} \quad \text{on} \quad z = h_0, \tag{4.38f}$$

$$\begin{aligned} -p_0 - \frac{2}{3r}\left[\frac{\partial}{\partial r}\left(ru_{r0}\right) + \frac{\partial u_{\theta 0}}{\partial \theta}\right] + \frac{4}{3}\frac{\partial u_{z0}}{\partial z} = \\ \gamma^* \left[\frac{1}{r}\frac{\partial}{\partial r}\left(r\frac{\partial h_0}{\partial r}\right) + \frac{1}{r^2}\frac{\partial^2 h_0}{\partial \theta^2}\right] \quad \text{on} \quad z = h_0, \end{aligned} \tag{4.38g}$$

where the right-hand side of (4.38g) represents the leading-order contribution of the dimensionless curvature (4.35).

Equations (4.37c) and (4.37d) and the associated boundary conditions (4.38a)–(4.38d) demonstrate that g_{s0}, g_{b0}, u_{r0}, and $u_{\theta 0}$ are independent of z. This is a key feature of extensional flows, and follows from the fluid experiencing zero tangential stress on its upper and lower surfaces. In addition, this enables us to integrate out the z dependence in the governing equations, to derive a two-dimensional closed system of equations for the leading-order variables [110, 120]. First, we introduce the depth-averaged cell volume fraction denoted with a bar,

$$\bar{\phi}_{n0} = \frac{1}{h_0}\int_0^{h_0} \phi_{n0}\,\mathrm{d}z. \tag{4.39}$$

We can now integrate out the z dependence in the conservation of mass equations (4.37a) and (4.37b), to reduce the dimension of the leading-order model. Integrating (4.37a) with respect to z across the biofilm depth from 0 to h, and applying the boundary conditions (4.38e) and (4.38f), we obtain

$$\frac{\partial h_0}{\partial t} + \frac{1}{r}\frac{\partial}{\partial r}\left(r u_{r0} h_0\right) + \frac{1}{r}\frac{\partial}{\partial \theta}\left(u_{\theta 0} h_0\right) = \left(1+\Psi_m\right)\bar{\phi}_{n0} g_{b0} h_0. \tag{4.40}$$

Similarly, integrating (4.37b) with respect to z and applying (4.38e) and (4.38f) yields

$$\begin{aligned}\phi_{n0}|_{z=h_0}\left(\frac{\partial h_0}{\partial t} + u_{r0}\frac{\partial h_0}{\partial r} + \frac{u_{\theta 0}}{r}\frac{\partial h_0}{\partial \theta}\right) = \int_0^{h_0} \phi_{n0} g_{b0} - \Psi_d \phi_{n0} \\ -\frac{\partial \phi_{n0}}{\partial t} - \frac{1}{r}\frac{\partial}{\partial r}\left(r\phi_{n0}u_{r0}\right) - \frac{1}{r}\frac{\partial}{\partial \theta}\left(\phi_{n0}u_{\theta 0}\right)\,\mathrm{d}z.\end{aligned} \tag{4.41}$$

As ϕ_{n0} depends on z, we apply Leibniz's rule to evaluate the integral. Doing

so gives

$$\begin{aligned}\phi_{n0}|_{z=h_0}\left(\frac{\partial h_0}{\partial t}+u_{r0}\frac{\partial h_0}{\partial r}+\frac{u_{\theta 0}}{r}\frac{\partial h_0}{\partial \theta}\right)&=\bar{\phi}_{n0}g_{b0}h_0\\ -\Psi_d\bar{\phi}_{n0}h_0-\left[\frac{\partial}{\partial t}\left(\bar{\phi}_{n0}h_0\right)-\phi_{n0}|_{z=h_0}\frac{\partial h_0}{\partial t}\right]&\\ -\left[\frac{1}{r}\frac{\partial}{\partial r}\left(r\bar{\phi}_{n0}u_{r0}\right)-\phi_{n0}|_{z=h_0}u_{r0}\frac{\partial h_0}{\partial r}\right]&\\ -\left[\frac{1}{r}\frac{\partial}{\partial \theta}\left(\bar{\phi}_{n0}u_{\theta 0}\right)-\phi_{n0}|_{z=h_0}\frac{u_{\theta 0}}{r}\frac{\partial h_0}{\partial \theta}\right].&\end{aligned} \tag{4.42}$$

Terms arising from the application of Leibniz's integral rule then cancel with those obtained from the kinematic boundary condition. The remaining terms give the conservation of mass equation for the depth-averaged cell volume fraction,

$$\begin{aligned}\frac{\partial}{\partial t}\left(\bar{\phi}_{n0}h_0\right)+\frac{1}{r}\frac{\partial}{\partial r}\left(ru_{r0}\bar{\phi}_{n0}h_0\right)+\frac{1}{r}\frac{\partial}{\partial \theta}\left(u_{\theta 0}\bar{\phi}_{n0}h_0\right)&\\ =\left(g_{b0}-\Psi_d\right)\bar{\phi}_{n0}h_0.&\end{aligned} \tag{4.43}$$

We can now multiply (4.40) by $\bar{\phi}_{n0}$, and subtract the result from (4.43). This eliminates the height from (4.43), giving

$$\frac{\partial\bar{\phi}_{n0}}{\partial t}+u_{r0}\frac{\partial\bar{\phi}_{n0}}{\partial r}+\frac{u_{\theta 0}}{r}\frac{\partial\bar{\phi}_{n0}}{\partial\theta}=\bar{\phi}_{n0}\left[g_{b0}-\Psi_d-\left(1+\Psi_m\right)\bar{\phi}_{n0}g_{b0}\right]. \tag{4.44}$$

Equations (4.40) and (4.44) are the z-independent conservation of fluid mass equations for our thin-film extensional flow model.

To obtain z-independent equations for the leading-order nutrient concentrations, we need to consider the higher-order correction terms to the governing equations (4.30c) and (4.30d). Upon substituting the expansions (4.36), matching $\mathcal{O}(1)$ terms gives

$$\frac{\partial^2 g_{s1}}{\partial z^2}=\frac{1}{D}\frac{\partial g_{s0}}{\partial t}-\frac{1}{r}\frac{\partial}{\partial r}\left(r\frac{\partial g_{s0}}{\partial r}\right)-\frac{1}{r^2}\frac{\partial^2 g_{s0}}{\partial\theta^2}, \tag{4.45a}$$

$$\frac{\partial^2 g_{b1}}{\partial z^2} = \mathrm{Pe}\left\{\frac{\partial g_{b0}}{\partial t} + \frac{1}{r}\frac{\partial}{\partial r}\left[r u_{r0}\left(1-\phi_{n0}\right) g_{b0}\right] + \frac{1}{r}\frac{\partial}{\partial \theta}\left[u_{\theta 0}\left(1-\phi_{n0}\right) g_{b0}\right] + \frac{\partial}{\partial z}\left[u_{z0}\left(1-\phi_{n0}\right) g_{b0}\right]\right\} - \frac{1}{r}\frac{\partial}{\partial r}\left(r\frac{\partial g_{b0}}{\partial r}\right) - \frac{1}{r^2}\frac{\partial^2 g_{b0}}{\partial \theta^2} + \Upsilon \phi_{n0} g_{b0}. \tag{4.45b}$$

Using (4.32a)–(4.32c) and (4.32g), we obtain the higher-order corrections to the boundary conditions,

$$\frac{\partial g_{s1}}{\partial z} = 0 \quad \text{on} \quad z = -1, \tag{4.46a}$$

$$\frac{\partial g_{s1}}{\partial z} = -Q_s\left(g_{s0} - g_{b0}\right) \quad \text{on} \quad z = 0, \tag{4.46b}$$

$$\frac{\partial g_{b1}}{\partial z} = -Q_b\left(g_{s0} - g_{b0}\right) \quad \text{on} \quad z = 0, \tag{4.46c}$$

$$\frac{\partial g_{b1}}{\partial z} = -\mathrm{Pe}\left(1-\phi_{n0}\right) g_{b0}\left(u_{r0}\frac{\partial h_0}{\partial r} + \frac{u_{\theta 0}}{r}\frac{\partial h_0}{\partial \theta} - u_{z0}\right) + \frac{\partial g_{b0}}{\partial r}\frac{\partial h_0}{\partial r} + \frac{1}{r^2}\frac{\partial g_{b0}}{\partial \theta}\frac{\partial h_0}{\partial \theta} \quad \text{on} \quad z = h_0. \tag{4.46d}$$

This technique is useful because the higher-order correction terms can be written solely in terms of leading-order quantities. Integrating (4.45a) with respect to z across the substratum depth gives

$$\left[\frac{\partial g_{s1}}{\partial z}\right]_{-1}^{0} = \frac{1}{D}\frac{\partial g_{s0}}{\partial t} - \frac{1}{r}\frac{\partial}{\partial r}\left(r\frac{\partial g_{s0}}{\partial r}\right) - \frac{1}{r^2}\frac{\partial^2 g_{s0}}{\partial \theta^2}. \tag{4.47}$$

On applying the boundary conditions (4.46a) and (4.46b), we obtain the z-independent leading-order mass balance equations for nutrients in the substratum,

$$\frac{\partial g_{s0}}{\partial t} = D\left[\frac{1}{r}\frac{\partial}{\partial r}\left(r\frac{\partial g_{s0}}{\partial r}\right) + \frac{1}{r^2}\frac{\partial^2 g_{s0}}{\partial \theta^2}\right] - DQ_s\left(g_{s0} - g_{b0}\right), \tag{4.48}$$

for $0 < r < S(\theta, t)$. We note that, unlike the other variables, the nutrient concentration in the substratum is defined over the entire Petri dish, instead

of only the biofilm. We scale the dimensional Petri dish radius R_p by the characteristic biofilm radius R_b. This introduces the dimensionless Petri dish radius

$$R = \frac{R_p}{R_b}. \tag{4.49}$$

In the region $S(\theta, t) < r < R$ that is not inhabited by the biofilm, the mass balance for nutrients in the substratum reads

$$\frac{\partial g_{s0}}{\partial t} = D\left[\frac{1}{r}\frac{\partial}{\partial r}\left(r\frac{\partial g_{s0}}{\partial r}\right) + \frac{1}{r^2}\frac{\partial^2 g_{s0}}{\partial \theta^2}\right]. \tag{4.50}$$

Equation (4.50) differs from (4.48) because nutrient depletion from the substratum cannot occur in regions the biofilm does not inhabit. A solution for g_{s0} then satisfies both (4.48) and (4.50), such that g_{s0} and its flux are both continuous at $r = S(\theta, t)$.

For the nutrient concentration in the biofilm, we can similarly integrate (4.45b) with respect to z across the biofilm depth. This gives

$$\begin{aligned}\left[\frac{\partial g_{b1}}{\partial z}\right]_0^{h_0} &= \mathrm{Pe} h_0 \frac{\partial g_{b0}}{\partial t} + \mathrm{Pe}\int_0^{h_0}\left\{\frac{1}{r}\frac{\partial}{\partial r}\left[r u_{r0}\left(1-\phi_{n0}\right) g_{b0}\right]\right. \\ &\left. + \frac{1}{r}\frac{\partial}{\partial \theta}\left[u_{\theta 0}\left(1-\phi_{n0}\right) g_{b0}\right]\right\} \mathrm{d}z + \mathrm{Pe}\left[u_{z0}\left(1-\phi_{n0}\right) g_{b0}\right]_0^{h_0} \\ &- h_0\left[\frac{1}{r}\frac{\partial}{\partial r}\left(r\frac{\partial g_{b0}}{\partial r}\right) + \frac{1}{r^2}\frac{\partial^2 g_{b0}}{\partial \theta^2}\right] + \Upsilon \bar{\phi}_{n0} g_{b0} h_0.\end{aligned} \tag{4.51}$$

Next, we apply the boundary conditions (4.38e), (4.38f), (4.46c) and (4.46d), and use Leibniz's integral rule to evaluate the integral on the right-hand side.

This gives

$$\begin{aligned}
&\frac{\partial g_{b0}}{\partial r}\frac{\partial h_0}{\partial r}+\frac{1}{r^2}\frac{\partial g_{b0}}{\partial \theta}\frac{\partial h_0}{\partial \theta}+\mathrm{Pe}\left(1-\phi_{n0}|_{z=h_0}\right)g_{b0}\frac{\partial h_0}{\partial t}\\
&+Q_b\left(g_{s0}-g_{b0}\right)=\mathrm{Pe}\left\{\frac{1}{r}\frac{\partial}{\partial r}\left[ru_{r0}(1-\bar{\phi}_{n0})g_{b0}h_0\right]\right.\\
&\left.-u_{r0}\left(1-\phi_{n0}|_{z=h_0}\right)g_{b0}\frac{\partial h_0}{\partial r}\right\}+\mathrm{Pe}\left\{\frac{1}{r}\frac{\partial}{\partial \theta}\left[u_{\theta 0}(1-\bar{\phi}_{n0})g_{b0}h_0\right]\right.\\
&\left.-\frac{u_{\theta 0}}{r}\left(1-\phi_{n0}|_{z=h_0}\right)g_{b0}\frac{\partial h_0}{\partial \theta}\right\}+\mathrm{Pe}\left[h_0\frac{\partial g_{b0}}{\partial t}\right.\\
&\left.+\left(1-\phi_{n0}|_{z=h_0}\right)g_{b0}\left(\frac{\partial h_0}{\partial t}+u_{r0}\frac{\partial h_0}{\partial r}+\frac{u_{\theta 0}}{r}\frac{\partial h_0}{\partial \theta}\right)\right]\\
&-h_0\left[\frac{1}{r}\frac{\partial}{\partial r}\left(r\frac{\partial g_{b0}}{\partial r}\right)+\frac{1}{r^2}\frac{\partial^2 g_{b0}}{\partial \theta^2}\right]+\Upsilon\bar{\phi}_{n0}g_{b0}h_0.
\end{aligned}\tag{4.52}$$

Again, we find that contributions from Leibniz's rule cancel with terms obtained from the boundary conditions. All terms involving $\phi_{n0}|_{z=h_0}$ vanish, and after simplifying we obtain the z-independent equation

$$\begin{aligned}
&\mathrm{Pe}\left\{h_0\frac{\partial g_{b0}}{\partial t}+\frac{1}{r}\frac{\partial}{\partial r}\left[ru_{r0}\left(1-\bar{\phi}_{n0}\right)g_{b0}h_0\right]\right.\\
&\left.+\frac{1}{r}\frac{\partial}{\partial \theta}\left[u_{\theta 0}\left(1-\bar{\phi}_{n0}\right)g_{b0}h_0\right]\right\}=\frac{1}{r}\frac{\partial}{\partial r}\left(rh_0\frac{\partial g_{b0}}{\partial r}\right)\\
&+\frac{1}{r^2}\frac{\partial}{\partial \theta}\left(h_0\frac{\partial g_{b0}}{\partial \theta}\right)+Q_b\left(g_{s0}-g_{b0}\right)-\Upsilon\bar{\phi}_{n0}g_{b0}h_0.
\end{aligned}\tag{4.53}$$

Together with (4.48) and (4.50), equation (4.53) completes the leading-order nutrient balance equations for our thin-film extensional flow model.

To obtain equations for the leading-order fluid velocity components, we consider the higher-order correction terms to the momentum equations (4.30e) and (4.30f). Using the leading-order mass balance equation (4.37a) to simplify,

these equations are

$$\begin{aligned}\frac{\partial^2 u_{r1}}{\partial z^2} &= \frac{\partial p_0}{\partial r} - \frac{2}{r}\frac{\partial}{\partial r}\left(r\frac{\partial u_{r0}}{\partial r}\right) + \frac{2}{3}\left(1+\Psi_m\right)\frac{\partial}{\partial r}\left(\phi_{n0}g_{b0}\right) \\ &\quad - \frac{1}{r}\frac{\partial}{\partial \theta}\left(\frac{\partial u_{\theta 0}}{\partial r} + \frac{1}{r}\frac{\partial u_{r0}}{\partial \theta}\right) - \frac{\partial^2 u_{z0}}{\partial r\,\partial z} + \frac{3}{r^2}\frac{\partial u_{\theta 0}}{\partial \theta} + \frac{2u_{r0}}{r^2},\end{aligned} \tag{4.54a}$$

$$\begin{aligned}\frac{\partial^2 u_{\theta 1}}{\partial z^2} &= \frac{1}{r}\frac{\partial p_0}{\partial \theta} - \frac{2}{r^2}\frac{\partial^2 u_{\theta 0}}{\partial \theta^2} + \frac{2}{3r}\left(1+\Psi_m\right)\frac{\partial}{\partial \theta}\left(\phi_{n0}g_{b0}\right) \\ &\quad - \frac{1}{r}\frac{\partial}{\partial r}\left(\frac{\partial u_{r0}}{\partial \theta} + r\frac{\partial u_{\theta 0}}{\partial r}\right) - \frac{1}{r}\frac{\partial^2 u_{z0}}{\partial \theta\,\partial z} - \frac{3}{r^2}\frac{\partial u_{r0}}{\partial \theta} + \frac{u_{\theta 0}}{r^2}.\end{aligned} \tag{4.54b}$$

We use (4.32e), (4.32f), (4.32i) and (4.32j) to obtain higher-order corrections to the boundary conditions for the fluid velocity components. This yields

$$\frac{\partial u_{r1}}{\partial z} = 0, \quad \text{on} \quad z = 0, \tag{4.55a}$$

$$\frac{\partial u_{\theta 1}}{\partial z} = 0, \quad \text{on} \quad z = 0, \tag{4.55b}$$

$$\begin{aligned}\frac{\partial u_{r1}}{\partial z} &= 2\frac{\partial h_0}{\partial r}\left(\frac{\partial u_{r0}}{\partial r} - \frac{\partial u_{z0}}{\partial z}\right) + \frac{\partial h_0}{\partial \theta}\left[\frac{1}{r^2}\frac{\partial u_{r0}}{\partial \theta} + \frac{\partial}{\partial r}\left(\frac{u_{\theta 0}}{r}\right)\right] \\ &\quad - \frac{\partial u_{z0}}{\partial r} \quad \text{on} \quad z = h_0,\end{aligned} \tag{4.55c}$$

$$\begin{aligned}\frac{\partial u_{\theta 1}}{\partial z} &= \frac{2}{r}\frac{\partial h_0}{\partial \theta}\left(\frac{1}{r}\frac{\partial u_{\theta 0}}{\partial \theta} + \frac{u_{r0}}{r} - \frac{\partial u_{z0}}{\partial z}\right) \\ &\quad + \frac{\partial h_0}{\partial r}\left[r\frac{\partial}{\partial r}\left(\frac{u_{\theta 0}}{r}\right) + \frac{1}{r}\frac{\partial u_{r0}}{\partial \theta}\right] - \frac{1}{r}\frac{\partial u_{z0}}{\partial \theta} \quad \text{on} \quad z = h_0.\end{aligned} \tag{4.55d}$$

To write (4.54) in terms of leading-order fluid velocities, we need to solve for the leading-order pressure p_0. As u_{r0} and $u_{\theta 0}$ are independent of z, (4.37e) simplifies to

$$\frac{\partial p_0}{\partial z} = \frac{4}{3}\frac{\partial^2 u_{z0}}{\partial z^2}. \tag{4.56}$$

Integrating (4.56) with respect to z, applying the boundary condition (4.38g),

and using (4.37a) to simplify, we obtain

$$\begin{aligned} p_0 = \frac{4}{3}\left(1+\Psi_m\right)\phi_{n0}g_{b0} - \frac{2}{r}\left[\frac{\partial}{\partial r}\left(ru_{r0}\right) + \frac{\partial u_{\theta 0}}{\partial \theta}\right] \\ - \gamma^*\left[\frac{1}{r}\frac{\partial}{\partial r}\left(r\frac{\partial h_0}{\partial r}\right) + \frac{1}{r^2}\frac{\partial^2 h_0}{\partial \theta^2}\right]. \end{aligned} \tag{4.57}$$

Substituting (4.57) into (4.54), we can rewrite the higher-order corrections for the fluid velocity components as

$$\begin{aligned} \frac{\partial^2 u_{r1}}{\partial z^2} = 2\left(1+\Psi_m\right)\frac{\partial}{\partial r}\left(\phi_{n0}g_{b0}\right) - 2\frac{\partial}{\partial r}\left[\frac{1}{r}\frac{\partial}{\partial r}\left(ru_{r0}\right) + \frac{1}{r}\frac{\partial u_{\theta 0}}{\partial \theta}\right] \\ - \frac{2}{r}\frac{\partial}{\partial r}\left(r\frac{\partial u_{r0}}{\partial r}\right) - \frac{1}{r}\frac{\partial^2 u_{\theta 0}}{\partial r\,\partial \theta} - \frac{1}{r^2}\frac{\partial^2 u_{r0}}{\partial \theta^2} - \frac{\partial^2 u_{z0}}{\partial r\,\partial z} \\ + \frac{3}{r^2}\frac{\partial u_{\theta 0}}{\partial \theta} + \frac{2u_{r0}}{r^2} - \gamma^*\frac{\partial}{\partial r}\left[\frac{1}{r}\frac{\partial}{\partial r}\left(r\frac{\partial h_0}{\partial r}\right) + \frac{1}{r^2}\frac{\partial^2 h_0}{\partial \theta^2}\right], \end{aligned} \tag{4.58a}$$

$$\begin{aligned} \frac{\partial^2 u_{\theta 1}}{\partial z^2} = \frac{2}{r}\left(1+\Psi_m\right)\frac{\partial}{\partial \theta}\left(\phi_{n0}g_{b0}\right) - \frac{2}{r}\frac{\partial}{\partial \theta}\left[\frac{1}{r}\frac{\partial}{\partial r}\left(ru_{r0}\right) + \frac{1}{r}\frac{\partial u_{\theta 0}}{\partial \theta}\right] \\ - \frac{2}{r^2}\frac{\partial^2 u_{\theta 0}}{\partial \theta^2} - \frac{1}{r}\frac{\partial^2 u_{r0}}{\partial r\,\partial \theta} - \frac{1}{r}\frac{\partial}{\partial r}\left(r\frac{\partial u_{\theta 0}}{\partial r}\right) - \frac{1}{r}\frac{\partial^2 u_{z0}}{\partial r\,\partial z} \\ - \frac{3}{r^2}\frac{\partial u_{r0}}{\partial \theta} + \frac{u_{\theta 0}}{r^2} - \frac{\gamma^*}{r}\frac{\partial}{\partial \theta}\left[\frac{1}{r}\frac{\partial}{\partial r}\left(r\frac{\partial h_0}{\partial r}\right) + \frac{1}{r^2}\frac{\partial^2 h_0}{\partial \theta^2}\right]. \end{aligned} \tag{4.58b}$$

Next, we integrate (4.58) with respect to z across the biofilm depth, and apply the boundary conditions (4.55). Using Leibniz's rule to integrate derivatives

of ϕ_{n0}, we obtain

$$\begin{aligned}
&2\frac{\partial h_0}{\partial r}\left(\frac{\partial u_{r0}}{\partial r}-\left.\frac{\partial u_{z0}}{\partial z}\right|_{z=h_0}\right)+\frac{\partial h_0}{\partial \theta}\left[\frac{1}{r^2}\frac{\partial u_{r0}}{\partial \theta}+\frac{\partial}{\partial r}\left(\frac{u_{\theta 0}}{r}\right)\right]\\
&-\left.\frac{\partial u_{z0}}{\partial r}\right|_{z=h_0}=2\left(1+\Psi_m\right)\left[\frac{\partial}{\partial r}\left(\bar{\phi}_{n0}g_{b0}h_0\right)-\phi_{n0}|_{z=h_0}\,g_{b0}\frac{\partial h_0}{\partial r}\right]\\
&-2h_0\frac{\partial}{\partial r}\left[\frac{1}{r}\frac{\partial}{\partial r}\left(ru_{r0}\right)+\frac{1}{r}\frac{\partial u_{\theta 0}}{\partial \theta}\right]-\frac{2h_0}{r}\frac{\partial}{\partial r}\left(r\frac{\partial u_{r0}}{\partial r}\right)\\
&-\frac{h_0}{r}\frac{\partial^2 u_{\theta 0}}{\partial r\,\partial \theta}-\frac{h_0}{r^2}\frac{\partial^2 u_{r0}}{\partial \theta^2}-\left[\frac{\partial u_{z0}}{\partial r}\right]_0^{h_0}+\frac{3h_0}{r^2}\frac{\partial u_{\theta 0}}{\partial \theta}\\
&+\frac{2u_{r0}h_0}{r^2}-\gamma^* h_0\frac{\partial}{\partial r}\left[\frac{1}{r}\frac{\partial}{\partial r}\left(r\frac{\partial h_0}{\partial r}\right)+\frac{1}{r^2}\frac{\partial^2 h_0}{\partial \theta^2}\right],
\end{aligned}\tag{4.59a}$$

$$\begin{aligned}
&\frac{2}{r}\frac{\partial h_0}{\partial \theta}\left(\frac{1}{r}\frac{\partial u_{\theta 0}}{\partial \theta}+\frac{u_{r0}}{r}-\left.\frac{\partial u_{z0}}{\partial z}\right|_{z=h_0}\right)+\frac{\partial h_0}{\partial r}\left[r\frac{\partial}{\partial r}\left(\frac{u_{\theta 0}}{r}\right)+\frac{1}{r}\frac{\partial u_{r0}}{\partial \theta}\right]\\
&-\left.\frac{1}{r}\frac{\partial u_{z0}}{\partial \theta}\right|_{z=h_0}=\frac{2}{r}\left(1+\Psi_m\right)\left[\frac{\partial}{\partial \theta}\left(\bar{\phi}_{n0}g_{b0}h_0\right)-\phi_{n0}|_{z=h_0}\,g_{b0}\frac{\partial h_0}{\partial \theta}\right]\\
&-\frac{2h_0}{r}\frac{\partial}{\partial \theta}\left[\frac{1}{r}\frac{\partial}{\partial r}\left(ru_{r0}\right)+\frac{1}{r}\frac{\partial u_{\theta 0}}{\partial \theta}\right]-\frac{2h_0}{r^2}\frac{\partial^2 u_{\theta 0}}{\partial \theta^2}-\frac{h_0}{r}\frac{\partial^2 u_{r0}}{\partial r\,\partial \theta}\\
&-\frac{h_0}{r}\frac{\partial}{\partial r}\left(r\frac{\partial u_{\theta 0}}{\partial r}\right)-\frac{1}{r}\left[\frac{\partial u_{z0}}{\partial \theta}\right]_0^{h_0}-\frac{3h_0}{r^2}\frac{\partial u_{r0}}{\partial \theta}\\
&+\frac{u_{\theta 0}h_0}{r^2}-\frac{\gamma^* h_0}{r}\frac{\partial}{\partial \theta}\left[\frac{1}{r}\frac{\partial}{\partial r}\left(r\frac{\partial h_0}{\partial r}\right)+\frac{1}{r^2}\frac{\partial^2 h_0}{\partial \theta^2}\right].
\end{aligned}\tag{4.59b}$$

To obtain z-independent equations for the leading-order velocities, we need to eliminate u_{z0}. We first rearrange the conservation of mass equation (4.37a), which gives

$$\frac{\partial u_{z0}}{\partial z}=\left(1+\Psi_m\right)\phi_{n0}g_{b0}-\frac{1}{r}\left[\frac{\partial}{\partial r}\left(ru_{r0}\right)+\frac{\partial u_{\theta 0}}{\partial \theta}\right].\tag{4.60}$$

Integrating (4.60) with respect to z, and applying (4.38e) yields

$$u_{z0}=\left(1+\Psi_m\right)\int_0^z \phi_{n0}g_{b0}\,\mathrm{d}\tilde{z}-\frac{z}{r}\left[\frac{\partial}{\partial r}\left(ru_{r0}\right)+\frac{\partial u_{\theta 0}}{\partial \theta}\right].\tag{4.61}$$

Substituting (4.61) into (4.59) then gives

$$
\begin{aligned}
&2\frac{\partial h_0}{\partial r}\left[\frac{\partial u_{r0}}{\partial r}+\frac{1}{r}\frac{\partial}{\partial r}\left(ru_{r0}\right)+\frac{1}{r}\frac{\partial u_{\theta 0}}{\partial \theta}\right]+\frac{\partial h_0}{\partial \theta}\left[\frac{1}{r^2}\frac{\partial u_{r0}}{\partial \theta}+\frac{\partial}{\partial r}\left(\frac{u_{\theta 0}}{r}\right)\right]\\
&\quad=2\left(1+\Psi_m\right)\frac{\partial}{\partial r}\left(\bar{\phi}_{n0}g_{b0}h_0\right)-2h_0\frac{\partial}{\partial r}\left[\frac{1}{r}\frac{\partial}{\partial r}\left(ru_{r0}\right)+\frac{1}{r}\frac{\partial u_{\theta 0}}{\partial \theta}\right]\\
&\qquad-\frac{2h_0}{r}\frac{\partial}{\partial r}\left(r\frac{\partial u_{r0}}{\partial r}\right)-\frac{h_0}{r}\frac{\partial^2 u_{\theta 0}}{\partial r\partial \theta}-\frac{h_0}{r^2}\frac{\partial^2 u_{r0}}{\partial \theta^2}+\frac{3h_0}{r^2}\frac{\partial u_{\theta 0}}{\partial \theta}\\
&\qquad+\frac{2u_{r0}h_0}{r^2}-\gamma^* h_0\frac{\partial}{\partial r}\left[\frac{1}{r}\frac{\partial}{\partial r}\left(r\frac{\partial h_0}{\partial r}\right)+\frac{1}{r^2}\frac{\partial^2 h_0}{\partial \theta^2}\right],
\end{aligned}
\tag{4.62a}
$$

$$
\begin{aligned}
&\frac{2}{r^2}\frac{\partial h_0}{\partial \theta}\left[2\frac{\partial u_{\theta 0}}{\partial \theta}+u_{r0}+\frac{\partial}{\partial r}\left(ru_{r0}\right)\right]+\frac{\partial h_0}{\partial r}\left[r\frac{\partial}{\partial r}\left(\frac{u_{\theta 0}}{r}\right)+\frac{1}{r}\frac{\partial u_{r0}}{\partial \theta}\right]\\
&\quad=\frac{2}{r}\left(1+\Psi_m\right)\frac{\partial}{\partial \theta}\left(\bar{\phi}_{n0}g_{b0}h_0\right)-\frac{2h_0}{r}\frac{\partial}{\partial \theta}\left[\frac{1}{r}\frac{\partial}{\partial r}\left(ru_{r0}\right)+\frac{1}{r}\frac{\partial u_{\theta 0}}{\partial \theta}\right]\\
&\qquad-\frac{2h_0}{r^2}\frac{\partial^2 u_{\theta 0}}{\partial \theta^2}-\frac{h_0}{r}\frac{\partial^2 u_{r0}}{\partial r\partial \theta}-\frac{h_0}{r}\frac{\partial}{\partial r}\left(r\frac{\partial u_{\theta 0}}{\partial r}\right)-\frac{3h_0}{r^2}\frac{\partial u_{r0}}{\partial \theta}\\
&\qquad+\frac{u_{\theta 0}h_0}{r^2}-\frac{\gamma^* h_0}{r}\frac{\partial}{\partial \theta}\left[\frac{1}{r}\frac{\partial}{\partial r}\left(r\frac{\partial h_0}{\partial r}\right)+\frac{1}{r^2}\frac{\partial^2 h_0}{\partial \theta^2}\right].
\end{aligned}
\tag{4.62b}
$$

After simplification, we obtain the leading-order momentum balance equations,

$$
\begin{aligned}
&4\frac{\partial}{\partial r}\left[\frac{h_0}{r}\frac{\partial}{\partial r}\left(ru_{r0}\right)\right]-\frac{2u_{r0}}{r}\frac{\partial h_0}{\partial r}+\frac{1}{r^2}\frac{\partial}{\partial \theta}\left(h_0\frac{\partial u_{r0}}{\partial \theta}\right)\\
&+\frac{\partial}{\partial \theta}\left[h_0\frac{\partial}{\partial r}\left(\frac{u_{\theta 0}}{r}\right)\right]+2\frac{\partial}{\partial r}\left(\frac{h_0}{r}\frac{\partial u_{\theta 0}}{\partial \theta}\right)-\frac{2h_0}{r^2}\frac{\partial u_{\theta 0}}{\partial \theta}=\\
&2\left(1+\Psi_m\right)\frac{\partial}{\partial r}\left(\bar{\phi}_{n0}g_{b0}h_0\right)-\gamma^* h_0\frac{\partial}{\partial r}\left[\frac{1}{r}\frac{\partial}{\partial r}\left(r\frac{\partial h_0}{\partial r}\right)+\frac{1}{r^2}\frac{\partial^2 h_0}{\partial \theta^2}\right],
\end{aligned}
\tag{4.63a}
$$

$$
\begin{aligned}
&\frac{4}{r^2}\frac{\partial}{\partial \theta}\left(h_0\frac{\partial u_{\theta 0}}{\partial \theta}\right)+\frac{1}{r}\frac{\partial}{\partial r}\left(rh_0\frac{\partial u_{\theta 0}}{\partial r}\right)-\frac{u_{\theta 0}}{r^2}\frac{\partial}{\partial r}\left(rh_0\right)\\
&+\frac{1}{r^2}\frac{\partial}{\partial r}\left(rh_0\frac{\partial u_{r0}}{\partial \theta}\right)+\frac{2}{r}\frac{\partial}{\partial \theta}\left(h_0\frac{\partial u_{r0}}{\partial r}\right)+\frac{4}{r^2}\frac{\partial}{\partial \theta}\left(u_{r0}h_0\right)=\\
&\frac{2}{r}\left(1+\Psi_m\right)\frac{\partial}{\partial \theta}\left(\bar{\phi}_{n0}g_{b0}h_0\right)-\frac{\gamma^* h_0}{r}\frac{\partial}{\partial \theta}\left[\frac{1}{r}\frac{\partial}{\partial r}\left(r\frac{\partial h_0}{\partial r}\right)+\frac{1}{r^2}\frac{\partial^2 h_0}{\partial \theta^2}\right].
\end{aligned}
\tag{4.63b}
$$

Equations (4.40), (4.44), (4.48), (4.50), (4.53), (4.63a) and (4.63b) then form a closed system of equations for the leading-order variables h_0, $\bar{\phi}_{n0}$, g_{s0}, g_{b0}, u_{r0}, and $u_{\theta 0}$. Together, these equations constitute our thin-film extensional flow model. Notably, all equations are now independent of z, demonstrating that the thin-film approximation makes it possible to simplify the original model.

4.3 Lubrication Regime

In §4.2, we considered biofilm expansion governed by weak adhesion to the substratum and low surface tension, as these conditions are thought to occur in sliding motility. However, strong biofilm–substratum adhesion is also possible, for which large pressure and surface tension contribute to expansion. We now undertake a similar process to §4.2, except this time we apply a new non-dimensionalisation to account for this large pressure and surface tension. This gives rise to a new model where the fluid velocities depend on z, and the fluid mass balances take the form of generalised lubrication equations.

4.3.1 Scaling and Non-Dimensionalisation

In the lubrication regime, pressure is large compared to the extensional flow regime. To model this, we introduce the rescaled pressure (where the dagger denotes a dimensionless quantity)

$$p = \frac{\psi_n G \mu}{\varepsilon^2} p^\dagger, \tag{4.64}$$

while retaining the same scaling (4.29) as the extensional flow regime for other variables. Under the lubrication regime scaling, the dimensionless conservation of mass equations (4.30a)–(4.30d) are unchanged from the extensional flow regime. The dimensionless conservation of momentum equations do change,

and instead become (dropping hats and daggers)

$$\begin{aligned}-\frac{1}{\varepsilon^2}\frac{\partial p}{\partial r}+\frac{2}{r}\frac{\partial}{\partial r}\left(r\frac{\partial u_r}{\partial r}\right)-\frac{2}{3}\frac{\partial}{\partial r}\left[\frac{1}{r}\frac{\partial}{\partial r}\left(ru_r\right)+\frac{1}{r}\frac{\partial u_\theta}{\partial \theta}+\frac{\partial u_z}{\partial z}\right]\\ +\frac{1}{r}\frac{\partial}{\partial \theta}\left(\frac{\partial u_\theta}{\partial r}+\frac{1}{r}\frac{\partial u_r}{\partial \theta}\right)+\frac{\partial}{\partial z}\left(\frac{\partial u_z}{\partial r}+\frac{1}{\varepsilon^2}\frac{\partial u_r}{\partial z}\right)\\ -\frac{3}{r^2}\frac{\partial u_\theta}{\partial \theta}-\frac{2u_r}{r^2}=0,\end{aligned} \tag{4.65a}$$

$$\begin{aligned}-\frac{1}{\varepsilon^2 r}\frac{\partial p}{\partial \theta}+\frac{2}{r^2}\frac{\partial^2 u_\theta}{\partial \theta^2}-\frac{2}{3r}\frac{\partial}{\partial \theta}\left[\frac{1}{r}\frac{\partial}{\partial r}\left(ru_r\right)+\frac{1}{r}\frac{\partial u_\theta}{\partial \theta}+\frac{\partial u_z}{\partial z}\right]\\ +\frac{1}{r}\frac{\partial}{\partial r}\left(\frac{\partial u_r}{\partial \theta}+r\frac{\partial u_\theta}{\partial r}\right)+\frac{\partial}{\partial z}\left(\frac{1}{r}\frac{\partial u_z}{\partial \theta}+\frac{1}{\varepsilon^2}\frac{\partial u_\theta}{\partial z}\right)\\ +\frac{3}{r^2}\frac{\partial u_r}{\partial \theta}-\frac{u_\theta}{r^2}=0,\end{aligned} \tag{4.65b}$$

$$\begin{aligned}-\frac{1}{\varepsilon^2}\frac{\partial p}{\partial z}+2\frac{\partial^2 u_z}{\partial z^2}-\frac{2}{3}\frac{\partial}{\partial z}\left[\frac{1}{r}\frac{\partial}{\partial r}\left(ru_r\right)+\frac{1}{r}\frac{\partial u_\theta}{\partial \theta}+\frac{\partial u_z}{\partial z}\right]\\ +\frac{1}{r}\frac{\partial}{\partial r}\left[r\left(\frac{\partial u_r}{\partial z}+\varepsilon^2\frac{\partial u_z}{\partial r}\right)\right]+\frac{1}{r}\frac{\partial}{\partial \theta}\left(\frac{\partial u_\theta}{\partial z}+\frac{\varepsilon^2}{r}\frac{\partial u_z}{\partial \theta}\right)=0,\end{aligned} \tag{4.65c}$$

where surface tension and pressure terms now appear in the leading-order momentum balance.

In the extensional flow regime, we assumed that there was weak adhesion between the fluid and the substratum, which is appropriate for modelling sliding motility. However, in the lubrication regime we instead assume that cells adhere strongly to the substratum. This involves taking $\lambda_\alpha \to \infty$ in the general tangential stress conditions (4.17). For the tangential stress to remain bounded, we need to impose no-slip conditions on the biofilm–substratum interface. These conditions read

$$u_r = u_\theta = 0 \quad \text{on} \quad z = 0. \tag{4.66}$$

Owing to the re-scaled pressure term, the free surface normal stress boundary condition also differs from the extensional flow case. In the lubrication regime

we instead have

$$\begin{aligned}
&-\frac{1}{\varepsilon^2}p-\frac{2}{3}\left[\frac{1}{r}\frac{\partial}{\partial r}\left(ru_r\right)+\frac{1}{r}\frac{\partial u_\theta}{\partial\theta}+\frac{\partial u_z}{\partial z}\right]+2\left[\varepsilon^2\left(\frac{\partial h}{\partial r}\right)^2\right.\\
&\qquad\left.+\varepsilon^2\left(\frac{1}{r}\frac{\partial h}{\partial\theta}\right)^2+1\right]^{-1}\left\{\varepsilon^2\left(\frac{\partial h}{\partial r}\right)^2\frac{\partial u_r}{\partial r}\right.\\
&+\varepsilon^2\frac{\partial h}{\partial r}\frac{\partial h}{\partial\theta}\left[\frac{1}{r^2}\frac{\partial u_r}{\partial\theta}+\frac{\partial}{\partial r}\left(\frac{u_\theta}{r}\right)\right]-\frac{\partial h}{\partial r}\left(\frac{\partial u_r}{\partial z}+\varepsilon^2\frac{\partial u_z}{\partial r}\right)\\
&+\frac{\varepsilon^2}{r^3}\left(\frac{\partial h}{\partial\theta}\right)^2\left(\frac{\partial u_\theta}{\partial\theta}+u_r\right)-\frac{1}{r}\frac{\partial h}{\partial\theta}\left(\frac{\partial u_\theta}{\partial z}+\frac{\varepsilon^2}{r}\frac{\partial u_z}{\partial\theta}\right)\\
&\qquad\left.+\frac{\partial u_z}{\partial z}\right\}=-\frac{1}{\varepsilon^2}\gamma^*\kappa^*\quad\text{on}\quad z=h.
\end{aligned}\tag{4.67}$$

In (4.67), $\gamma^*=1/\mathrm{Ca}^\dagger$ is defined in the same way as (4.33), but now incorporates the new capillary number

$$\mathrm{Ca}^\dagger=\frac{\psi_n G R_b\mu}{\varepsilon^3\gamma}.\tag{4.68}$$

The new capillary number represents that we expect the new large pressure to be balanced by a comparatively large surface tension. The remaining dimensionless boundary conditions (4.32a)–(4.32d) and (4.32g)–(4.32j) remain unchanged from the extensional flow regime.

4.3.2 Thin-Film Equations

As with the extensional flow regime, we use the thin-film approximation to simplify the lubrication model. On substituting the same power series expansions (4.36) into the dimensionless governing equations (4.30a)–(4.30d) and (4.65), the leading-order mass conservation equations (4.37a)–(4.37c) are unchanged. At leading-order, the momentum balance equations (4.65) become

$$\frac{\partial p_0}{\partial r}=\frac{\partial^2 u_{r0}}{\partial z^2},\tag{4.69a}$$

$$\frac{1}{r}\frac{\partial p_0}{\partial \theta} = \frac{\partial^2 u_{\theta 0}}{\partial z^2}, \tag{4.69b}$$

$$\frac{\partial p_0}{\partial z} = 0. \tag{4.69c}$$

The leading-order boundary conditions consist of (4.38a), (4.38b), (4.38d) and (4.38f), along with no-slip and no-penetration conditions on the biofilm–substratum interface,

$$u_{r0} = u_{\theta 0} = u_{z0} = 0 \quad \text{on} \quad z = 0, \tag{4.70}$$

and the normal stress condition

$$p_0 = -\gamma^* \left[\frac{1}{r}\frac{\partial}{\partial r}\left(r\frac{\partial h_0}{\partial r}\right) + \frac{1}{r^2}\frac{\partial^2 h_0}{\partial \theta^2}\right] \quad \text{on} \quad z = h_0. \tag{4.71}$$

In (4.71), the right-hand side term contains the leading-order contribution of the dimensionless free surface curvature (4.35).

The next step is to derive a closed system of equations in terms of leading-order quantities. Unlike in the extensional flow regime, in the lubrication regime we do not need to consider higher-order correction terms in the momentum equations. Instead, we integrate (4.69c) with respect to z and apply the normal stress boundary condition (4.71) to obtain

$$p_0 = -\gamma^* \left[\frac{1}{r}\frac{\partial}{\partial r}\left(r\frac{\partial h_0}{\partial r}\right) + \frac{1}{r^2}\frac{\partial^2 h_0}{\partial \theta^2}\right]. \tag{4.72}$$

By (4.71) and (4.72), the pressure throughout the biofilm is equal to the pressure on the free surface. We can use this to obtain explicit formulae for the leading-order fluid velocity components. Integrating the leading-order radial and azimuthal momentum equations (4.69a) and (4.69b) twice with respect to z, and applying the conditions (4.38d) and (4.70), we obtain

$$u_{r0} = z\left(\frac{z}{2} - h_0\right)\frac{\partial p_0}{\partial r}, \tag{4.73a}$$

$$u_{\theta 0} = \frac{z}{r}\left(\frac{z}{2} - h_0\right)\frac{\partial p_0}{\partial \theta}. \tag{4.73b}$$

Using (4.72) to eliminate the pressure then gives

$$u_{r0} = -\gamma^* z\left(\frac{z}{2} - h_0\right)\frac{\partial}{\partial r}\left[\frac{1}{r}\frac{\partial}{\partial r}\left(r\frac{\partial h_0}{\partial r}\right) + \frac{1}{r^2}\frac{\partial^2 h_0}{\partial \theta^2}\right], \tag{4.74a}$$

$$u_{\theta 0} = -\frac{\gamma^* z}{r}\left(\frac{z}{2} - h_0\right)\frac{\partial}{\partial \theta}\left[\frac{1}{r}\frac{\partial}{\partial r}\left(r\frac{\partial h_0}{\partial r}\right) + \frac{1}{r^2}\frac{\partial^2 h_0}{\partial \theta^2}\right]. \tag{4.74b}$$

In the extensional flow regime, it was not possible to solve for these velocity components explicitly. However, in the lubrication regime these velocities (4.74) depend on the depth z. Therefore, we cannot eliminate the z-dependence from the leading-order lubrication model, as was possible in the extensional flow regime.

Like in the extensional flow regime, we now derive leading-order mass conservation equations for the fluids in terms of the biofilm height. Integrating (4.37a) with respect to z across the biofilm depth yields, on application of the kinematic (4.38f) and no-slip (4.70) conditions,

$$\begin{aligned}\frac{\partial h_0}{\partial t} + u_{r0}|_{z=h_0}\frac{\partial h_0}{\partial r} + \frac{u_{\theta 0}|_{z=h_0}}{r}\frac{\partial h_0}{\partial \theta} &= (1+\Psi_m)\,\bar{\phi}_{n0} g_{b0} h_0 \\ -\frac{1}{r}\left(\int_0^{h_0}\frac{\partial}{\partial r}\left(r u_{r0}\right)\mathrm{d}z + \int_0^{h_0}\frac{\partial u_{\theta 0}}{\partial \theta}\,\mathrm{d}z\right).\end{aligned} \tag{4.75}$$

To evaluate the right-hand side of (4.75), we use Leibniz's integral rule to obtain

$$\begin{aligned}\frac{\partial h_0}{\partial t} + u_{r0}|_{z=h_0}\frac{\partial h_0}{\partial r} + \frac{u_{\theta 0}|_{z=h_0}}{r}\frac{\partial h_0}{\partial \theta} &= (1+\Psi_m)\,\bar{\phi}_{n0} g_{b0} h_0 \\ -\frac{1}{r}\left[\frac{\partial}{\partial r}\left(\int_0^{h_0} r u_{r0}\,\mathrm{d}z\right) - r u_{r0}|_{z=h_0}\frac{\partial h_0}{\partial r}\right. & \\ \left. +\frac{\partial}{\partial \theta}\left(\int_0^{h_0} u_{\theta 0}\,\mathrm{d}z\right) - u_{\theta 0}|_{z=h_0}\frac{\partial h_0}{\partial \theta}\right].\end{aligned} \tag{4.76}$$

All terms evaluated at the free surface then cancel, yielding

$$\begin{aligned}\frac{\partial h_0}{\partial t} &= (1+\Psi_m)\,\bar{\phi}_{n0} g_{b0} h_0 \\ -\frac{1}{r}\left[\frac{\partial}{\partial r}\left(\int_0^{h_0} r u_{r0}\,\mathrm{d}z\right) + \frac{\partial}{\partial \theta}\left(\int_0^{h_0} u_{\theta 0}\,\mathrm{d}z\right)\right].\end{aligned} \tag{4.77}$$

On replacing the velocity terms in (4.77) with the explicit formulae (4.74), we obtain the leading-order conservation of total fluid mass equation,

$$\begin{aligned}&\frac{\partial h_0}{\partial t} + \frac{\gamma^*}{3r}\frac{\partial}{\partial r}\left\{r h_0^3 \frac{\partial}{\partial r}\left[\frac{1}{r}\frac{\partial}{\partial r}\left(r\frac{\partial h_0}{\partial r}\right) + \frac{1}{r^2}\frac{\partial^2 h_0}{\partial \theta^2}\right]\right\} \\ &\quad + \frac{\gamma^*}{3r^2}\frac{\partial}{\partial \theta}\left\{h_0^3 \frac{\partial}{\partial \theta}\left[\frac{1}{r}\frac{\partial}{\partial r}\left(r\frac{\partial h_0}{\partial r}\right) + \frac{1}{r^2}\frac{\partial^2 h_0}{\partial \theta^2}\right]\right\} \\ &\quad = (1+\Psi_m)\,\bar{\phi}_{n0} g_{b0} h_0.\end{aligned} \tag{4.78}$$

Since the leading-order cell volume fraction ϕ_{n0} and the fluid velocity components (4.74) both depend on z, a similar approach based on vertical integration is not possible for the cellular phase mass conservation equation. In the lubrication model, we instead retain the three-dimensional mass balance equation (4.37b). Substituting the known radial and azimuthal velocity components (4.74) into (4.37b), we obtain

$$\begin{aligned}&\frac{\partial \phi_{n0}}{\partial t} - \frac{\gamma^* z}{r}\frac{\partial}{\partial r}\left\{r\phi_{n0}\left(\frac{z}{2}-h_0\right)\frac{\partial}{\partial r}\left[\frac{1}{r}\frac{\partial}{\partial r}\left(r\frac{\partial h_0}{\partial r}\right) + \frac{1}{r^2}\frac{\partial^2 h_0}{\partial \theta^2}\right]\right\} \\ &\quad - \frac{\gamma^* z}{r^2}\frac{\partial}{\partial \theta}\left\{\phi_{n0}\left(\frac{z}{2}-h_0\right)\frac{\partial}{\partial \theta}\left[\frac{1}{r}\frac{\partial}{\partial r}\left(r\frac{\partial h_0}{\partial r}\right) + \frac{1}{r^2}\frac{\partial^2 h_0}{\partial \theta^2}\right]\right\} \\ &\quad + \frac{\partial}{\partial z}\left(u_{z0}\phi_{n0}\right) = \phi_{n0} g_{b0} - \Psi_d \phi_{n0}.\end{aligned} \tag{4.79}$$

As we cannot integrate out the z dependence, solving the model in the lubrication regime requires keeping track of u_{z0}. We achieve this by integrating (4.37a) with respect to z, and applying the boundary condition (4.70), which

gives

$$\begin{aligned} u_{z0} = {} & (1+\Psi_m)\, g_{b0} \int_0^z \phi_{n0}\, \mathrm{d}\tilde{z} \\ & + \gamma^* \int_0^z \frac{1}{r}\frac{\partial}{\partial r}\left\{ r\tilde{z}\left(\frac{\tilde{z}}{2} - h_0\right) \frac{\partial}{\partial r}\left[\frac{1}{r}\frac{\partial}{\partial r}\left(r\frac{\partial h_0}{\partial r}\right) + \frac{1}{r^2}\frac{\partial^2 h_0}{\partial \theta^2}\right]\right\} \mathrm{d}\tilde{z} \\ & + \gamma^* \int_0^z \frac{1}{r^2}\frac{\partial}{\partial \theta}\left\{ \tilde{z}\left(\frac{\tilde{z}}{2} - h_0\right) \frac{\partial}{\partial \theta}\left[\frac{1}{r}\frac{\partial}{\partial r}\left(r\frac{\partial h_0}{\partial r}\right) + \frac{1}{r^2}\frac{\partial^2 h_0}{\partial \theta^2}\right]\right\} \mathrm{d}\tilde{z}. \end{aligned} \tag{4.80}$$

Evaluating integrals in (4.80) involving the surface tension coefficient analytically, we obtain

$$\begin{aligned} u_{z0} = {} & (1+\Psi_m)\, g_{b0} \int_0^z \phi_{n0}\, \mathrm{d}\tilde{z} \\ & + \frac{\gamma^*}{r}\frac{\partial}{\partial r}\left\{ \frac{rz^2}{2}\left(\frac{z}{3} - h_0\right) \frac{\partial}{\partial r}\left[\frac{1}{r}\frac{\partial}{\partial r}\left(r\frac{\partial h_0}{\partial r}\right) + \frac{1}{r^2}\frac{\partial^2 h_0}{\partial \theta^2}\right]\right\} \\ & + \frac{\gamma^*}{r^2}\frac{\partial}{\partial \theta}\left\{ \frac{z^2}{2}\left(\frac{z}{3} - h_0\right) \frac{\partial}{\partial \theta}\left[\frac{1}{r}\frac{\partial}{\partial r}\left(r\frac{\partial h_0}{\partial r}\right) + \frac{1}{r^2}\frac{\partial^2 h_0}{\partial \theta^2}\right]\right\}, \end{aligned} \tag{4.81}$$

which is our leading-order equation for the vertical component of fluid velocity.

To close the model, we require leading-order equations for the nutrient concentrations. The derivation of the equation for the nutrient concentration in the substratum is unchanged from the extensional flow regime, which gives (4.48). To obtain an equation for g_{b0}, we apply a similar process to the extensional flow regime. The only difference is that, in the lubrication regime, we cannot explicitly integrate terms involving products of u_{r0}, $u_{\theta 0}$, and ϕ_{n0}, as all of these depend on z. The lubrication model equation is

$$\begin{aligned} & \mathrm{Pe}\left\{ h_0\frac{\partial g_{b0}}{\partial t} + \frac{1}{r}\frac{\partial}{\partial r}\left[r g_{b0}\int_0^{h_0} u_{r0}\,(1-\phi_{n0})\,\mathrm{d}z\right]\right. \\ & \left. + \frac{\partial}{\partial \theta}\left[g_{b0}\int_0^{h_0} u_{\theta 0}\,(1-\phi_{n0})\,\mathrm{d}z\right]\right\} = \frac{1}{r}\frac{\partial}{\partial r}\left(r h_0 \frac{\partial g_{b0}}{\partial r}\right) \\ & + \frac{1}{r^2}\frac{\partial}{\partial \theta}\left(h_0\frac{\partial g_{b0}}{\partial \theta}\right) + Q_b\,(g_{s0} - g_{b0}) - \Upsilon \bar{\phi}_{n0} g_{b0} h_0, \end{aligned} \tag{4.82}$$

which upon substitution of the leading-order radial and azimuthal velocity

components (4.74), becomes

$$\begin{aligned}\mathrm{Pe}\Bigg\{h_0\frac{\partial g_{b0}}{\partial t}-\frac{\gamma^*}{r}\frac{\partial}{\partial r}\left[rg_{b0}\frac{\partial}{\partial r}\left(\frac{1}{r}\frac{\partial}{\partial r}\left[r\frac{\partial h_0}{\partial r}\right]+\frac{1}{r^2}\frac{\partial^2 h_0}{\partial\theta^2}\right)\int_0^{h_0} z\left(\frac{z}{2}-h_0\right)(1-\phi_{n0})\,\mathrm{d}z\right]\\ -\frac{\gamma^*}{r}\frac{\partial}{\partial\theta}\left[g_{b0}\frac{\partial}{\partial\theta}\left(\frac{1}{r}\frac{\partial}{\partial r}\left[r\frac{\partial h_0}{\partial r}\right]+\frac{1}{r^2}\frac{\partial^2 h_0}{\partial\theta^2}\right)\int_0^{h_0} z\left(\frac{z}{2}-h_0\right)(1-\phi_{n0})\,\mathrm{d}z\right]\Bigg\}\\ =\frac{1}{r}\frac{\partial}{\partial r}\left(rh_0\frac{\partial g_{b0}}{\partial r}\right)+\frac{1}{r^2}\frac{\partial}{\partial\theta}\left(h_0\frac{\partial g_{b0}}{\partial\theta}\right)+Q_b\left(g_{s0}-g_{b0}\right)-\Upsilon\bar{\phi}_{n0}g_{b0}h_0.\end{aligned} \tag{4.83}$$

Equations (4.39), (4.48), (4.50), (4.78), (4.79), (4.81) and (4.83) now form a closed system of equations for h_0, ϕ_{n0}, $\bar{\phi}_{n0}$, u_{z0}, g_{s0} and g_{b0}. These equations constitute our thin-film model in the lubrication regime.

4.4 Summary

To investigate the effect of colony mechanics on biofilm expansion, we derived a two-phase fluid model for yeast biofilm growth. We treated the biofilm as a mixture of living cells and an ECM, both of which we considered Newtonian viscous fluids. We modelled three-dimensional biofilm growth on a solid substratum, from which the biofilm takes up nutrients. We obtained governing equations by applying conservation of mass and momentum for each fluid phase and the nutrient concentrations. This, combined with initial and boundary conditions, provided a closed model for biofilm growth.

The full model was a complicated system of equations in three dimensions, which makes analytical and numerical progress difficult. To simplify the model, we assumed that living cells and the ECM have the same physical properties, and that each moves with a common velocity. Next, as the biofilm height is small compared to its radius, we used the thin-film approximation to further simplify the model. In doing so, our choice of distinguished limits depended on the balance between biofilm mechanics and nutrient movement, uptake, and consumption. This led us to consider two regimes that have possible relevance to biofilm growth.

First, we derived a model in the extensional flow regime, in which cell proliferation and weak biofilm–substratum adhesion drives expansion. This modelled biofilm growth by sliding motility, a candidate mechanism for *S. cerevisiae* mat expansion. The key assumption of this model was imposing zero-stress on the biofilm–substratum interface, which ensured that the leading-order fluid velocity components did not depend on z. We then obtained the two-dimensional extensional flow model (dropping the zero subscript on leading-order variables),

$$\frac{\partial h}{\partial t} + \frac{1}{r}\frac{\partial}{\partial r}\left(r u_r h\right) + \frac{1}{r}\frac{\partial}{\partial \theta}\left(u_\theta h\right) = \left(1+\Psi_m\right)\bar{\phi}_n g_b h, \tag{4.84a}$$

$$\frac{\partial \bar{\phi}_n}{\partial t} + u_r\frac{\partial \bar{\phi}_n}{\partial r} + \frac{u_\theta}{r}\frac{\partial \bar{\phi}_n}{\partial \theta} = \bar{\phi}_n\left[g_b - \Psi_d - \left(1+\Psi_m\right)\bar{\phi}_n g_b\right]. \tag{4.84b}$$

$$\frac{\partial g_s}{\partial t} = D\left[\frac{1}{r}\frac{\partial}{\partial r}\left(r\frac{\partial g_s}{\partial r}\right) + \frac{1}{r^2}\frac{\partial^2 g_s}{\partial \theta^2}\right] - DQ_s\left(g_s - g_b\right), \tag{4.84c}$$

$$\frac{\partial g_s}{\partial t} = D\left[\frac{1}{r}\frac{\partial}{\partial r}\left(r\frac{\partial g_s}{\partial r}\right) + \frac{1}{r^2}\frac{\partial^2 g_s}{\partial \theta^2}\right] \quad \text{on} \quad S(\theta,t) < r < R, \tag{4.84d}$$

$$\begin{aligned}&\mathrm{Pe}\left\{h\frac{\partial g_b}{\partial t} + \frac{1}{r}\frac{\partial}{\partial r}\left[r u_r\left(1-\bar{\phi}_n\right)g_b h\right] + \frac{1}{r}\frac{\partial}{\partial \theta}\left[u_\theta\left(1-\bar{\phi}_n\right)g_b h\right]\right\}\\ &= \frac{1}{r}\frac{\partial}{\partial r}\left(rh\frac{\partial g_b}{\partial r}\right) + \frac{1}{r^2}\frac{\partial}{\partial \theta}\left(h\frac{\partial g_b}{\partial \theta}\right) + Q_b\left(g_s - g_b\right) - \Upsilon\bar{\phi}_n g_b h,\end{aligned} \tag{4.84e}$$

$$\begin{aligned}&4\frac{\partial}{\partial r}\left[\frac{h}{r}\frac{\partial}{\partial r}\left(r u_r\right)\right] - \frac{2u_r}{r}\frac{\partial h}{\partial r} + \frac{1}{r^2}\frac{\partial}{\partial \theta}\left(h\frac{\partial u_r}{\partial \theta}\right)\\ &+\frac{\partial}{\partial \theta}\left[h\frac{\partial}{\partial r}\left(\frac{u_\theta}{r}\right)\right] + 2\frac{\partial}{\partial r}\left(\frac{h}{r}\frac{\partial u_\theta}{\partial \theta}\right) - \frac{2h}{r^2}\frac{\partial u_\theta}{\partial \theta} =\\ &2\left(1+\Psi_m\right)\frac{\partial}{\partial r}\left(\bar{\phi}_n g_b h\right) - \gamma^* h\frac{\partial}{\partial r}\left[\frac{1}{r}\frac{\partial}{\partial r}\left(r\frac{\partial h}{\partial r}\right) + \frac{1}{r^2}\frac{\partial^2 h}{\partial \theta^2}\right],\end{aligned} \tag{4.84f}$$

$$\begin{aligned}
&\frac{4}{r^2}\frac{\partial}{\partial\theta}\left(h\frac{\partial u_\theta}{\partial\theta}\right)+\frac{1}{r}\frac{\partial}{\partial r}\left(rh\frac{\partial u_\theta}{\partial r}\right)-\frac{u_\theta}{r^2}\frac{\partial}{\partial r}\left(rh\right)\\
&+\frac{1}{r^2}\frac{\partial}{\partial r}\left(rh\frac{\partial u_r}{\partial\theta}\right)+\frac{2}{r}\frac{\partial}{\partial\theta}\left(h\frac{\partial u_r}{\partial r}\right)+\frac{4}{r^2}\frac{\partial}{\partial\theta}\left(u_r h\right)=\\
&\frac{2}{r}\left(1+\Psi_m\right)\frac{\partial}{\partial\theta}\left(\bar{\phi}_n g_b h\right)-\frac{\gamma^* h}{r}\frac{\partial}{\partial\theta}\left[\frac{1}{r}\frac{\partial}{\partial r}\left(r\frac{\partial h}{\partial r}\right)+\frac{1}{r^2}\frac{\partial^2 h}{\partial\theta^2}\right].
\end{aligned}\tag{4.84g}$$

Unless otherwise stated, all of these equations are defined on the moving boundary $0 < r < S(\theta, t)$, which represents the area occupied by the biofilm.

In the lubrication regime, we assumed strong adhesion between the biofilm and substratum, and large surface tension and pressure. In the biofilm growth context, surface tension represents the strength of cell–cell adhesion at the biofilm surface. This provided an additional expansion mechanism that was not present in the extensional flow model. In the lubrication regime, we assumed no-slip on the biofilm–substratum interface, and the leading-order fluid velocities depended on z. We then obtained the three-dimensional model (again dropping the zero subscripts),

$$\begin{aligned}
&\frac{\partial h}{\partial t}+\frac{\gamma^*}{3r}\frac{\partial}{\partial r}\left\{rh^3\frac{\partial}{\partial r}\left[\frac{1}{r}\frac{\partial}{\partial r}\left(r\frac{\partial h}{\partial r}\right)+\frac{1}{r^2}\frac{\partial^2 h}{\partial\theta^2}\right]\right\}\\
&+\frac{\gamma^*}{3r^2}\frac{\partial}{\partial\theta}\left\{h^3\frac{\partial}{\partial\theta}\left[\frac{1}{r}\frac{\partial}{\partial r}\left(r\frac{\partial h}{\partial r}\right)+\frac{1}{r^2}\frac{\partial^2 h}{\partial\theta^2}\right]\right\}=\left(1+\Psi_m\right)\bar{\phi}_n g_b h,
\end{aligned}\tag{4.85a}$$

$$\begin{aligned}
&\frac{\partial\phi_n}{\partial t}-\frac{\gamma^* z}{r}\frac{\partial}{\partial r}\left\{r\phi_n\left(\frac{z}{2}-h\right)\frac{\partial}{\partial r}\left[\frac{1}{r}\frac{\partial}{\partial r}\left(r\frac{\partial h}{\partial r}\right)+\frac{1}{r^2}\frac{\partial^2 h}{\partial\theta^2}\right]\right\}\\
&-\frac{\gamma^* z}{r^2}\frac{\partial}{\partial\theta}\left\{\phi_n\left(\frac{z}{2}-h\right)\frac{\partial}{\partial\theta}\left[\frac{1}{r}\frac{\partial}{\partial r}\left(r\frac{\partial h}{\partial r}\right)+\frac{1}{r^2}\frac{\partial^2 h}{\partial\theta^2}\right]\right\}\\
&+\frac{\partial}{\partial z}\left(u_z\phi_n\right)=\phi_n g_b-\Psi_d\phi_n,
\end{aligned}\tag{4.85b}$$

$$\bar{\phi}_n=\frac{1}{h}\int_0^h \phi_n\,\mathrm{d}z,\tag{4.85c}$$

$$u_z = (1+\Psi_m)\, g_b \int_0^z \phi_n \,\mathrm{d}\tilde{z} + \frac{\gamma^*}{r}\frac{\partial}{\partial r}\left\{\frac{rz^2}{2}\left(\frac{z}{3}-h\right)\frac{\partial}{\partial r}\left[\frac{1}{r}\frac{\partial}{\partial r}\left(r\frac{\partial h}{\partial r}\right)+\frac{1}{r^2}\frac{\partial^2 h}{\partial \theta^2}\right]\right\} + \frac{\gamma^*}{r^2}\frac{\partial}{\partial \theta}\left\{\frac{z^2}{2}\left(\frac{z}{3}-h\right)\frac{\partial}{\partial \theta}\left[\frac{1}{r}\frac{\partial}{\partial r}\left(r\frac{\partial h}{\partial r}\right)+\frac{1}{r^2}\frac{\partial^2 h}{\partial \theta^2}\right]\right\}, \tag{4.85d}$$

$$\frac{\partial g_s}{\partial t} = D\left[\frac{1}{r}\frac{\partial}{\partial r}\left(r\frac{\partial g_s}{\partial r}\right)+\frac{1}{r^2}\frac{\partial^2 g_s}{\partial \theta^2}\right] - DQ_s\left(g_s - g_b\right), \tag{4.85e}$$

$$\mathrm{Pe}\left\{h\frac{\partial g_b}{\partial t} - \frac{\gamma^*}{r}\frac{\partial}{\partial r}\left[rg_b\frac{\partial}{\partial r}\left(\frac{1}{r}\frac{\partial}{\partial r}\left[r\frac{\partial h}{\partial r}\right]+\frac{1}{r^2}\frac{\partial^2 h}{\partial \theta^2}\right)\int_0^h z\left(\frac{z}{2}-h\right)(1-\phi_n)\,\mathrm{d}z\right] - \frac{\gamma^*}{r}\frac{\partial}{\partial \theta}\left[g_b\frac{\partial}{\partial \theta}\left(\frac{1}{r}\frac{\partial}{\partial r}\left[r\frac{\partial h}{\partial r}\right]+\frac{1}{r^2}\frac{\partial^2 h}{\partial \theta^2}\right)\int_0^h z\left(\frac{z}{2}-h\right)(1-\phi_n)\,\mathrm{d}z\right]\right\} = \frac{1}{r}\frac{\partial}{\partial r}\left(rh\frac{\partial g_b}{\partial r}\right)+\frac{1}{r^2}\frac{\partial}{\partial \theta}\left(h\frac{\partial g_b}{\partial \theta}\right)+Q_b\left(g_s-g_b\right)-\Upsilon\bar{\phi}_n g_b h, \tag{4.85f}$$

where all equations are to be solved on $0 < r < R$. Having derived the thin-film models, the next two chapters involve their analysis and numerical solutions. In Chapter 5, we use the extensional flow model and experimental data to determine the extent to which sliding motility can explain yeast biofilm expansion. We then contrast this with solutions to the lubrication model in Chapter 6.

Depending on the desired application, our modelling framework retains the possibility of investigating different mechanisms. A more detailed model could involve treating the agar as viscoelastic, rather than solid. We could then impose continuity of shear stress at biofilm–substratum interface, instead of the zero tangential stress assumed here. The multi-phase framework can also incorporate more complicated cell production mechanisms, for example ECM production regulated by quorum sensing. It is also possible to include additional mechanical behaviour, for example biofilm viscoelasticity or expansion driven by osmotic swelling. We intend to tackle some of these scenarios in future work, to shed further light on the mechanisms governing biofilm expansion.

Chapter 5

Extensional Flow Regime: Sliding Motility

We use the extensional flow model derived in §4.2 to test the hypothesis that sliding motility is the mechanism governing yeast biofilm expansion. To achieve this, we compare results from the *S. cerevisiae* mat formation experiments with numerical solutions to the model. We restrict attention to the one-dimensional axisymmetric form of the model, which captures the radial expansion speed and profile shape of the biofilm. First, we propose appropriate initial and boundary conditions for the axisymmetric model. Next, we solve the one-dimensional axisymmetric problem numerically, and find good agreement between numerical solutions and experimental data. Having established the biological utility of the model, we then investigate the effect of parameters on the biofilm size and shape.

5.1 One-Dimensional Axisymmetric Model

To test whether sliding motility is a possible mechanism for biofilm expansion, we compare the speed of expansion with experimental data. Although we derived a two-dimensional leading-order extensional flow model in §4.2, the one-dimensional axisymmetric model is sufficient to achieve this objective.

Accordingly, we neglect azimuthal dependence in (4.84), which yields the one-dimensional axisymmetric model (where all equations are defined for $0 < r < S(t)$ unless otherwise specified)

$$\frac{\partial h}{\partial t} + \frac{1}{r}\frac{\partial}{\partial r}\left(r u_r h\right) = \left(1 + \Psi_m\right)\bar{\phi}_n g_b h, \tag{5.1a}$$

$$\frac{\partial \bar{\phi}_n}{\partial t} + u_r \frac{\partial \bar{\phi}_n}{\partial r} = \bar{\phi}_n \left[g_b - \Psi_d - \left(1 + \Psi_m\right)\bar{\phi}_n g_b\right], \tag{5.1b}$$

$$\frac{\partial g_s}{\partial t} = \frac{D}{r}\frac{\partial}{\partial r}\left(r\frac{\partial g_s}{\partial r}\right) - DQ_s\left(g_s - g_b\right), \tag{5.1c}$$

$$\frac{\partial g_s}{\partial t} = \frac{D}{r}\frac{\partial}{\partial r}\left(r\frac{\partial g_s}{\partial r}\right) \quad \text{on} \quad S(t) < r < R, \tag{5.1d}$$

$$\begin{aligned} &\mathrm{Pe}\left\{h\frac{\partial g_b}{\partial t} + \frac{1}{r}\frac{\partial}{\partial r}\left[r u_r\left(1 - \bar{\phi}_n\right) g_b h\right]\right\} = \\ &\frac{1}{r}\frac{\partial}{\partial r}\left(r h\frac{\partial g_b}{\partial r}\right) + Q_b\left(g_s - g_b\right) - \Upsilon\bar{\phi}_n g_b h, \end{aligned} \tag{5.1e}$$

$$\begin{aligned} &4\frac{\partial}{\partial r}\left[\frac{h}{r}\frac{\partial}{\partial r}\left(r u_r\right)\right] - \frac{2u_r}{r}\frac{\partial h}{\partial r} = \\ &2\left(1 + \Psi_m\right)\frac{\partial}{\partial r}\left(\bar{\phi}_n g_b h\right) - \gamma^* h\frac{\partial}{\partial r}\left[\frac{1}{r}\frac{\partial}{\partial r}\left(r\frac{\partial h}{\partial r}\right)\right]. \end{aligned} \tag{5.1f}$$

We obtain boundary conditions for (5.1) from experimental observations and the boundary conditions of the general mechanical model introduced in §4.1.2. This enables us to close the axisymmetric model (5.1), and proceed with numerical solutions.

5.1.1 Initial and Boundary Conditions

In the experiments, the Petri dish is initially filled uniformly with nutrients, and a small droplet containing cells and fluid is inoculated in the centre of the dish using a pipette. The fluid in the droplet is rapidly absorbed into the agar substratum, leaving a thin layer of cells, which we assume adopts a parabolic profile. Experiments of *C. albicans* show that extracellular material

only emerges in mature biofilm [151], hence we assume the biofilm is initially made up of cells only. Appropriate initial conditions are therefore

$$\begin{aligned} S(0) = 1, \quad h(r,0) = H_0\left(1 - r^2\right), \quad \bar{\phi}_n(r,0) = 1, \\ g_s(r,0) = 1, \quad g_b(r,0) = 0, \end{aligned} \tag{5.2}$$

where H_0 is the initial biofilm height, which we expect to be $\mathcal{O}(\varepsilon)$ as $\varepsilon \to 0$. In specifying (5.2), we have chosen the characteristic length scales to be the initial biofilm height and radius, and scale both nutrient concentrations by the initial concentration in the substratum.

For the boundary conditions, we first assume that the centre of the biofilm is fixed. Since the biofilm and nutrient concentration both radially symmetric, we obtain the conditions

$$\begin{aligned} \left.\frac{\partial h}{\partial r}\right|_{(0,t)} = 0, \quad \left.\frac{\partial \bar{\phi}_n}{\partial r}\right|_{(0,t)} = 0, \\ \left.\frac{\partial g_s}{\partial r}\right|_{(0,t)} = 0, \quad \left.\frac{\partial g_b}{\partial r}\right|_{(0,t)} = 0, \quad u_r(0,t) = 0. \end{aligned} \tag{5.3}$$

In addition, the contact line position $S(t)$ evolves according to the local fluid velocity, that is

$$\frac{\mathrm{d}S}{\mathrm{d}t} = u_r\left(S(t), t\right). \tag{5.4}$$

To close the one-dimensional axisymmetric model, we require additional boundary conditions for both nutrient concentrations and the radial fluid velocity. Regarding the nutrient concentration in the biofilm, we note that the leading edge of the biofilm is rounded by a meniscus, where the height changes over a region in r with $\mathcal{O}(\varepsilon)$ size [148]. This meniscus is not captured under the original thin-film scaling. With this in mind, close to the contact line we instead consider a re-scaling of the original variables,

$$(r,z) = \left(S(t) + \varepsilon R_b r^{\dagger}, \varepsilon R_b z^{\dagger}\right), \quad (u_r, u_z) = \left(\varepsilon\chi R_b {u_r}^{\dagger}, \varepsilon\chi R_b {u_z}^{\dagger}\right). \tag{5.5}$$

With this scaling, the leading-order balance for the flux boundary condition

(4.20) becomes (dropping daggers)

$$\frac{\partial g_b}{\partial z} = \frac{\partial g_b}{\partial r}\frac{\partial h}{\partial r} \quad \text{on} \quad z = h. \tag{5.6}$$

At the contact line, the left-hand side of (5.6) vanishes due to (4.38b), and in general h can depend on r. The boundary condition on the biofilm nutrient concentration is therefore

$$\left.\frac{\partial g_b}{\partial r}\right|_{(S(t),t)} = 0. \tag{5.7}$$

To close the momentum equation (5.1f), we impose that the biofilm experiences zero radial stress at the contact line, that is $\sigma_{rr}\left(S(t),t\right) = 0$. Using the radial component of (4.57) to eliminate pressure from the radial stress (4.10a), we find that

$$\sigma_{rr} = 2\frac{u_r}{r} + \frac{2}{r}\frac{\partial}{\partial r}\left(ru_r\right) - 2\left(1+\Psi_m\right)\phi_n g_b + \frac{\gamma^*}{r}\frac{\partial}{\partial r}\left(r\frac{\partial h}{\partial r}\right). \tag{5.8}$$

Setting this to zero at the contact line, we obtain the condition

$$4\frac{\partial u_r}{\partial r} + 2\frac{u_r}{r} = 2\left(1+\Psi_m\right)\bar{\phi}_n g_b - \frac{\gamma^*}{r}\frac{\partial}{\partial r}\left(r\frac{\partial h}{\partial r}\right), \quad \text{on} \quad r = S(t). \tag{5.9}$$

We note that (5.9) contains the depth-averaged cell volume fraction term. For $h\left(S(t),t\right) \neq 0$, the condition (5.9) arises from depth-averaging of the radial stress (5.8). If $h\left(S(t),t\right) = 0$, L'Hôpital's rule gives

$$\lim_{h\to 0}\bar{\phi}_n = \lim_{h\to 0}\frac{1}{h}\int_0^h \phi_n \,\mathrm{d}z = \left.\phi_n\right|_{z=0}, \tag{5.10}$$

and hence (5.9) still applies.

For the nutrient concentration in the substratum, it is natural to impose the no-flux condition

$$\left.\frac{\partial g_s}{\partial r}\right|_{(R,t)} = 0 \tag{5.11}$$

at the boundary of the Petri dish. We require a solution to (5.1c) and (5.1d)

such that g_s and its flux are continuous at the contact line, yielding the conditions

$$\lim_{r\to S(t)^-} g_s = \lim_{r\to S(t)^+} g_s, \quad \lim_{r\to S(t)^-} \frac{\partial g_s}{\partial r} = \lim_{r\to S(t)^+} \frac{\partial g_s}{\partial r}. \tag{5.12}$$

The equations (5.1), together with the boundary conditions (5.3), (5.4), (5.7), (5.9) and (5.11), continuity conditions (5.12), and initial conditions (5.2), form the one-dimensional axisymmetric model which we are to solve.

5.1.2 Parameters

To obtain appropriate values for the dimensionless parameters, we require estimates for all dimensional quantities in equations (4.29), (4.31), (4.33) and (4.34). In lieu of an accurate experimental measurement, we assume that the thin-film parameter is $\varepsilon = 0.1$. This is the same value used in the extensional flow model of Ward and King [120], and signifies that the biofilm thickness is an order of magnitude smaller than its radius. Accordingly, we also assume the initial biofilm height is $H_0 = 0.1$.

As in §3.1.2, we can determine many parameters directly from the experimental design. For example, the mean initial biofilm radius across the thirteen experiments was $R_b = 2.875\,\mathrm{mm}$. The radius of the medium on which the biofilms were grown was $R_p = 41.5\,\mathrm{mm}$ [2], giving $R = 14.4$. We also have $G = 9.24 \times 10^{-5}\,\mathrm{g \cdot mm^{-2}}$ and $D_s = 4.01 \times 10^{-2}\,\mathrm{mm^2 \cdot min^{-1}}$, since (3.6) and (3.7) still apply for the extensional flow model.

Since the substratum and biofilm are made of different materials, we do not necessarily expect $D_b = D_s$. Indeed, a review of experimental measurements of diffusivity in biofilms by Stewart [152] found that the the mean effective diffusivity in a microbial biofilm is $0.24D_{aq}$, where $D_{aq} = 4.04 \times 10^{-2}\,\mathrm{mm^2 \cdot min^{-1}}$ is the diffusivity of glucose in water [136]. Our estimate is thus $D_b = 9.70 \times 10^{-3}\,\mathrm{mm^2 \cdot min^{-1}}$. This is of the same order of magnitude as an estimate for a *S. cerevisiae* floc, which Vicente et al. [153] gave as $D_b = 6.6 \times 10^{-3}\,\mathrm{mm^2 \cdot min^{-1}}$. Vicente et al. [153] also estimated the

mass transfer coefficient of glucose in yeast to be $Q = 2.92 \times 10^{-3}\,\mathrm{mm} \cdot \mathrm{min}^{-1}$, and we adopt this as our estimate.

In experiments, it is difficult to obtain measurements for the ECM production rate, ψ_m, cell death rate, ψ_d, and surface tension coefficient, γ. Using the observation that extracellular material makes up approximately 10% of mature *S. cerevisiae* mats by volume, we assume a dimensionless value of $\Psi_m = 1/9$. Since the cell viability assay in Figure 1.6 shows that the proportion of dead cells at the end of the experiment is low, we assume $\Psi_d = 0$. Finally, we assume $\gamma^* = 0$ when comparing the extensional flow model with experiments. This is because sliding motility is associated with weak adhesion and low friction on the substratum [150], and therefore we expect the effect of surface tension to be negligible.

It remains to estimate the cell production rate, ψ_n, and nutrient consumption rate, η, which are difficult to measure experimentally. We obtain estimates by fitting these parameters to experimental data. We find that $\psi_n = 12.1\,\mathrm{mm}^2 \cdot \mathrm{g}^{-1} \cdot \mathrm{min}^{-1}$ and $\eta = 3.7 \times 10^{-3}\,\mathrm{min}^{-1}$ produces a local minimum in the sum of squared differences between a numerical solution and the biofilm size data in Figure 2.7. Using these values completes our parameter estimation, and enables us to compute the dimensionless model parameters. These estimates are listed in Table 5.1. The constant T is the dimensionless

Table 5.1: Dimensionless parameters for the thin-film extensional flow model, estimated from yeast (*S. cerevisiae*) biofilm experiments.

Parameter	Value	Parameter	Value
H_0	0.1	D	4.34
Ψ_m	0.111	Pe	0.953
Ψ_d	0	Υ	3.15
R	14.4	Q_b	8.65
T	15.9	Q_s	2.09
γ^*	0		

experimental time, computed using the time scale in (4.29). Importantly, all of the constants in right-hand column of Table 5.1 are $\mathcal{O}(1)$. This indicates that the extensional flow scaling is appropriate for our yeast biofilm experiments.

5.2 Numerical Solutions

To compute numerical solutions to the one-dimensional axisymmetric model (5.1), it is convenient to make a change of variables that maps the biofilm and unoccupied Petri dish domains to the unit interval. Following Crank [154], this involves defining

$$\xi = \frac{r}{S(t)}, \quad \xi_o = \frac{r - S(t)}{R - S(t)}, \quad \text{and} \quad \tau = t. \tag{5.13}$$

so that the biofilm always inhabits $\xi \in [0, 1]$, and the interval $\xi_o \in [0, 1]$ represents the remainder of the Petri dish not occupied by the biofilm. We then use a Crank–Nicolson scheme to discretise (5.1). For all non-linear terms, we linearise using data from the previous time step. At each time step, we solve the governing equations in the same order as they are derived in (5.1). When solving for the nutrient concentration in the substratum, we use data from the previous time step as an initial guess for $g_s\left(S(t), t\right)$ at the current time step. We then solve both (5.1c) and (5.1d), and use Newton's method to correct the initial guess, and ensure that the first spatial derivative of g_s is continuous at $r = S(t)$, which corresponds to $\xi = 1$ and $\xi_o = 0$. We compute solutions using an equispaced grid with $\Delta\xi = \Delta\xi_o = 1.25 \times 10^{-4}$ and $\Delta\tau = 9.93 \times 10^{-5} \approx 1 \times 10^{-4}$, which ensures convergence with grid spacing and time step size. Further details on the numerical method are provided in Appendix B.2.

5.2.1 Comparison with Experiments

To facilitate comparison with experiments, we compute the solution to the one-dimensional axisymmetric model with the parameters given in Table 5.1. We then compare the numerical contact line position with the measured radius of the experimental *S. cerevisiae* mats. These results, depicted in Figure 5.1, reveal excellent agreement between the numerical solution and experimental data. The extensional flow model can therefore explain the biofilm expansion

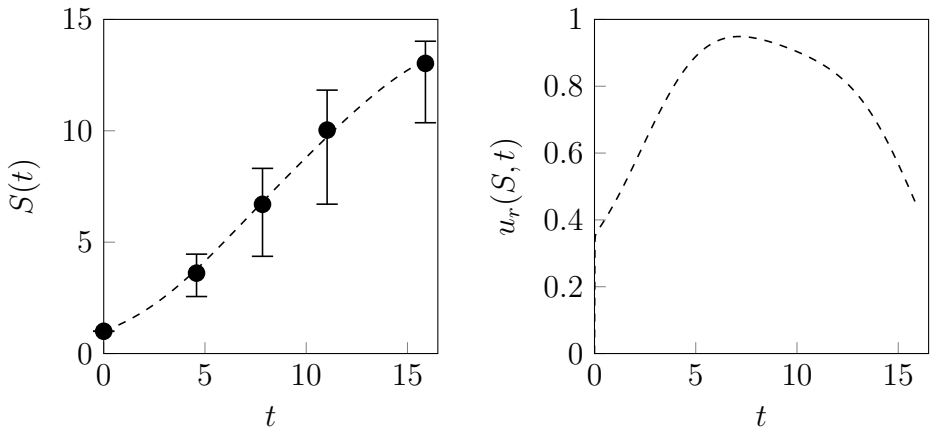

Figure 5.1: A comparison between experimental data and the numerical solution to the thin-film extensional flow model with parameters listed in Table 5.1. (a) Comparison of numerical contact line position (dashed curve), with data from the thirteen experiments. Dots indicate the mean data, and error bars indicate the experimental range. (b) Instantaneous biofilm expansion speed $u_r(S(t), t)$ in the numerical solution.

speed observed in experiments. Furthermore, by relaxing the assumption of constant expansion speed used in Chapter 3, the extensional flow model provides an even better fit to experimental data than the reaction–diffusion model. Instead of constant-speed expansion, the velocity profile in Figure 5.1b resembles the experimental results of Srinivasan, Kaplan, and Mahadevan [127] for *B. subtilis* biofilms, featuring an initial period of acceleration followed by a deceleration. A likely explanation of the acceleration observed early in

biofilm growth is that cells initially proliferate in nutrient-rich conditions. With abundant nutrients, both existing and newly-produced cells are able to proliferate, accelerating expansion. However, as time passes nutrients become depleted in the centre of the colony, as Figures 5.2e and 5.2f show. Reduced nutrient availability decreases the ability of cells to proliferate, resulting in the decrease in net biofilm growth illustrated in Figure 5.2d, and the decrease in fluid velocity observed in Figure 5.2b. This decrease in biomass creation and fluid velocity slows the expansion of the colony.

The distribution of nutrients also influences the shape a biofilm attains as is expands. As Figure 5.2a shows, our model predicts that the biofilm will expand vertically and radially when nutrients are abundant. However, biomass production occurs mostly at the leading edge when nutrients deplete in the centre of the biofilm, as Figure 5.2d illustrates. This causes the biofilm to stop thickening, and subsequent expansion is in the radial direction only. Furthermore, this corresponds to the radial fluid velocity profile (Figure 5.2b) within the biofilm becoming more localised to the leading edge. The model even predicts that the height at the centre of the biofilm will begin to decrease, which occurs when radial advection exceeds the net fluid production. Our results are qualitatively similar to results of other thin-film models [52, 127, 129]. In these models, nutrient limitation drives a transition from bulk growth to an edge regime, in which growth only occurs close to the contact line.

Finally, Figure 5.2c shows that the cell volume fraction quickly settles towards $\phi_n = 0.9$ in our numerical solutions. This is expected, because we used the observation that mature yeast mats contain approximately 90% living cells by volume to estimate Ψ_m. We also assumed $\Psi_d = 0$, which prevents existing cells from degrading to extracellular material.

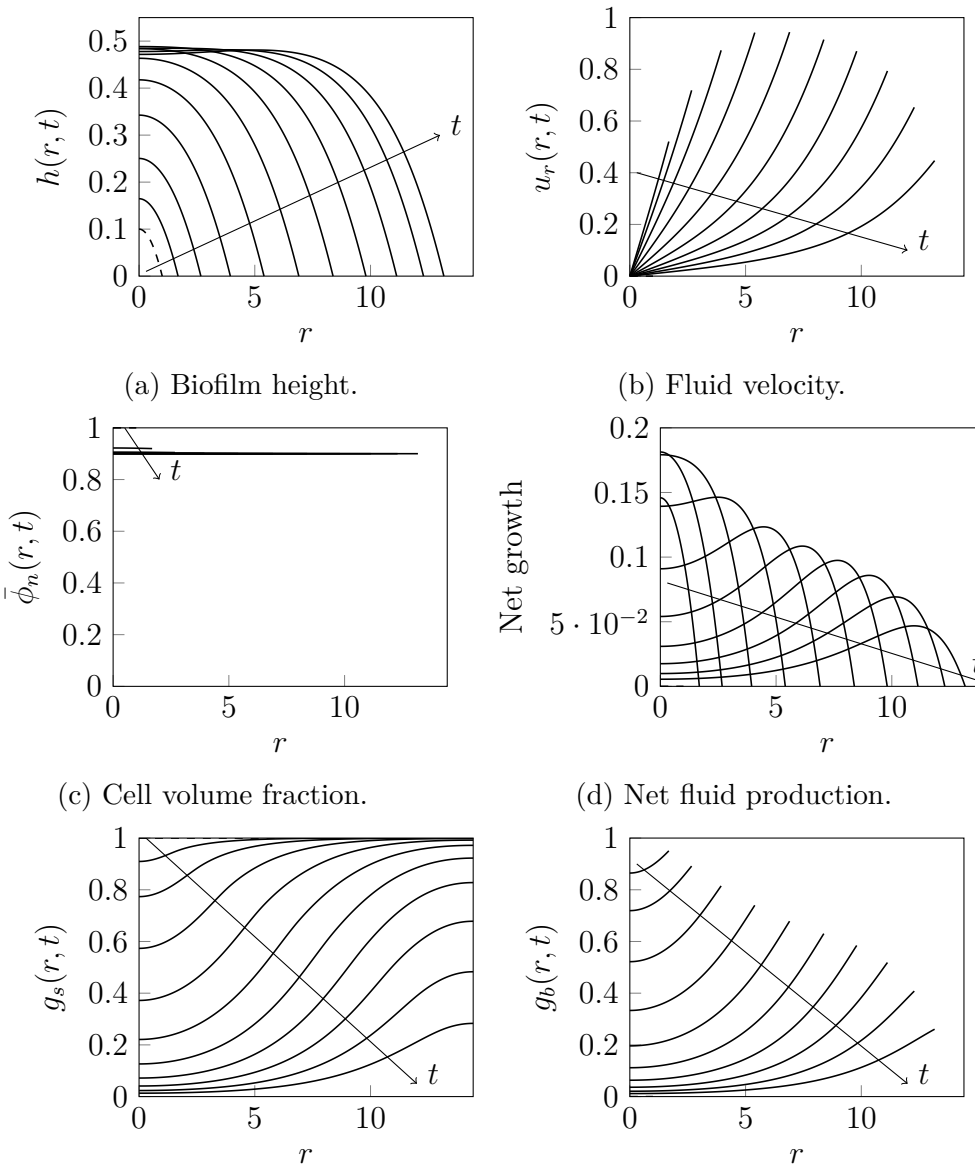

(a) Biofilm height.

(b) Fluid velocity.

(c) Cell volume fraction.

(d) Net fluid production.

(e) Nutrient concentration (substratum).

(f) Nutrient concentration (biofilm).

Figure 5.2: The numerical solution with the parameters listed in Table 5.1. Solutions are plotted for $t \in [0, 15.9]$, and $r \in [0, 14.4]$, at ten equispaced time intervals. Dashed curves indicate initial conditions. Arrows indicate the direction of increasing time.

5.2.2 The Effect of Model Parameters on Biofilm Size

In §5.2, we considered one set of parameters relevant to the *S. cerevisiae* mat formation experiments. However, biofilms can grow in vastly different ways depending on the microbial species and environmental conditions. For example, although the ECM fraction is approximately 10% in *S. cerevisiae* mats, it is commonly 50–90% in bacterial biofilms [54], and can be as high as 95–98% [21, 55]. Since some bacterial biofilms are also hypothesised to expand by sliding motility [50], we aim to predict biofilm growth in different conditions.

To investigate the effect of deviations from our experimental parameters on expansion, we perform a local sensitivity analysis. For each set of solutions, we use the default parameters given in Table 5.1, and vary one parameter at a time over a realistic range. We then compute numerical solutions and measure the predicted biofilm size after five days of growth. This enables us to isolate the effect of each parameter on biofilm size. Of the dimensionless parameters, we found that the Petri dish size R and surface tension coefficient γ^* had negligible effect on the biofilm size. Sensitivity results for other parameters are shown in Figure 5.3. In Figure 5.3a, we vary the dimensional cell production rate ψ_n, which is otherwise scaled out of the dimensionless model. When changing ψ_n, we update the values for D, Pe, and T, all of which depend on ψ_n. This enables us to directly compare the effects of cell production rate, ECM production rate, and cell death rate.

Overall, a vast range of behaviour is possible while keeping dimensionless parameters within one order of unity. Figures 5.3a and 5.3b describe how fluid production and cell death affect expansion speed. As expected, higher rates of fluid (either living cells or ECM) production result in larger biofilms. However, unlike the production of ECM, the production of new cells facilitates increased cell proliferation in the future, and therefore cell production rate is a stronger determinant of size than ECM production rate. This further justifies

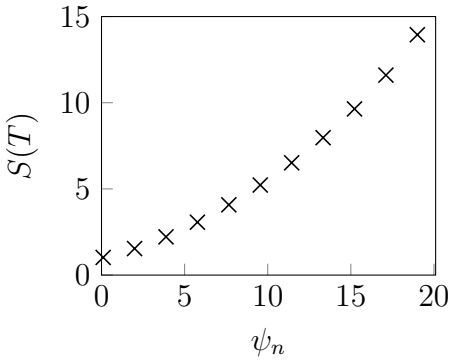

(a) Cell production rate.

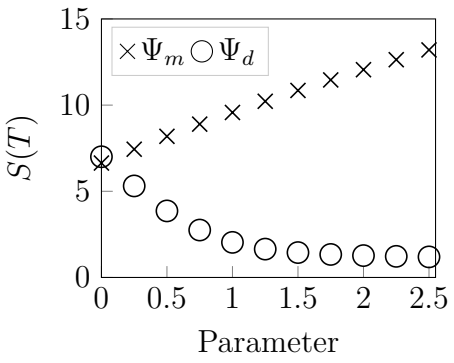

(b) Source term parameters.

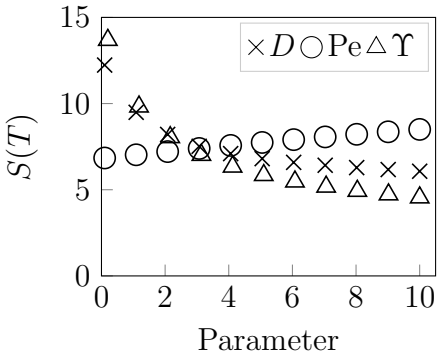

(c) Nutrient parameters.

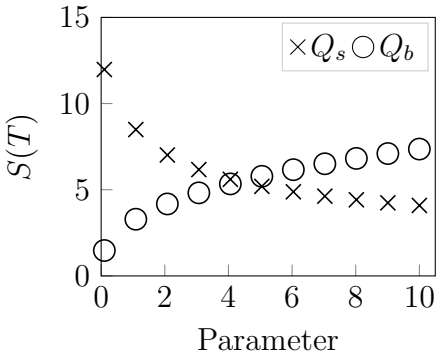

(d) Mass transfer parameters.

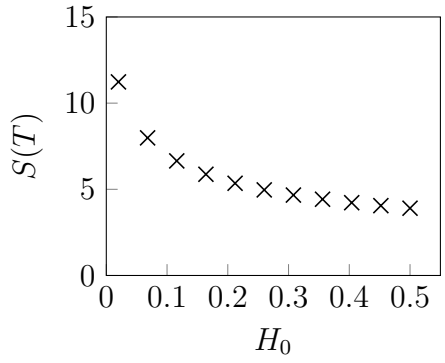

(e) Initial biofilm height.

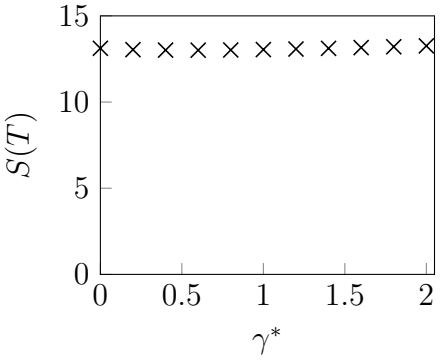

(f) Surface tension coefficient.

Figure 5.3: The effect of model parameters on predicted biofilm radius, $S(T)$, after five days of growth. In each solution, we use the initial conditions (5.2). When held constant, all parameters (excepting T) are as in Table 5.1.

using the extensional flow model to investigate sliding motility, in which cell proliferation primarily drives expansion. In addition, Figure 5.3b shows that increasing the cell death rate decreases biofilm size, which is expected because fewer living cells are subsequently available to proliferate.

The remaining plots in Figure 5.3 show how the dimensionless parameters affect expansion speed and final size. The effect of nutrient diffusion and consumption is revealed in Figure 5.3c. Increasing the nutrient diffusion coefficient, D, will result in more uniform nutrient concentrations across the Petri dish than seen in Figures 5.2e and 5.2f. This promotes thickening of the biofilm as opposed to radial expansion. In addition, increasing the nutrient consumption rate, Υ, results in larger quantities of nutrient being required to produce a new cell, thereby slowing expansion. The Péclet number indicates how readily nutrients advect radially with the extracellular fluid. Larger values of Pe increase nutrient supply to the proliferating rim, enabling faster expansion. However, the slender biofilm and substratum geometries are such that nutrient availability depends more strongly on uptake from the substratum than advection in the biofilm. Therefore, the Péclet number has a weaker effect on expansion speed than the nutrient depletion and uptake rates, as Figure 5.3d illustrates. Larger values of nutrient depletion rate, Q_s, decrease nutrient availability to the cells, which slows expansion. Conversely, increasing nutrient uptake rate, Q_b, aids cell production, because more nutrients become available for consumption. Finally, Figure 5.3e shows that thinner biofilms tend to expand faster than thicker ones. This is because cell proliferation causes radial expansion in thin biofilms, whereas in thicker biofilms cell proliferation proportionately favours vertical growth.

Overall, in the extensional flow regime several physical parameters affect the ability of cells (particularly those close to the leading edge) to proliferate, and hence expansion speed. This contrasts with the reaction–diffusion model of Chapter 3, in which the expansion speed depended uniquely on a single parameter, the diffusion ratio. These findings are relevant to clinical settings, where expansion speed correlates with the invasiveness of infection. Our

model describes environmental conditions that result in decreased expansion speed.

5.2.3 Ridge Formation and Surface Tension Effects

In addition to the size, our model also predicts the shape a growing biofilm will attain. Although not observed in our *S. cerevisiae* mat formation experiments, some bacterial biofilms [127] and yeast colony biofilms [46] develop a ridge structure. An example of this in yeast is shown in Figure 5.4. To observe

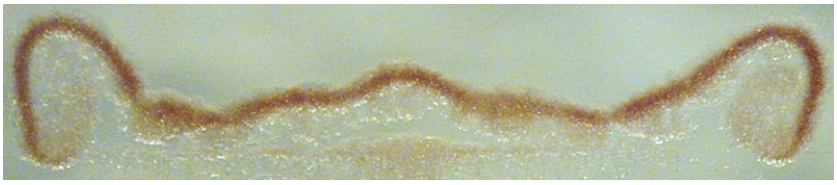

Figure 5.4: A biofilm of the BR-F wild strain of *S. cerevisiae*, displaying ridge formation. Image reproduced from Maršíková et al. [46] under the Creative Commons Attribution 4.0 International License (CC BY 4.0), https://creativecommons.org/licenses/by/4.0/.

ridge formation in our model, we compute a numerical solution with the experimental parameters given in Table 5.1, except with $D = 1.5$, $\Upsilon = 10$, and $\mathrm{Pe} = 10$. Compared to the experimental parameters, this combination of decreased nutrient diffusion, and increased nutrient consumption and advection leads to faster nutrient depletion behind the proliferating rim. Cell proliferation then becomes concentrated close to the leading edge, which in conjunction with increased advection of mass outwards from the biofilm centre, creates the noticeable ridge seen in Figure 5.5a. To quantify ridge formation, we compute the normalised ridge height

$$I_r(t) = \max_{r \in [0, S(t)]} \frac{h(r,t)}{h(0,t)}, \tag{5.14}$$

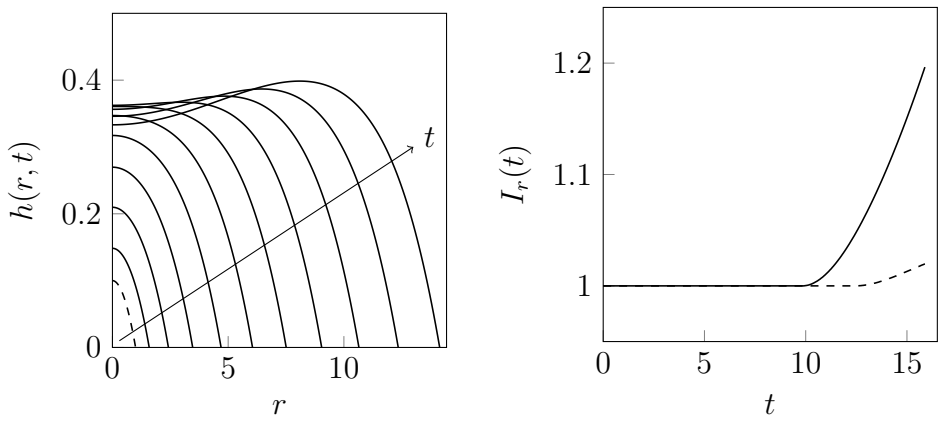

(a) (b)

Figure 5.5: The numerical solution with $D = 1.5$, $\Upsilon = 10$, and $\mathrm{Pe} = 10$, with other parameters as in Table 5.1. (a) Biofilm height. (b) Normalised ridge height (solid line), compared with the experimental case (dashed line).

and compare with the experimental case. Figure 5.5b shows the normalised ridge height increasing faster than the base solution with experimental parameters. Although we do not investigate the mechanisms of ridge formation in detail, our model shows that interplay between sliding motility and nutrient-limited growth can initiate ridge formation. Importantly, this can occur without the need to invoke other mechanisms such as osmotic swelling.

Finally, we investigate the effect of the surface tension coefficient on the biofilm shape. We achieve this by computing numerical solutions with the parameters as in Figure 5.5, varying the surface coefficient over the range $\gamma^* \in [0, 2]$. These results are shown in Figure 5.6. We observe that increasing the surface tension coefficient reduces the extent of the ridge, and that $\gamma^* = 2$ is sufficient to prevent ridge formation. As surface tension appears only in the momentum equation (5.1f) and boundary condition (5.9), we expect the fluid velocity profile to explain this behaviour. Figure 5.6b shows that increasing γ^* decreases the radial velocity near the centre of the biofilm. This decreases movement of fluid and nutrients towards the leading edge of the biofilm, thereby inhibiting ridge formation.

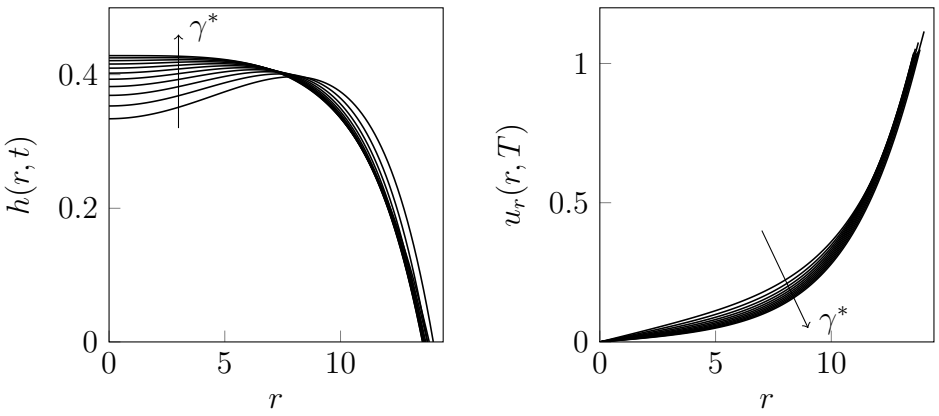

(a) Biofilm height.

(b) Fluid velocity.

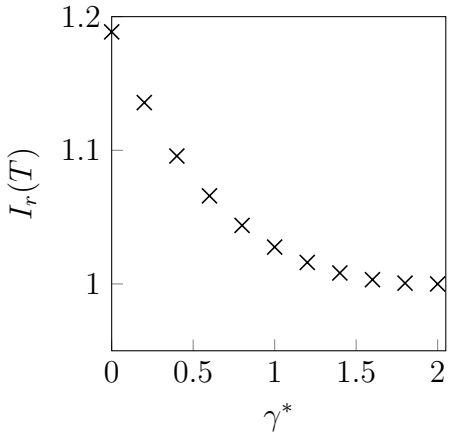

(c) Normalised ridge height.

Figure 5.6: Numerical solutions with parameters (excepting γ^*) as in Figure 5.5, plotted for $\gamma^* \in [0, 2]$, at increments of $\gamma^* = 0.2$.

5.3 Summary

In this chapter, we used the extensional flow regime of the thin-film model derived in Chapter 4 to investigate the hypothesis that sliding motility is the mechanism by which yeast biofilms expand. We considered the one-dimensional axisymmetric form of the model, which is sufficient to capture the speed of expansion and biofilm profile. Using the experimental design, we estimated all model parameters except ψ_n, the cell production rate, and η, the nutrient consumption rate. Fitting these two parameters to the experimental data for biofilm size, we obtained excellent agreement between the model and data. Since all estimated parameters were $\mathcal{O}(1)$, we concluded that sliding motility is a potential explanation for yeast biofilm expansion. These results improved on the reaction–diffusion model proposed in Chapter 3, as they predicted a non-constant expansion speed.

Comparison with experiments established that our extensional flow model can predict yeast biofilm expansion. Based on this finding, we used the model to investigate the effect of deviations from the experimental parameters on expansion speed. We found that the cell production rate had the strongest positive effect on biofilm size, which was expected as sliding motility is a form of passive expansion driven by cell proliferation. In addition, we found that increasing nutrient availability, especially close to the leading edge, enabled faster expansion. This could be achieved by increasing the nutrient uptake rate, decreasing the rates of nutrient diffusion, depletion and consumption, or decreasing the initial biofilm thickness. This sensitivity analysis revealed mechanical effects that inhibit or enhance biofilm growth.

Using different parameters, our extensional flow model predicted ridge formation close to the leading edge. We did not observe ridge formation in *S. cerevisiae* experiments, but it has been observed for other microbial colonies. Although it had negligible effect on biofilm size, we found that the surface tension coefficient, γ^*, influenced the biofilm shape. Larger values of γ^* decreased the radial velocity close to the centre of the biofilm, which

inhibited ridge formation.

Analysis of the axisymmetric form of our thin-film extensional flow model for sliding motility showed that the model can explain the speed of expansion and biofilm shape observed in experiments. The full two-dimensional model derived in §4.2 provides an opportunity for future work. Since the model is more complicated than the reaction–diffusion system analysed in Chapter 3, we have not yet considered whether the extensional flow model can predict petal formation. In the future, we could investigate the linear stability of one-dimensional model solutions to azimuthal perturbations. We could then combine these results with numerical solutions to the two-dimensional model to determine whether sliding motility is a possible explanation for the floral morphology.

Chapter 6

Lubrication Regime: Strong Biofilm–Substratum Adhesion

In this chapter, we use the lubrication model to investigate growth of biofilms that adhere strongly to the substratum, where surface tension and pressure are assumed large. Our analysis takes a similar form to Chapter 5, in which we compute numerical solutions to the axisymmetric model and investigate the effect of parameters on biofilm size and shape. In the lubrication regime, the axisymmetric model is two-dimensional. This is because the leading-order cell volume fraction, ϕ_n, and radial fluid velocity, u_r, depend on z. This was not true in the extensional flow regime. Although the two-dimensional model enables us to predict the spatial variation in ϕ_n and u_r, it is computationally expensive. Since ϕ_n exhibits weak dependence with z, we also consider a simplification to the model where we assume that cell volume fraction is independent of z. The resulting one-dimensional model produces qualitatively similar results to the full model, and represents an alternative that is more analytically tractable and computationally efficient.

6.1 Two-Dimensional Axisymmetric Model

To investigate the effect of biofilm mechanics, we analyse the thin-film models in axisymmetric form. Unlike the extensional regime considered in Chapter 5, in the lubrication regime the leading-order cell volume fraction and fluid velocities depend on z. Hence, when we neglect azimuthal dependence, the full lubrication model (4.85) reduces to the two-dimensional axisymmetric model

$$\frac{\partial h}{\partial t}+\frac{\gamma^*}{3r}\frac{\partial}{\partial r}\left\{rh^3\frac{\partial}{\partial r}\left[\frac{1}{r}\frac{\partial}{\partial r}\left(r\frac{\partial h}{\partial r}\right)\right]\right\}=(1+\Psi_m)\,\bar{\phi}_n g_b h, \tag{6.1a}$$

$$\begin{aligned}\frac{\partial \phi_n}{\partial t}-\frac{\gamma^* z}{r}\frac{\partial}{\partial r}\left\{r\phi_n\left(\frac{z}{2}-h\right)\frac{\partial}{\partial r}\left[\frac{1}{r}\frac{\partial}{\partial r}\left(r\frac{\partial h}{\partial r}\right)\right]\right\}\\ +\frac{\partial}{\partial z}\left(u_z\phi_n\right)=\phi_n g_b-\Psi_d\phi_n,\end{aligned} \tag{6.1b}$$

$$\bar{\phi}_n=\frac{1}{h}\int_0^h \phi_n\,\mathrm{d}z, \tag{6.1c}$$

$$\begin{aligned}u_z=&\left(1+\Psi_m\right)g_b\int_0^z\phi_n\,\mathrm{d}\tilde{z}\\ &+\frac{\gamma^*}{r}\frac{\partial}{\partial r}\left\{\frac{rz^2}{2}\left(\frac{z}{3}-h\right)\frac{\partial}{\partial r}\left[\frac{1}{r}\frac{\partial}{\partial r}\left(r\frac{\partial h}{\partial r}\right)\right]\right\},\end{aligned} \tag{6.1d}$$

$$\frac{\partial g_s}{\partial t}=\frac{D}{r}\frac{\partial}{\partial r}\left(r\frac{\partial g_s}{\partial r}\right)-DQ_s\left(g_s-g_b\right), \tag{6.1e}$$

$$\begin{aligned}\mathrm{Pe}h\frac{\partial g_b}{\partial t}=&\frac{1}{r}\frac{\partial}{\partial r}\left(rh\frac{\partial g_b}{\partial r}\right)+Q_b\left(g_s-g_b\right)-\Upsilon\bar{\phi}_n g_b h\\ &+\frac{\mathrm{Pe}\gamma^*}{r}\frac{\partial}{\partial r}\left\{rg_b\frac{\partial}{\partial r}\left[\frac{1}{r}\frac{\partial}{\partial r}\left(r\frac{\partial h}{\partial r}\right)\right]\int_0^h z\left(\frac{z}{2}-h\right)\left(1-\phi_n\right)\,\mathrm{d}z\right\}.\end{aligned} \tag{6.1f}$$

The system (6.1) constitutes the lubrication model for the biofilm height $h(r,t)$, cell volume fraction $\phi_n(r,z,t)$, fluid velocity $u_z(r,z,t)$, and nutrient concentrations $g_s(r,t)$ and $g_b(r,t)$. We compute solutions to this model subject to appropriate regularisation, initial conditions, and boundary conditions, which we detail below.

6.1.1 Regularisation

Much like in the extensional flow regime, we are interested in computing numerical solutions in which there is non-zero radial velocity close to the biofilm–substratum interface, which enables the biofilm to expand. However, an important assumption in the lubrication regime is that the biofilm adheres strongly to the substratum. In the general slip conditions (4.17), this involves assuming that the adhesion strength of each phase $\lambda_\alpha \to \infty$, which gives rise to the standard no-slip condition on the biofilm–substratum interface. However, applying the no-slip condition means that the contact line cannot move, and hence the biofilm cannot expand. This apparent paradox is commonly encountered in models involving a generalised lubrication equation [120, 127, 155–157], and is resolved by applying a suitable regularisation.

One method for dealing with moving contact lines is to introduce a precursor film [156]. This is a thin layer of fluid with thickness $b \ll 1$ existing ahead of the biofilm front. Physically, this represents the characteristic scale of surface roughness in the agar [155]. Following Ward and King [120], we adopt this precursor film to regularise the model. We assume that the precursor layer consists entirely of passive fluid (no cells), and that nutrient uptake or consumption does not occur in the precursor film. Mathematically, this involves modifying the model equations to extinguish the relevant terms wherever $h \leq h^*$, for some $h^* \geq b$ [156]. We write the regularised model as

$$\begin{aligned} &\frac{\partial h}{\partial t} + \frac{\gamma^*}{3r}\frac{\partial}{\partial r}\left\{rh^3\frac{\partial}{\partial r}\left[\frac{1}{r}\frac{\partial}{\partial r}\left(r\frac{\partial h}{\partial r}\right)\right]\right\} \\ &\qquad = H\left(h-h^*\right)\left[\left(1+\Psi_m\right)\bar{\phi}_n g_b h\right], \end{aligned} \tag{6.2a}$$

$$\begin{aligned} &\frac{\partial \phi_n}{\partial t} - \frac{\gamma^* z}{r}\frac{\partial}{\partial r}\left\{r\phi_n\left(\frac{z}{2}-h\right)\frac{\partial}{\partial r}\left[\frac{1}{r}\frac{\partial}{\partial r}\left(r\frac{\partial h}{\partial r}\right)\right]\right\} \\ &\qquad + \frac{\partial}{\partial z}\left(u_z\phi_n\right) = \phi_n g_b - \Psi_d\phi_n, \end{aligned} \tag{6.2b}$$

$$\bar{\phi}_n = \frac{1}{h}\int_0^h \phi_n \,\mathrm{d}z, \tag{6.2c}$$

$$u_z = (1+\Psi_m)\, g_b \int_0^z \phi_n \,\mathrm{d}\tilde{z} + \frac{\gamma^*}{r}\frac{\partial}{\partial r}\left\{\frac{rz^2}{2}\left(\frac{z}{3}-h\right)\frac{\partial}{\partial r}\left[\frac{1}{r}\frac{\partial}{\partial r}\left(r\frac{\partial h}{\partial r}\right)\right]\right\}, \tag{6.2d}$$

$$\frac{\partial g_s}{\partial t} = \frac{D}{r}\frac{\partial}{\partial r}\left(r\frac{\partial g_s}{\partial r}\right) - H\left(h-h^*\right)\left[DQ_s\left(g_s-g_b\right)\right], \tag{6.2e}$$

$$\mathrm{Pe}h\frac{\partial g_b}{\partial t} = H\left(h-h^*\right)\left[\frac{1}{r}\frac{\partial}{\partial r}\left(rh\frac{\partial g_b}{\partial r}\right) + Q_b\left(g_s-g_b\right) - \Upsilon\bar{\phi}_n g_b h + \frac{\mathrm{Pe}\gamma^*}{r}\frac{\partial}{\partial r}\left\{rg_b\frac{\partial}{\partial r}\left[\frac{1}{r}\frac{\partial}{\partial r}\left(r\frac{\partial h}{\partial r}\right)\right]\int_0^h z\left(\frac{z}{2}-h\right)\left(1-\phi_n\right)\,\mathrm{d}z\right\}\right], \tag{6.2f}$$

where H is the Heaviside step function. The formulation (6.2) assumes that cells are not present without sufficient biofilm thickness to support them, and that the biofilm cannot take up nutrients in regions with no cells. The constant h^* represents the dimensionless thickness of a single cell. Given that the diameter of yeast cells is approximately 4 µm, and the characteristic biofilm height is approximately 2 mm, the value $h^* = 0.002$ is appropriate. Computing numerical solutions of the lubrication model then involves solving the regularised system (6.2), subject to appropriate initial and boundary conditions.

6.1.2 Initial and Boundary Conditions

We obtain the first initial conditions from the observation that the Petri dish is initially filled uniformly with nutrients, and that no nutrients are yet present in the biofilm. For $h(r,0)$, we require a function such that there is a defined region with $h = b$ ahead of the biofilm, and that relevant higher derivatives of h with respect to r are continuous throughout the entire domain. For this purpose, we modify the parabolic initial condition of the extensional flow case in the same way as Ward and King [120]. Finally, for the cell volume fraction $\phi_n(r,z,0)$, we choose a polynomial form such that $\phi_n = 0$ in the precursor film, and that the first derivatives of ϕ_n with respect to r and z are

continuous throughout the domain. The initial conditions are then

$$h\left(r,0\right) = b + \left(H_0 - b\right)\left(1 - r^2\right)^4 H\left(r-1\right), \tag{6.3a}$$

$$\phi_n(r,z,0) = \left(3z^2 - 2z^3\right)\left(1 - 3r^2 + 2r^3\right) H\left(r-1\right), \tag{6.3b}$$

$$g_s\left(r,0\right) = 1, \tag{6.3c}$$

$$g_b\left(r,0\right) = 0, \tag{6.3d}$$

which sets the initial contact line position at $r = 1$, and satisfies $h = b$ for $r \geq 1$ and $\phi_n = 0$ for $r \geq 1$.

For the boundary conditions, as with the extensional flow regime we assume that we have radial symmetry at $r = 0$ in all of the variables. Therefore, we obtain the conditions

$$\left.\frac{\partial h}{\partial r}\right|_{(0,t)} = 0, \quad \left.\frac{\partial \phi_n}{\partial r}\right|_{(0,z,t)} = 0, \quad \left.\frac{\partial g_s}{\partial r}\right|_{(0,t)} = 0, \quad \left.\frac{\partial g_b}{\partial r}\right|_{(0,t)} = 0. \tag{6.4}$$

In addition, just as with the extensional flow regime, we also assume that the centre of the biofilm is fixed, and that fluid cannot cross $r = 0$. The radial component of the fluid velocity must then be zero there, that is $u_r\left(0,z,t\right) = 0$. Using the explicit form (4.74a), this gives rise to an additional boundary condition for the biofilm height,

$$\frac{\partial}{\partial r}\left[\frac{1}{r}\frac{\partial}{\partial r}\left(r\frac{\partial h}{\partial r}\right)\right] \to 0 \quad \text{as} \quad r \to 0. \tag{6.5}$$

To remove the singularity as $r \to 0$, we expand (6.5), which gives

$$\frac{\partial^3 h}{\partial r^3} + \frac{1}{r}\frac{\partial^2 h}{\partial r^2} - \frac{1}{r^2}\frac{\partial h}{\partial r} \to 0 \quad \text{as} \quad r \to 0. \tag{6.6}$$

For this to be well defined, we require this limit to exist and be finite. Using L'Hôpital's rule, we obtain (where primes denote differentiation)

$$\lim_{r\to 0}\frac{rh''(r) - h'(r)}{r^2} = \lim_{r\to 0}\frac{rh'''(r) + h''(r) - h''(r)}{2r} = \frac{h'''(r)}{2} \tag{6.7}$$

and therefore we can re-write the boundary condition (6.5) as

$$\left.\frac{\partial^3 h}{\partial r^3}\right|_{(0,t)} = 0. \tag{6.8}$$

At the edge of the Petri dish, we impose no-flux conditions for the nutrient concentrations in both the substratum and biofilm. Owing to the precursor regularisation, we also have that the biofilm height is fixed at $h = b$, and that the precursor film has a constant height over its extent. This yields the conditions

$$\left.\frac{\partial g_s}{\partial r}\right|_{(R,t)} = 0, \quad \left.\frac{\partial g_b}{\partial r}\right|_{(R,t)} = 0, \quad h(R,t) = b, \quad \left.\frac{\partial h}{\partial r}\right|_{(R,t)} = 0. \tag{6.9}$$

We now have a closed, axisymmetric system of model equations (6.2) that we can solve subject to the initial conditions (6.3), and boundary conditions (6.4), (6.8) and (6.9).

6.1.3 Numerical Solutions

We now undertake numerical solution of the regularised axisymmetric model in the lubrication regime. A major task in this process is solving the fourth-order generalised lubrication equation (6.2a) for the biofilm height. We solve this equation using a non-linear Crank–Nicolson scheme [158]. To validate the scheme and ensure convergence, we compare results with the no-slip model of Ward and King [120], in which cell volume fraction is considered constant. We then proceed to solving the full two-dimensional axisymmetric model. The main difficulty here arises in solving (6.2b) for the cell volume fraction. Since this equation is two-dimensional, the numerical method is computationally expensive. Furthermore, large gradients in ϕ_n emerge in thin regions close to $z = 0$. A large number of grid points in the thin region is required to resolve these gradients, which otherwise introduce spurious numerical oscillations into the solution. This motivates our work on a one-dimensional simplified

model in §6.2.

Constant Cell Volume Fraction

Before solving the full two-dimensional lubrication model (6.2), we first consider a simplified case in which ϕ_n is a prescribed constant, instead of a function of space and time. Although this is not necessarily the case in the full model, our motivation for computing these solutions is two-fold. First, this regime enables comparison to the results of Ward and King [120], who computed numerical solutions in Cartesian geometry. This provides a means of investigating the effect of radial geometry on the solution. Secondly, these solutions will enable us to validate the numerical method used to solve the generalised lubrication equation for h, and ensure convergence of the numerical method.

Re-writing the no-slip model of Ward and King [120] in radial geometry, we obtain

$$\frac{\partial h}{\partial t} + \frac{\gamma^*}{3r}\frac{\partial}{\partial r}\left\{rh^3\frac{\partial}{\partial r}\left[\frac{1}{r}\frac{\partial}{\partial r}\left(r\frac{\partial h}{\partial r}\right)\right]\right\} = J. \tag{6.10}$$

This is of the same form as the generalised lubrication equation (6.2a), except Ward and King [120] use the source term

$$J = H\left(h - h^*\right)\left[\frac{1}{\sqrt{\sigma}}\tanh\left(\sqrt{\sigma}h\right) - \rho h\right], \tag{6.11}$$

where $\sigma = \Upsilon/\varepsilon^2$, and ρ is a parameter that encapsulates cell death. To compare our radial model with the results of Ward and King [120], we compute a numerical solution to (6.10) with (6.11). Our numerical method is a fully non-linear Crank–Nicolson scheme incorporating Newton iteration for non-linear terms in h. We found this method to produce more accurate results than a linearised Crank–Nicolson scheme. Therefore, throughout this chapter we will use this method whenever the generalised lubrication equation (6.2a) arises. Full details on the numerical scheme, including convergence tests with space and time, are provided in Appendix B.3.1.

In the numerical solution, we use the same values of ρ, σ, and γ^* as Ward and King [120], and found that H_0 and h^* had negligible effect on the solution. This solution is shown in Figure 6.1. The solution develops in a

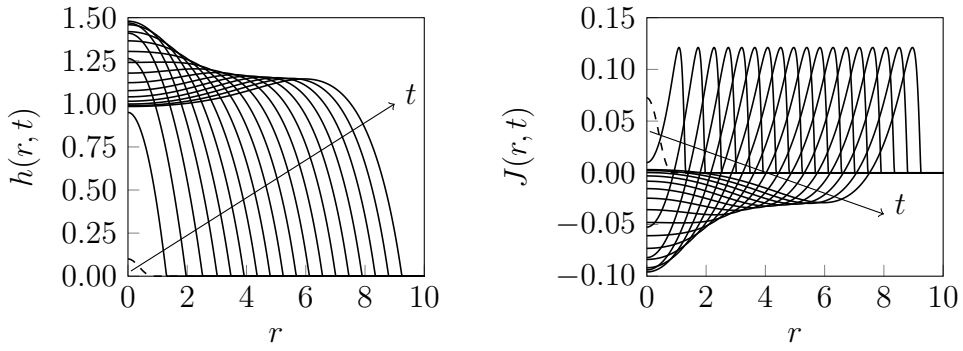

(a) Biofilm height, $h(r,t)$.

(b) Net growth, $J(r,t)$.

Figure 6.1: Numerical solution of (6.10), with $\rho = 0.2$, $\sigma = 24.995$, $\gamma^* = 1$, $h^* = 0.002$, and $b = 1 \times 10^{-4}$. The initial condition is $h(r,0) = b + (H_0 - b)(1 - r^2)^4 H(r-1)$, and the solution is computed for $r \in [0, 10]$ and $t \in [0, 180]$. The profiles are plotted at increments of $t = 10$, where the dashed curve denotes the initial conditions and the arrow indicates the direction of increasing time.

similar way to Figure 4 in the paper by Ward and King [120]. Initially, the biofilm grows in both the radial and vertical directions, before the height in the centre of the biofilm settles to $h = 1$. At the leading edge, a ridge forms and the biofilm appears to approach a constant expansion speed as its radius increases. Therefore, numerical solutions in radial geometry produce the same qualitative behaviour as the planar solutions of Ward and King [120].

Full Model

We now proceed to solving the full two-dimensional multi-phase model in the lubrication regime, (6.2)–(6.4), (6.8) and (6.9). Compared to the model of Ward and King [120], our model introduces a depleting nutrient supply in the substratum, and tracks how the volume fractions of cells and extracellular fluid change with space and time. As a result, the numerical method is more complicated. Most notably, the equation for the cell volume fraction (6.2b)

needs to be solved on the moving two-dimensional domain $0 < r < R$, and $0 < z < h(r,t)$. For computational convenience, we make a change of variables to map the domain to a rectangle with unit height. We then use a Crank–Nicolson scheme to solve (6.2b), and solve (6.2e) and (6.2f) for the nutrient concentrations using similar methods to those used for the extensional flow regime. Where necessary, we compute the integrals appearing in (6.2c), (6.2d) and (6.2f) using the trapezoidal rule. Full details of the numerical scheme are provided in Appendix B.3.2.

We first select a default set of model parameters that we will use throughout the numerical solutions in the lubrication regime. In all solutions, we choose a dimensional cell production rate of $\psi_n = 50\,\mathrm{mm}^2 \cdot \mathrm{g}^{-1} \cdot \mathrm{min}^{-1}$. As the surface tension coefficient is difficult to determine from experiments, we use $\gamma^* = 1$. We also choose $R = 10$ and $T = 50$, which provide suitable length and time scales. All other dimensional parameters are the same experimental estimates from the extensional flow model, described in §5.1.2. Although we do not believe that the lubrication regime is directly applicable to *S. cerevisiae* experiments, this choice of values facilitates comparison with the results of Chapter 5 and gives $\mathcal{O}(1)$ dimensionless parameters. We list these parameters in Table 6.1. The numerical solution to the two-dimensional axisymmetric

Table 6.1: Dimensionless parameters for the thin-film lubrication model.

Parameter	Value	Parameter	Value
H_0	0.1	D	1.05
Ψ_m	0.111	Pe	3.94
Ψ_d	0	Υ	3.15
R	10	Q_b	8.65
T	50	Q_s	2.09
γ^*	1	h^*	0.002

model with these parameters is shown in Figure 6.2 and 6.3.

Comparing Figure 6.2 to the results in Figure 6.1 reveals how nutrient

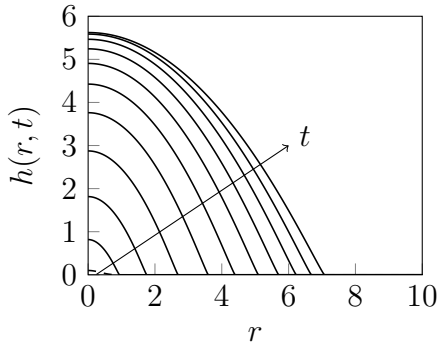

(a) Biofilm height.

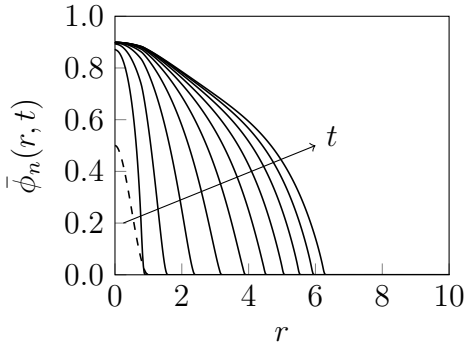

(b) Depth-averaged cell volume fraction.

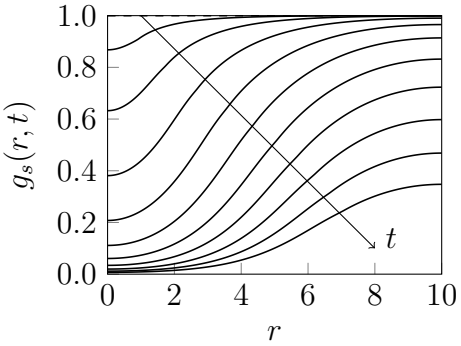

(c) Nutrient concentration in the substratum.

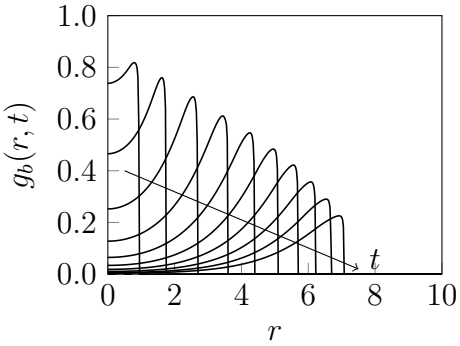

(d) Nutrient concentration in the biofilm.

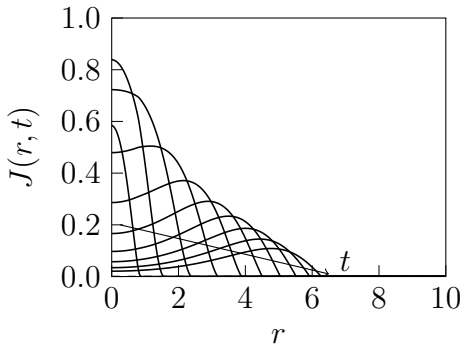

(e) Net biofilm growth.

Figure 6.2: Numerical solution of the full thin-film lubrication model, with $\psi_n = 50$, $\gamma^* = 1$, $h^* = 0.002$, and $b = 1 \times 10^{-4}$. The initial conditions are (6.3) and the solution is computed with $N_r = 2001$, $N_z = 1001$, and $N_t = 40001$, for $r \in [0, 10]$ and $t \in [0, 50]$. Where visible, the dashed curves represent the initial conditions, and the arrows indicate the direction of increasing time.

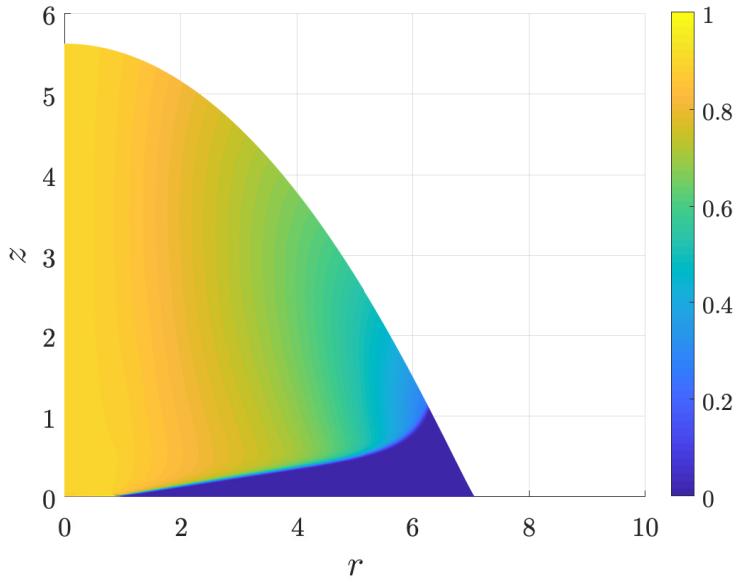

(a) Cell volume fraction, $\phi_n(r, z, T)$.

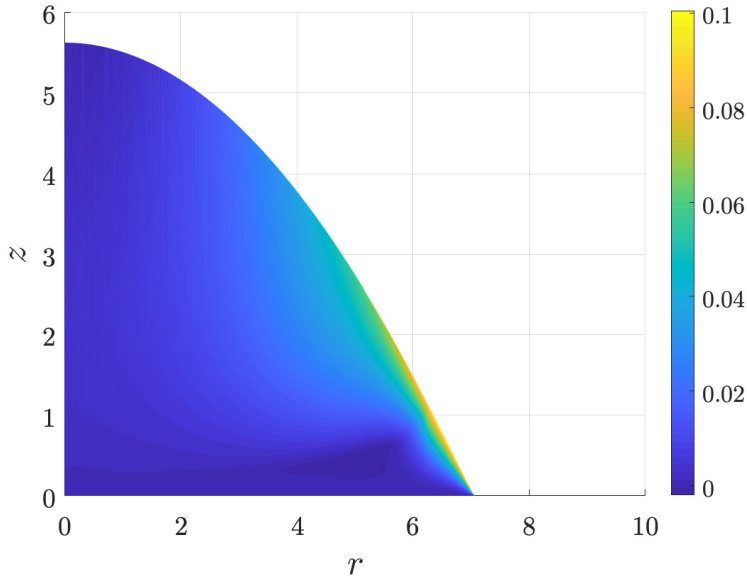

(b) Fluid velocity $u_z(r, z, T)$.

Figure 6.3: Numerical solution for $\phi_n(r, z, T)$ and $u_z(r, z, T)$ in the full thin-film lubrication model.

limitation and non-constant cell volume fraction affect the evolution of the biofilm. A notable change is that here we observe a non-constant expansion speed, which is caused by nutrient limitation. Initially, biofilm expansion is comparatively fast due to the presence of abundant nutrients. Expansion then decelerates as nutrients deplete. This behaviour is to be expected, because in our model the net biofilm growth, given by the source term $J(r,t)$, is proportional to g_b. As Figures 6.2d and 6.2e illustrate, both of these decrease with time. In addition to the decelerating expansion, Figure 6.2a shows that nutrient distribution affects the biofilm shape. With the depleting nutrient, the biofilm grows faster in the vertical direction, and attains a thicker shape to that seen in Figure 6.1a. A possible reason for this is that the source term in (6.1a) does not admit an equilibrium height, whereas (6.11) guarantees that $h(0) = 1$ is eventually attained.

Figure 6.3a illustrates the spatial dependence of the cell volume fraction ϕ_n at $t = 50$. The cell volume fraction distribution shown in Figure 6.3a depends on the radial velocity component, u_r, which in axisymmetric geometry becomes

$$u_r = -\gamma^* z \left(\frac{z}{2} - h\right) \frac{\partial}{\partial r}\left[\frac{1}{r}\frac{\partial}{\partial r}\left(r\frac{\partial h}{\partial r}\right)\right]. \tag{6.12}$$

As we have assumed no-slip on $z = 0$, in Figure 6.3a we observe a region where $\phi_n = 0$ close to $z = 0$. This occurs because we initially assume $\phi_n = 0$ in the precursor film, and the fluid velocity components u_r and u_z ensure that no cells are present close to $z = 0$. Indeed, the radial velocity (6.12) is parabolic in z, which matches the shape of the region for which $\phi_n = 0$. The cell volume fraction profile in Figure 6.3a is therefore consistent with the mathematical model. However, we cannot confirm whether such a profile will arise in experiments, because our experiments correspond to the extensional flow regime, and not the lubrication regime.

In the full lubrication model, the vertical velocity component u_z also depends on z. On the free surface $z = h$, this velocity indicates regions of the biofilm that are changing shape. As equation (6.2d) suggests, this velocity depends on the local cell volume fraction, nutrient concentration, and the

fourth-order surface tension term. Therefore, the velocity increases due to local production of cells, or large values of surface tension. In Figure 6.3b, we observe that the largest velocities occur on the free surface close to the contact line. One possible explanation for this is that the nutrient concentration is higher close to the contact line than in the centre of the biofilm, as Figure 6.2d showed. However, since cell volume fraction is low near the contact line, the high velocity there is unlikely to be driven by cell proliferation. This suggests that surface tension plays an important role in driving biofilm expansion.

6.2 One-Dimensional Simplified Model

In Figure 6.3a, we observed that the cell volume fraction exhibited only slight dependence on z, except in a thin region close to the biofilm–substratum interface. If we assume that the cell volume fraction is independent of z, we can reduce the two-dimensional axisymmetric model to one-dimensional form, and eliminate u_z and $\bar{\phi}_n$ from the model. Previous work by Srinivasan, Kaplan, and Mahadevan [127] showed that a thin-film model that uses this assumption can reproduce experimental data for bacterial biofilm growth driven by osmotic swelling. Here, we investigate whether the same assumption is valid for expansion driven by cell proliferation and strong adhesion.

Although the assumption loses the two-dimensional structure, the one-dimensional simplification saves computational time, which is a major advantage. In addition, for some parameter values two-dimensional numerical solutions require a small grid spacing close to $z = 0$ to avoid numerical artefacts (results not shown). Since the one-dimensional solutions to follow eliminate this problem, they provide a means of validating the full two-dimensional solutions. To achieve this, we repeat the numerical results of §6.1.3 in the following sections. The one-dimensional simplified model achieves similar qualitative results to the full two-dimensional model.

6.2.1 Derivation

We first derive the one-dimensional lubrication model that arises if we assume that the cell volume fraction is independent of z. Since the equations (6.1a) and (6.1e) for h and g_s do not depend on z, they remain the same as the full model. To obtain a z-independent equation for the nutrient concentration in the biofilm, we can now evaluate the integral in (6.1f) explicitly. This yields

$$\begin{aligned} \mathrm{Pe}h\frac{\partial g_b}{\partial t} + \frac{\mathrm{Pe}\gamma^*}{3r}\frac{\partial}{\partial r}\left\{rh^3\left(1-\phi_n\right)g_b\frac{\partial}{\partial r}\left[\frac{1}{r}\frac{\partial}{\partial r}\left(r\frac{\partial h}{\partial r}\right)\right]\right\} \\ = \frac{1}{r}\frac{\partial}{\partial r}\left(rh\frac{\partial g_b}{\partial r}\right) + Q_b\left(g_s - g_b\right) - \Upsilon\bar{\phi}_n g_b h. \end{aligned} \tag{6.13}$$

The next step is to extend the thin-film modelling undertaken in §4.3 to derive a new equation for cell volume fraction, ϕ_n. As this derivation does not require higher-order correction terms, we treat each variable as leading-order, and do not return to subscript notation. To begin, we consider the leading-order mass balance equation for living cells,

$$\frac{\partial \phi_n}{\partial t} + \frac{1}{r}\frac{\partial}{\partial r}\left(ru_r\phi_n\right) + \frac{\partial}{\partial z}\left(u_z\phi_n\right) = \phi_n g_b - \Psi_d\phi_n, \tag{6.14}$$

where u_r is known explicitly by (6.12). Now that we have assumed that ϕ_n is independent of z, it is possible to simplify the model by integrating (6.14) across the biofilm depth. Doing so, we obtain

$$\int_0^h \frac{\partial \phi_n}{\partial t}\,\mathrm{d}z + \int_0^h \frac{1}{r}\frac{\partial}{\partial r}\left(ru_r\phi_n\right)\,\mathrm{d}z + \left[u_z\phi_n\right]_0^h = \left(\phi_n g_b - \Psi_d\phi_n\right)h. \tag{6.15}$$

Application of the no-penetration (4.38e) and kinematic (4.38f) boundary conditions then enable us to eliminate u_z, giving

$$\begin{aligned} \int_0^h \frac{\partial \phi_n}{\partial t}\,\mathrm{d}z + \int_0^h \frac{1}{r}\frac{\partial}{\partial r}\left(ru_r\phi_n\right)\,\mathrm{d}z \\ + \phi_n\left(\frac{\partial h}{\partial t} + u_r\frac{\partial h}{\partial r}\right) = \left(\phi_n g_b - \Psi_d\phi_n\right)h. \end{aligned} \tag{6.16}$$

Applying Leibniz's rule to the integrals in (6.16) then yields

$$\begin{aligned}\left[\frac{\partial}{\partial t}\left(\int_0^h \phi_n \,\mathrm{d}z\right) - \phi_n \frac{\partial h}{\partial t}\right] + \frac{1}{r}\left[\frac{\partial}{\partial r}\left(\int_0^h r u_r \phi_n \,\mathrm{d}z\right) - r\phi_n u_r \frac{\partial h}{\partial r}\right] \\ + \phi_n\left(\frac{\partial h}{\partial t} + u_r \frac{\partial h}{\partial r}\right) = \left(\phi_n g_b - \Psi_d \phi_n\right) h.\end{aligned} \tag{6.17}$$

Now, as we saw in the extensional flow regime, terms evaluated at the free surface arising from Leibniz's rule and the kinematic boundary condition cancel. We then obtain

$$\frac{\partial}{\partial t}\left(\int_0^h \phi_n \,\mathrm{d}z\right) + \frac{1}{r}\frac{\partial}{\partial r}\left(\int_0^h r u_r \phi_n \,\mathrm{d}z\right) = \left(\phi_n g_b - \Psi_d \phi_n\right) h. \tag{6.18}$$

As ϕ_n is now assumed to be independent of z, we can evaluate the integrals explicitly. Using the known form of u_r (6.12), we obtain the one-dimensional model equation for leading-order cell volume fraction,

$$\frac{\partial}{\partial t}\left(\phi_n h\right) + \frac{\gamma^*}{3r}\frac{\partial}{\partial r}\left\{r\phi_n h^3 \frac{\partial}{\partial r}\left[\frac{1}{r}\frac{\partial}{\partial r}\left(r\frac{\partial h}{\partial r}\right)\right]\right\} = \left(\phi_n g_b - \Psi_d \phi_n\right) h. \tag{6.19}$$

Here, like in the extensional flow regime, we can use the total fluid mass conservation equation (6.1a) to simplify (6.19). Multiplying (6.1a) by ϕ_n, we can then subtract the result from (6.19), and divide by h to obtain

$$\frac{\partial \phi_n}{\partial t} + \frac{\gamma^* h^2}{3}\frac{\partial}{\partial r}\left[\frac{1}{r}\frac{\partial}{\partial r}\left(r\frac{\partial h}{\partial r}\right)\right]\frac{\partial \phi_n}{\partial r} = \phi_n\left[g_b - \Psi_d - \left(1 + \Psi_m\right)\phi_n g_b\right]. \tag{6.20}$$

The equation (6.20) is similar to the corresponding equation in the extensional flow regime (5.1b), where in both instances the advection coefficient is given by

$$\frac{1}{h}\int_0^h u_r \,\mathrm{d}z. \tag{6.21}$$

Integrating (6.12) with respect to z confirms that this is true for (6.20).

With the leading-order equation for ϕ_n now derived, the simplified one-dimensional lubrication model now consists of the four equations (6.1a), (6.1e),

(6.13) and (6.20). To close the model, we apply the same boundary conditions (6.4), (6.8) and (6.9) as the full two-dimensional model. To enable numerical solution, we again introduce a precursor film to regularise the equations. Similar to the two-dimensional model, we then adopt the initial conditions

$$h\left(r,0\right)=b+\left(H_0-b\right)\left(1-r^2\right)^4 H\left(r-1\right), \tag{6.22a}$$

$$\phi_n(r,0)=\left(1-3r^2+2r^3\right)H\left(r-1\right), \tag{6.22b}$$

$$g_s\left(r,0\right)=1, \tag{6.22c}$$

$$g_b\left(r,0\right)=0. \tag{6.22d}$$

Numerical solution of the model then involves solving regularised forms of the model equations, given by

$$\begin{aligned}\frac{\partial h}{\partial t}+\frac{\gamma^*}{3r}\frac{\partial}{\partial r}\left\{rh^3\frac{\partial}{\partial r}\left[\frac{1}{r}\frac{\partial}{\partial r}\left(r\frac{\partial h}{\partial r}\right)\right]\right\}\\ =H\left(h-h^*\right)\left[\left(1+\Psi_m\right)\phi_n g_b h\right],\end{aligned} \tag{6.23a}$$

$$\begin{aligned}\frac{\partial \phi_n}{\partial t}+\frac{\gamma^* h^2}{3}\frac{\partial}{\partial r}\left[\frac{1}{r}\frac{\partial}{\partial r}\left(r\frac{\partial h}{\partial r}\right)\right]\frac{\partial \phi_n}{\partial r}\\ =\phi_n\left[g_b-\Psi_d-\left(1+\Psi_m\right)\phi_n g_b\right],\end{aligned} \tag{6.23b}$$

$$\frac{\partial g_s}{\partial t}=\frac{D}{r}\frac{\partial}{\partial r}\left(r\frac{\partial g_s}{\partial r}\right)-H\left(h-h^*\right)\left[DQ_s\left(g_s-g_b\right)\right], \tag{6.23c}$$

$$\begin{aligned}\mathrm{Pe}h\frac{\partial g_b}{\partial t}=H\left(h-h^*\right)\left\{\frac{1}{r}\frac{\partial}{\partial r}\left(rh\frac{\partial g_b}{\partial r}\right)+Q_b\left(g_s-g_b\right)-\Upsilon\phi_n g_b h\right.\\ \left.-\frac{\mathrm{Pe}\gamma^*}{3r}\frac{\partial}{\partial r}\left(rh^3\left(1-\phi_n\right)g_b\frac{\partial}{\partial r}\left[\frac{1}{r}\frac{\partial}{\partial r}\left(r\frac{\partial h}{\partial r}\right)\right]\right)\right\}.\end{aligned} \tag{6.23d}$$

Through this derivation, we have shown how the assumption that ϕ_n is independent of z enables us to reduce the model to one spatial dimension, as well as eliminate the variables u_z and $\bar{\phi}_n$. We now undertake numerical solution of (6.23), subject to the initial conditions (6.22), and boundary conditions (6.4), (6.8) and (6.9). We then compare these results to the full numerical solutions computed in §6.1.3, to investigate the validity of the

$\phi_n(r,t)$ assumption.

6.2.2 Numerical Solutions

To compute the one-dimensional numerical solution, we use similar methods to the full two-dimensional model. Since (6.23a) and (6.23c) are unchanged from the full model, we use the same numerical methods to solve them. For the nutrient concentration in the biofilm, we solve (6.23d) using a similar Crank–Nicolson method to that used to solve (6.2f). The only difference arises in the advection term, where we no longer need to compute an integral. Finally, we adopt an explicit upwind finite difference scheme to solve (6.23b), completing the numerical method. As the boundary conditions are unchanged from the two-dimensional model, we apply each in the same way. Complete details on the numerical method are provided in Appendix B.3.3.

The numerical solution using parameters listed in Table 6.1 is presented in Figure 6.4. This solution enables us to determine how closely the one-dimensional results match the full model. The biofilm expansion in Figure 6.4a is similar to the two-dimensional results in Figure 6.2a. In the one-dimensional model, we observe slightly faster expansion than the full model. This faster expansion is particularly noticeable early in the solution, when nutrients are abundant and cell proliferation is comparatively rapid. However, with time we see faster nutrient depletion in the one-dimensional case, which decreases the expansion speed. As a result, the biofilm profiles at $t = 50$ are similar in both the one-dimensional and two-dimensional cases.

The cell volume fraction profile provides a possible explanation for the faster expansion observed in the one-dimensional model. Since we ignore the vertical dependence in this model, we cannot capture the region close to $z = 0$ where volume fraction is low. As a result, the profile in Figure 6.4b maintains a cell volume fraction close to $\phi_n = 0.9$ for a larger radius than the equivalent plot for the full model in Figure 6.2b. Consequently, the one-dimensional model slightly overestimates the cell volume fraction, and we observe a corresponding increase in nutrient consumption and cell proliferation.

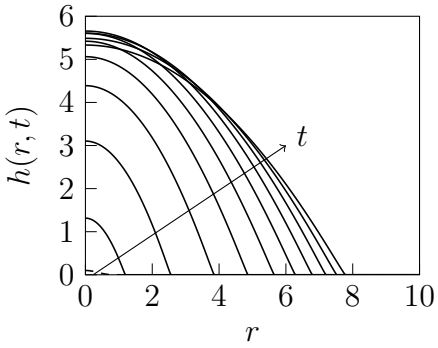

(a) Biofilm height.

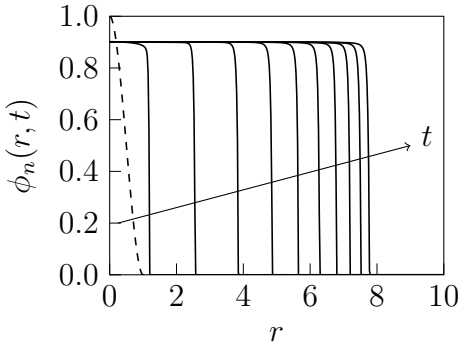

(b) Depth-averaged cell volume fraction.

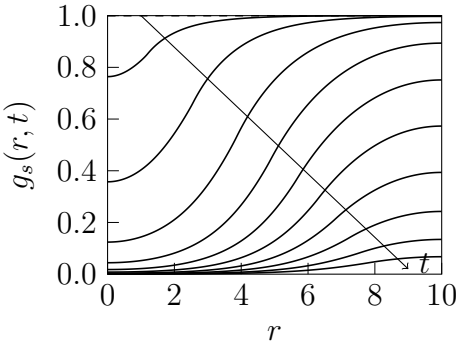

(c) Nutrient concentration in the substratum.

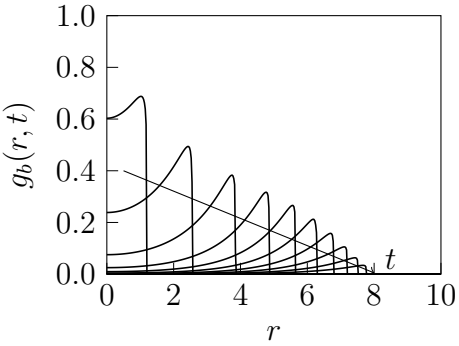

(d) Nutrient concentration in the biofilm.

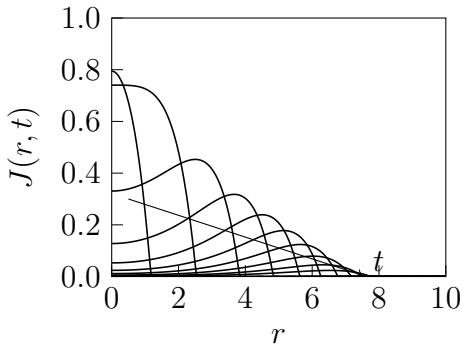

(e) Net biofilm growth.

Figure 6.4: Numerical solution of the 1D thin-film lubrication model, with $\psi_n = 50$, $\gamma^* = 1$, $h^* = 0.002$, and $b = 1 \times 10^{-4}$. The initial conditions are (6.22), and the solution is computed with $N_r = 4001$, and $N_t = 80001$, for $r \in [0, 10]$ and $t \in [0, 50]$. Where visible, the dashed curves represent the initial conditions, and the arrows indicate the direction of increasing time.

However, the biofilm size and shape in the one-dimensional model (Figure 6.4a) remains similar to the two-dimensional result (Figure 6.2a). These results suggest that the simplified model provides a good approximation to the full solution. This justifies the assumption that cell volume fraction does not depend on z, used here and by Srinivasan, Kaplan, and Mahadevan [127].

6.3 Sensitivity Analysis

Having computed numerical solutions to the two-dimensional lubrication model and one-dimensional simplification, we now investigate the effect of parameters on the expansion speed. We follow a similar approach as in §5.2.2, where we perform a local sensitivity analysis with respect to our original parameters. In each solution set, we vary one parameter at a time from those listed in Table 6.1, and find the biofilm radius and thickness for $T = 25$. Like in §5.2.2, to investigate the effect of the cell proliferation rate, we vary the dimensional parameter ψ_n, which is otherwise scaled out of the model. In doing so, we update D and Pe, which depend on ψ_n, and compute solutions until $T = \psi_n/2$. We can then directly compare the effect of ψ_n with Ψ_m and Ψ_d, to determine how the rates of cell production, ECM production, and cell death respectively affect the growth. The numerical results of Figure 6.4 suggest that the one-dimensional simplified model can produce qualitatively similar results to the full two-dimensional model. To investigate this further, in each of Figures 6.5–6.8 we plot sensitivity results for both models, and discuss the results below.

6.3.1 Biofilm Size

We first investigate the effect of model parameters on the biofilm size for $T = 25$, which provides a measure of expansion speed. To measure the biofilm

radius, we compute the contact line position

$$S(T) = \max_{r\in[0,R]} h(r,T) > b. \tag{6.24}$$

The results are presented in Figures 6.5 and 6.6. As with the extensional flow regime, a wide range of biofilm growth is possible for parameters that remain within an order of unity. The major difference between the two regimes is that the surface tension coefficient γ^* affects biofilm size in the lubrication regime, as Figure 6.5d shows. This was not observed in the extensional flow results of Figure 5.3f. In contrast, the initial biofilm height affected biofilm size in the extensional flow regime (see Figure 5.3e), but has minimal effect in the lubrication regime, as shown in Figure 6.5e.

In the lubrication regime, there is a competition between the strong biofilm–substratum adhesion and surface tension effects. When cells proliferate, strong adhesion opposes radial expansion, which restricts biofilm growth to the vertical direction. Conversely, surface tension forces oppose curvature on the free surface, and this curvature increases when the biofilm grows vertically. Surface tension forces subsequently flatten the biofilm profile and transport mass radially, facilitating biofilm expansion. We therefore observe faster radial expansion when the surface tension coefficient, γ^*, is increased. This explains the behaviour seen in Figure 6.5d.

The difference in expansion mechanisms between the lubrication and extensional flow regimes also explains the observation that initial biofilm height H_0 has negligible effect on biofilm size. In sliding motility, thinner biofilms expand quickly, because a relatively smaller quantity of new cells at the leading edge is required for the biofilm to spread. However, due to the strong biofilm–substratum adhesion, this mechanism is not available in the lubrication regime, where the biofilm thickness is instead determined by surface tension forces. When the other parameters are held constant, the biofilm will tend to adopt the same final shape regardless of initial height, and expand at similar speed. This also justifies how the initial condition does not affect biofilm thickness, as Figure 6.7e will show. In their model,

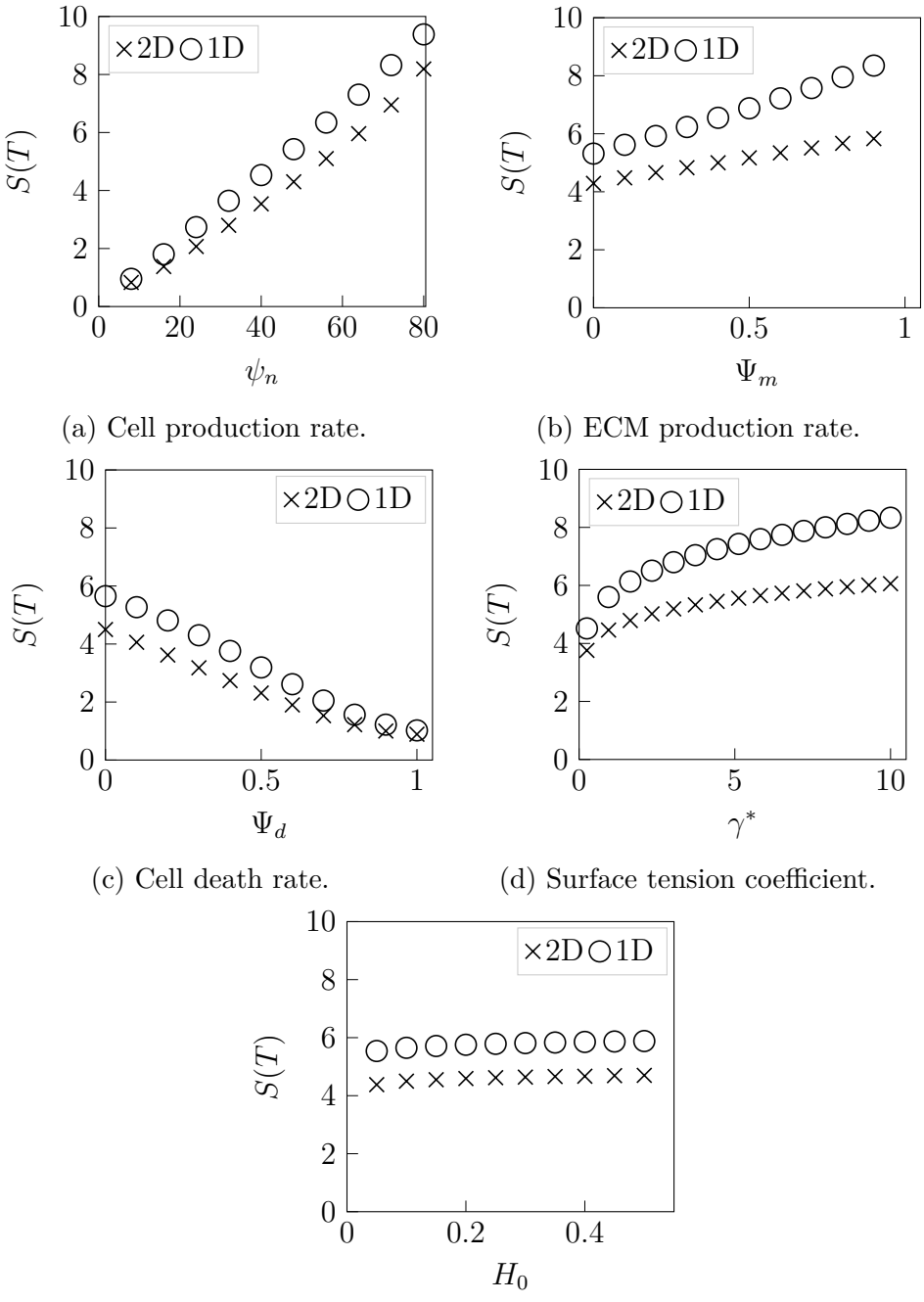

(a) Cell production rate.

(b) ECM production rate.

(c) Cell death rate.

(d) Surface tension coefficient.

(e) Initial biofilm height.

Figure 6.5: The effects of net biomass production rates, surface tension, and the initial height on biofilm size.

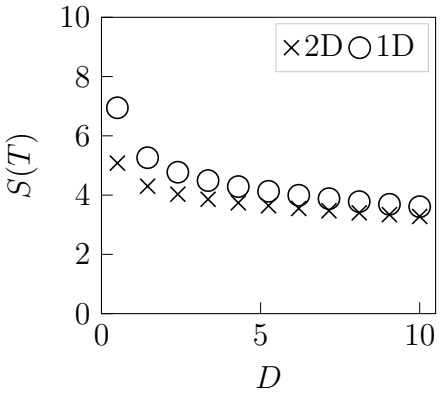

(a) Diffusion coefficient.

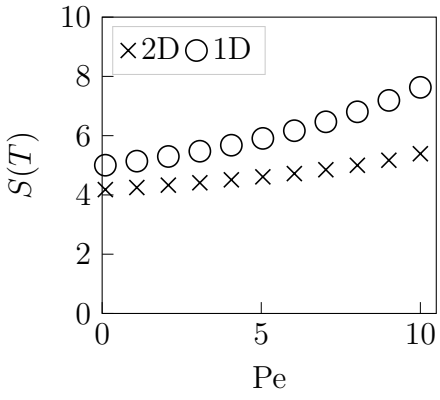

(b) Péclet number.

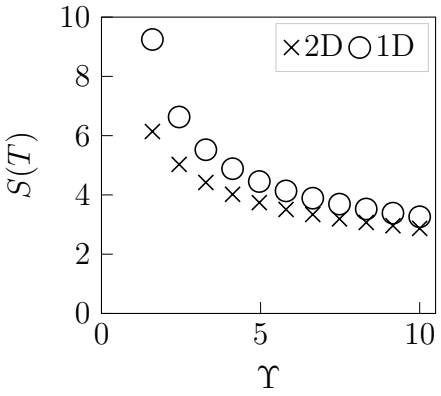

(c) Nutrient consumption rate.

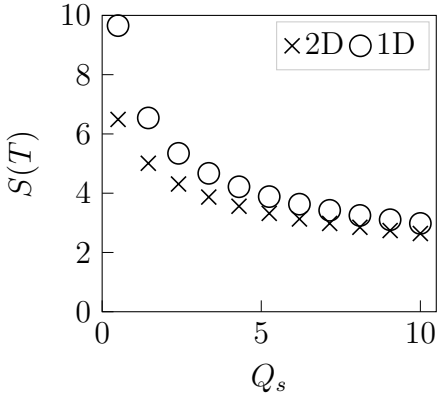

(d) Nutrient depletion rate.

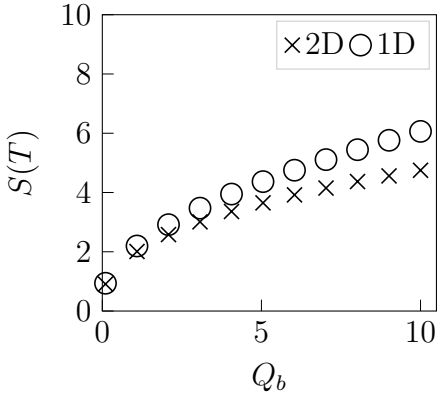

(e) Nutrient uptake rate.

Figure 6.6: The effects of parameters that govern the movement, consumption, and uptake of nutrients on biofilm size.

Ward and King [120] observe the same behaviour, in which expansion depends on the initial conditions in the extensional flow regime, but does not in the lubrication regime.

Since we use the same source terms in both regimes, the effects of cell production rate ψ_n, ECM production rate Ψ_m, and cell death rate Ψ_d shown in Figures 6.5a–6.5c are similar to the extensional results in Figure 5.3. When γ^* is held constant but non-zero, increased biomass production leads to faster expansion. This is because biomass production and vertical growth cause faster increases in curvature. Surface tension then drives greater radial redistribution of mass, increasing expansion speed. Increased rates of cell death reduce the cell volume fraction, thereby reducing future biomass production. Biomass production also explains the discrepancies between the one-dimensional and two-dimensional models observed throughout Figure 6.5. As shown in Figure 6.4b, the cell volume fraction remains closer to $\phi_n = 0.9$ for a larger radius than in the two-dimensional model. This overestimation of cell volume fraction corresponds to an overestimation of biomass production, leading to larger biofilm sizes in the one-dimensional model.

The nutrient mass balance equations in the lubrication regime are the same as in the extensional flow case. As a result, the trends in nutrient transport, uptake, and consumption parameters are similar to the extensional flow regime, which is illustrated in Figure 6.6. In addition, we observe a similar dependence of the biofilm size on the Péclet number, Pe, as in the extensional flow regime. This is because again the nutrient supply to the biofilm depends more strongly on uptake from the substratum than advection within the biofilm. Overall, as outlined in §5.2.2, increasing nutrient availability to the biofilm facilitates faster expansion. Like Figure 6.5, the one-dimensional lubrication model shows the same qualitative trends as the full two-dimensional model, while slightly over-predicting $S(T)$.

6.3.2 Biofilm Thickness

In addition to biofilm size, the biofilm thickness also depends on the model parameters. To illustrate this, for each solution set we compute the index

$$I_t(T) = \frac{\max_{r\in[0,R]} h(r,T)}{S(T)}, \tag{6.25}$$

which measures the dimensionless thickness of the biofilm. We plot these results in Figure 6.7 and 6.8. As described above, Figure 6.7e shows that the initial biofilm height has negligible impact on thickness. In addition, the surface tension coefficient γ^* affects the distribution of biomass in the biofilm, and not its quantity. Since increasing γ^* increased the radial size, this occurs in conjunction with a reduction in thickness, as Figure 6.7d shows. Conversely, changes to Ψ_m, Ψ_d, and all parameters in Figure 6.8 affect the quantity of biomass created. Therefore, changes that increase the biofilm radius also increase the thickness, as Figures 6.7b, 6.7c and 6.8 show.

Throughout Figures 6.7 and 6.8, we observe similar trends in biofilm thickness between the two-dimensional and one-dimensional models. Combining this with the results of Figures 6.5 and 6.6, we conclude that the one-dimensional model captures the key mechanisms of the lubrication regime, including the effects of cell proliferation, nutrient transport and uptake, and surface tension. The only discrepancies between the one-dimensional and two-dimensional models are that the one-dimensional model slightly overestimates biomass production and expansion speed, and slightly biases radial expansion over thickening as ψ_n increases (see Figure 6.7a). Therefore, although the one-dimensional model does not capture the vertical variation in the cell volume fraction, it provides a viable alternative to the two-dimensional model. The advantage of the one-dimensional model is that it is computationally more efficient, and potentially more amenable to analysis, than the two-dimensional model.

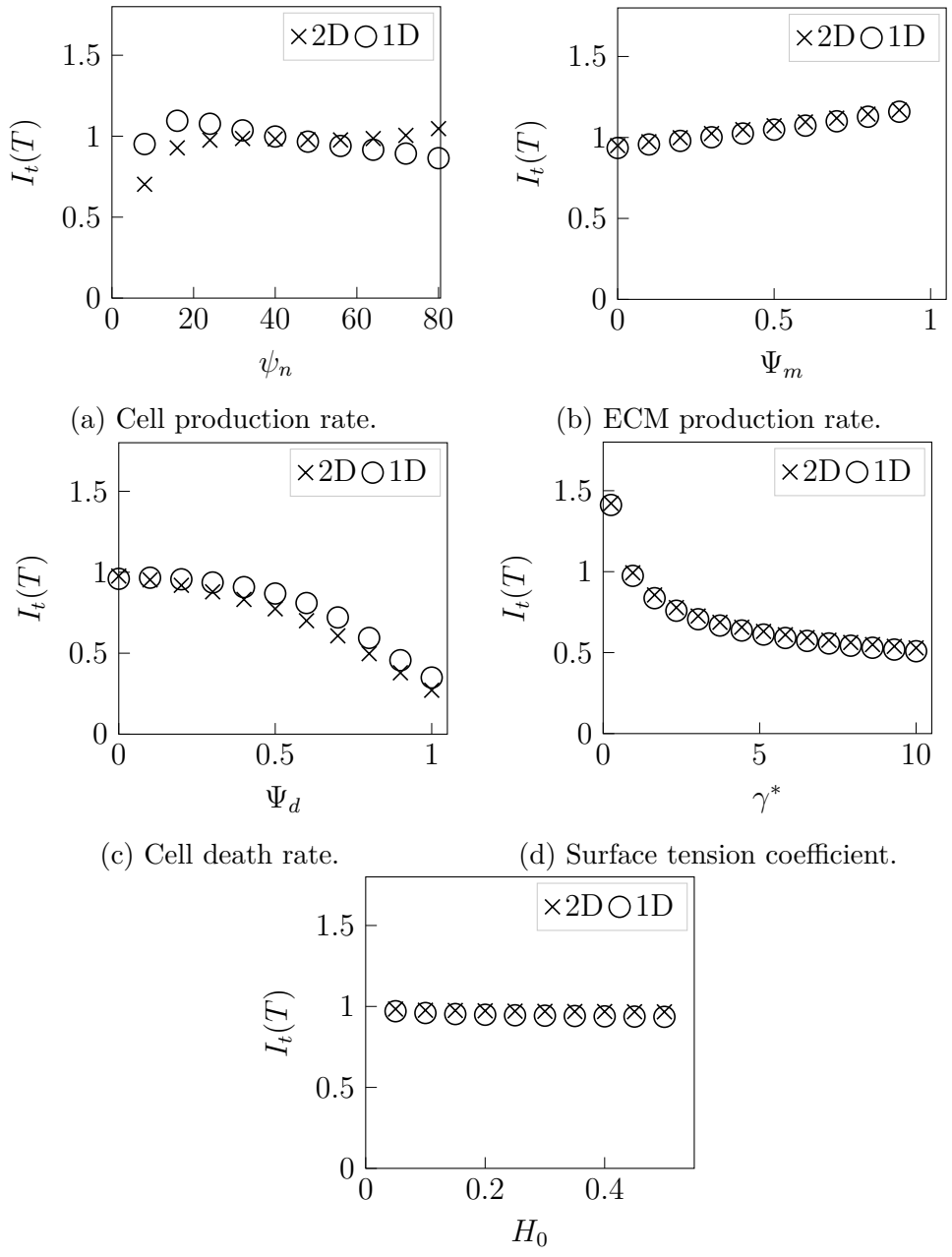

(a) Cell production rate.

(b) ECM production rate.

(c) Cell death rate.

(d) Surface tension coefficient.

(e) Initial biofilm height.

Figure 6.7: The effects of net biomass production rates, surface tension, and the initial height on dimensionless biofilm thickness, $I_t(T)$.

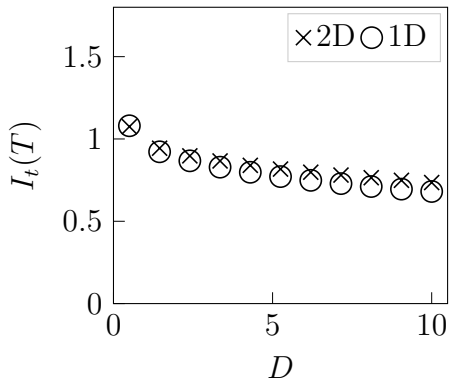

(a) Diffusion coefficient.

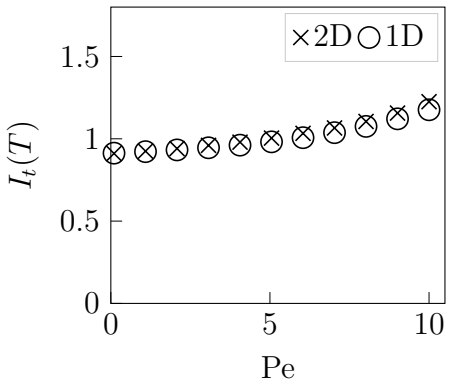

(b) Péclet number.

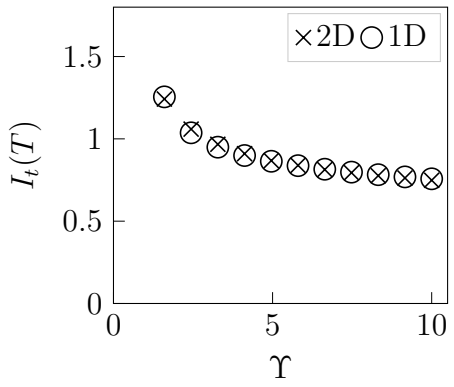

(c) Nutrient consumption rate.

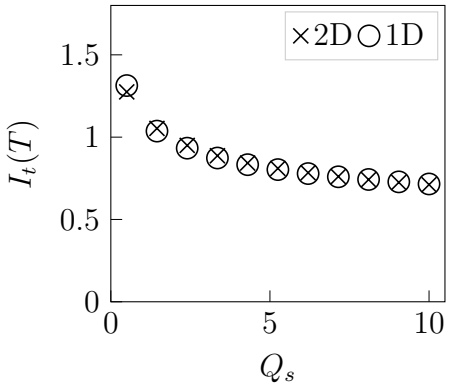

(d) Nutrient depletion rate.

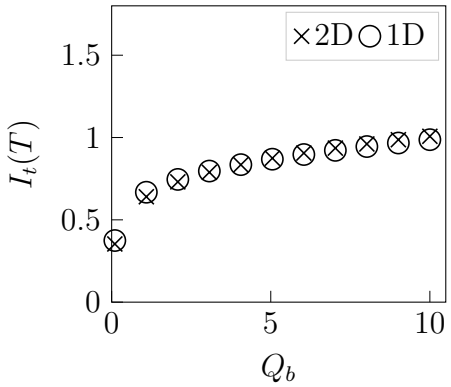

(e) Nutrient uptake rate.

Figure 6.8: The effects of parameters that govern the movement, consumption, and uptake of nutrients on dimensionless biofilm thickness, $I_t(T)$.

6.4 Summary

In this chapter, we investigated the lubrication model, where cells adhere strongly to the substratum, and surface tension plays an important role in biofilm expansion. This is in contrast to the sliding motility hypothesis underpinning the extensional flow model, where biofilm–substratum adhesion and surface tension are assumed weak. Our investigation of the lubrication model followed a similar path to the extensional flow analysis in Chapter 5. We again considered an axisymmetric geometry, which in this regime gives rise to a complicated two-dimensional system of integro-differential equations. Computing numerical solutions to this model posed a challenge, as it involved solving a coupled system of six equations on a changing domain. Therefore, we first presented a solution to the no-slip model of Ward and King [120]. This validated the non-linear Crank–Nicolson method used throughout, and demonstrated its numerical convergence. In these solutions, the radial geometry did not significantly affect expansion speed and the biofilm profile.

Two-dimensional numerical solutions enabled us to predict expansion speed, biofilm shape, and the distribution of cells in the biofilm. We found that a thin region with low cell volume fraction developed close to the biofilm–substratum interface. However, away from this region the cell volume fraction only depended weakly on z. Exploiting this, we proposed a simplification to the model where we assumed that ϕ_n is independent of z, reducing the model to one spatial dimension. Despite overestimating the depth-averaged cell volume fraction, numerical solutions to the one-dimensional model were qualitatively similar to the full two-dimensional model. The one-dimensional model therefore provided a computationally efficient alternative for predicting biofilm expansion under strong biofilm–substratum adhesion and large pressure and surface tension.

To investigate the effect of model parameters on the biofilm size and shape, we computed numerical solutions to the two-dimensional and simplified one-dimensional models. This also enabled comparison of expansion mechanisms

between the lubrication and extensional flow regimes. Although the biofilm profile was thicker in the lubrication regime, the qualitative dependence of expansion speed on the model parameters was similar in both regimes. The key difference was that in the lubrication regime, the value of the surface tension coefficient γ^* affects expansion speed. This was due to a competition between surface tension and the strong adhesion on the biofilm–substratum interface. Strong adhesion opposes radial expansion, and promotes vertical growth when cells proliferate. However, vertical growth increases the free surface curvature. To relieve this curvature, surface tension forces flatten the biofilm profile by redistributing mass radially, facilitating expansion. Unlike in the extensional flow regime, the initial condition did not affect the expansion speed. These results confirmed that surface tension forces and cell proliferation drive biofilm expansion in the lubrication regime.

As with the extensional flow model results from Chapter 5, the complexity of the lubrication model makes analysis of two-dimensional pattern formation more difficult than for the reaction–diffusion model. A potential advantage of the one-dimensional simplified model is that it may be more analytically tractable than the full model. This opens the possibility of investigating the linear stability of solutions to the one-dimensional model to azimuthal perturbations, which would provide a mechanism for floral pattern formation. Furthermore, under the assumption that ϕ_n is independent of z, the full non-axisymmetric model reduces from three to two dimensions. We could then compute these two-dimensional solutions numerically, and compare them with the linear stability analysis. In addition to these mathematical extensions, in the future we could also design new experiments to measure and adjust surface tension and cell–cell adhesion. This will enable us to distinguish between the extensional flow and lubrication regimes, and could provide data with which to compare the lubrication regime results.

Chapter 7

Conclusion

Yeasts have extensive effects on human life, from their use in food and drink production, to their emergence as a leading cause of hospital-acquired infections. In nature, yeasts often exist in biofilm colonies, which are sticky communities of microbes residing on a surface. These biofilms are responsible for pathogenic infections, as their collective structure enables them to resist anti-fungal treatment. This has motivated scientists to investigate the mechanisms responsible biofilm growth and pattern formation. An important milestone in yeast research was the sequencing of the *Saccharomyces cerevisiae* genome. Commonly known as the budding or bakers' yeast, *S. cerevisiae* cells have much in common with more complex plant and animal cells. For these reasons, *S. cerevisiae* is often used as a model organism in yeast research.

When inoculated on semi-solid agar in the laboratory, *S. cerevisiae* can initiate biofilm formation. These biofilms consist of a thin layer of cells that initially expands in a uniform circular manner. After some time, the biofilm then attains the floral morphology, which is a non-uniform pattern characterised by petal-like structures. Repeated observations of this morphology led researchers to hypothesise common mechanisms for its origin. One simple hypothesis was that nutrient-limited growth, which involves the movement and consumption of a depleting nutrient, can generate the pattern. Others suggested that mechanical interactions between the cells and their

environment also contributed. This led to the hypothesis that sliding motility, a passive form of growth driven by cell proliferation and weak adhesion to the substratum, could explain biofilm growth.

The need for quantitative methods of testing these hypotheses motivated this thesis. To achieve this, we used a combination of mathematical modelling and experiments. Our first contribution was the implementation of spatial statistics to quantify biofilm expansion speed and petal formation. Next, we demonstrated that nutrient-limited growth is a possible explanation for petal formation, using experimental data and insights from a reaction–diffusion model. Another major contribution was the development and analysis of two thin-film fluid models for biofilm growth. Our models combined the mechanics of the cells and extracellular matrix, and nutrient limitation in a single framework. Analysis of our extensional flow model showed that sliding motility can explain the experimental expansion speed. We then contrasted these results with biofilm growth driven by surface tension and strong adhesion to the substratum using our lubrication model.

We used spatial statistics to obtain data for expansion speed and petal formation from experimental photographs of yeast biofilm growth. First, we processed these photographs by converting them to binary images indicating the area occupied by the biofilm. We then introduced the radial statistic, which enabled us to measure the biofilm radius. Tracking this radius over time, we found that the assumption of constant-speed radial expansion was consistent with *S. cerevisiae* mat formation experiments. To quantify petal formation, we used an angular pair-correlation function, the power spectrum of which provided a count of the number of petals. Across all experiments, we found that mature biofilms contained between two and twelve petals, with two to five being most common. Combining both metrics provided a quantitative description of the non-uniform biofilm growth. Spatial statistics provided a bridge between experiments and mathematical models, and enabled quantitative comparison between them.

The remainder of our research involved the construction and analysis of

mathematical models, and the comparison of modelling results with experimental data. Abstract mathematical models provided simplified representations of the complex processes of biofilm formation, and allowed us to focus on whether particular mechanisms could drive pattern formation. We began by investigating the hypothesis that nutrient-limited growth is the mechanism of petal formation. We analysed a reaction–diffusion system for the numerical cell density and nutrient concentration. Since cell spread is not consistent with Fickian diffusion, the key feature of our model was a non-linear, degenerate diffusion term for the yeast cells. Our minimal reaction–diffusion model neglected cell mechanics and the extracellular matrix, which enabled us to isolate the effect of nutrient-limited growth on pattern formation.

We showed that the reaction–diffusion model admits travelling wave solutions with compact support, and used these solutions to estimate the ratio of cell to nutrient diffusivity. Our motivation was that travelling wave solutions provide an explanation for constant-speed radial expansion, an assumption consistent with data from *S. cerevisiae* experiments. Making the ansatz that travelling waves exist reduced the reaction–diffusion model to a three-dimensional dynamical system. We used geometric singular perturbation theory to investigate the existence of travelling wave solutions in the limit of small diffusivity ratio, D. Analysis of the reduced problem showed that travelling waves exist for $D = 0$. We then used the layer problem to obtain an approximation for the slow manifold, on which solutions for small, but non-zero, D exist. Numerical solutions to the dynamical system then suggested that, for each value of D, sharp-fronted travelling waves existed for a unique critical wave speed, c_{crit}. Sharp-fronted travelling waves solutions arose in numerical solutions to the full model with arbitrary initial conditions. Since these solutions represent biofilms of finite size, we used them to estimate D from experimental data. This provided a complete set of parameters for the reaction–diffusion model.

Having parametrised the model, we used the linear stability analysis of Müller and van Saarloos [64] to show that the reaction–diffusion model predicts

petal formation. For each experimentally feasible D, linear stability analysis predicted that planar travelling wave solutions are unstable to transverse perturbations. We found good agreement between the unstable wave numbers and the petal width measured in experiments. Two-dimensional numerical solutions verified the linear stability analysis results, and confirmed that planar results provide a good approximation to circular biofilms. Based on this, we concluded that nutrient-limited growth is a possible mechanism for the formation of floral patterns in yeast biofilms, and that non-linear degenerate cell diffusion can provide an appropriate description of cell spread.

To investigate the effect of mechanics on biofilm growth, we derived a two-phase fluid model. This model addressed weaknesses in the reaction–diffusion model, which did not model biofilm mechanics or uptake of nutrients from the substratum, and could not predict the biofilm height explicitly; the cell density profile merely provided a proxy for height. In this mechanical model, we treated the biofilm as a mixture of active living cells and a passive extracellular matrix. For both fluids, we adopted the Newtonian viscous constitutive relation. We then used conservation of mass and momentum to obtain governing equations for the fluid volume fractions and nutrient concentration. These equations described the mechanics of each fluid phase, interactions between phases, and the movement, uptake, and consumption of nutrients. Together with initial and boundary conditions, this constituted a model for biofilm growth in three dimensions.

The thin-film approximation provided a systematic way to simplify the three-dimensional mechanical model, and to highlight particular mechanisms thought to affect growth. The approximation exploited the observation that the biofilm radius significantly exceeds its height and the substratum depth. Non-dimensionalisation then introduced the aspect ratio, a small parameter, into the model equations. We obtained simplified leading-order models by expanding the variables in power series of the small aspect ratio. An important step in this process was the identification of distinguished limits to balance physical features of similar importance, while neglecting those

of lesser importance. First, we derived a thin-film model in the extensional flow regime, in which the biofilm adheres weakly to the substratum and cell proliferation drives expansion. We then considered strong biofilm–substratum adhesion in the lubrication regime, in which surface tension plays an important role in biofilm expansion. The extensional flow and lubrication models were both simpler than the general model, and enabled us to investigate the effects on growth of sliding motility and cell–cell adhesion respectively.

We used the extensional flow model to show that sliding motility is a possible mechanism for yeast biofilm expansion. Reynolds and Fink [17] hypothesised that sliding motility could explain growth in their initial *S. cerevisiae* mat formation experiments. Sliding motility involves a sheet of cells expanding passively as a unit, facilitated by cell proliferation and low friction between the biofilm and substratum. Our extensional flow model described this form of growth. We used experimental data and numerical solutions to estimate parameters for the extensional flow model. All parameters were $\mathcal{O}(1)$, justifying the extensional flow scaling. We obtained excellent agreement between the model and one-dimensional axisymmetric numerical solutions. This suggested that sliding motility could explain the experimental growth. The extensional flow model predicted a non-constant expansion speed, which provided an even better fit to experimental data than the reaction–diffusion model.

Having established the biological utility of the extensional flow model, we used it to show how parameters affected biofilm size and shape. We performed a local sensitivity analysis to investigate the effect of deviations from the experimental parameters on biofilm size. We showed that increased production of cells and EPS promoted faster expansion, with cell production rate being the most important determinant. We also attained faster expansion by increasing nutrient supply to the leading edge of the biofilm. This was achieved by increasing the nutrient uptake rate, or by decreasing nutrient depletion, diffusion, and consumption rates. Initially thinner biofilms also expanded faster, because they required less nutrient to sustain their thickness.

Compared to the reaction–diffusion model for which diffusion ratio was the only determinant, this analysis provided a richer description of the factors affecting expansion speed.

Unlike the reaction–diffusion model, the extensional flow model also enabled us to predict the biofilm height. Although not present in *S. cerevisiae* mats, some biofilms of wild yeast form a ridge close to the leading edge. Using different parameters to the *S. cerevisiae* mats, the extensional flow model reproduced this ridge formation. We then investigated how the biofilm profile depends on the surface tension coefficient, γ^*. Increased values of γ^* generated stronger resistance to free surface curvature, and inhibited ridge formation.

In contrast to the extensional flow model, the lubrication model represented a regime where cells adhered strongly to the substratum. In this regime, pressure in the biofilm could be large, and we also assumed surface tension to be large. Since the leading-order fluid velocities and volume fractions depended on z, the axisymmetric lubrication model was two-dimensional. We computed numerical solutions to this model, which described biofilm expansion and the spatial distribution of cells. Since the cell volume fraction depended weakly on z, we proposed a simplified model that neglected this dependence. This simplified model was one-dimensional, and represented a computationally more efficient alternative to the full two-dimensional model.

We performed a local sensitivity analysis to investigate the mechanisms governing expansion speed and thickness in biofilms adhering strongly to the substratum. In these solutions, we observed a competition between strong adhesion and surface tension. When cells proliferated, strong adhesion drove growth in the vertical direction. However, this vertical growth increased the curvature of the biofilm surface. Surface tension forces opposed this curvature by redistributing mass radially, facilitating expansion. Sensitivity analysis also revealed that although the simplified one-dimensional model overestimated expansion speed, it captured the same qualitative trends as the full two-dimensional model. This validated the assumption that cell volume fraction depended weakly on z.

Synthesising the reaction–diffusion and mechanical model provides a more complete understanding of biofilm growth and pattern formation. Being simpler, the minimal reaction–diffusion model was more amenable to analysis than both thin-film fluid models. We exploited this major advantage of the reaction–diffusion model, and showed that nutrient-limited growth is a plausible explanation for both biofilm expansion and the floral morphology. However, the non-linear diffusion mechanism for cell spread was phenomenological, and the reaction–diffusion model neglected mechanics, the details of nutrient uptake from the substratum, and the biofilm thickness. The extensional flow model for sliding motility addressed these weaknesses, and provided a more detailed and accurate explanation of biofilm expansion.

In the future, we plan to investigate whether the thin-film extensional flow model predicts floral pattern formation. This would involve investigating the linear stability of model solutions to small-amplitude azimuthal perturbations. Since these solutions are not travelling waves, the stability analysis will involve time-dependent base states, increasing its complexity. Therefore, we also plan to investigate petal formation using two-dimensional numerical solutions of the extensional flow model. If these solutions predict petal formation, this would provide more evidence that sliding motility underpins yeast biofilm growth. Furthermore, we have now shown that the simplified one-dimensional axisymmetric lubrication model is a good approximation of the full lubrication model. We also plan to use the one-dimensional lubrication model to determine whether petals can form in this regime.

Our mechanical model also provides a framework on which to add more features that may affect yeast biofilm expansion. For example, we plan to investigate the mechanism of osmotic swelling. This will enable us to understand how fluid transport between the agar and biofilm affects the divergent growth observed on media of different agar concentration. We could extend this further by considering growth on viscoelastic agar, rather than the rigid substrata considered here. We would then impose continuity of shear stress on the biofilm–substratum interface, and investigate the effect of

agar deformation on biofilm expansion and shape. The additional questions raised by our research provide a rich source of future work. We hope that a detailed understanding of the mechanisms of biofilm growth will enable the development of new techniques to combat infections, and to harness the industrial potential of biofilms.

Appendix A

Experimental Data

A.1 Mat Biofilm Images

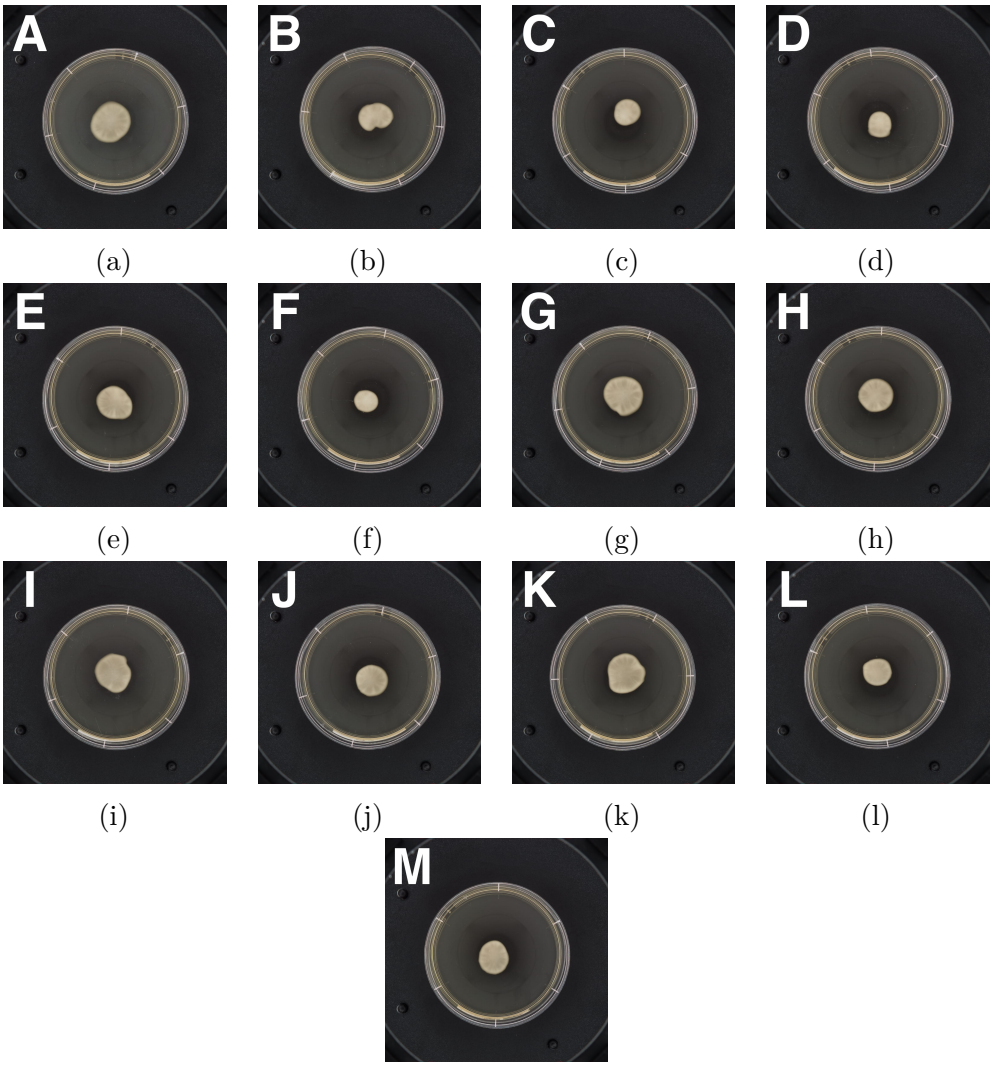

Figure A.1: Photographs of the mat formation experiments, taken $t = 4099\,\mathrm{min} \approx 68\,\mathrm{h}$ after inoculation.

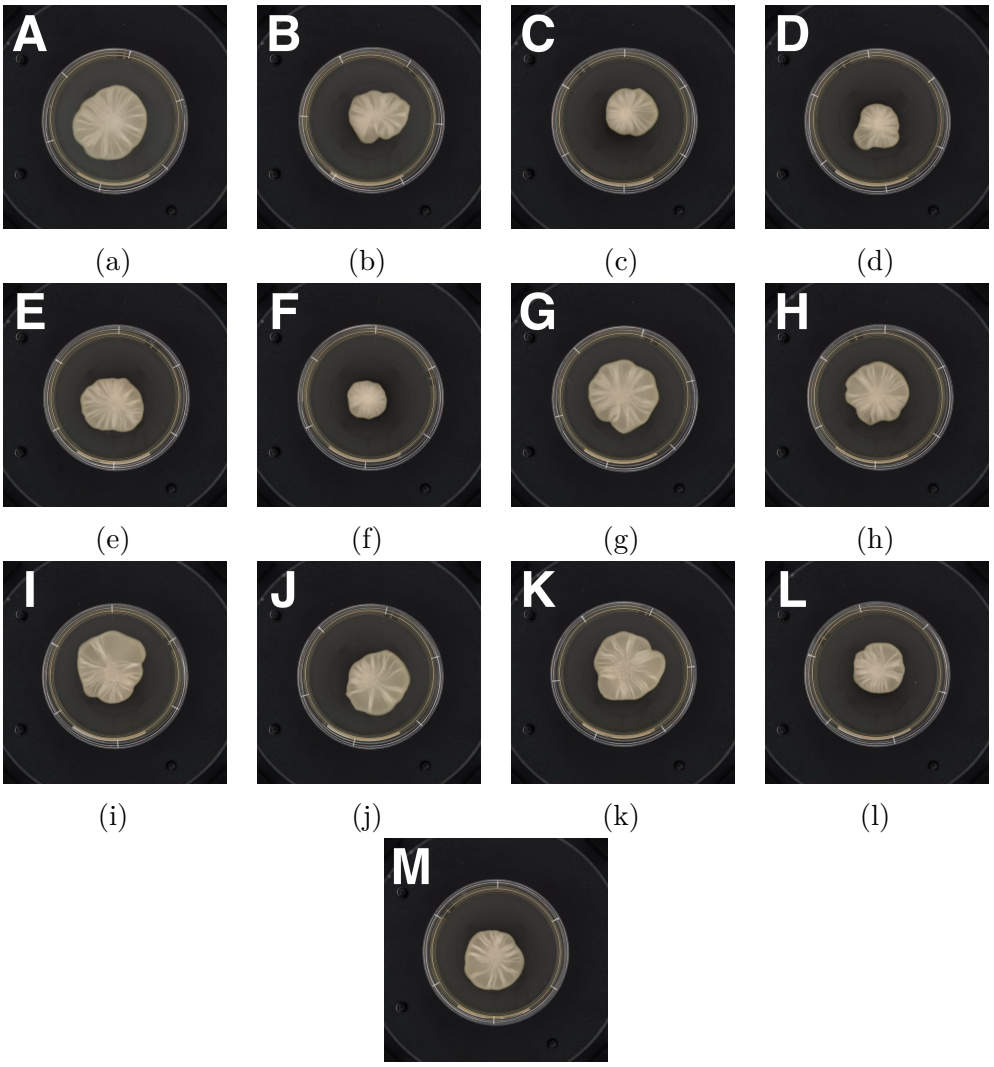

Figure A.2: Photographs of the mat formation experiments, taken $t = 7013\,\mathrm{min} \approx 117\,\mathrm{h}$ after inoculation.

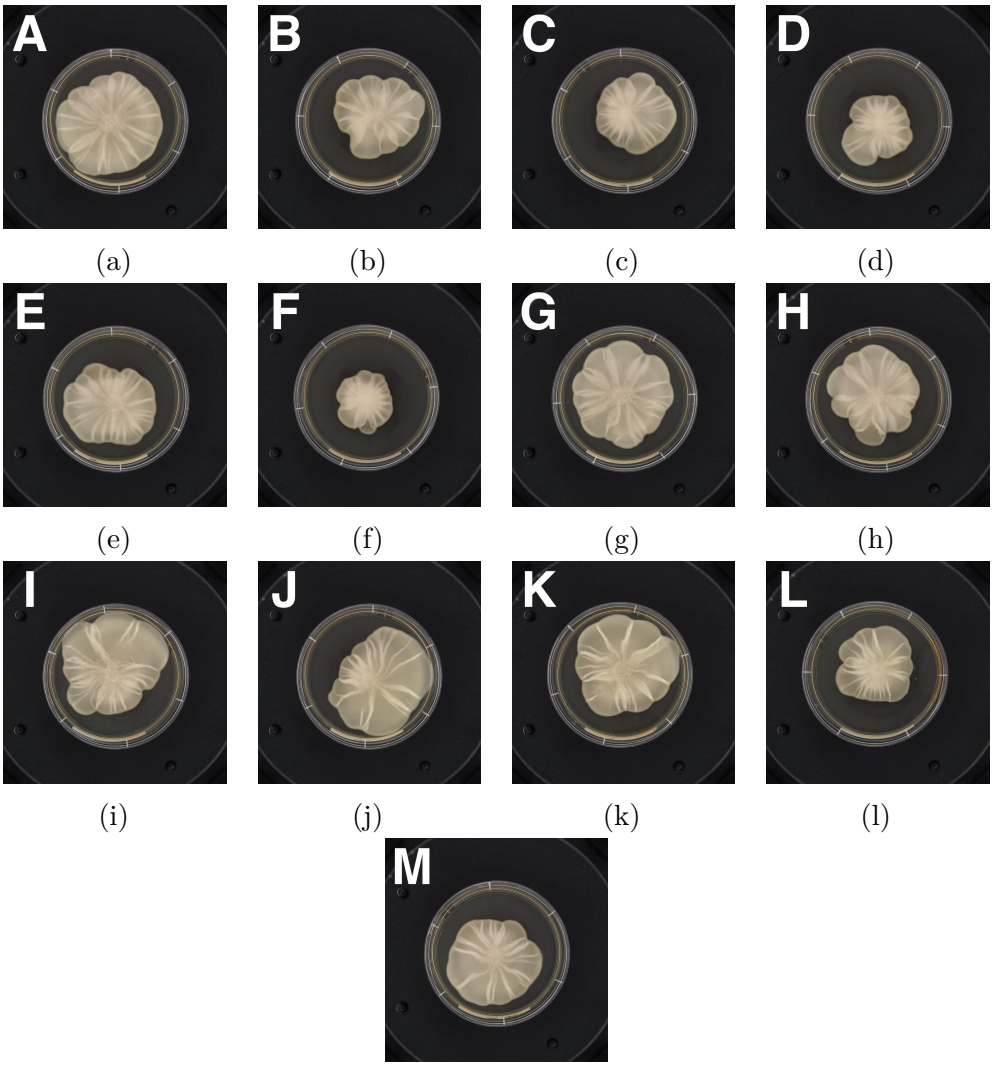

(a) (b) (c) (d)

(e) (f) (g) (h)

(i) (j) (k) (l)

(m)

Figure A.3: Photographs of the mat formation experiments, taken $t = 9866\,\text{min} \approx 164\,\text{h}$ after inoculation.

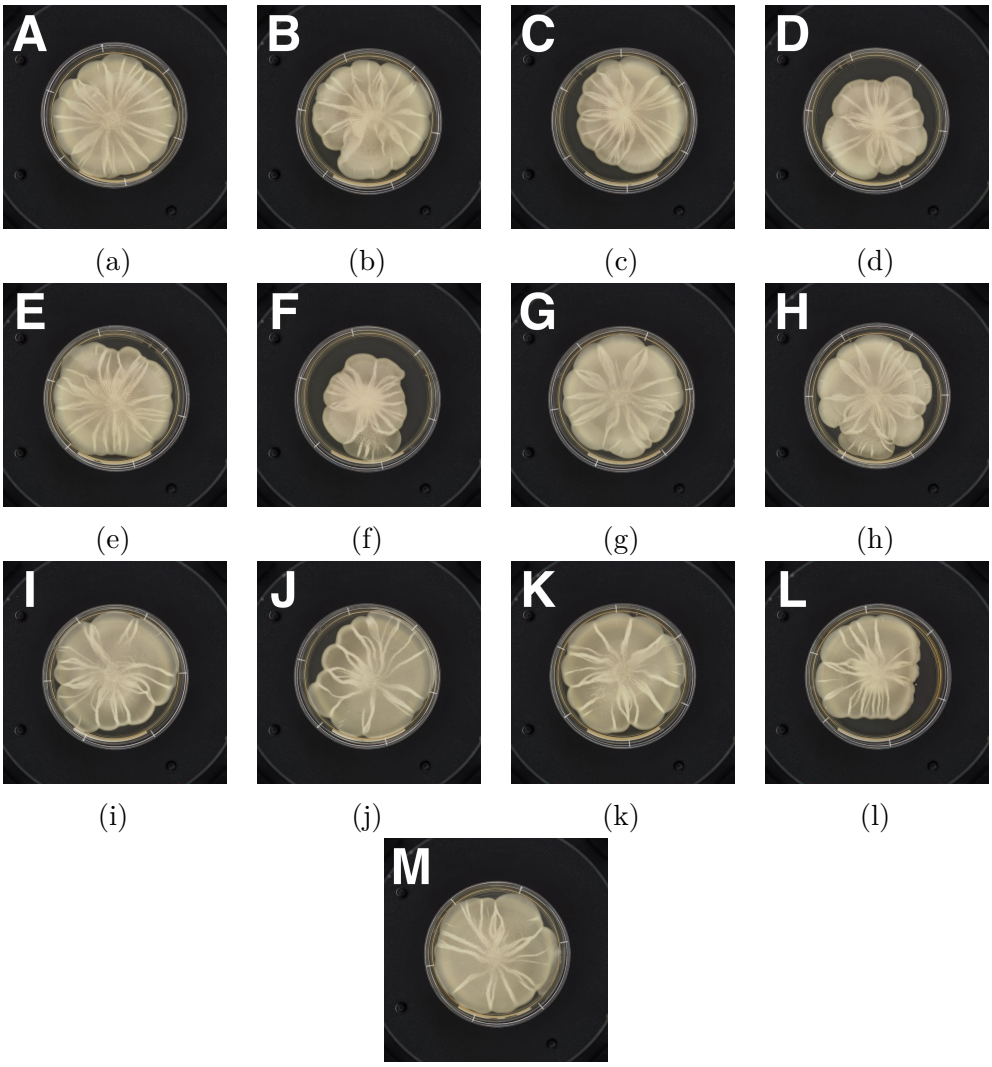

Figure A.4: Photographs of the mat formation experiments, taken at the end of the experiment, $t = 14\,208\,\mathrm{min} \approx 237\,\mathrm{h}$ after inoculation.

A.2 Mat Size Data

Table A.1: Biofilm radius for each experiment, computed using the radial statistic.

Mat	Radius (mm)			
	Day 3	Day 5	Day 7	Day 10
A	12.8	23.9	34.0	39.5
B	10.0	18.3	27.5	38.1
C	8.48	16.3	25.4	36.4
D	8.06	14.8	22.5	33.0
E	11.0	19.4	29.2	38.6
F	7.36	12.5	19.3	29.8
G	12.5	22.6	32.9	38.8
H	10.9	20.0	29.4	37.9
I	11.8	22.8	33.3	39.7
J	10.2	20.7	34.0	40.3
K	12.5	22.4	32.7	39.9
L	9.04	16.9	25.2	34.6
M	10.2	19.7	29.5	40.3
Mean	10.4	19.3	28.8	37.5

Table A.2: The approximate cell count and the final biofilm area for each experiment.

Mat	Cell count	Area (mm^2)
A	1.55×10^{10}	4898
B	1.50×10^{10}	4556
C	1.71×10^{10}	4145
D	1.46×10^{10}	3489
E	1.54×10^{10}	4664
F	1.49×10^{10}	2999
G	1.69×10^{10}	4758
H	1.28×10^{10}	4522
I	1.29×10^{10}	5037
J	1.55×10^{10}	5036
K	1.40×10^{10}	4999
L	1.07×10^{10}	3889
M	1.48×10^{10}	5052
Mean	1.46×10^{10}	4465

A.3 Power Spectra

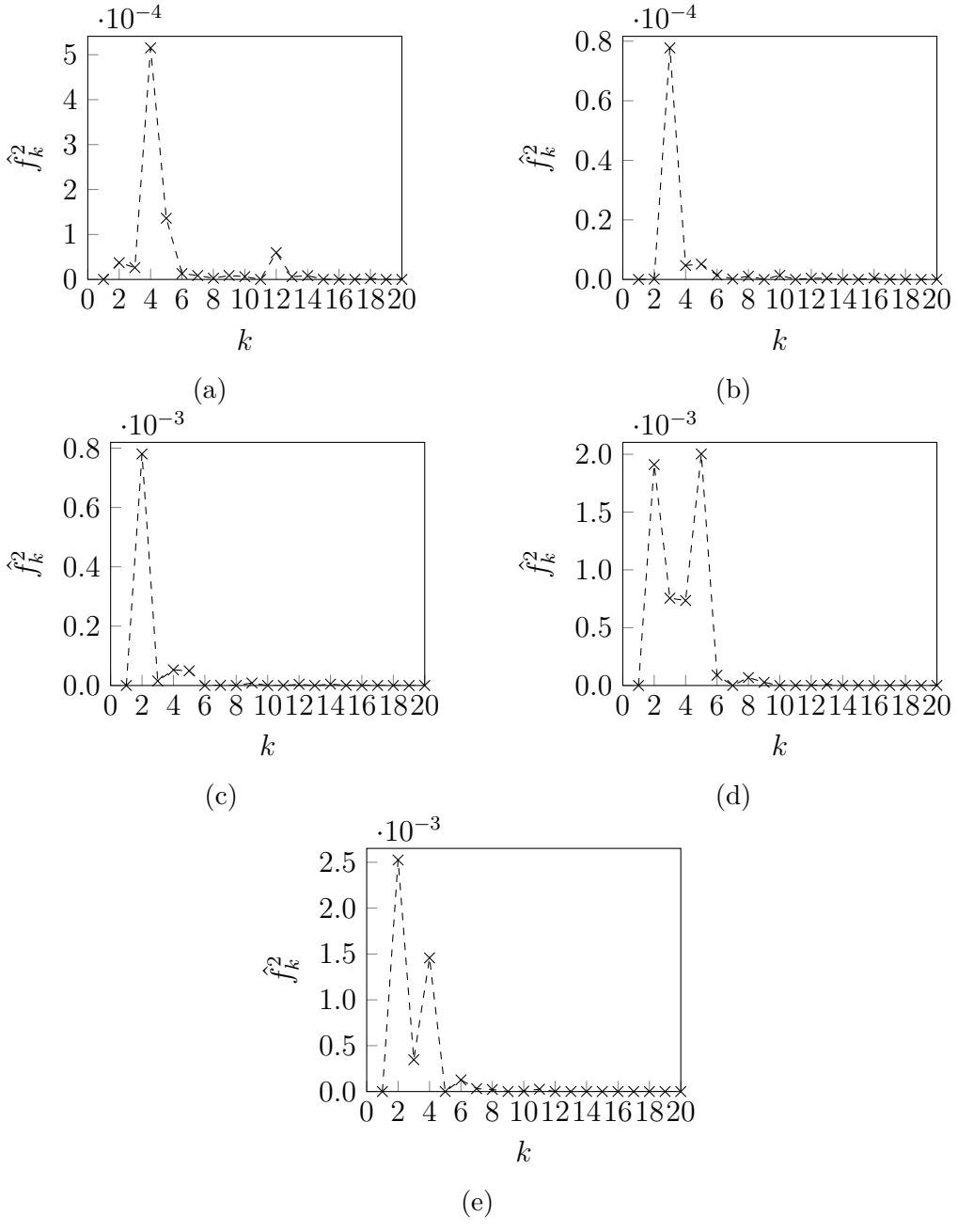

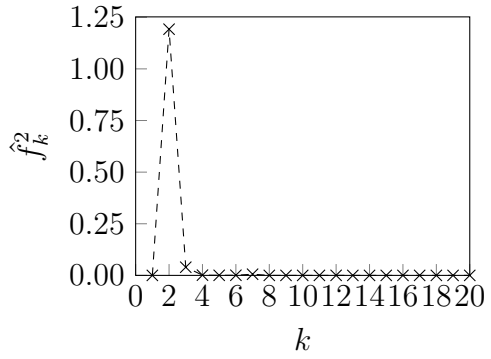
1.25
1.00
0.75
0.50
0.25
0.00
$\hat{f}_k^2$
0 2 4 6 8 10 12 14 16 18 20
k

(f)

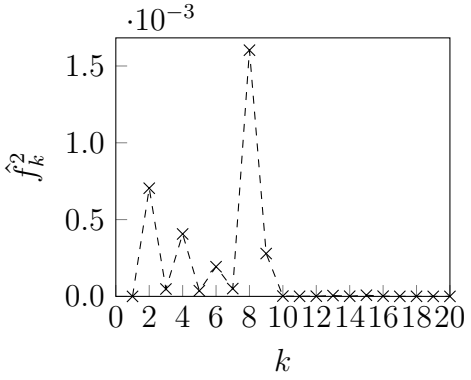
$\cdot 10^{-3}$
1.5
1.0
0.5
0.0
$\hat{f}_k^2$
0 2 4 6 8 10 12 14 16 18 20
k

(g)

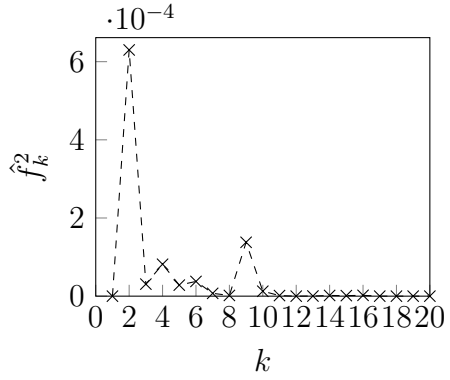
$\cdot 10^{-4}$
6
4
2
0
$\hat{f}_k^2$
0 2 4 6 8 10 12 14 16 18 20
k

(h)

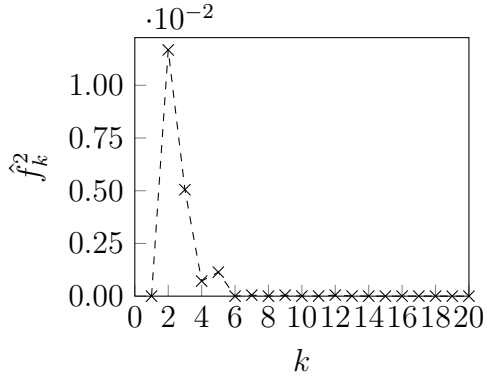
$\cdot 10^{-2}$
1.00
0.75
0.50
0.25
0.00
$\hat{f}_k^2$
0 2 4 6 8 10 12 14 16 18 20
k

(i)

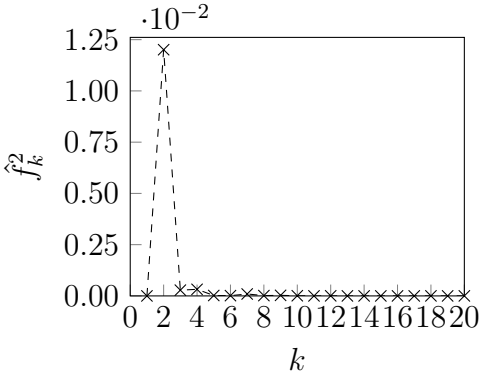
$\cdot 10^{-2}$
1.25
1.00
0.75
0.50
0.25
0.00
$\hat{f}_k^2$
0 2 4 6 8 10 12 14 16 18 20
k

(j)

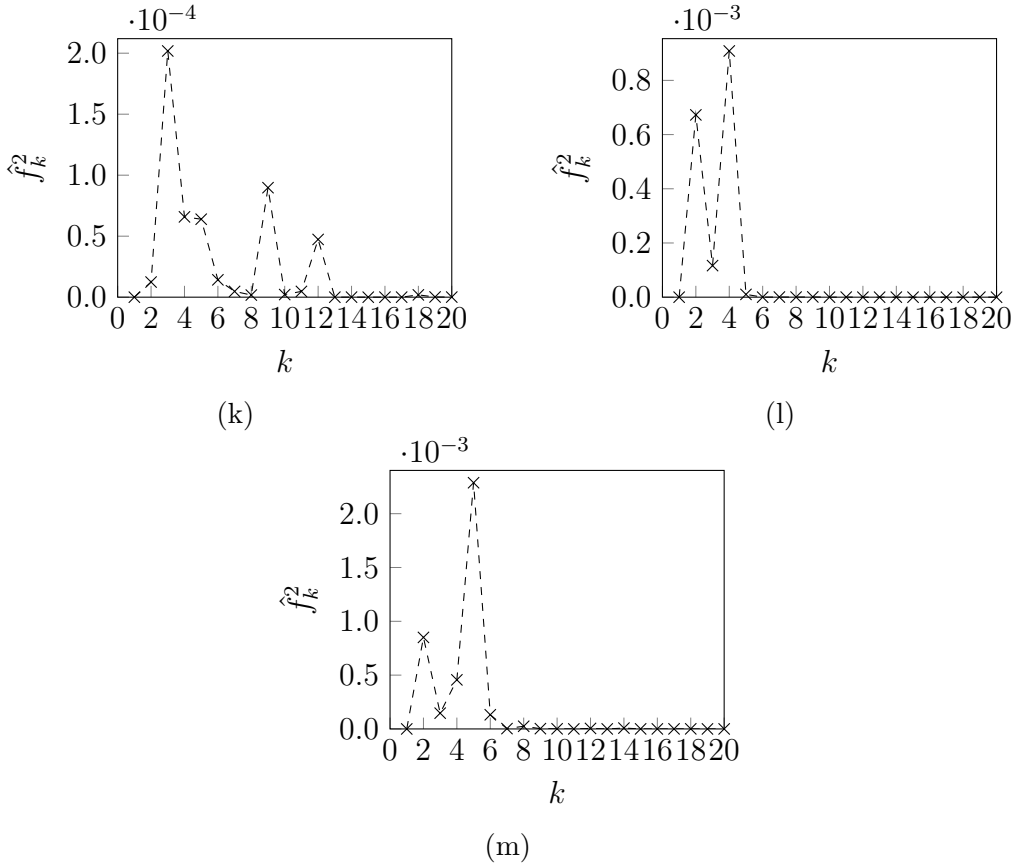

Figure A.5: Power spectra of the angular pair-correlation functions computed from the mat images in Figure A.4, taken at the end of the mat formation experiment.

Appendix B

Numerical Methods

In this appendix, we describe the numerical methods used throughout the thesis. We first introduce our method of solving the reaction–diffusion model in two dimensions, which is used to produce results in Chapter 3. We then discuss the methods used to solve the axisymmetric thin-film models. This covers both the extensional flow and lubrication regimes, the results of which are relevant to Chapters 5 and 6 respectively.

B.1 Reaction–Diffusion Model

We compute solutions to the two-dimensional reaction–diffusion model (3.40) on an equispaced Cartesian grid. We define Δx and Δy to be the constant grid spacing in the x and y directions respectively, and Δt is the constant time step size. We denote the cell density $n_{i,j}^k = n(x_i, y_j, t^k)$ and nutrient concentration $g_{i,j}^k = g(x_i, y_j, t^k)$, where $i = 1, \ldots, N_x$, $j = 1, \ldots, N_y$, and $k = 1, \ldots N_t$ are indices of grid points x_i and y_j, and time steps t^k, respectively. To discretise the equations, we employ a second-order accurate central finite difference scheme in space, and a Crank–Nicolson scheme for time stepping. We linearise the equations by approximating the non-linear terms using known data from the previous time step. Under this scheme, discretising the model equations

(3.40) yields

$$\begin{aligned}
\frac{n_{i,j}^{k+1}-n_{i,j}^{k}}{\Delta t} &= \frac{D}{2}\left[\frac{n_{i,j}^{k}+n_{i+1,j}^{k}}{2\Delta x^2}n_{i+1,j}^{k+1}-\frac{n_{i+1,j}^{k}+2n_{i,j}^{k}+n_{i-1,j}^{k}}{2\Delta x^2}n_{i,j}^{k+1}\right.\\
&\quad+\frac{n_{i,j}^{k}+n_{i-1,j}^{k}}{2\Delta x^2}n_{i-1,j}^{k+1}+\frac{n_{i,j}^{k}+n_{i+1,j}^{k}}{2\Delta x^2}n_{i+1,j}^{k}\\
&\quad\left.-\frac{n_{i+1,j}^{k}+2n_{i,j}^{k}+n_{i-1,j}^{k}}{2\Delta x^2}n_{i,j}^{k}+\frac{n_{i,j}^{k}+n_{i-1,j}^{k}}{2\Delta x^2}n_{i-1,j}^{k}\right]\\
&\quad+\frac{D}{2}\left[\frac{n_{i,j}^{k}+n_{i,j+1}^{k}}{2\Delta y^2}n_{i,j+1}^{k+1}-\frac{n_{i,j+1}^{k}+2n_{i,j}^{k}+n_{i,j-1}^{k}}{2\Delta y^2}n_{i,j}^{k+1}\right.\\
&\quad+\frac{n_{i,j}^{k}+n_{i,j-1}^{k}}{2\Delta y^2}n_{i,j-1}^{k+1}+\frac{n_{i,j}^{k}+n_{i,j+1}^{k}}{2\Delta y^2}n_{i,j+1}^{k}\\
&\quad\left.-\frac{n_{i,j+1}^{k}+2n_{i,j}^{k}+n_{i,j-1}^{k}}{2\Delta y^2}n_{i,j}^{k}+\frac{n_{i,j}^{k}+n_{i,j-1}^{k}}{2\Delta y^2}n_{i,j-1}^{k}\right]\\
&\quad+\frac{1}{2}\left[n_{i,j}^{k+1}g_{i,j}^{k}+n_{i,j}^{k}g_{i,j}^{k}\right],
\end{aligned} \tag{B.1a}$$

$$\begin{aligned}
\frac{g_{i,j}^{k+1}-g_{i,j}^{k}}{\Delta t} &= \frac{1}{2}\left[\frac{g_{i+1,j}^{k+1}-2g_{i,j}^{k+1}+g_{i-1,j}^{k+1}}{\Delta x^2}+\frac{g_{i+1,j}^{k}-2g_{i,j}^{k}+g_{i-1,j}^{k}}{\Delta x^2}\right]\\
&\quad+\frac{1}{2}\left[\frac{g_{i,j+1}^{k+1}-2g_{i,j}^{k+1}+g_{i,j-1}^{k+1}}{\Delta y^2}+\frac{g_{i,j+1}^{k}-2g_{i,j}^{k}+g_{i,j-1}^{k}}{\Delta y^2}\right]\\
&\quad-\frac{1}{2}\left[n_{i,j}^{k}g_{i,j}^{k+1}+n_{i,j}^{k}g_{i,j}^{k}\right],
\end{aligned} \tag{B.1b}$$

for $i = 1, \ldots, N_x$, $j = 1, \ldots, N_y$, and $k = 1, \ldots N_t - 1$. We enforce periodic conditions on all spatial boundaries by defining fictitious grid points such that $n_{0,j}^k = n_{N_x,j}^k$, $n_{N_x+1,j}^k = n_{1,j}^k$, $n_{i,0}^k = n_{i,N_y}^k$, and $n_{i,N_y+1}^k = n_{i,1}^k$, and apply these in (B.1) at the relevant boundary points.

The discretised equations (B.1) define a linear system to solve for the $2N_xN_y$ unknowns $n_{i,j}^{k+1}$ and $g_{i,j}^{k+1}$, given knowledge of the solution at the previous time step, $n_{i,j}^k$ and $g_{i,j}^k$. We use the generalised minimal residual (GMRES) method to solve this system of equations at each time step. GMRES is an iterative method for solving linear systems $A\boldsymbol{x} = \boldsymbol{b}$, whereby the exact

solution is approximated by the vector in the n-th Krylov subspace,

$$\boldsymbol{x}_n \in K_n = \text{span}\{\boldsymbol{b}, A\boldsymbol{b}, A^2\boldsymbol{b}, \ldots, A^{n-1}\boldsymbol{b}\}, \tag{B.2}$$

that minimises the Euclidean norm of the residual $\boldsymbol{r}_n = A\boldsymbol{x}_n - \boldsymbol{b}$ [147]. An advantage of the method is that there is no need to define the matrix A explicitly, and we instead proceed by defining the matrix-vector product $A\boldsymbol{x}$, and the known vector $\boldsymbol{b}$ at each time step. At each time step, we use the solution at the previous time step as the initial guess, and accept the solution if the relative residual norm $\|\boldsymbol{r}_n\|/\|\boldsymbol{b}\| < 1 \times 10^{-6}$.

B.1.1 Convergence of the Numerical Method

To determine an appropriate grid spacing and time step size, we perform a grid convergence study using the test value of $D = 0.47$, which has a theoretical wave speed of $v = 0.34794$. In our tests, we solve (B.1) for $t \in [0, 100]$ using the theoretical travelling wave profiles as initial conditions, and compute the mean speed at which the front advances in the numerical solution. Convergence results using $\Delta x = \Delta y = 0.1$, and $\Delta t = 0.001$ are shown in Figure B.1.

The biofilm size exhibits approximately quadratic convergence with grid spacing and linear convergence with time step size. By fitting an appropriate polynomial to the data in Figures B.1a and B.1b and extrapolating, we can estimate the numerical wave speed in the zero grid spacing and time step limit respectively. Doing so, we find that when $\Delta t = 0.001$, the estimated wave speed as $\Delta x_i \to 0$ is $v = 0.34778$. When $\Delta x_i = 0.1$, the estimated wave speed as $\Delta t \to 0$ is $v = 0.34809$. As these are both accurate to within 0.05% of the theoretical value, we adopt $\Delta x = \Delta y = 0.1$ and $\Delta t = 0.001$ in all numerical solutions.

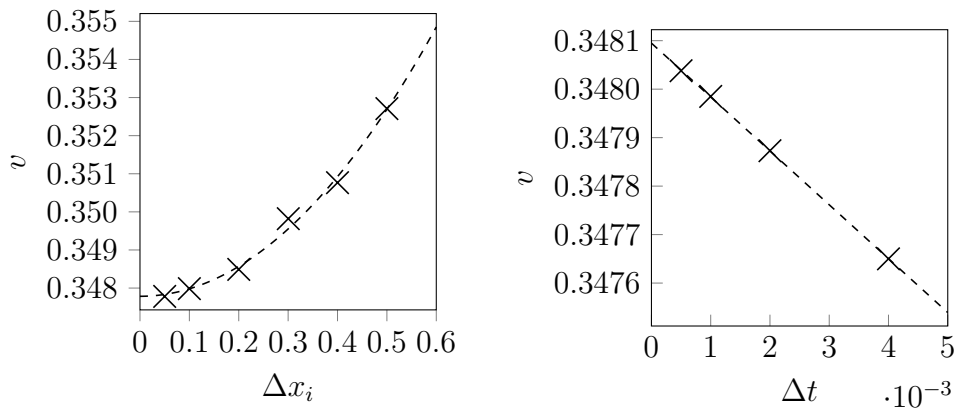

(a) Numerical results for $\Delta t = 0.001$, and Δx, $\Delta y \to 0$.

(b) Numerical results for $\Delta x = \Delta y = 0.1$, and $\Delta t \to 0$.

Figure B.1: Numerical convergence results for the scheme (B.1), solved with the GMRES iterative method. For each data point, we plot the mean wave speed computed at $t = 100$.

B.1.2 Circular Numerical Solutions

In §3.3.2, we computed two-dimensional numerical solutions to the reaction–diffusion model in circular geometry. To test whether the planar linear stability results are accurate in circular geometry, we used initial conditions with random perturbations of the form (3.48). Full details of these random perturbations (before normalisation) appear in Tables B.1–B.3 below. The corresponding power spectra of the initial condition (left panel) and numerical solution at $t = 10$ (right panel) are presented in Figure B.2–B.4.

Table B.1: Ensembles of random perturbations used in two-dimensional circular numerical solutions to the reaction–diffusion model with $D = 0.181$.

Coefficient	Trial 1	Trial 2	Trial 3
α_2	0.313	-0.741	-0.114
α_3	0.665	0.541	0.846
α_4	0.959	-0.416	0.752
α_5	0.079	0.458	0.968
α_6	0.357	0.695	-0.598
α_7	0.972	-0.888	0.097
α_8	-0.075	-0.593	-0.399
α_9	0.698	-0.304	0.726
α_{10}	0.069	-0.919	-0.506
α_{11}	0.785	0.425	0.542
α_{12}	-0.973	-0.672	-0.347

Table B.2: Ensembles of random perturbations used in two-dimensional circular numerical solutions to the reaction–diffusion model with $D = 0.47$.

Coefficient	Trial 1	Trial 2	Trial 3
α_2	0.827	-0.333	-0.609
α_3	0.323	-0.582	0.818
α_4	0.815	0.841	-0.591
α_5	-0.595	-0.505	0.205
α_6	0.052	0.078	0.540
α_7	-0.482	-0.094	-0.446
α_8	-0.977	0.005	-0.132
α_9	0.841	-0.742	0.868
α_{10}	0.192	0.335	0.661
α_{11}	0.617	-0.783	-0.166
α_{12}	0.688	-0.672	-0.405

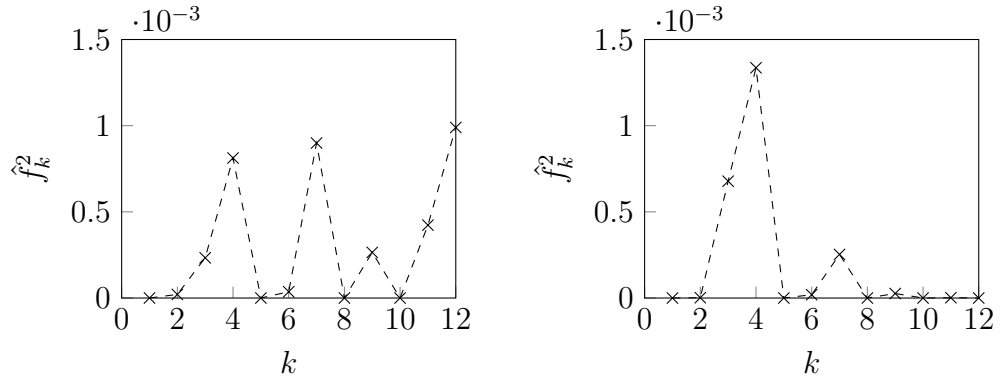

(a) Trial 1

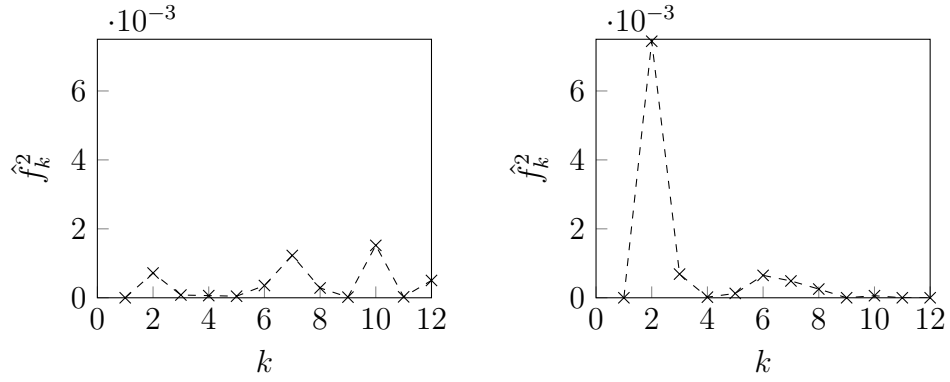

(b) Trial 2

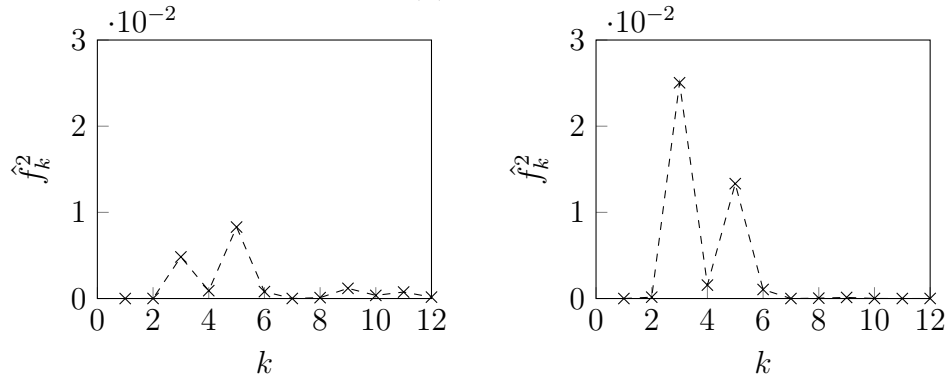

(c) Trial 3

Figure B.2: Power spectra of the initial condition (left panels) and two-dimensional circular numerical solutions at $t = 10$ (right panels), for $D = 0.181$. Initial conditions are given by (3.48), with the coefficients (before normalisation) given in Table B.1.

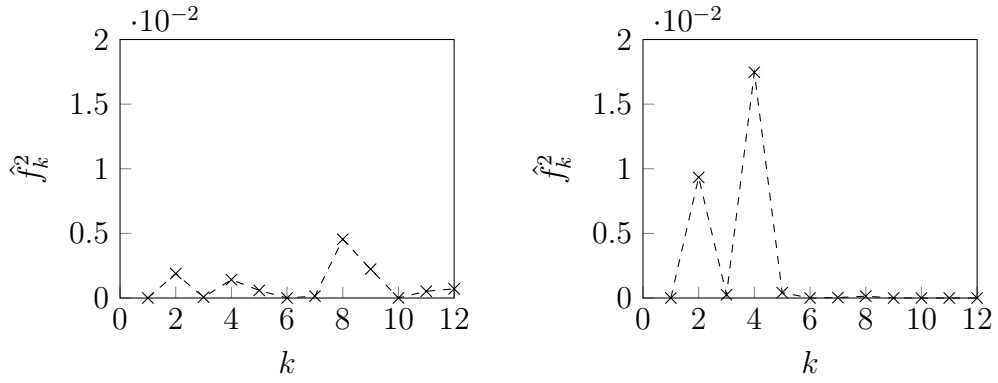

(a) Trial 1

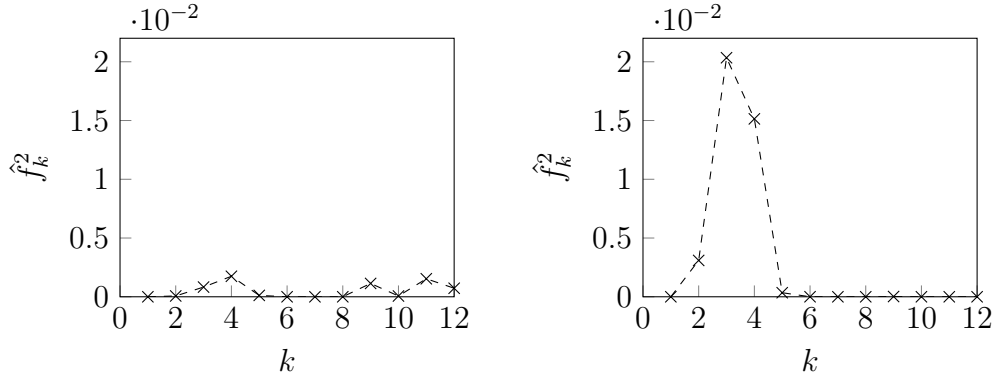

(b) Trial 2

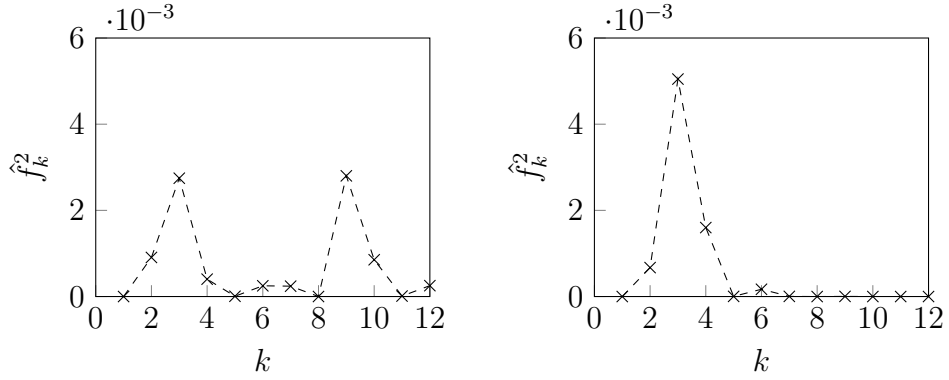

(c) Trial 3

Figure B.3: Power spectra of the initial condition (left panels) and two-dimensional circular numerical solutions at $t = 10$ (right panels), for $D = 0.47$. Initial conditions are given by (3.48), with the coefficients (before normalisation) given in Table B.2.

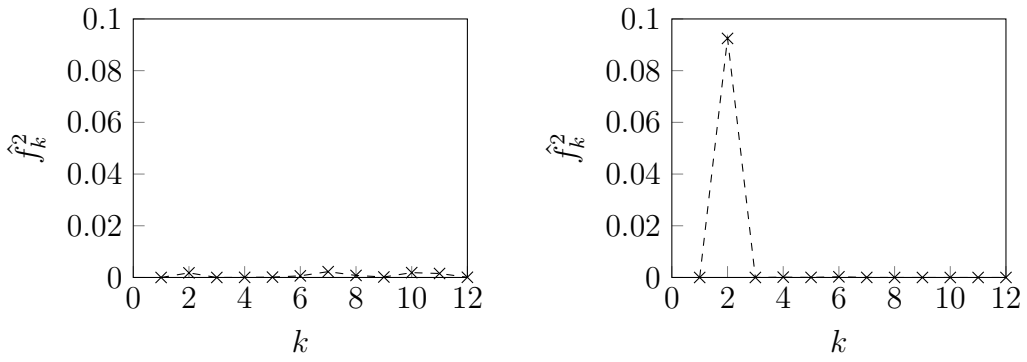

(a) Trial 1

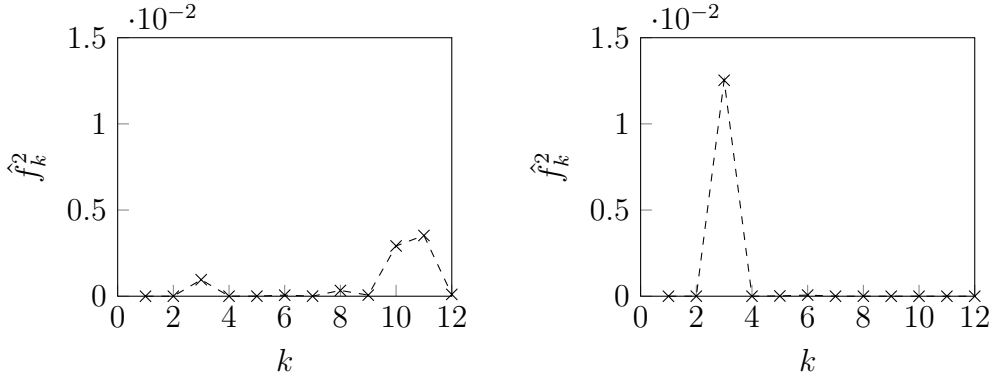

(b) Trial 2

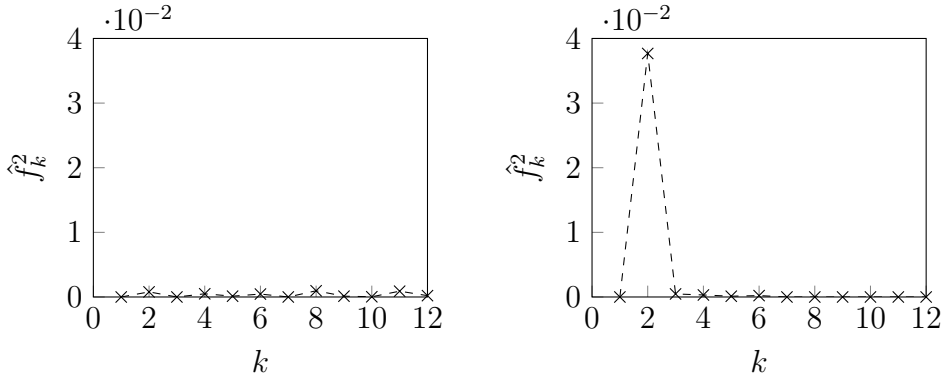

(c) Trial 3

Figure B.4: Power spectra of the initial condition (left panels) and two-dimensional circular numerical solutions at $t = 10$ (right panels), for $D = 1.02$. Initial conditions are given by (3.48), with the coefficients (before normalisation) given in Table B.3.

Table B.3: Ensembles of random perturbations used in two-dimensional circular numerical solutions to the reaction–diffusion model with $D = 1.02$.

Coefficient	Trial 1	Trial 2	Trial 3
α_2	-0.675	0.100	0.823
α_3	-0.008	0.703	0.166
α_4	-0.319	0.120	-0.690
α_5	-0.404	0.162	-0.464
α_6	0.533	0.402	-0.676
α_7	0.611	0.182	-0.182
α_8	0.529	-0.436	0.869
α_9	0.397	-0.252	0.589
α_{10}	0.724	0.840	0.434
α_{11}	-0.705	0.941	-0.853
α_{12}	0.260	0.292	-0.543

B.2 Axisymmetric Extensional Flow Model

We now describe the methods used to solve the thin-film models derived in Chapter 4. We first consider the extensional flow regime. As mentioned in §5.2, before solving the axisymmetric extensional flow model numerically, we apply the change of variables (5.13) to map both the biofilm and unoccupied Petri dish domains to the unit interval. The governing equations to solve then become

$$\frac{\partial h}{\partial \tau} - \frac{\xi}{S}\frac{\mathrm{d}S}{\mathrm{d}\tau}\frac{\partial h}{\partial \xi} + \frac{1}{S\xi}\frac{\partial}{\partial \xi}\left(\xi u_r h\right) = \left(1 + \Psi_m\right)\bar{\phi}_n g_b h, \tag{B.3a}$$

$$\frac{\partial \bar{\phi}_n}{\partial \tau} + \frac{1}{S}\left(u_r - \xi\frac{\mathrm{d}S}{\mathrm{d}\tau}\right)\frac{\partial \bar{\phi}_n}{\partial \xi} = \bar{\phi}_n\left[g_b - \Psi_d - \left(1 + \Psi_m\right)\bar{\phi}_n g_b\right], \tag{B.3b}$$

$$\frac{\partial g_s}{\partial \tau} - \frac{\xi}{S}\frac{\mathrm{d}S}{\mathrm{d}\tau}\frac{\partial g_s}{\partial \xi} = \frac{D}{S^2\xi}\frac{\partial}{\partial \xi}\left(\xi\frac{\partial g_s}{\partial \xi}\right) - DQ_s\left(g_s - g_b\right), \tag{B.3c}$$

$$\frac{\partial g_{so}}{\partial \tau} + \frac{1-\xi_o}{R-S}\frac{\mathrm{d}S}{\mathrm{d}\tau}\frac{\partial g_{so}}{\partial \xi_o} = \frac{D}{(R-S)^2}\frac{\partial^2 g_{so}}{\partial \xi_o^2} + \frac{D}{S(R-S)+\xi_o(R-S)^2}\frac{\partial g_{so}}{\partial \xi_o}, \tag{B.3d}$$

$$\mathrm{Pe}\left[h\frac{\partial g_b}{\partial \tau} - h\frac{\xi}{S}\frac{\mathrm{d}S}{\mathrm{d}\tau}\frac{\partial g_b}{\partial \xi} + \frac{1}{S\xi}\frac{\partial}{\partial \xi}\left(\xi u_r\left(1-\bar{\phi}_n\right)g_b h\right)\right] = \frac{1}{S^2\xi}\frac{\partial}{\partial \xi}\left(\xi h\frac{\partial g_b}{\partial \xi}\right) + Q_b\left(g_s - g_b\right) - \Upsilon\bar{\phi}_n g_b h, \tag{B.3e}$$

$$\frac{4}{S}\frac{\partial}{\partial \xi}\left[\frac{h}{\xi}\frac{\partial}{\partial \xi}\left(\xi u_r\right)\right] - \frac{2u_r}{S\xi}\frac{\partial h}{\partial \xi} = 2\left(1+\Psi_m\right)\frac{\partial}{\partial \xi}\left(\bar{\phi}_n g_b h\right) - \frac{\gamma^* h}{S^2}\frac{\partial}{\partial \xi}\left[\frac{1}{\xi}\frac{\partial}{\partial \xi}\left(\xi\frac{\partial h}{\partial \xi}\right)\right], \tag{B.3f}$$

$$\frac{\mathrm{d}S}{\mathrm{d}\tau} = u_r\left(1,\tau\right), \tag{B.3g}$$

where g_{so} denotes the nutrient concentration in the region of the substratum that is not occupied by the biofilm. Under the change of variables (5.13), the initial conditions are

$$S(0)=1, \quad h(\xi,0)=H_0\left(1-\xi^2\right), \quad \bar{\phi}_n(\xi,0)=1, \quad g_s(\xi,0)=g_{so}(\xi_o,0)=1, \quad g_b(\xi,0)=0, \tag{B.4}$$

the boundary conditions become

$$\left.\frac{\partial h}{\partial \xi}\right|_{(0,\tau)} = 0, \quad \left.\frac{\partial \bar{\phi}_n}{\partial \xi}\right|_{(0,\tau)} = 0, \quad \left.\frac{\partial g_s}{\partial \xi}\right|_{(0,\tau)} = 0, \quad \left.\frac{\partial g_b}{\partial \xi}\right|_{(0,\tau)} = 0, \quad u_r(0,\tau)=0, \tag{B.5a}$$

$$\left.\frac{\partial g_{so}}{\partial \xi_o}\right|_{(1,\tau)} = 0, \quad \left.\frac{\partial g_b}{\partial \xi}\right|_{(1,\tau)} = 0, \tag{B.5b}$$

$$\left.\frac{4}{S}\frac{\partial u_r}{\partial \xi}\right|_{(1,\tau)} + \frac{2u_r(1,\tau)}{S} = 2\left(1+\Psi_m\right)\bar{\phi}_n(1,\tau)g_b(1,\tau) - \left.\frac{\gamma^*}{S^2}\frac{\partial}{\partial \xi}\left(\xi\frac{\partial h}{\partial \xi}\right)\right|_{(1,\tau)}, \tag{B.5c}$$

and we must also satisfy the continuity conditions

$$g_s\left(1,\tau\right) = g_{so}\left(0,\tau\right), \quad \left.\frac{1}{S}\frac{\partial g_s}{\partial \xi}\right|_{(1,\tau)} = \left.\frac{1}{R-S}\frac{\partial g_{so}}{\partial \xi_o}\right|_{(0,\tau)}. \tag{B.6}$$

Producing a numerical solution to the 1D axisymmetric extensional flow model then requires solving the system (B.3), subject to (B.4)–(B.6), on $\xi \in [0,1]$, $\xi_o \in [0,1]$, and $\tau \in [0,T]$.

We solve the model on equispaced grids in time and space. For the time domain, we denote the discrete grid points by $\tau^k = (k-1)\Delta\tau$, for $k = 1,\ldots,N_\tau$, where $\Delta\tau = T/(N_\tau - 1)$. For both the biofilm and outer Petri dish domains, we define $\xi_j = (j-1)\Delta\xi$ and $\xi_{oj} = (j-1)\Delta\xi_o$ for $j = 1,\ldots,N_\xi$, where $\Delta\xi = 1/(N_\xi - 1)$ and $\Delta\xi_o = 1/(N_{\xi_o} - 1)$, to represent the discrete grid points. After prescribing the initial conditions, we first solve (B.3f) to determine the initial fluid velocity. Following this, at each time step we solve the equations in the order listed in (B.3), until the final time $\tau^{N_\tau} = T$ is reached.

We discretise the governing equations using a finite difference Crank–Nicolson scheme. Where necessary, we linearise non-linear terms using data from the previous time step. In the equations for h and u_r, we first expand relevant derivative terms using the product rule before discretising the equations. At the interior grid points $j = 2,\ldots N_\xi - 1$, the numerical scheme then reads

$$\begin{aligned}&\frac{h_j^k - h_j^{k-1}}{\Delta\tau} + \left(\frac{{u_r}_j^{k-1} - \xi_j {u_r}_{N_\xi}^{k-1}}{S^{k-1}}\right)\frac{h_{j+1}^{k-1/2} - h_{j-1}^{k-1/2}}{2\Delta\xi} \\ &+ \left(\frac{{u_r}_{j+1}^{k-1} - {u_r}_{j-1}^{k-1}}{2S^{k-1}\Delta\xi} + \frac{{u_r}_j^{k-1}}{S^{k-1}\xi_j}\right) h_j^{k-1/2} = \left(1+\Psi_m\right)\bar{\phi}_{nj}^{\,k-1} {g_b}_j^{k-1} h_j^{k-1/2},\end{aligned} \tag{B.7a}$$

$$\begin{aligned}&\frac{\bar{\phi}_{nj}^{\,k} - \bar{\phi}_{nj}^{\,k-1}}{\Delta\tau} + \left(\frac{{u_r}_j^{k-1} - \xi_j {u_r}_{N_\xi}^{k-1}}{S^{k-1}}\right)\frac{\bar{\phi}_{nj+1}^{\,k-1/2} - \bar{\phi}_{nj-1}^{\,k-1/2}}{2\Delta\xi} \\ &= \bar{\phi}_{nj}^{\,k-1/2}\left[{g_b}_j^{k-1} - \Psi_d - \left(1+\Psi_m\right)\bar{\phi}_{nj}^{\,k-1} {g_b}_j^{k-1}\right],\end{aligned} \tag{B.7b}$$

$$
\begin{aligned}
&\frac{g_{s_j}^{\,k} - g_{s_j}^{\,k-1}}{\Delta\tau} - \left(\frac{\xi_j u_{r_{N_\xi}}^{\,k-1}}{S^{k-1}}\right)\frac{g_{s_{j+1}}^{\,k-1/2} - g_{s_{j-1}}^{\,k-1/2}}{2\Delta\xi} \\
&= \frac{D}{\left(S^{k-1}\right)^2 \xi_j}\left[\frac{\left(\xi_{j+1}+\xi_j\right)\left(g_{s_{j+1}}^{\,k-1/2} - g_{s_j}^{\,k-1/2}\right)}{2\left(\Delta\xi\right)^2}\right] \\
&-\frac{D}{\left(S^{k-1}\right)^2 \xi_j}\left[\frac{\left(\xi_j+\xi_{j-1}\right)\left(g_{s_j}^{\,k-1/2} - g_{s_{j-1}}^{\,k-1/2}\right)}{2\left(\Delta\xi\right)^2}\right] \\
&-DQ_s\left(g_{s_j}^{\,k-1/2} - g_{b_j}^{\,k-1}\right),
\end{aligned}
\tag{B.7c}
$$

$$
\begin{aligned}
&\frac{g_{s_{oj}}^{\,k} - g_{s_{oj}}^{\,k-1}}{\Delta\tau} + \left(\frac{1-\xi_{oj}}{R-S^{k-1}}u_{r_{N_\xi}}^{\,k-1}\right)\frac{g_{s_{oj+1}}^{\,k-1/2} - g_{s_{oj-1}}^{\,k-1/2}}{2\Delta\xi_o} \\
&= \frac{D}{\left(R-S^{k-1}\right)^2}\frac{g_{s_{oj+1}}^{\,k-1/2} - 2g_{s_{oj}}^{\,k-1/2} + g_{s_{oj-1}}^{\,k-1/2}}{\left(\Delta\xi_o\right)^2} \\
&+\left[\frac{D}{S^{k-1}\left(R-S^{k-1}\right)+\xi_{oj}\left(R-S^{k-1}\right)^2}\right]\frac{g_{s_{oj+1}}^{\,k-1/2} - g_{s_{oj-1}}^{\,k-1/2}}{2\Delta\xi},
\end{aligned}
\tag{B.7d}
$$

$$
\begin{aligned}
&\mathrm{Pe}h_j^{k-1}\frac{g_{b_j}^{\,k} - g_{b_j}^{\,k-1}}{\Delta\tau} - \left(\frac{\mathrm{Pe}h_j^{k-1}\xi_j u_{r_{N_\xi}}^{\,k-1}}{S^{k-1}}\right)\frac{g_{b_{j+1}}^{\,k-1/2} - g_{b_{j-1}}^{\,k-1/2}}{2\Delta\xi} \\
&+\frac{\mathrm{Pe}}{S^{k-1}\xi_j}\frac{\left[\xi u_r\left(1-\bar{\phi}_n\right)h\right]_{j+1}^{k-1} g_{b_{j+1}}^{\,k-1/2} - \left[\xi u_r\left(1-\bar{\phi}_n\right)h\right]_{j-1}^{k-1} g_{b_{j-1}}^{\,k-1/2}}{2\Delta\xi} \\
&= \frac{1}{\left(S^{k-1}\right)^2\xi_j}\left[\frac{\left(\xi_{j+1}h_{j+1}^{k-1}+\xi_j h_j^{k-1}\right)\left(g_{b_{j+1}}^{\,k-1/2} - g_{b_j}^{\,k-1/2}\right)}{2\left(\Delta\xi\right)^2}\right] \\
&-\frac{1}{\left(S^{k-1}\right)^2\xi_j}\left[\frac{\left(\xi_j h_j^{k-1}+\xi_{j-1}h_{j-1}^{k-1}\right)\left(g_{b_j}^{\,k-1/2} - g_{b_{j-1}}^{\,k-1/2}\right)}{2\left(\Delta\xi\right)^2}\right] \\
&+Q_b\left(g_{s_j}^{\,k-1} - g_{b_j}^{\,k-1/2}\right) - \Upsilon\bar{\phi}_{n_j}^{\,k-1} g_{b_j}^{\,k-1/2} h_j^{k-1},
\end{aligned}
\tag{B.7e}
$$

$$\left(\frac{4h_j^k}{S^{k-1}}\right)\frac{u_{r}{}_{j+1}^{k}-2u_{r}{}_{j}^{k}+u_{r}{}_{j-1}^{k}}{(\Delta\xi)^2}$$
$$+\frac{4}{S^{k-1}}\left(\frac{h_{j+1}^k-h_{j-1}^k}{2\Delta\xi}+\frac{h_j^k}{\xi_j}\right)\frac{u_{r}{}_{j+1}^{k}-u_{r}{}_{j-1}^{k}}{2\Delta\xi}$$
$$+\frac{2}{S^{k-1}\xi_j}\left(\frac{h_{j+1}^k-h_{j-1}^k}{2\Delta\xi}-\frac{2h_j^k}{\xi_j}\right)u_{r}{}_{j}^{k} \tag{B.7f}$$
$$=2\left(1+\Psi_m\right)\left[\frac{\left(\bar{\phi}_n g_b h\right)_{j+1}^{k}-\left(\bar{\phi}_n g_b h\right)_{j-1}^{k}}{2\Delta\xi}\right]-\Gamma_j^k,$$

$$\frac{S^k-S^{k-1}}{\Delta\tau}=u_{r}{}_{N_\xi}^{k-1/2}, \tag{B.7g}$$

where we approximate terms at the half time steps using

$$h_j^{k-1/2}=\frac{h_j^k+h_j^{k-1}}{2}, \tag{B.8}$$

and so on. In (B.7f), Γ_j^k denotes the discretised surface tension term, which we discuss in detail later. In conjunction with appropriate boundary schemes, each equation in (B.7) describes a linear system to solve for the variables at $\tau=\tau^k$.

We need to take particular care at domain boundaries to prevent spurious oscillations appearing in the solution. At $\xi=0$ and $\xi_o=0$, we obtained the best results by substituting the boundary conditions into discretised forms of the equations (B.3c) and (B.3e), using one-sided differences for first derivative terms and introducing fictitious grid points for second derivative terms. For (B.3a), (B.3b), (B.3d) and (B.3f) we apply the relevant boundary conditions explicitly. Although the equations (B.3c) and (B.3e) are singular at $\xi=0$, we can use L'Hôpital's rule to evaluate the relevant terms as $\xi\to 0$. The boundary schemes are then

$$\frac{-3h_1^k+4h_2^k-h_3^k}{2\Delta\xi}=0, \tag{B.9a}$$

$$\frac{-3\phi_{n1}^{\ k} + 4\phi_{n2}^{\ k} - \phi_{n3}^{\ k}}{2\Delta\xi} = 0, \tag{B.9b}$$

$$\frac{g_{s1}^{\ k} - g_{s1}^{\ k-1}}{\Delta\tau} = \frac{4D}{\left(S^{k-1}\right)^2}\frac{g_{s2}^{\ k-1/2} - g_{s1}^{\ k-1/2}}{\left(\Delta\xi\right)^2} - DQ_s\left(g_{s1}^{\ k-1/2} - g_{b1}^{\ k-1}\right), \tag{B.9c}$$

$$g_{so1}^{\ k} = a, \tag{B.9d}$$

$$\begin{aligned} &\mathrm{Pe}h_1^{k-1}\frac{g_{b1}^{\ k} - g_{b1}^{\ k-1}}{\Delta\tau} \\ &+\frac{\mathrm{Pe}\left(1-\bar{\phi}_{n1}^{\ k-1}\right)h_1^{k-1}\left(-3u_{r1}^{\ k-1} + 4u_{r2}^{\ k-1} - u_{r3}^{\ k-1}\right)}{S^{k-1}\Delta\xi}g_{b1}^{\ k-1/2} \\ &= \frac{4h_1^{k-1}}{\left(S^{k-1}\right)^2}\frac{g_{b2}^{\ k-1/2} - g_{b1}^{\ k-1/2}}{\left(\Delta\xi\right)^2} + Q_b\left(g_{b1}^{\ k-1/2} - g_{s1}^{\ k}\right) \\ &-\Upsilon\bar{\phi}_{n1}^{\ k-1}g_{b1}^{\ k-1/2}h_1^{k-1}, \end{aligned} \tag{B.9e}$$

$$u_{r1}^{\ k} = 0, \tag{B.9f}$$

where a is the value of $g_s(S(t),t)$. At $\xi = 1$ and $\xi_o = 1$, we solve the equations (B.3a), (B.3b) and (B.3d) directly, again using one-sided differences for first derivatives and introducing fictitious grid points for second derivatives. We apply the Dirichlet condition for g_s, and as (B.3e) is singular as $h \to 0$, we impose the boundary condition for g_b directly using a one-sided difference. We also obtained best results by applying the zero radial stress condition (B.5c) directly at $\xi = 1$. The boundary schemes are then

$$\begin{aligned} &\frac{h_{N_\xi}^{k} - h_{N_\xi}^{k-1}}{\Delta\tau} + \left(\frac{3u_{rN_\xi}^{\ k-1} - 4u_{rN_\xi-1}^{\ k-1} + u_{rN_\xi-2}^{\ k-1}}{2S^{k-1}\Delta\xi} + \frac{u_{rN_\xi}^{\ k-1}}{S^{k-1}}\right)h_{N_\xi}^{k-1/2} \\ &= \left(1+\Psi_m\right)\bar{\phi}_{nN_\xi}^{\ k-1}g_{bN_\xi}^{\ k-1}h_{N_\xi}^{k-1/2}, \end{aligned} \tag{B.10a}$$

$$\frac{\bar{\phi}_{nN_\xi}^{\ k} - \bar{\phi}_{nN_\xi}^{\ k-1}}{\Delta\tau} = \bar{\phi}_{nN_\xi}^{\ k-1/2}\left[g_{bN_\xi}^{\ k-1} - \Psi_d - \left(1+\Psi_m\right)\bar{\phi}_{nN_\xi}^{\ k-1}g_{bN_\xi}^{\ k-1}\right], \tag{B.10b}$$

$$g_{sN_\xi}^{\ k} = a, \tag{B.10c}$$

$$\frac{g_{soN_\xi}^{\ k} - g_{soN_\xi}^{\ k-1}}{\Delta\tau} = \frac{D}{\left(R-S\right)^2}\frac{2g_{soN_\xi-1}^{\ k-1/2} - 2g_{soN_\xi}^{\ k-1/2}}{\left(\Delta\xi\right)^2}, \tag{B.10d}$$

$$\frac{3g_{b}{}^{k}_{N_\xi} - 4g_{b}{}^{k}_{N_\xi-1} + g_{b}{}^{k}_{N_\xi-2}}{2\Delta\xi} = 0, \tag{B.10e}$$

$$\begin{aligned}\frac{2}{S^{k-1}}\left(\frac{3u_{r}{}^{k}_{N_\xi} - 4u_{r}{}^{k}_{N_\xi-1} + u_{r}{}^{k}_{N_\xi-2}}{\Delta\xi} + u_{r}{}^{k}_{N_\xi}\right) \\ = 2\left(1+\Psi_m\right)\bar{\phi}_{n}{}^{k}_{N_\xi} g_{b}{}^{k}_{N_\xi} - \Gamma^{k}_{N_\xi},\end{aligned} \tag{B.10f}$$

where $\Gamma^{k}_{N_\xi}$ is the contribution of surface tension to the no radial stress boundary condition (B.5c).

For the surface tension terms, we expand the derivative terms and write

$$\Gamma^{k}_{j} = \frac{h^{k}_{j}}{(S^{k})^2}\left[\frac{\partial^3 h}{\partial\xi^3} + \frac{1}{\xi}\frac{\partial^2 h}{\partial\xi^2} - \frac{1}{\xi^2}\frac{\partial h}{\partial\xi}\right]^{k}_{j}, \quad \text{for} \quad j = 2, \dots N_\xi - 1, \tag{B.11a}$$

$$\Gamma^{k}_{N_\xi} = \frac{1}{(S^{k})^2}\left[\xi\frac{\partial^2 h}{\partial\xi^2} + \frac{\partial h}{\partial\xi}\right]^{k}_{N_\xi}. \tag{B.11b}$$

To compute the first spatial derivative of h, we use standard sixth-order accurate finite difference formulae. We then use the same scheme to compute the higher derivatives sequentially, that is

$$\frac{\partial^2 h}{\partial\xi^2} = \frac{\partial}{\partial\xi}\left(\frac{\partial h}{\partial\xi}\right), \quad \text{and} \quad \frac{\partial^3 h}{\partial\xi^3} = \frac{\partial}{\partial\xi}\left[\frac{\partial}{\partial\xi}\left(\frac{\partial h}{\partial\xi}\right)\right], \tag{B.12}$$

where we use the same sixth-order finite difference scheme for each derivative. This applies a sixth-order accurate finite difference scheme over a wider stencil than the standard formulae. When $\gamma^* \neq 0$, we required a larger number of time steps to produce solutions without spurious oscillations in the surface tension term. Therefore, all solutions involving surface tension were computed with $N_\xi = 1001$ and $N_t = 2000001$. The convergence analysis in §B.2.1 suggests that these solutions will have a relative error of approximately 0.4%.

A feature of our model is that finding the nutrient concentration in the substratum requires solving both (B.3c) and (B.3d), and ensuring that the continuity conditions (B.6) are satisfied. To do this, we first solve (B.3c)

and (B.3d), subject to the Dirichlet conditions $g_s(1,\tau^k) = g_{s_o}(0,\tau^k) = a$, with $a = g_s(1,\tau^{k-1})$, as an initial guess. We then define and compute

$$f(a) = \frac{1}{R-S}\frac{\partial g_{s_o}}{\partial \xi_o}\bigg|_{(0,\tau)} - \frac{1}{S}\frac{\partial g_s}{\partial \xi}\bigg|_{(1,\tau)}, \tag{B.13}$$

where a is the initial guess, and we approximate both derivatives in (B.13) using second-order accurate one-sided finite differences. To satisfy the continuity condition (B.6), we require $f(a) = 0$, which we achieve numerically using Newton's method. We compute the derivative

$$\frac{\mathrm{d}f}{\mathrm{d}a} = \frac{f(a+\delta) - f(a)}{\delta}, \tag{B.14}$$

for $\delta = 1 \times 10^{-6}$, and iterate until a is accurate to 1×10^{-6}. This procedure allows us to solve for g_s over the entire Petri dish domain at each time step.

B.2.1 Convergence of the Numerical Method

We used $N_\xi = 8001$ grid points and $N_\tau = 160001$ time steps in the numerical solutions for $\gamma^* = 0$ in §5.2, giving $\Delta\xi = 1.25 \times 10^{-4}$ and $\Delta\tau = 9.93 \times 10^{-5} \approx 1 \times 10^{-4}$. To verify that this is sufficient to produce a converged solution, we repeat the computation using a range of grid spacings and time step sizes. In each case, we compute the contact line position at $\tau = 15.9$, which yields the results shown in Figure B.5. The contact line position exhibits linear convergence with both grid spacing and time step size. By fitting a straight line to the data in Figure B.5 and extrapolating, we can estimate the numerical contact line position in the zero grid spacing and time step limit. Doing so, we find that when $\Delta\tau \approx 1 \times 10^{-4}$, the estimated contact line position as $\Delta\xi \to 0$ is $S(T) = 13.1752$. When $\Delta\xi = 1.25 \times 10^{-4}$, the estimated contact line position as $\Delta\tau \to 0$ is $S(T) = 13.1678$. As these are within approximately 0.05% of each other and the numerical value for the chosen grid spacing and time step size, $S(T) = 13.1681$, we conclude that our numerical solution is sufficiently converged.

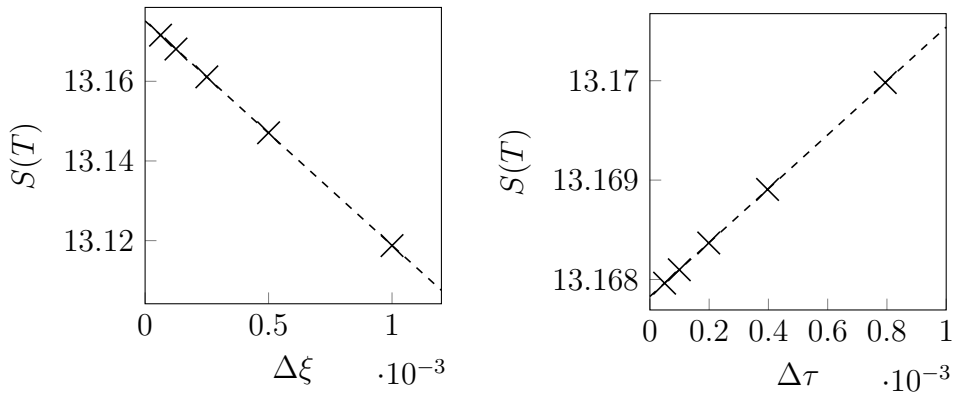

(a) Numerical results for $\Delta\tau \approx 1 \times 10^{-4}$, and $\Delta\xi \to 0$.

(b) Numerical results for $\Delta\xi = 1.25 \times 10^{-4}$, and $\Delta\tau \to 0$.

Figure B.5: Convergence of the numerical scheme used to solve the axisymmetric extensional flow model. At each data point, we plot the biofilm radius attained at the experimental time $\tau = T$.

B.3 Axisymmetric Lubrication Model

Here, we describe the numerical schemes used to solve the thin-film lubrication model, which describes biofilm expansion driven by strong adhesion and surface tension. In this model, we consider three cases. First, we describe our non-linear Crank–Nicolson method of solving the generalised lubrication equation for the biofilm height. We demonstrate that our method converges, and then proceed to the full thin-film lubrication model. This requires the solution of a two-dimensional hyperbolic PDE for the cell volume fraction, an additional equation for the vertical fluid velocity, and equations for nutrient concentrations. Finally, we consider the one-dimensional simplified model, which provides a good approximation to the full model while saving computational time.

B.3.1 Generalised Lubrication Equation

We present the numerical method used to solve the generalised lubrication equation for conservation of total fluid mass. This equation is

$$\frac{\partial h}{\partial t} + \frac{\gamma^*}{3r}\frac{\partial}{\partial r}\left\{ rh^3 \frac{\partial}{\partial r}\left[\frac{1}{r}\frac{\partial}{\partial r}\left(r\frac{\partial h}{\partial r}\right)\right]\right\} = J, \tag{B.15}$$

and is the no-slip model of Ward and King [120] written in radial geometry. We solve (B.15) on the domain $r \in [0, R]$, and $t \in [0, T]$, subject to some initial condition $h(r, 0) = H_0(r)$, and the boundary conditions

$$\left.\frac{\partial h}{\partial r}\right|_{(0,t)} = 0, \quad \left.\frac{\partial^3 h}{\partial r^3}\right|_{(0,t)} = 0, \quad h(R, t) = b, \quad \left.\frac{\partial h}{\partial r}\right|_{(R,t)} = 0. \tag{B.16}$$

We discretise (B.15) on equispaced grids in space and time, defining $r_j = (j-1)\Delta r$ and $t^k = (k-1)\Delta t$ for $j = 1, \ldots, N_r$, and $k = 1, \ldots N_t$, where Δr and Δt are the constant grid spacing and time step size respectively. To solve the equation, we implement a fully non-linear Crank–Nicolson scheme [158], and use Newton iteration to address the non-linearity in h. Under this scheme, the discretisation of (B.15) is

$$\begin{aligned}\frac{h_j^k - h_j^{k-1}}{\Delta t} + \frac{\gamma^*}{3r_j(\Delta r)^4}\Big\{ & r_{j+1/2}\left(h^3\right)_{j+1/2}^{k-1/2}\Theta\left(h_{j+1/2}^{k-1/2}\right) \\ & - r_{j-1/2}\left(h^3\right)_{j-1/2}^{k-1/2}\Theta\left(h_{j-1/2}^{k-1/2}\right)\Big\} = J_j^{k-1/2},\end{aligned} \tag{B.17}$$

for the interior grid points $j = 3, \ldots N_r - 2$. In writing (B.17), we have defined the function

$$\begin{aligned}\Theta\left(h_j\right) = \frac{1}{(\Delta r)^3}\Bigg[& \frac{r_{j+1}(h_{j+3/2} - h_{j+1/2}) - r_j(h_{j+1/2} - h_{j-1/2})}{r_{j+1/2}} \\ & - \frac{r_j(h_{j+1/2} - h_{j-1/2}) - r_{j-1}(h_{j-1/2} - h_{j-3/2})}{r_{j-1/2}}\Bigg],\end{aligned} \tag{B.18}$$

which is linear in h. The equation (B.18) represents a discretisation of the

third-order term

$$\Theta = \frac{\partial}{\partial r}\left[\frac{1}{r}\frac{\partial}{\partial r}\left(r\frac{\partial h}{\partial r}\right)\right], \tag{B.19}$$

which appears in (B.15). As in previous schemes, we approximate terms defined at half points using the averaging

$$h^k_{j+1/2} = \frac{h^k_{j+1} + h^k_j}{2}, \quad \text{and} \quad h^{k-1/2}_j = \frac{h^k_j + h^{k-1}_j}{2}, \tag{B.20}$$

for the spatial and temporal grids respectively.

As Θ depends on h, the discretisation (B.17) is non-linear in h, and requires Newton iteration to solve. To derive the linear system for the Newton iteration, at each time step we make the initial guess $(h^k_j)^{(0)} = h^{k-1}_j$, and update the solution using

$$(h^k_j)^{(n+1)} = (h^k_j)^{(n)} + \tilde{h}, \tag{B.21}$$

where $\tilde{h}$ is the correction term, and the index n represents the number of Newton iterations. To derive a linear system for the correction, we substitute (B.21) into (B.17). For sufficiently small time step size, we expect the correction term $\tilde{h}$ to be small. We thus ignore terms of $\mathcal{O}(\tilde{h}^2)$, and obtain the linear system

$$\begin{aligned}
&\frac{\tilde{h}_j}{\Delta t} + \frac{\gamma^*}{6r_j(\Delta r)^4}\left[r_{j+1/2}(h^3)^k_{j+1/2}\Theta(\tilde{h}_{j+1/2})\right. \\
&\qquad \left. -r_{j-1/2}(h^3)^k_{j-1/2}\Theta(\tilde{h}_{j-1/2})\right] \\
&+\frac{\gamma^*}{6r_j(\Delta r)^4}\left[3r_{j+1/2}(h^2)^k_{j+1/2}\Theta(h^k_{j+1/2})\tilde{h}_{j+1/2}\right. \\
&\left. -3r_{j-1/2}(h^2)^k_{j-1/2}\Theta(h^k_{j-1/2})\tilde{h}_{j-1/2}\right] - \frac{\tilde{h}_j}{2}\left[\frac{\partial J}{\partial h}\right]^k_j \\
&= -\frac{h^k_j - h^{k-1}_j}{\Delta t} - \frac{\gamma^*}{3r_j(\Delta r)^4}\left[r_{j+1/2}(h^3)^{k-1/2}_{j+1/2}\Theta(h^{k-1/2}_{j+1/2})\right. \\
&\left. -r_{j-1/2}(h^3)^{k-1/2}_{j-1/2}\Theta(h^{k-1/2}_{j-1/2})\right] + \frac{J(h^k_j) + J(h^{k-1}_j)}{2}.
\end{aligned} \tag{B.22}$$

Given the initial guess for h_j^k, we then solve (B.22) for the corrections $\tilde{h}$, update the guess using (B.21), and iterate until $\|\tilde{h}\| < \delta$, where we use the tolerance $\delta = 1 \times 10^{-6}$. This scheme is then used to compute solutions to (B.15), and provides a framework for solving the generalised lubrication equations that appear in our full model and one-dimensional simplification.

Convergence

Before solving the full two-dimensional model, we investigate the numerical convergence of solutions to (B.15). As per Ward and King [120], we use the source term

$$J = H\left(h - h^*\right)\left[\frac{1}{\sqrt{\sigma}}\tanh\left(\sqrt{\sigma}h\right) - \rho h\right], \tag{B.23}$$

which we can discretise as

$$J_j^k = H\left(h_j^k - h^*\right)\left[\frac{1}{\sqrt{\sigma}}\tanh\left(\sqrt{\sigma}h_j^k\right) - \rho h_j^k\right]. \tag{B.24}$$

Equation (B.22) also involves the derivative of (B.23) with respect to h, which in discretised form is

$$\left[\frac{\partial J}{\partial h}\right]_j^k = H\left(h_j^k - h^*\right)\left[\operatorname{sech}^2\left(\sqrt{\sigma}h_j^k\right) - \rho\right] \tag{B.25}$$

respectively. We then use the non-linear Crank–Nicolson scheme to compute numerical solutions to the generalised lubrication equation (B.15).

Unlike the extensional flow regime, in the lubrication regime the contact line position is not computed directly. Therefore, to investigate convergence we instead use the sequence

$$\left(e_{rel}\right)_i = \frac{\|h_i - h_{N_g}\|}{\|h_{N_g}\|}, \tag{B.26}$$

where $\|\cdot\|$ represents the L^2-norm, and $(h)_i$ for $i = 1, \ldots, N_g$ represent numerical solutions to (B.15) computed with successively finer grids. When

computing $\|h_i - h_{N_g}\|$, we ensure the vectors are the same length by sampling at the coarsest grid spacing used. The sequence (B.26) contains the relative errors in numerical solutions with successively finer grids, which we can use to compute the rate of convergence.

To investigate convergence with both space and time, we compute solutions with $\Delta r = \Delta t$, and refine both simultaneously. In all numerical solutions we use the dish size $R = 10$, and compute solutions until $t = 130$, as in Ward and King [120]. For each successive solution, we double the number of grid points and time steps, and compute the relative error norm (B.26) once all solutions are complete. A log-log plot of these results is presented in Figure B.6. We

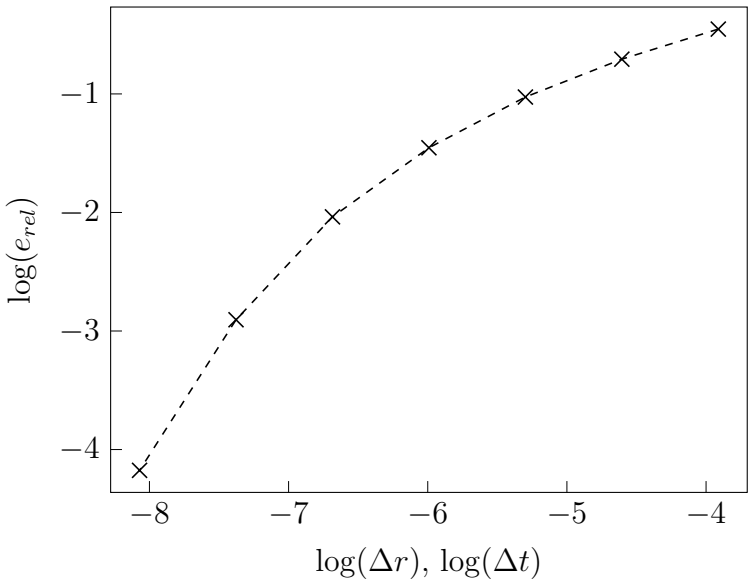

Figure B.6: A log-log plot of the relative norm (B.26) of the differences between numerical solutions to the Ward–King model at successively finer grid spacings. In each solution we use $\Delta r = \Delta t$. The slope of the graph indicates the rate of convergence of the numerical method with both time and space.

observe that the relative error norm (B.26) converges to zero as we refine the grids. The rate of convergence, given by the slope of the graph, appears to approach 2 as $\Delta r, \Delta t \to 0$ (between the two finest grids, the slope of the log-log plot is 1.833). This is consistent with theory, which predicts that the

non-linear Crank–Nicolson method will converge quadratically in both space and time.

B.3.2 Two-Dimensional Full Model

We now outline the numerical method used to solve the full two-dimensional lubrication model. This method builds on the scheme described in Appendix B.3.1, which we use to solve the mass conservation equation for the biofilm height, (6.2a). The only change is that here we consider the source term $J = H(h - h^*)[(1 + \Psi_m)\bar{\phi}_n g_b h]$, which we discretise as

$$J_j^k = H\left(h_j^k - h^*\right)\left[(1 + \Psi_m)\,\bar{\phi}_{n_j}^{\,k} g_{b_j}^{\,k} h_j^k\right]. \tag{B.27}$$

The numerical method also requires us to discretise the derivative of J with respect to h, which gives

$$\left[\frac{\partial J}{\partial h}\right]_j^k = H\left(h_j^k - h^*\right)\left[(1 + \Psi_m)\,\bar{\phi}_{n_j}^{\,k} g_{b_j}^{\,k}\right]. \tag{B.28}$$

We then solve for h using the non-linear Crank–Nicolson method of Appendix B.3.1.

Next, we describe our method for solving for the cell volume fraction, $\phi_n(r, z, t)$. Unlike the other variables, the cell volume fraction varies z, and the equation for ϕ_n (6.2b) needs to be solved on the domain $0 < r < R$, and $0 < z < h(r, t)$, which changes with time. To solve (6.2b), we make a change of variables to map the moving biofilm domain to a rectangle. Introducing

$$(\xi, \zeta, \tau) = \left(r, \frac{z}{h}, t\right), \tag{B.29}$$

we can re-write (6.2b) as

$$\frac{\partial \phi_n}{\partial \tau} + \frac{A_1}{\xi}\frac{\partial}{\partial \xi}\left(\xi h^2 \Theta \phi_n\right) + A_2 \frac{\partial \phi_n}{\partial \zeta} = A_3 \phi_n, \tag{B.30}$$

where Θ is given by (B.19). The new coefficients are given by

$$A_1(\xi,\zeta,\tau) = -\gamma^*\zeta\left(\frac{\zeta}{2}-1\right), \tag{B.31a}$$

$$A_2(\xi,\zeta,\tau) = \frac{u_\zeta}{h} - \frac{\zeta}{h}\frac{\partial h}{\partial \tau} + \gamma^* h\Theta\frac{\partial h}{\partial \xi}\zeta^2\left(\frac{\zeta}{2}-1\right), \tag{B.31b}$$

$$A_3(\xi,\zeta,\tau) = g_b - \Psi_d - \frac{1}{h}\frac{\partial u_\zeta}{\partial \zeta} - \gamma^*\zeta\left(\zeta-1\right)h\Theta\frac{\partial h}{\partial \xi}, \tag{B.31c}$$

where $u_\zeta = u_z$ is the vertical velocity component in the new variables. The advantage of writing the equation in the form (B.30) is that the equation is defined for the fixed rectangular domain $(r,\zeta) \in (0,R)\times(0,1)$.

To obtain a solution for ϕ_n, we solve (B.30) subject to the boundary condition

$$\left.\frac{\partial \phi_n}{\partial \xi}\right|_{(0,\zeta,\tau)} = 0, \tag{B.32}$$

and some suitable initial condition. As with previous schemes, we adopt equispaced grids (ξ_i,ζ_j,τ^k), with $\xi_i = (i-1)\Delta\xi$, $\zeta_j = (j-1)\Delta\zeta$, and $\tau^k = (k-1)\Delta\tau$, for $i = 1,\dots,N_\xi$, $j = 1,\dots N_\zeta$, and $k = 1,\dots N_\tau$, and where $\Delta\xi$, $\Delta\zeta$, and $\Delta\tau$ are the constant spacings for each variable. When solving (B.30), we use solutions computed at the previous time step to obtain the coefficients (B.31). In doing so, we compute derivatives with respect to ξ using standard second-order accurate finite difference formulae, and replace the time derivative in (B.31b) with a discretised form of the right-hand side of (6.2a). To discretise Θ, we use the scheme (B.18) for interior grid points $j = 3,\dots N_r-2$, and apply

$$\Theta_2^k = \frac{r_3\left(h_4^k - h_2^k\right) - r_2\left(h_3^k - h_1^k\right)}{\left(r_2+r_3\right)\left(\Delta r\right)^3} - \frac{r_2\left(h_3^k - h_1^k\right)}{r_2\left(\Delta r\right)^3}, \tag{B.33a}$$

$$\begin{aligned}\Theta_{N_r-1}^k = &\frac{r_{N_r}\left(3h_{N_r}^k - 4h_{N_r-1}^k + h_{N_r-2}^k\right) - r_{N_r-1}\left(h_{N_r}^k - h_{N_r-2}^k\right)}{\left(r_{N_r}+r_{N_r-1}\right)\left(\Delta r\right)^3} \\ &- \frac{r_{N_r-1}\left(h_{N_r}^k - h_{N_r-2}^k\right) - r_{N_r-2}\left(h_{N_r-1}^k - h_{N_r-3}^k\right)}{\left(r_{N_r-1}+r_{N_r-2}\right)\left(\Delta r\right)^3},\end{aligned} \tag{B.33b}$$

$$\begin{aligned}\Theta_{N_r}^k = \frac{3}{r_{N_r}(\Delta r)^2}\Bigg[&\frac{3r_{N_r}\left(3h_{N_r}^k - 4h_{N_r-1}^k + h_{N_r-2}^k\right)}{2\Delta r} \\ &- \frac{4\left(r_{N_r}+r_{N_r-1}\right)\left(h_{N_r}^k - h_{N_r-1}^k\right)}{2\Delta r} + \frac{r_{N_r-1}\left(h_{N_r}^k - h_{N_r-2}^k\right)}{2\Delta r}\Bigg] \\ - \frac{8}{\left(r_{N_r}+r_{N_r-1}\right)(\Delta r)^2}\Bigg[&\frac{r_{N_r}\left(3h_{N_r}^k - 4h_{N_r-1}^k + h_{N_r-2}^k\right)}{2\Delta r} \\ &- \frac{r_{N_r-1}\left(h_{N_r}^k - h_{N_r-2}^k\right)}{2\Delta r}\Bigg] \\ + \frac{1}{r_{N_r-1}(\Delta r)^2}\Bigg[&\frac{\left(r_{N_r}+r_{N_r-1}\right)\left(h_{N_r}^k - h_{N_r-1}^k\right)}{2\Delta r} \\ &- \frac{\left(r_{N_r-1}+r_{N_r-2}\right)\left(h_{N_r-1}^k - h_{N_r-2}^k\right)}{2\Delta r}\Bigg],\end{aligned} \tag{B.33c}$$

at the boundaries. By the symmetry condition (6.8), we enforce $\Theta_1 = 0$, completing the discretisation for all j.

Having discretised the coefficients $(A_{1_{i,j}}^{k-1}, A_{2_{i,j}}^{k-1}, A_{3_{i,j}}^{k-1})$, we use a Crank–Nicolson scheme to solve (B.30). At the interior grid points where $i = 2,\ldots,N_\xi$, and $j = 2,\ldots,N_\zeta$, we apply

$$\begin{aligned}&\frac{\phi_{ni,j}^{\ k} - \phi_{ni,j}^{\ k-1}}{\Delta\tau} \\ +\frac{A_{1_{i,j}}^{k-1}}{\xi_i}&\frac{\xi_{i+1}\left(h_{i+1}^{k-1}\right)^2\Theta_{i+1}^{k-1}\phi_{ni+1,j}^{\ k-1/2} - \xi_{i-1}\left(h_{i-1}^{k-1}\right)^2\Theta_{i-1}^{k-1}\phi_{ni-1,j}^{\ k-1/2}}{2\Delta\xi} \\ &+A_{2_{i,j}}^{k-1}\frac{\phi_{ni,j+1}^{\ k-1/2} - \phi_{ni,j-1}^{\ k-1/2}}{2\Delta\zeta} = A_{3_{i,j}}^{k-1}\phi_{ni,j}^{\ k-1/2},\end{aligned} \tag{B.34}$$

where $\phi_{ni,j}^{\ k-1/2} = (\phi_{ni,j}^{\ k} + \phi_{ni,j}^{\ k-1})/2$ denotes the usual half time step. At $r = 0$, we impose the symmetry boundary condition explicitly, by applying

$$\frac{-3\phi_{n1,j}^{\ k} + 4\phi_{n2,j}^{\ k} - \phi_{n3,j}^{\ k}}{2\Delta\xi} = 0, \tag{B.35}$$

for all $j = 1,\ldots,N_\zeta$. Finally, at all other boundaries we replace relevant

derivatives with second-order accurate one-sided finite difference formulae. We have

$$\begin{aligned}
&\frac{\phi_{ni,1}^{\ k} - \phi_{ni,1}^{\ k-1}}{\Delta\tau} \\
&+\frac{A_{1_{i,1}}^{k-1}}{\xi_i}\frac{\xi_{i+1}\left(h_{i+1}^{k-1}\right)^2\Theta_{i+1}^{k-1}\phi_{ni+1,1}^{\ k-1/2} - \xi_{i-1}\left(h_{i-1}^{k-1}\right)^2\Theta_{i-1}^{k-1}\phi_{ni-1,N_\zeta}^{\ k-1/2}}{2\Delta\xi} \\
&+A_{2_{i,1}}^{k-1}\frac{-3\phi_{ni,1}^{\ k-1/2} + 4\phi_{ni,2}^{\ k-1/2} - \phi_{ni,3}^{\ k-1/2}}{2\Delta\zeta} = A_{3_{i,1}}^{k-1}\phi_{ni,1}^{\ k-1/2},
\end{aligned} \tag{B.36a}$$

$$\begin{aligned}
&\frac{\phi_{ni,N_\zeta}^{\ k} - \phi_{ni,N_\zeta}^{\ k-1}}{\Delta\tau} \\
&+\frac{A_{1_{i,N_\zeta}}^{k-1}}{\xi_i}\frac{\xi_{i+1}\left(h_{i+1}^{k-1}\right)^2\Theta_{i+1}^{k-1}\phi_{ni+1,N_\zeta}^{\ k-1/2} - \xi_{i-1}\left(h_{i-1}^{k-1}\right)^2\Theta_{i-1}^{k-1}\phi_{ni-1,N_\zeta}^{\ k-1/2}}{2\Delta\xi} \\
&+A_{2_{i,N_\zeta}}^{k-1}\frac{3\phi_{ni,N_\zeta}^{\ k-1/2} - 4\phi_{ni,N_\zeta-1}^{\ k-1/2} + \phi_{ni,N_\zeta-2}^{\ k-1/2}}{2\Delta\zeta} = A_{3_{i,N_\zeta}}^{k-1}\phi_{ni,N_\zeta}^{\ k-1/2},
\end{aligned} \tag{B.36b}$$

for $i = 2, N_\xi - 1$. At the corners of the rectangular domain, we have

$$\begin{aligned}
&\frac{\phi_{nN_\xi,1}^{\ k} - \phi_{nN_\xi,1}^{\ k-1}}{\Delta\tau} + 3\frac{A_{1_{N_\xi,1}}^{k-1}}{\xi_{N_\xi}}\frac{\xi_{N_\xi}\left(h_{N_\xi}^{k-1}\right)^2\Theta_{N_\xi}^{k-1}\phi_{nN_\xi,1}^{\ k-1/2}}{2\Delta\xi} \\
&-4\frac{A_{1_{N_\xi,1}}^{k-1}}{\xi_{N_\xi}}\frac{\xi_{N_\xi-1}\left(h_{N_\xi-1}^{k-1}\right)^2\Theta_{N_\xi-1}^{k-1}\phi_{nN_\xi-1,1}^{\ k-1/2}}{2\Delta\xi} \\
&+\frac{A_{1_{N_\xi,1}}^{k-1}}{\xi_{N_\xi}}\frac{\xi_{N_\xi-2}\left(h_{N_\xi-2}^{k-1}\right)^2\Theta_{N_\xi-2}^{k-1}\phi_{nN_\xi-2,1}^{\ k-1/2}}{2\Delta\xi} \\
&+A_{2_{N_\xi,1}}^{k-1}\frac{-3\phi_{nN_\xi,1}^{\ k-1/2} + 4\phi_{nN_\xi,2}^{\ k-1/2} - \phi_{nN_\xi,3}^{\ k-1/2}}{2\Delta\zeta} = A_{3_{N_\xi,1}}^{k-1}\phi_{nN_\xi,1}^{\ k-1/2},
\end{aligned} \tag{B.37a}$$

$$\begin{aligned}
&\frac{\phi_{n}{}^{k}_{N_\xi,N_\zeta} - \phi_{n}{}^{k-1}_{N_\xi,N_\zeta}}{\Delta\tau} + 3\frac{A_{1}{}^{k-1}_{N_\xi,1}}{\xi_{N_\xi}}\frac{\xi_{N_\xi}\left(h^{k-1}_{N_\xi}\right)^2\Theta^{k-1}_{N_\xi}\phi_{n}{}^{k-1/2}_{N_\xi,N_\zeta}}{2\Delta\xi} \\
&\quad -4\frac{A_{1}{}^{k-1}_{N_\xi,1}}{\xi_{N_\xi}}\frac{\xi_{N_\xi-1}\left(h^{k-1}_{N_\xi-1}\right)^2\Theta^{k-1}_{N_\xi-1}\phi_{n}{}^{k-1/2}_{N_\xi-1,N_\zeta}}{2\Delta\xi} \\
&\quad +\frac{A_{1}{}^{k-1}_{N_\xi,1}}{\xi_{N_\xi}}\frac{\xi_{N_\xi-2}\left(h^{k-1}_{N_\xi-2}\right)^2\Theta^{k-1}_{N_\xi-2}\phi_{n}{}^{k-1/2}_{N_\xi-2,N_\zeta}}{2\Delta\xi} \\
&+A_{2}{}^{k-1}_{N_\xi,N_\zeta}\frac{3\phi_{n}{}^{k-1/2}_{N_\xi,N_\zeta} - 4\phi_{n}{}^{k-1/2}_{N_\xi,N_\zeta-1} + \phi_{n}{}^{k-1/2}_{N_\xi,N_\zeta-2}}{2\Delta\zeta} = A_{3}{}^{k-1}_{N_\xi,N_\zeta}\phi_{n}{}^{k-1/2}_{N_\xi,N_\zeta},
\end{aligned} \tag{B.37b}$$

The discretisation (B.34)–(B.37) defines a large, sparse linear system that can be solved for $\phi_{n}{}^{k}_{i,j}$ at each time step. Similar to the reaction–diffusion model in Appendix B.1, we solve this system iteratively using the generalised minimal residual (GMRES) method. When doing so, we supply the A matrix explicitly, and use its incomplete LU factorisation as a pre-conditioner. As with Appendix B.1, at each time step, we use the solution from the previous time step as the initial guess, and accept the solution if the relative residual norm $\|\boldsymbol{r}_n\|/\|\boldsymbol{b}\| < 1 \times 10^{-6}$.

The next step is to solve (6.2e) and (6.2f) for the nutrient concentrations. For the nutrient concentration in the substratum, we apply the compact conservative Crank–Nicolson scheme

$$\begin{aligned}
\frac{g_{s}{}^{k}_{j} - g_{s}{}^{k-1}_{j}}{\Delta t} &= D\frac{(r_{j+1}+r_j)\left(g_{s}{}^{k-1/2}_{j+1} - g_{s}{}^{k-1/2}_{j}\right)}{2r_j\left(\Delta r\right)^2} \\
&\quad -D\frac{(r_j+r_{j-1})\left(g_{s}{}^{k-1/2}_{j} - g_{s}{}^{k-1/2}_{j-1}\right)}{2r_j\left(\Delta r\right)^2} \\
&\quad -DQ_s\left(g_{s}{}^{k-1/2}_{j} - g_{b}{}^{k-1}_{j}\right)H\left(h^{k-1}_{j} - h^{*}\right),
\end{aligned} \tag{B.38}$$

at the interior grid points $j = 2, \ldots, N_r - 1$. To impose the Neumann conditions at the boundaries, we introduce fictitious grid points such that $g_{s0} = g_{s2}$, and $g_{sN_r+1} = g_{sN_r+1}$, and apply the discretisation (B.38) at $j = 1$ and $j = N_r$. We apply L'Hôpital's rule to deal with the singular term as $r \to 0$. This yields

the boundary schemes

$$\begin{aligned}\frac{g_{s1}^{k}-g_{s1}^{k-1}}{\Delta t} &= 4D\frac{g_{s2}^{k-1}-g_{s1}^{k-1/2}}{(\Delta r)^2}\\ -DQ_s\left(g_{s1}^{k-1/2}-g_{b1}^{k-1}\right)H\left(h_1^{k-1}-h^*\right),&\end{aligned} \tag{B.39a}$$

$$\begin{aligned}\frac{g_{sN_r}^{k}-g_{sN_r}^{k-1}}{\Delta t} &= 2D\frac{g_{sN_r-1}^{k-1}-g_{sN_r}^{k-1/2}}{(\Delta r)^2}\\ -DQ_s\left(g_{sN_r}^{k-1/2}-g_{bN_r}^{k-1}\right)H\left(h_{N_r}^{k-1}-h^*\right).&\end{aligned} \tag{B.39b}$$

The schemes (B.38) and (B.39) then define a linear system to solve for g_{sj}^{k}.

We use a similar scheme for the nutrient concentration in the biofilm, g_b. Before solving, we use (B.19) to re-write the model equation (6.2f) as

$$\begin{aligned}\mathrm{Pe}h\frac{\partial g_b}{\partial t} &= H\left(h-h^*\right)\left[\frac{\mathrm{Pe}\gamma^*}{3r}\frac{\partial}{\partial r}\left(r\Theta\Phi g_b\right)\right]\\ +H\left(h-h^*\right)&\left[\frac{1}{r}\frac{\partial}{\partial r}\left(rh\frac{\partial g_b}{\partial r}\right)+Q_b\left(g_s-g_b\right)-\Upsilon\phi_n g_b h\right].\end{aligned} \tag{B.40}$$

The term Θ is defined as in (B.19), and we have introduced

$$\Phi=\int_0^h z\left(\frac{z}{2}-h\right)\left(1-\phi_n\right)\,\mathrm{d}z, \tag{B.41}$$

and we compute the discretised form Φ_j^k using the trapezoidal rule. At the boundaries, we again use L'Hôpital's rule to evaluate singular terms and otherwise introduce fictitious grid points to apply the Neumann conditions. Incorporating both interior and boundary points, the full scheme is then

$$\frac{-3g_{b1}^{k}+4g_{b2}^{k}-g_{b3}^{k}}{2\Delta r}=0, \tag{B.42a}$$

$$\mathrm{Pe}h_j^{k-1}\frac{g_{bj}^{k}-g_{bj}^{k-1}}{\Delta t}=H\left(h_j^k-h^*\right)\frac{\mathrm{Pe}\gamma^*}{3r_j}\Bigg[$$
$$\frac{r_{j+1}\left(h_{j+1}^{k-1}\right)^3\Theta_{j+1}^{k-1}\Phi_{j+1}^{k-1}g_{bj+1}^{k-1/2}-r_{j-1}\left(h_{j-1}^{k-1}\right)^3\Theta_{j-1}^{k-1}\Phi_{j-1}^{k-1}g_{bj-1}^{k-1/2}}{2\Delta r}\Bigg]$$
$$+H(h_j^{k-1}-h^*)\Bigg[\frac{(r_{j+1}+r_j)\left(h_{j+1}^{k-1}+h_j^{k-1}\right)\left(g_{bj+1}^{k-1/2}-g_{bj}^{k-1/2}\right)}{4r_j\left(\Delta r\right)^2} \tag{B.42b}$$
$$-\frac{(r_j+r_{j-1})\left(h_j^{k-1}+h_{j-1}^{k-1}\right)\left(g_{bj}^{k-1/2}-g_{bj-1}^{k-1/2}\right)}{4r_j\left(\Delta r\right)^2}$$
$$+Q_b\left(g_{sj}^{k-1}-g_{bj}^{k-1/2}\right)-\Upsilon\phi_n g_{bj}^{k-1/2}h_j^{k-1}\Bigg],$$

$$\mathrm{Pe}h_{N_r}^{k-1}\frac{g_{bN_r}^{k}-g_{bN_r}^{k-1}}{\Delta t}=H\left(h_j^k-h^*\right)\frac{\mathrm{Pe}\gamma^*}{3r_{N_r}}\Bigg[\frac{3r_{N_r}\left(h_{N_r}^{k-1}\right)^3\Theta_{N_r}^{k-1}\Phi_{N_r}^{k-1}}{2\Delta r}$$
$$-\frac{4r_{N_r-1}\left(h_{N_r-1}^{k-1}\right)^3\Theta_{N_r-1}^{k-1}\Phi_{N_r-1}^{k-1}}{2\Delta r}+\frac{r_{N_r-2}\left(h_{N_r-2}^{k-1}\right)^3\Theta_{N_r-2}^{k-1}\Phi_{N_r-2}^{k-1}}{2\Delta r}\Bigg]g_{bN_r}^{k-1/2}$$
$$+H(h_{N_r}^{k-1}-h^*)\Bigg[h_{N_r}^{k-1}\frac{2g_{bN_r-1}^{k-1/2}-2g_{bN_r}^{k-1/2}}{\left(\Delta r\right)^2}$$
$$+Q_b\left(g_{sN_r}^{k-1}-g_{bN_r}^{k-1/2}\right)-\Upsilon\phi_n g_{bN_r}^{k-1/2}h_{N_r}^{k-1}\Bigg], \tag{B.42c}$$

where the discretisation for Θ follows (B.18) and (B.33).

Finally, the full lubrication model requires us to solve (6.2c) for the depth-averaged cell volume fraction, and (6.2d) for the vertical component of the velocity. In both equations, we compute the integrals using the trapezoidal rule. We solve (6.2d) in the original (r, z, t) variables, which creates a non-constant grid spacing in z. To compute the second term in (6.2d), we use standard second-order accurate finite difference formulae, where we allow z to vary with r to deal with the non-constant grid spacing.

B.3.3 One-Dimensional Simplified Model

The one-dimensional simplified model requires computing a solution to (6.23). As the equations (6.23a) and (6.23c) for h and g_s are the same as the full two-dimensional model, we use the methods described in Appendix B.3.2. Similarly, our scheme to solve (6.23d) is also the same as in Appendix B.3.2, except here the integral (B.41) can be evaluated analytically to give

$$\Phi = -\frac{h^3\left(1-\phi_n\right)}{3}, \tag{B.43}$$

which we then discretise as

$$\Phi_j^k = -\frac{\left(h_j^k\right)^3\left(1-{\phi_n}_j^k\right)}{3}. \tag{B.44}$$

We then use (B.42) to compute the solution for g_b.

Compared to the full two-dimensional model, the largest saving in computational time is in solving for the cell volume fraction, ϕ_n. This is because we now need to only solve the one-dimensional equation (6.23b). To achieve this, we exploit that the coefficient of the spatial derivative of ϕ_n is always non-negative by using an explicit upwind finite difference scheme. This scheme is

$$\begin{aligned}&\frac{{\phi_n}_j^k - {\phi_n}_j^{k-1}}{\Delta t} + u_j^{k-1}\frac{{\phi_n}_j^{k-1} - {\phi_n}_{j-1}^{k-1}}{\Delta r}\\ &= {\phi_n}_j^{k-1}\left[{g_b}_j^{k-1} - \Psi_d - \left(1+\Psi_m\right){\phi_n}_j^{k-1}{g_b}_j^{k-1}\right],\end{aligned} \tag{B.45}$$

for $j = 2, \ldots N_r$. The advection coefficients are given by

$$u_j^k = \frac{\gamma^*\left(h_j^k\right)^2\Theta_j^k}{3}, \tag{B.46}$$

where Θ is again discretised according to (B.18) and (B.33). To apply the symmetry condition at $r = 0$, we solve

$$\frac{{\phi_n}_1^k - {\phi_n}_1^{k-1}}{\Delta t} = {\phi_n}_1^{k-1}\left[{g_b}_1^{k-1} - \Psi_d - \left(1+\Psi_m\right){\phi_n}_1^{k-1}{g_b}_1^{k-1}\right], \tag{B.47}$$

which holds when we apply the boundary condition

$$\left.\frac{\partial \phi_n}{\partial r}\right|_{(0,t)} = 0. \tag{B.48}$$

This completes the numerical scheme used to solve the one-dimensional simplified model.

Bibliography

[1] H. Fujikawa and M. Matsushita, "Fractal growth of *Bacillus subtilis* on agar plates", *Journal of the Physical Society of Japan* 58 (1989), pp. 3875–3878, DOI: 10.1143/JPSJ.58.3875.

[2] H. Tronnolone, A. Tam, Z. Szenczi, J. E. F. Green, S. Balasuriya, E. L. Tek, J. M. Gardner, J. F. Sundstrom, V. Jiranek, S. G. Oliver, and B. J. Binder, "Diffusion-limited growth of microbial colonies", *Scientific Reports* 8 (2018), 5992, DOI: 10.1038/s41598-018-23649-z.

[3] A. Sirota-Madi, T. Olender, C. Ingham, I. Brainis, D. Roth, E. Hagi, L. Brodsky, D. Leshkowitz, V. Galatenko, V. Nikolaev, R. C. Mugasimangalam, S. Bransburg-Zabary, D. L. Gutnick, D. Lancet, and E. Ben-Jacob, "Genome sequence of the pattern forming *Paenibacillus vortex* bacterium reveals potential for thriving in complex environments", *BMC Microbiology* 11 (2010), 710, DOI: 10.1186/1471-2180-8-36.

[4] A. M. Turing, "The chemical basis of morphogenesis", *Philosophical Transactions of the Royal Society of London* 237 (1952), pp. 37–72, DOI: 10.1098/rstb.1952.0012.

[5] S. Kondo and T. Miura, "Reaction–diffusion model as a framework for understanding biological pattern formation", *Science* 329 (2010), pp. 1616–1620, DOI: 10.1126/science.1179047.

[6] J. D. Murray, *Mathematical Biology I: An Introduction*, Third edition, Springer, 2002, DOI: 10.1007/b98868.

[7] M. D. Murtey and P. Ramasamy, "Sample Preparations for Scanning Electron Microscopy – Life Sciences", *Modern Electron Microscopy in Physical and Life Sciences*, Intech Open, 2016, chap. 8, pp. 161–185, DOI: 10.5772/61720.

[8] C. P. Kurtzman, J. W. Fell, and T. Boekhout, *The yeasts*, Elsevier Science, 2010.

[9] S. Brückner and H. U. Mösch, "Choosing the right lifestyle: adhesion and development in *Saccharomyces cerevisiae*", *FEMS Microbiology Reviews* 36 (2012), pp. 25–58, DOI: 10.1111/j.1574-6976.2011.00275.x.

[10] E. L. Tek, J. F. Sundstrom, J. M. Gardner, S. G. Oliver, and V. Jiranek, "Evaluation of the ability of commercial wine yeasts to form biofilms (mats) and adhere to plastic: implications for the microbiota of the winery environment", *FEMS Microbiology Ecology* 94 (2018), fix188, DOI: 10.1093/femsec/fix188.

[11] B. J. Binder, J. F. Sundstrom, J. M. Gardner, V. Jiranek, and S. G. Oliver, "Quantifying two-dimensional filamentous and invasive growth spatial patterns in yeast colonies", *PLOS Computational Biology* 11 (2015), e1004070, DOI: 10.1371/journal.pcbi.1004070.

[12] C. J. Gimeno, P. O. Ljungdahl, C. A. Styles, and G. R. Fink, "Unipolar cell divisions in the yeast S. cerevisiae lead to filamentous growth: regulation by starvation and RAS", *Cell* 68 (1992), pp. 1077–1090, DOI: 10.1016/0092-8674(92)90079-r.

[13] Z. Palková and L. Váchová, "Life within a community: benefit to yeast long-term survival", *FEMS Microbiology Reviews* 30 (2006), pp. 806–824, DOI: 10.1111/j.1574-6976.2006.00034.x.

[14] Y. J. Zhou, N. A. Buijs, Z. Zhu, J. Qin, V. Siewers, and J. Nielsen, "Production of fatty acid-derived oleochemicals and biofuels by synthetic yeast cell factories", *Nature Communications* 7 (2016), 11709, DOI: 10.1038/ncomms11709.

[15] R. Mans, J. G. Daran, and J. T. Pronk, "Under pressure: evolutionary engineering of yeast strains for improved performance in fuels and chemicals production", *Current Opinion in Biotechnology* 50 (2018), pp. 47–56, DOI: 10.1016/j.copbio.2017.10.011.

[16] S. Smukalla, M. Caldara, N. Pochet, A. Beauvais, S. Guadagnini, C. Yan, M. D. Vinces, A. Jansen, M. C. Prevost, J. P. Latgé, G. R. Fink, and K. R. Foster, "*FLO1* is a variable green beard gene that drives biofilm-like cooperation in budding yeast", *Cell* 135 (2008), pp. 726–737, DOI: 10.1016/j.cell.2008.09.037.

[17] T. B. Reynolds and G. R. Fink, "Bakers' yeast, a model for fungal biofilm formation", *Science* 291 (2001), pp. 878–881, DOI: 10.1126/science.291.5505.878.

[18] M. W. Harding, L. L. R. Marques, R. J. Howard, and M. E. Olson, "Can filamentous fungi form biofilms?", *Trends in Microbiology* 17 (2009), pp. 475–480, DOI: 10.1016/j.tim.2009.08.007.

[19] L. M. Martinez and B. C. Fries, "Fungal biofilms: relevance in the setting of human disease", *Current Fungal Infection Reports* 4 (2010), pp. 266–275, DOI: 10.1007/s12281-010-0035-5.

[20] H. Flemming and J. Wingender, "The biofilm matrix", *Nature Reviews Microbiology* 8 (2010), pp. 623–633, DOI: 10.1038/nrmicro2415.

[21] I. W. Sutherland, "The biofilm matrix — an immobilized but dynamic microbial environment", *Trends in Microbiology* 9 (2001), pp. 222–227, DOI: 10.1016/S0966-842X(01)02012-1.

[22] L. Váchová, V. Štovíček, O. Hlaváček, O. Chernyavskiy, L. Štěpánek, L. Kubínová, and Z. Palková, "Flo11p, drug efflux pumps, and the extracellular matrix cooperate to form biofilm yeast colonies", *Journal of Cell Biology* 194 (2011), pp. 679–687, DOI: 10.1083/jcb.201103129.

[23] M. P. Brenner, "Fluid mechanical responses to nutrient depletion in fungi and biofilms", *Physics of Fluids* 26 (2014), 101306, DOI: 10.1063/1.4896587.

[24] A. Beauvais, C. Loussert, M. C. Prevost, K. Verstrepen, and J. P. Latgé, "Characterization of a biofilm-like extracellular matrix in FLO1-expressing *Saccharomyces cerevisiae* cells", *FEMS Yeast Research* 9 (2009), pp. 411–419, DOI: 10.1111/j.1567-1364.2009.00482.x.

[25] C. Nicolella, M. C. M. van Loosdrecht, and J. J. Heijnen, "Wastewater treatment with particulate biofilm reactors", *Journal of Biotechnology* 80 (2000), pp. 1–33, DOI: 10.1016/S0168-1656(00)00229-7.

[26] C. Picioreanu, I. M. Head, K. P. Katuri, M. C. M. van Loosdrecht, and K. Scott, "A computational model for biofilm-based microbial fuel cells", *Water Research* 41 (2007), pp. 2921–2940, DOI: 10.1016/j.watres.2007.04.009.

[27] P. D. Marsh, "Dental plaque as a microbial biofilm", *Caries Research* 38 (2004), pp. 204–211, DOI: 10.1159/000077756.

[28] C. J. Nobile and A. D. Johnson, "*Candida albicans* biofilms and human disease", *Annual Review of Microbiology* 69 (2015), pp. 71–92, DOI: 10.1146/annurev-micro-091014-104330.

[29] R. T. Wheeler, M. Kupiec, P. Magnelli, C. Abeijon, and G. R. Fink, "A *Saccharomyces cerevisiae* mutant with increased virulence", *Proceedings of the National Academy of Sciences of the United States of America* 100 (2003), pp. 2766–2770, DOI: 10.1073/pnas.0437995100.

[30] G. Ramage, R. Rajendran, L. Sherry, and C. Williams, "Fungal biofilm resistance", *International Journal of Microbiology* (2012), 528521, DOI: 10.1155/2012/528521.

[31] P. G. Pappas, M. S. Lionakis, M. C. Arendrup, L. Ostrosky-Zeichner, and B. J. Kullberg, "Invasive candidiasis", *Nature Reviews Disease Primers* 4 (2018), 18026, DOI: 10.1038/nrdp.2018.26.

[32] M. S. Lionakis, "New insights into innate immune control of systemic candidiasis", *Medical Mycology* 52 (2014), pp. 555–564, DOI: 10.1093/mmy/myu029.

[33] A. Jeffery-Smith, S. K. Taori, S. Schelenz, K. Jeffery, E. M. Johnson, A. Borman, R. Manuel, and C. S. Brown, "*Candida auris*: a review of the literature", *Clinical Microbiology Reviews* 31 (2018), e00029–17, DOI: 10.1128/CMR.00029-17.

[34] L. Sherry, G. Ramage, R. Kean, A. Borman, E. M. Johnson, M. D. Richardson, and R. Rautemaa-Richardson, "Biofilm-forming capability of highly virulent, multidrug-resistant *Candida auris*", *Emerging Infectious Diseases* 23 (2017), pp. 328–331, DOI: 10.3201/eid2302.161320.

[35] L. Chen, J. Noorbakhsh, R. M. Adams, J. Samaniego-Evans, G. Agollah, D. Nevozhay, J. Kuzdzal-Fick, P. Mehta, and G. Balázsi, "Two-dimensonality of yeast colony expansion accompanied by pattern formation", *PLOS Computational Biology* 10 (2014), e1003979, DOI: 10.1371/journal.pcbi.1003979.

[36] J. R. Blankenship and A. P. Mitchell, "How to build a biofilm: a fungal perspective", *Current Opinion in Microbiology* 9 (2006), pp. 588–594, DOI: 10.1016/j.mib.2006.10.003.

[37] T. R. Hughes, "Yeast and drug discovery", *Functional and Integrative Genomics* 2 (2002), pp. 199–211, DOI: 10.1007/s10142-002-0059-1.

[38] A. Goffeau, B. G. Barrell, H. Bussey, R. W. Davis, B. Dujon, H. Feldmann, F. Galibert, J. D. Hoheisel, C. Jacq, M. Johnston, E. J. Louis, H. W. Mewes, Y. Murakami, P. Philippsen, H. Tettelin, and S. G. Oliver, "Life with 6000 Genes", *Science* 274 (1996), pp. 546–567, DOI: 10.1126/science.274.5287.546.

[39] P. Stoodley, K. Sauer, D. G. Davies, and J. W. Costerton, "Biofilms as complex differentiated communities", *Annual Review of Microbiology* 56 (2002), pp. 187–209, DOI: 10.1146/annurev.micro.56.012302.160705.

[40] G. Ramage, E. Mowat, B. Jones, C. Williams, and J. L. Lopez-Ribot, "Our current understanding of fungal biofilms", *Critical Reviews in Microbiology* 35 (2009), pp. 340–355, DOI: 10.3109/10408410903241436.

[41] L. H. Hartwell, "*Saccharomyces cerevisiae* cell cycle", *Bacteriological Reviews* 38 (1974), pp. 164–198.

[42] T. B. Reynolds, A. Jansen, X. Peng, and G. R. Fink, "Mat formation in *Saccharomyces cerevisiae* requires nutrient and pH gradients", *Eukaryotic Cell* 7 (2008), pp. 122–130, DOI: 10.1128/ec.00310-06.

[43] B. Regenberg, K. E. Hanghøj, K. S. Andersen, and J. J. Boomsma, "Clonal yeast biofilms can reap competitive advantages through cell differentiation without being obligatorily multicellular", *Proceedings of the Royal Society of London B* 283 (2016), 20161303, DOI: 10.1098/rspb.2016.1303.

[44] A. Tam, J. E. F. Green, S. Balasuriya, E. L. Tek, J. M. Gardner, J. F. Sundstrom, V. Jiranek, and B. J. Binder, "Nutrient-limited growth with non-linear cell diffusion as a mechanism for floral pattern formation in yeast biofilms", *Journal of Theoretical Biology* 448 (2018), pp. 122–141, DOI: 10.1016/j.jtbi.2018.04.004.

[45] N. Minois, M. Frajnt, C. Wilson, and J. W. Vaupel, "Advances in measuring lifespan in the yeast *Saccharomyces cerevisiae*", *Proceedings of the National Academy of Sciences of the United States of America* 102 (2005), pp. 402–406, DOI: 10.1073/pnas.0408332102.

[46] J. Maršíková, D. Wilkinson, O. Hlaváček, G. D. Gilfillan, A. Mizeranschi, T. R. Hughes, M. Begany, S. Rešetárová, L. Váchová, and Z. Palková, "Metabolic differentiation of surface and invasive cells of yeast colony biofilms revealed by gene expression profiling", *BMC Genomics* 18 (2017), pp. 1–16, DOI: 10.1186/s12864-017-4214-4.

[47] T. Shaw, M. Winston, C. J. Rupp, I. Klapper, and P. Stoodley, "Commonality of elastic relaxation times in biofilms", *Physical Review Letters* 93 (2004), 098102, DOI: 10.1103/PhysRevLett.93.098102.

[48] N. G. Cogan and R. D. Guy, "Multiphase flow models of biogels from crawling cells to bacterial biofilms", *Frontiers in Life Sciences* 4 (2010), pp. 11–25, DOI: 10.2976/1.3291142.

[49] A. Persat, C. D. Nadell, M. K. Kim, F. Ingremeau, A. Siryaporn, K. Drescher, N. S. Wingreen, B. L. Bassler, Z. Gitai, and H. A. Stone, "The mechanical world of bacteria", *Cell* 161 (2015), pp. 988–997, DOI: 10.1016/j.cell.2015.05.005.

[50] J. Recht, A. Martínez, S. Torello, and R. Kolter, "Genetic analysis of sliding motility in *Mycobacterium smegmatis*", *Journal of Bacteriology* 182 (2000), pp. 4348–4351, DOI: 10.1128/JB.182.15.4348-4351.2000.

[51] A. Seminara, T. E. Angelini, J. N. Wilking, H. Vlamakis, S. Ebrahim, R. Kolter, D. A. Weitz, and M. P. Brenner, "Osmotic spreading of *Bacillus subtilis* biofilms driven by an extracellular matrix", *Proceedings of the National Academy of Sciences of the United States of America* 109 (2012), pp. 1116–1121, DOI: 10.1073/pnas.1109261108.

[52] S. Trinschek, K. John, and U. Thiele, "From a thin film model for passive suspensions towards the description of osmotic biofilm spreading", *AIMS Materials Science* 3 (2016), pp. 1138–1159, DOI: 10.3934/matersci.2016.3.1138.

[53] J. Yan, C. D. Nadell, H. A. Stone, N. S. Wingreen, and B. L. Bassler, "Extracellular-matrix-mediated osmotic pressure drives *Vibrio cholerae* biofilm expansion and cheater exclusion", *Nature Communications* 8 (2017), 327, DOI: 10.1038/s41467-017-00401-1.

[54] M. R. Mattei, L. Frunzo, B. D'Acunto, Y. Pechaud, F. Pirozzi, and G. Esposito, "Continuum and discrete approach in modeling biofilm development and structure: a review", *Journal of Mathematical Biology* 76 (2018), pp. 945–1003, DOI: 10.1007/s00285-017-1165-y.

[55] H. F. Winstanley, M. Chapwanya, M. J. McGuinness, and A. C. Fowler, "A polymer–solvent model of biofilm growth", *Proceedings of the Royal Society of London A* 467 (2010), pp. 1449–1467, DOI: 10.1098/rspa.2010.0327.

[56] J. Gunawardena, "Models in biology: 'accurate descriptions of our pathetic thinking'", *BMC Biology* 12 (2014), 29, DOI: 10.1186/1741-7007-12-29.

[57] C. Picioreanu, M. C. M. van Loosdrecht, and J. J. Heijnen, "Mathematical modeling of biofilm structure with a hybrid differential-discrete cellular automaton approach", *Biotechnology and Bioengineering* 58 (1998), pp. 101–116, DOI: 10.1002/(SICI)1097-0290(19980405)58:1<101::AID-BIT11>3.0.CO;2-M.

[58] S. Matsuura, "Random growth of fungal colony model on diffusive and non-diffusive media", *Forma* 15 (2000), pp. 309–319.

[59] T. Walther, H. Reinsch, A. Große, K. Ostermann, A. Deutsch, and T. Bley, "Mathematical modeling of regulatory mechanisms in yeast colony development", *Journal of Theoretical Biology* 229 (2004), pp. 327–338, DOI: 10.1016/j.jtbi.2004.04.004.

[60] F. D. Farrell, M. Gralka, O. Hallatschek, and B. Waclaw, "Mechanical interactions in bacterial colonies and the surfing probability of beneficial mutations", *Journal of the Royal Society Interface* 14 (2017), 20170073, DOI: 10.1098/rsif.2017.0073.

[61] M. Ginovart, D. López, J. Valls, and M. Silbert, "Individual based simulations of bacterial growth on agar plates", *Physica A: Statistical Mechanics and its Applications* 305 (2002), pp. 604–618, DOI: 10.1016/S0378-4371(01)00581-7.

[62] K. Kawasaki, A. Mochizuki, M. Matsushita, T. Umeda, and N. Shigesada, "Modeling spatio-temporal patterns generated by *Bacillus subtilis*", *Journal of Theoretical Biology* 188 (1997), pp. 177–185, DOI: 10.1006/jtbi.1997.0462.

[63] E. Ben-Jacob, I. Cohen, and H. Levine, "Co-operative self organisation in micro-organisms", *Advances in Physics* 49 (2000), pp. 395–554, DOI: 10.1080/000187300405228.

[64] J. Müller and W. van Saarloos, "Morphological instability and dynamics of fronts in bacterial growth models with nonlinear diffusion", *Physical Review E* 65 (2002), 061111, DOI: 10.1103/physreve.65.061111.

[65] K. A. Rahman, R. Sudarsan, and H. J. Eberl, "A mixed-culture biofilm model with cross-diffusion", *Bulletin of Mathematical Biology* 77 (2015), pp. 2086–2124, DOI: 10.1007/s11538-015-0117-1.

[66] A. C. Fowler, T. M. Kyrke-Smith, and H. F. Winstanley, "The development of biofilm architecture", *Proceedings of the Royal Society of London A* 472 (2016), 20150798, DOI: 10.1098/rspa.2015.0798.

[67] S. Balasuriya and V. A. Volpert, "Wavespeed analysis: approximating Arrhenius kinetics with step-function kinetics", *Combustion Theory and Modelling* 12 (2008), pp. 643–670, DOI: 10.1080/13647830801968860.

[68] S. Balasuriya, G. Gottwald, J. Hornibrook, and S. Lafortune, "High Lewis number combustion wavefront: a perturbative Melnikov analysis", *SIAM Journal on Applied Mathematics* 67 (2007), pp. 464–486, DOI: 10.1137/050640849.

[69] G. I. Sivashinsky, "Diffusion-thermal theory of cellular flames", *Combustion Science and Technology* 15 (1977), pp. 137–146, DOI: 10.1080/00102207708946779.

[70] J. Billingham and D. J. Needham, "The development of travelling waves in quadratic and cubic autocatalysis with unequal diffusion rates. I. Permanent form travelling waves", *Philosophical Transactions of the Royal Society of London* 334 (1991), pp. 1–24, DOI: 10.1098/rsta.1991.0001.

[71] J. H. Merkin and I. H. Kiss, "Dispersion curves in the diffusional instability of autocatalytic reaction fronts", *Physical Review E* 72 (2005), 026219, DOI: 10.1103/physreve.72.026219.

[72] D. Horváth, V. Petrov, S. K. Scott, and K. Showalter, "Instabilities in propagating reaction–diffusion fronts", *Journal of Chemical Physics* 98 (1993), pp. 6332–6343, DOI: 10.1063/1.465062.

[73] J. Yang, A. D'Onofrio, S. Kalliadasis, and A. De Wit, "Rayleigh–Taylor instability of reaction–diffusion acidity fronts", *Journal of Chemical Physics* 117 (2002), 9395, DOI: 10.1063/1.1516595.

[74] D. A. Kessler and H. Levine, "Fluctuation-induced diffusive instabilities", *Nature* 394 (1998), pp. 556–558, DOI: 10.1038/29020.

[75] A. J. Perumpanani, J. A. Sherratt, J. Norbury, and H. M. Byrne, "A two paramter family of travelling waves with a singular barrier arising from the modelling of extracellular matrix mediated cellular invasion", *Physica D: Nonlinear Phenomena* 126 (1999), pp. 145–159, DOI: 10.1016/s0167-2789(98)00272-3.

[76] B. P. Marchant, J. Norbury, and A. J. Perumpanani, "Traveling shock waves arising in a model of malignant invasion", *SIAM Journal on Applied Mathematics* 60 (2000), pp. 463–476, DOI: 10.1137/s0036139998328034.

[77] G. Carey, N. Fowkes, A. Staelens, and A. Pardhanani, "A class of coupled nonlinear reaction diffusion models exhibiting fingering", *Journal of Computational and Applied Mathematics* 166 (2003), pp. 87–99, DOI: 10.1016/j.cam.2003.09.037.

[78] L. Sewalt, K. Harley, P. van Heijster, and S. Balasuriya, "Influences of Allee effects in the spreading of malignant tumours", *Journal of Theoretical Biology* 394 (2016), pp. 77–92, DOI: 10.1016/j.jtbi.2015.12.024.

[79] B. F. Gray and N. A. Kirwan, "Growth rates of yeast colonies on solid media", *Biophysical Chemistry* 1 (1974), pp. 204–213, DOI: 10.1016/0301-4622(74)80006-2.

[80] A. Gallegos, B. Mazzag, and A. Mogilner, "Two continuum models for the spreading of myxobacteria swarms", *Bulletin of Mathematical Biology* 68 (2006), pp. 837–861, DOI: 10.1007/s11538-005-9031-2.

[81] R. A. Satnoianu, P. K. Maini, F. Sánchez-Garduño, and J. P. Armitage, "Travelling waves in a nonlinear degenerate diffusion model for bacterial pattern formation", *Discrete and Continuous Dynamical Systems – Series B* 1 (2001), pp. 339–362, DOI: 10.3934/dcdsb.2001.1.339.

[82] L. Edelstein-Keshet, *Mathematical Models in Biology*, Society for Industrial and Applied Mathematics, 1988, DOI: 10.1137/1.9780898719147.

[83] J. Y. Wakano, A. Komoto, and Y. Yamaguchi, "Phase transition of traveling waves in bacterial colony pattern", *Physical Review E* 69 (2004), 051904, DOI: 10.1103/PhysRevE.69.051904.

[84] M. Matsushita, J. Wakita, H. Itoh, I. Ràfols, T. Matsuyama, H. Sakaguchi, and M. Mimura, "Interface growth and pattern formation in bacterial colonies", *Physica A* 249 (1998), pp. 517–524, DOI: 10.1016/S0378-4371(97)00511-6.

[85] P. Ghosh and H. Levine, "Morphodynamics of a growing microbial colony driven by cell death", *Physical Review E* 96 (2017), 052404, DOI: 10.1103/PhysRevE.96.052404.

[86] J. Billingham and D. J. Needham, "The development of travelling waves in quadratic and cubic autocatalysis with unequal diffusion rates. II. An initial-value problem with an immobilized or nearly immobilized autocatalyst", *Philosophical Transactions of the Royal Society of London* 336 (1991), pp. 497–539, DOI: 10.1098/rsta.1991.0098.

[87] S. Kitsunezaki, "Interface dynamics for bacterial colony formation", *Journal of the Physical Society of Japan* 66 (1997), pp. 1544–1550, DOI: 10.1143/jpsj.66.1544.

[88] M. J. Simpson, R. E. Baker, and S. W. McCue, "Models of collective cell spreading with variable cell aspect ratio: a motivation for degenerate diffusion models", *Physical Review E* 83 (2011), 0121901, DOI: 10.1103/physreve.83.021901.

[89] A. Aotani, M. Mimura, and T. Mollee, "A model aided understanding of spot pattern formation in chemotactic *E. coli* colonies", *Japan Journal of Industrial and Applied Mathematics* 27 (2010), pp. 5–22, DOI: 10.1007/s13160-010-0011-z.

[90] E. F. Keller and L. A. Segel, "Traveling bands of chemotactic bacteria: a theoretical analysis", *Journal of Theoretical Biology* 30 (1971), pp. 235–248, DOI: 10.1016/0022-5193(71)90051-8.

[91] O. Wanner and W. Gujer, "A multispecies biofilm model", *Biotechnology and Bioengineering* 28 (1986), pp. 314–328, DOI: 10.1002/bit.260280304.

[92] H. J. Eberl, D. F. Parker, and M. C. M. van Loosdrecht, "A new deterministic spatio-temporal continuum model for biofilm development", *Journal of Theoretical Medicine* 3 (2001), pp. 161–175, DOI: 10.1080/10273660108833072.

[93] I. Klapper and J. Dockery, "Mathematical description of microbial biofilms", *SIAM Review* 52 (2010), pp. 221–265, DOI: 10.1137/080739720.

[94] M. S. Steinberg, "Reconstruction of tissues by dissociated cells", *Science* 141 (1963), pp. 401–408, DOI: 10.1126/science.141.3579.401.

[95] G. Forgacs, R. A. Foty, Y. Shafrir, and M. S. Steinberg, "Viscoelastic properties of living embryonic tissues: a quantitative study", *Biophysical Journal* 74 (1998), pp. 2227–2234, DOI: 10.1016/S0006-3495(98)77932-9.

[96] L. Paterson, "Diffusion-limited aggregation and two-fluid displacements in porous media", *Physical Review Letters* 52 (1984), pp. 1621–1624, DOI: 10.1103/PhysRevLett.52.1621.

[97] E. Ben-Jacob, R. Godbey, N. D. Goldenfeld, J. Koplik, H. Levine, T. Mueller, and L. M. Sander, "Experimental demonstration of the role of anisotropy in interfacial pattern formation", *Physical Review Letters* 55 (1985), pp. 1315–1320, DOI: 10.1103/PhysRevLett.55.1315.

[98] E. Ben-Jacob, P. Garik, and D. Grier, "Interfacial pattern formation far from equilibrium", *Superlattices and Microstructures* 3 (1987), pp. 599–615, DOI: 10.1016/0749-6036(87)90190-X.

[99] I. Klapper, C. J. Rupp, R. Cargo, B. Purvedorj, and P. Stoodley, "Viscoelastic fluid description of bacterial biofilm material properties", *Biotechnology and Bioengineering* 80 (2002), pp. 289–296, DOI: 10.1002/bit.10376.

[100] P. Stoodley, R. Cargo, C. J. Rupp, S. Wilson, and I. Klapper, "Biofilm material properties as related to shear-induced deformation and detachment phenomena", *Journal of Industrial Microbiology & Biotechnology* 29 (2002), pp. 361–367, DOI: 10.1038/sj.jim.7000282.

[101] J. Lega and T. Passot, "Hydrodynamics of bacterial colonies: a model", *Physical Review E* 67 (2003), 031906, DOI: 10.1103/physreve.67.031906.

[102] B. Nguyen, A. Upadhyaya, A. van Oudenaarden, and M. P. Brenner, "Elastic instability in growing yeast colonies", *Biophysical Journal* 86 (2004), pp. 2740–2747, DOI: 10.1016/s0006-3495(04)74327-1.

[103] C. Giverso, M. Verani, and P. Ciarletta, "Branching instability in expanding bacterial colonies", *Journal of the Royal Society Interface* 12 (2015), 20141290, DOI: 10.1098/rsif.2014.1290.

[104] L. S. Kimpton, J. P. Whiteley, S. L. Waters, J. R. King, and J. M. Oliver, "Multiple travelling-wave solutions in a minimal model for cell motility", *Mathematical Medicine and Biology* 30 (2013), pp. 241–272, DOI: 10.1093/imammb/dqs023.

[105] L. S. Kimpton, J. P. Whiteley, S. L. Waters, and J. M. Oliver, "On a poroviscoelastic model for cell crawling", *Journal of Mathematical Biology* 70 (2015), pp. 133–171, DOI: 10.1007/s00285-014-0755-1.

[106] R. D. O'Dea, S. L. Waters, and H. M. Byrne, "A two-fluid model for tissue growth within a dynamic flow environment", *European Journal of Applied Mathematics* 19 (2008), pp. 607–634, DOI: 10.1017/S0956792508007687.

[107] J. E. F. Green, S. L. Waters, K. M. Shakesheff, and H. M. Byrne, "A mathematical model of liver cell aggregation *In vitro*", *Bulletin of Mathematical Biology* 71 (2009), pp. 906–930, DOI: 10.1007/s11538-008-9387-1.

[108] S. R. Lubkin and T. L. Jackson, "Multiphase mechanics of capsule formation in tumors", *Journal of Biomechanical Engineering* 124 (2002), pp. 237–243, DOI: 10.1115/1.1427925.

[109] T. L. Jackson and H. M. Byrne, "A mechanical model of tumor encapsulation and transcapsular spread", *Mathematical Biosciences* 180 (2002), pp. 307–328, DOI: 10.1016/S0025-5564(02)00118-9.

[110] J. R. King and J. M. Oliver, "Thin-film modelling of poroviscous free surface flows", *European Journal of Applied Mathematics* 16 (2005), pp. 519–553, DOI: 10.1017/s095679250500584x.

[111] N. G. Cogan and J. P. Keener, "The role of biofilm matrix in structural development", *Mathematical Medicine and Biology* 21 (2004), pp. 147–166, DOI: 10.1093/imammb21.2.147.

[112] K. Anguige, J. R. King, and J. P. Ward, "A multi-phase mathematical model of quorum sensing in a maturing *Pseudomonas aeruginosa* biofilm", *Mathematical Biosciences* 203 (2006), pp. 240–276, DOI: 10.1016/j.mbs.2006.05.009.

[113] T. Zhang, N. G. Cogan, and Q. Wang, "Phase-field models for biofilms II: 2-D numerical simulations of biofilm–flow interaction", *Communications in Computational Physics* 4 (2008), pp. 72–101.

[114] B. Lindley, Q. Wang, and T. Zhang, "Multicomponent hydrodynamic model for heterogeneous biofilms: two-dimensional numerical simulations of growth and interaction with flows", *Physical Review E* 85 (2012), 031908, DOI: 10.1103/PhysRevE.85.031908.

[115] F. Clarelli, C. Di Russo, R. Natalini, and M. Ribot, "A fluid dynamics multidimensional model of biofilm growth: stability, influence of environment and sensitivity", *Mathematical Medicine and Biology* (2015), pp. 1–25, DOI: 10.1093/imammb/dqv024.

[116] D. A. Drew, "Mathematical modeling of two-phase flow", *Annual Review of Fluid Mechanics* 15 (1983), pp. 261–291, DOI: 10.1146/annurev.fl.15.010183.001401.

[117] D. J. Acheson, *Elementary Fluid Dynamics*, Oxford University Press, 1990.

[118] S. J. Franks, H. M. Byrne, J. R. King, J. C. E. Underwood, and C. E. Lewis, "Modelling the early growth of ductal carcinoma in situ of the breast", *Journal of Mathematical Biology* 47 (2003), pp. 424–452, DOI: 10.1007/s00285-003-0214-x.

[119] R. D. O'Dea, S. L. Waters, and H. M. Byrne, "A multiphase model for tissue construct growth in a perfusion bioreactor", *Mathematical Medicine and Biology* 27 (2010), pp. 95–127, DOI: 10.1093/imammb/dqp003.

[120] J. P. Ward and J. R. King, "Thin-film modelling of biofilm growth and quorum sensing", *Journal of Engineering Mathematics* 73 (2012), pp. 71–92, DOI: 10.1007/s10665-011-9490-4.

[121] C. J. W. Breward, H. M. Byrne, and C. E. Lewis, "The role of cell–cell interactions in a two-phase model for avascular tumour growth", *Journal of Mathematical Biology* 45 (2002), pp. 125–152, DOI: 10.1007/s002850200149.

[122] G. Lemon, J. R. King, H. M. Byrne, O. E. Jensen, and K. M. Shakesheff, "Mathematical modelling of engineered tissue growth using a multiphase porous flow mixture theory", *Journal of Mathematical Biology* 52 (2006), pp. 571–594, DOI: 10.1007/s00285-005-0363-1.

[123] J. E. F. Green, J. P. Whiteley, J. M. Oliver, H. M. Byrne, and S. L. Waters, "Pattern formation in multiphase models of chemotactic cell aggregation", *Mathematical Medicine and Biology* 35 (2017), pp. 319–346, DOI: 10.1093/imammb/dqx005.

[124] O. A. Croze, G. P. Ferguson, M. E. Cates, and W. C. K. Poon, "Migration of chemotactic bacteria in soft agar: role of gel concentration", *Biophysical Journal* 101 (2011), pp. 525–534, DOI: 10.1016/j.bpj.2011.06.023.

[125] M. A. Bees, P. Andresén, E. Mosekilde, and M. Givskov, "The interaction of thin-film flow, bacterial swarming and cell differentiation in colonies of *Serratia liquefaciens*", *Journal of Mathematical Biology* 40 (2000), pp. 27–63, DOI: 10.1007/s002850050004.

[126] T. E. Angelini, M. Roper, R. Kolter, D. A. Weitz, and M. P. Brenner, "*Bacillus subtilis* spreads by surfing on waves of surfactant", *Proceedings of the National Academy of Sciences of the United States of America* 106 (2009), pp. 18109–18113, DOI: 10.1073/pnas.0905890106.

[127] S. Srinivasan, C. N. Kaplan, and L. Mahadevan, "A multiphase theory for spreading microbial swarms and films", *eLife* 8 (2019), e42697, DOI: 10.7554/eLife.42697.

[128] J. P. Ward, J. R. King, A. J. Koerber, J. M. Croft, R. E. Sockett, and P. Williams, "Early development and quorum sensing in bacterial biofilms", *Journal of Mathematical Biology* 47 (2003), pp. 23–55, DOI: 10.1007/s00285-002-0190-6.

[129] S. Trinschek, K. John, S. Lecuyer, and U. Thiele, "Continuous versus arrested spreading of biofilms at solid–gas interfaces: the role of surface

forces", *Physical Review Letters* 119 (2017), 078003, DOI: 10.1103/PhysRevLett.119.078003.

[130] S. Trinschek, K. John, and U. Thiele, "Modelling of surfactant-driven front instabilities in spreading bacterial colonies", *Soft Matter* 14 (2018), pp. 4464–4476, DOI: 10.1039/c8sm00422f.

[131] S. D. Howison, *Practical Applied Mathematics*, Cambridge University Press, 2005, DOI: 10.1017/CBO9780511813252.

[132] A. Tam, J. E. F. Green, S. Balasuriya, E. L. Tek, J. M. Gardner, J. F. Sundstrom, V. Jiranek, and B. J. Binder, "A thin-film extensional flow model for biofilm expansion by sliding motility", *Proceedings of the Royal Society of London A* 475 (2019), 20190175, DOI: 10.1098/rspa.2019.0175.

[133] N. Otsu, "A threshold selection method from gray-level histograms", *IEEE Transactions on Systems, Man, and Cybernetics* 9 (1979), pp. 62–66, DOI: 10.1109/TSMC.1979.4310076.

[134] B. J. Binder and M. J. Simpson, "Spectral analysis of pair-correlation bandwidth: application to cell biology images", *Royal Society Open Science* 2 (2015), 140494, DOI: 10.1098/rsos.140494.

[135] A. L. Slade, A. E. Cremers, and H. C. Thomas, "The obstruction effect in the self-diffusion coefficients of sodium and cesium in agar gels", *Journal of Physical Chemistry* 70 (1966), pp. 2840–2844, DOI: 10.1021/j100881a020.

[136] L. G. Longsworth, "Diffusion in liquids and the Stokes–Einstein relation", *Electrochemistry in biology and medicine*, ed. by T. Shedlovsky, John Wiley & Sons, Inc., 1955, chap. 12, pp. 225–247, DOI: 10.1016/0002-8703(55)90290-8.

[137] D. G. Aronson, "Density-dependent interaction–diffusion systems", *Dynamics and modelling of reactive systems*, Proceedings of an Advanced Seminar Conducted by the Mathematics Research Center, the

University of Wisconsin, Madison, ed. by W. E. Stewart, W. H. Ray, and C. C. Conley, vol. 44, Academic Press, 1980, pp. 161–176, DOI: 10.1016/B978-0-12-669550-2.50010-5.

[138] N. Fenichel, "Geometric singular perturbation theory for ordinary differential equations", *Journal of Differential Equations* 31 (1979), pp. 53–98, DOI: 10.1016/0022-0396(79)90152-9.

[139] N. Fenichel, "Persistence and smoothness of invariant manifolds for flows", *Indiana University Mathematics Journal* 21 (1972), pp. 193–226, DOI: 10.1512/iumj.1971.21.21017.

[140] G. Hek, "Geometric singular perturbation theory in biological practice", *Journal of Mathematical Biology* 60 (2010), pp. 347–386, DOI: 10.1007/s00285-009-0266-7.

[141] C. K. R. T. Jones, "Geometric singular perturbation theory", *Dynamical systems*, ed. by R. Johnson, Lecture Notes in Math. 1609, Springer, 1995, chap. 2, pp. 44–118, DOI: 10.1007/bfb0095237.

[142] J. Alexander, R. Gardner, and C. K. R. T. Jones, "A topological invariant arising in the stability analysis of travelling waves", *Journal für die reine und angewandte Mathematik* 410 (1990), pp. 167–212, DOI: 10.1515/crll.1990.410.167.

[143] K. T. Alligood, T. D. Sauer, and J. A. Yorke, *Chaos: an Introduction to Dynamical Systems*, Springer, 1996, DOI: 10.1007/b97589.

[144] W. H. Press, S. A. Teukolsky, W. T. Vetterling, and B. P. Flannery, *Numerical Recipes: The Art of Scientific Computing*, Third edition, Cambridge University Press, 2007.

[145] D. Hilhorst, R. Kersner, E. Logak, and M. Mimura, "Interface dynamics of the Fisher equation with degenerate diffusion", *Journal of Differential Equations* 244 (2008), pp. 2870–2889, DOI: 10.1016/j.jde.2008.02.018.

[146] J. Francisco Leyva, C. Málaga, and R. G. Plaza, "The effects of nutrient chemotaxis on bacterial aggregation patterns with non-linear degenerate cross diffusion", *Physica A: Statistical Mechanics and its Applications* 392 (2013), pp. 5644–5662, DOI: 10.1016/j.physa.2013.07.022.

[147] Y. Saad and M. H. Schultz, "GMRES: A generalized minimal residual algorithm for solving nonsymmetric linear systems", *SIAM Journal on Scientific and Statistical Computing* 7 (1986), pp. 856–869, DOI: 10.1137/0907058.

[148] P. D. Howell, B. Scheid, and H. A. Stone, "Newtonian pizza: spinning a viscous sheet", *Journal of Fluid Mechanics* 659 (2010), pp. 1–23, DOI: 10.1017/S0022112010001564.

[149] G. K. Batchelor, *An Introduction to Fluid Dynamics*, Cambridge University Press, 1967.

[150] R. M. Harshey, "Bacterial motility on a surface: many ways to a common goal", *Annual Review of Microbiology* 57 (2003), pp. 249–273, DOI: 10.1146/annurev.micro.57.030502.091014.

[151] J. Chandra, D. M. Kuhn, P. K. Mukherjee, L. L. Hoyer, T. McCormick, and M. A. Ghannoum, "Biofilm formation by the fungal pathogen *Candida albicans*: development, architecture, and drug resistance", *Journal of Bacteriology* 183 (2001), pp. 5385–5394, DOI: 10.1128/JB.183.18.5385-5394.2001.

[152] P. S. Stewart, "A review of experimental measurements of effective diffusive permeabilities and effective diffusion coefficients in biofilms", *Biotechnology and Bioengineering* 59 (1998), pp. 261–272, DOI: 10.1002/(SICI)1097-0290(19980805)59:3<261::AID-BIT1>3.0.CO;2-9.

[153] A. A. Vicente, M. Dluhý, E. C. Ferreira, M. Mota, and J. A. Teixeira, "Mass transfer properties of glucose and O_2 in *Saccharomyces cerevisiae*

flocs", *Biochemical Engineering Journal* 2 (1998), pp. 35–43, DOI: 10.1016/S1369-703X(98)00015-1.

[154] J. Crank, *Free and Moving Boundary Problems*, Oxford Science Publications, 1984.

[155] A. L. Bertozzi and M. P. Brenner, "Linear stability and transient growth in driven contact lines", *Physics of Fluids* 9 (1997), pp. 530–539, DOI: 10.1063/1.869217.

[156] T. G. Myers, "Thin films with high surface tension", *SIAM Review* 40 (1998), pp. 441–462, DOI: 10.1137/S003614459529284X.

[157] L. C. Mayo, S. W. McCue, and T. J. Moroney, "Gravity-driven fingering simulations for a thin liquid film flowing down the outside of a vertical cylinder", *Physical Review E* 87 (2013), 053018, DOI: 10.1103/physreve.87.053018.

[158] C. T. Kelley, *Iterative methods for linear and nonlinear equations*, Society for Industrial and Applied Mathematics, 1995, DOI: 10.1137/1.9781611970944.